

Copyright  
by  
John Andrew Evans  
2011

The Dissertation Committee for John Andrew Evans  
certifies that this is the approved version of the following dissertation:

**Divergence-free B-spline Discretizations for Viscous  
Incompressible Flows**

Committee:

---

Thomas J. R. Hughes, Supervisor

---

Ivo Babuška

---

Leszek F. Demkowicz

---

Omar Ghattas

---

Robert D. Moser

---

Yuri Bazilevs

**Divergence-free B-spline Discretizations for Viscous  
Incompressible Flows**

**by**

**John Andrew Evans, B.S.; M.S.; M.S.C.A.M.**

**DISSERTATION**

Presented to the Faculty of the Graduate School of  
The University of Texas at Austin  
in Partial Fulfillment  
of the Requirements  
for the Degree of

**DOCTOR OF PHILOSOPHY**

THE UNIVERSITY OF TEXAS AT AUSTIN

December 2011

Dedicated to the memory of John Grover Evans.

## Acknowledgments

It is said there is no such thing as an original idea. I find this statement incredibly telling in the modern world of research. Indeed, most of the notions that form the backbone of this dissertation emanate from long hours spent reading papers, attending seminars, and speaking to colleagues. Only with the knowledge obtained from these activities was I finally able to connect the dots and develop what may be conceived of as a “novelty”. Hence, I advise all current and future graduate students to keep on reading the literature and attending those seminars. Eventually, the spark will light.

My thanks goes out to those who supported me throughout my academic career. I would not have been able to complete this dissertation without their help. In particular, I would like to thank the following: Professor Thomas J.R. Hughes, my advisor, for his endless guidance, vision, patience, and encouragement. Sarah, my fiancée, for her care, understanding, and willingness to listen to the inane details of my work. My parents, John and Suzanne, for instilling in me a strong sense of responsibility, commitment, and perseverance. Professors Kurt S. Anderson and Kenneth E. Jansen, my bachelor’s and master’s advisors, for introducing me to the wonderful world of scientific research. Professors Giancarlo Sangalli and Annalisa Buffa, my collaborators from the University of Pavia in Italy, for their helpful contributions and for their many discussions regarding the work presented in this dissertation. Professors Ivo Babuška, Leszek F. Demkowicz, Omar Ghattas, Robert D. Moser, and Yuri Bazilevs, my committee members, for their useful comments

and suggestions to improve the quality of this work. The Department of Energy's Office of Science and National Nuclear Security Administration for supporting my research through the Computational Science Graduate Fellowship program. And finally, my many colleagues, for their friendship and for creating a fun and exciting atmosphere without which I would never have made it through the doctoral process.

# **Divergence-free B-spline Discretizations for Viscous Incompressible Flows**

John Andrew Evans, Ph.D.  
The University of Texas at Austin, 2011

Supervisor: Thomas J. R. Hughes

The incompressible Navier-Stokes equations are among the most important partial differential systems arising from classical physics. They are utilized to model a wide range of fluids, from water moving around a naval vessel to blood flowing through the arteries of the cardiovascular system. Furthermore, the secrets of turbulence are widely believed to be locked within the Navier-Stokes equations. Despite the enormous applicability of the Navier-Stokes equations, the underlying behavior of solutions to the partial differential system remains little understood. Indeed, one of the Clay Mathematics Institute's famed Millennium Prize Problems involves the establishment of existence and smoothness results for Navier-Stokes solutions, and turbulence is considered, in the words of famous physicist Richard Feynman, to be "the last great unsolved problem of classical physics."

Numerical simulation has proven to be a very useful tool in the analysis of the Navier-Stokes equations. Simulation of incompressible flows now plays a major role in the industrial design of automobiles and naval ships, and simulation has even been utilized to study the Navier-Stokes existence and smoothness problem. In spite of these successes, state-of-the-art incompressible flow solvers are not without

their drawbacks. For example, standard turbulence models which rely on the existence of an energy spectrum often fail in non-trivial settings such as rotating flows. More concerning is the fact that most numerical methods do not respect the fundamental geometric properties of the Navier-Stokes equations. These methods only satisfy the incompressibility constraint in an approximate sense. While this may seem practically harmless, conservative semi-discretizations are typically guaranteed to balance energy if and only if incompressibility is satisfied pointwise. This is especially alarming as both momentum conservation and energy balance play a critical role in flow structure development. Moreover, energy balance is inherently linked to the numerical stability of a method.

In this dissertation, novel B-spline discretizations for the generalized Stokes and Navier-Stokes equations are developed. The cornerstone of this development is the construction of smooth generalizations of Raviart-Thomas-Nédélec elements based on the new theory of isogeometric discrete differential forms. The discretizations are (at least) patch-wise  $C^0$  and hence can be directly utilized in the Galerkin solution of viscous flows for single-patch configurations. When applied to incompressible flows, the discretizations produce pointwise divergence-free velocity fields. This results in methods which properly balance both momentum and energy at the semi-discrete level. In the presence of multi-patch geometries or no-slip walls, the discontinuous Galerkin framework can be invoked to enforce tangential continuity without upsetting the conservation and stability properties of the method across patch boundaries. This also allows our method to default to a compatible discretization of Darcy or Euler flow in the limit of vanishing viscosity. These attributes in conjunction with the local stability properties and resolution power of B-splines make these discretizations an attractive candidate for reliable numerical simulation of viscous incompressible flows.

# Table of Contents

<b>Acknowledgments</b>	<b>v</b>
<b>Abstract</b>	<b>vii</b>
<b>List of Tables</b>	<b>xiii</b>
<b>List of Figures</b>	<b>xv</b>
<b>Chapter 1. Introduction</b>	<b>1</b>
1.1 Motivation . . . . .	1
1.2 Accomplishments of the Dissertation . . . . .	3
1.3 Structure of the Dissertation . . . . .	5
<b>Chapter 2. The Algebraic Structure of Generalized Stokes Flow</b>	<b>7</b>
2.1 Generalized Stokes Flow and Inf-Sup Stability . . . . .	7
2.2 Vector Potentials and Harmonic Forms . . . . .	13
<b>Chapter 3. The Geometric Structure of Navier-Stokes Flow</b>	<b>19</b>
3.1 Balance of Momentum . . . . .	22
3.2 Balance of Kinetic Energy . . . . .	22
3.3 Balance of Vorticity . . . . .	24
3.4 Balance of Enstrophy . . . . .	26
3.5 Balance of Helicity . . . . .	28
<b>Chapter 4. B-splines and Geometrical Mappings</b>	<b>32</b>
4.1 Univariate B-splines . . . . .	33
4.2 Multivariate B-splines . . . . .	35
4.3 Piecewise Smooth Functions, Geometrical Mappings, and Physical Mesh Entities . . . . .	37

<b>Chapter 5. Discretization of Velocity and Pressure Fields</b>	<b>42</b>
5.1 Notation: Sobolev Spaces . . . . .	42
5.2 B-spline Spaces Satisfying the de Rham Diagram . . . . .	45
5.3 The Stokes Hilbert Complex . . . . .	57
5.4 B-spline Spaces Satisfying the Stokes Diagram . . . . .	61
5.5 Interpolation Estimates . . . . .	66
5.6 Inverse and Trace Inequalities . . . . .	67
<b>Chapter 6. Approximation of the Generalized Stokes Problem</b>	<b>70</b>
6.1 The Continuous Problem . . . . .	72
6.2 The Discretized Problem . . . . .	73
6.3 Continuity and Stability . . . . .	77
6.4 <i>A Priori</i> Error Estimates . . . . .	85
6.5 Extension to Multi-Patch Domains . . . . .	94
6.6 Numerical Verification of Convergence Estimates . . . . .	98
6.6.1 Two-Dimensional Manufactured Solution . . . . .	99
6.6.2 Three-Dimensional Manufactured Solution . . . . .	104
6.6.3 Two-Dimensional Problem with a Singular Solution . . . . .	109
6.6.4 Cylindrical Couette Flow . . . . .	113
6.6.5 Annular Poiseuille Flow . . . . .	123
6.7 Benchmark Problems . . . . .	126
6.7.1 Two-Dimensional Lid-Driven Cavity Flow . . . . .	131
6.7.2 Three-Dimensional Lid-Driven Cavity Flow . . . . .	135
6.7.3 Flow Over a Backwards Facing Step . . . . .	140
6.7.4 Darcy-Dominated Flow with Sharp Boundary Layers . . . . .	144
<b>Chapter 7. Approximation of the Steady Navier-Stokes Problem</b>	<b>150</b>
7.1 The Continuous Problem . . . . .	152
7.2 The Discretized Problem . . . . .	154
7.3 Well-Posedness for Small Data . . . . .	158
7.4 <i>A Priori</i> Error Estimates for Small Data . . . . .	165
7.5 Extension to Multi-Patch Domains . . . . .	170
7.6 Numerical Verification of Convergence Estimates . . . . .	172

7.6.1	Two-Dimensional Manufactured Solution . . . . .	172
7.6.2	Three-Dimensional Manufactured Solution . . . . .	176
7.6.3	Kovaszny Flow . . . . .	179
7.7	Benchmark Problems . . . . .	180
7.7.1	Two-Dimensional Lid-Driven Cavity Flow . . . . .	183
7.7.2	Confined Jet Impingement . . . . .	198
<b>Chapter 8.</b>	<b>Approximation of the Unsteady Stokes Problem</b>	<b>203</b>
8.1	The Continuous Problem . . . . .	204
8.2	The Semi-Discrete Problem . . . . .	206
8.3	Global Existence and Uniqueness . . . . .	209
8.4	<i>A Priori</i> Error Estimates . . . . .	211
8.5	Spectrum Analysis . . . . .	224
<b>Chapter 9.</b>	<b>Approximation of the Unsteady Navier-Stokes Problem</b>	<b>232</b>
9.1	The Continuous Problem . . . . .	235
9.2	The Semi-Discrete Problem . . . . .	237
9.3	Energy Balance . . . . .	238
9.4	Global Existence and Uniqueness . . . . .	240
9.5	<i>A Priori</i> Error Estimates . . . . .	240
9.6	Conservation Properties on Rectilinear Domains . . . . .	246
9.7	Conservation Properties on Cylindrical Domains . . . . .	248
9.8	Vorticity, Enstrophy, and Helicity . . . . .	252
9.9	Extension to Multi-Patch Domains . . . . .	257
9.10	Numerical Verification of Convergence Estimates . . . . .	257
9.10.1	Two-Dimensional Taylor-Green Vortex Flow . . . . .	258
9.10.2	Alternating Cylindrical Couette Flow . . . . .	262
9.11	Benchmark Problems . . . . .	268
9.11.1	Two-Dimensional Flow Over a Cylinder . . . . .	268
9.11.2	Three-Dimensional Taylor-Green Vortex Flow . . . . .	273
<b>Chapter 10.</b>	<b>Conclusions and Future Work</b>	<b>280</b>
<b>Bibliography</b>		<b>283</b>

## List of Tables

1.1	Notational convections . . . . .	6
6.1	Dependence of the inf-sup constant on Nitsche’s penalty constant . . .	85
6.2	Generalized Stokes convergence rates in 2-D: $Da = 0$ . . . . .	101
6.3	Generalized Stokes convergence rates in 2-D: $Da = 1$ . . . . .	102
6.4	Generalized Stokes convergence rates in 2-D: $Da = 1000$ . . . . .	103
6.5	Generalized Stokes convergence rates in 3-D: $Da = 0$ . . . . .	106
6.6	Generalized Stokes convergence rates in 3-D: $Da = 1$ . . . . .	107
6.7	Generalized Stokes convergence rates in 3-D: $Da = 1000$ . . . . .	108
6.8	Singular Stokes convergence rates in 2-D . . . . .	112
6.9	Cylindrical Couette flow convergence rates: $\gamma = 0$ . . . . .	119
6.10	Cylindrical Couette flow convergence rates: $\gamma = \sqrt{50}$ . . . . .	120
6.11	Cylindrical Couette flow: Patch template control points . . . . .	122
6.12	Annular Poiseuille convergence rates for polar meshes and $\gamma = 0$ . .	127
6.13	Annular Poiseuille convergence rates for NURBS and $\gamma = 0$ . . . .	128
6.14	Annular Poiseuille convergence rates for polar meshes and $\gamma = \sqrt{50}$	129
6.15	Annular Poiseuille convergence rates for NURBS and $\gamma = \sqrt{50}$ . .	130
6.16	Convergence for lid-driven Stokes flow in a two-dimensional cavity	136
6.17	Convergence for Stokes flow over a backward facing step . . . . .	142
7.1	Steady vortex flow convergence rates in 2-D: $Re = 1$ . . . . .	174
7.2	Robustness of 2-D divergence-free B-splines as $Re \rightarrow \infty$ . . . . .	175
7.3	Instability of 2-D Taylor-Hood elements as $Re \rightarrow \infty$ . . . . .	175
7.4	Steady vortex flow convergence rates in 3-D: $Re = 1$ . . . . .	178
7.5	Robustness of 3-D divergence-free B-splines as $Re \rightarrow \infty$ . . . . .	179
7.6	Steady Kovasznay flow convergence rates: $Re = 40$ . . . . .	182
7.7	Two-dimensional lid-driven cavity flow: Velocity extrema . . . . .	188

9.1	Taylor-Green vortex flow: Convergence rates at $Re = 100$	259
9.2	Alternating Couette flow: Convergence rates at $Re = 200$	266

## List of Figures

2.1	An alternative view of the de Rham complex . . . . .	16
3.1	Tangling of vortex tubes . . . . .	31
4.1	Cubic B-spline basis functions . . . . .	34
4.2	Independence of the parametric mapping from $h$ . . . . .	39
5.1	Visualization of control net and physical mesh . . . . .	52
5.2	Visualization of basis function of $\mathcal{S}_h$ . . . . .	53
5.3	Visualization of first-component vector basis function of $\mathcal{RT}_h$ . . . . .	54
5.4	Visualization of second-component vector basis function of $\mathcal{RT}_h$ . . . . .	55
5.5	Visualization of basis function of $\mathcal{W}_h$ . . . . .	56
5.6	Divergence-preserving property of the Piola transform . . . . .	57
6.1	Multi-patch construction . . . . .	95
6.2	Generalized Stokes manufactured solution in 2-D . . . . .	100
6.3	Generalized Stokes manufactured solution in 3-D . . . . .	105
6.4	Singular Stokes solution in 2-D: Problem setup . . . . .	110
6.5	Singular Stokes solution in 2-D: Exact solution . . . . .	111
6.6	Cylindrical Couette flow: Problem setup . . . . .	115
6.7	Cylindrical Couette flow: Flow velocity arrows . . . . .	116
6.8	Cylindrical Couette flow: Sequence of polar meshes . . . . .	117
6.9	Cylindrical Couette flow: NURBS multi-patch construction . . . . .	121
6.10	Cylindrical Couette flow: Patch template control points . . . . .	121
6.11	Annular Poiseuille flow: Problem setup . . . . .	123
6.12	Annular Poiseuille flow: Axial velocity . . . . .	125
6.13	Lid-driven Stokes flow in a two-dimensional cavity: Problem setup . . . . .	132
6.14	Lid-driven Stokes flow in a two-dimensional cavity: Streamlines . . . . .	133
6.15	Lid-driven Stokes flow in a two-dimensional cavity: Velocity field . . . . .	134

6.16	Lid-driven Stokes flow in a three-dimensional cavity: Problem setup	137
6.17	Lid-driven Stokes flow in a three-dimensional cavity: Streamlines	138
6.18	Lid-driven Stokes flow in a three-dimensional cavity: Velocity field	139
6.19	Stokes flow over a backward facing step: Problem setup	141
6.20	Stokes flow over a backward facing step: Streamlines	143
6.21	Darcy-dominated flow with boundary layers: Velocity field	146
6.22	Darcy-dominated flow with boundary layers: First-component view	147
6.23	Darcy-dominated flow with boundary layers: Cross-section view	148
6.24	Darcy-dominated flow with boundary layers: Compression	149
7.1	Steady Kovasznay flow solution	181
7.2	Lid-driven cavity flow: Streamlines for $Re = 100$	184
7.3	Lid-driven cavity flow: Streamlines for $Re = 400$	185
7.4	Lid-driven cavity flow: Streamlines for $Re = 1000$	186
7.5	Lid-driven cavity flow: Velocity field for $h = 1/32$ and $Re = 100$	189
7.6	Lid-driven cavity flow: Velocity field for $h = 1/64$ and $Re = 100$	190
7.7	Lid-driven cavity flow: Velocity field for $h = 1/128$ and $Re = 100$	191
7.8	Lid-driven cavity flow: Velocity field for $h = 1/32$ and $Re = 400$	192
7.9	Lid-driven cavity flow: Velocity field for $h = 1/64$ and $Re = 400$	193
7.10	Lid-driven cavity flow: Velocity field for $h = 1/128$ and $Re = 400$	194
7.11	Lid-driven cavity flow: Velocity field for $h = 1/32$ and $Re = 1000$	195
7.12	Lid-driven cavity flow: Velocity field for $h = 1/64$ and $Re = 1000$	196
7.13	Lid-driven cavity flow: Velocity field for $h = 1/128$ and $Re = 1000$	197
7.14	Confined jet impingement: Physical setup	199
7.15	Confined jet impingement: Model problem description	200
7.16	Confined jet impingement: Results for a coarse mesh	201
7.17	Confined jet impingement: Results for a resolved mesh	202
8.1	Stokes spectrum for divergence-free B-splines	226
8.2	Stokes spectrum for Taylor-Hood elements	227
8.3	Stokes spectrum for $\mathbf{Q}^{k+1} - P^k$ elements	228
8.4	Stokes spectrum for the MAC scheme	229
8.5	Stokes spectrum for divergence-free Raviart-Thomas elements	231

9.1	Phase errors for the first-order wave equation . . . . .	234
9.2	2-D Taylor-Green vortex flow: Error versus time . . . . .	260
9.3	2-D Taylor-Green vortex flow: Blow up of Taylor-Hood elements . . . . .	261
9.4	Alternating Couette flow: Problem setup . . . . .	263
9.5	Alternating Couette flow: Evolution of the angular velocity field . . . . .	264
9.6	Alternating Couette flow: Error versus time . . . . .	267
9.7	Unsteady flow over a cylinder: Problem setup . . . . .	269
9.8	Unsteady flow over a cylinder: Multi-patch construction . . . . .	270
9.9	Unsteady flow over a cylinder: Mesh for Patches 1-4 . . . . .	270
9.10	Unsteady flow over a cylinder: Streamlines for $Re = 100$ . . . . .	271
9.11	3-D Taylor-Green vortex flow: Time history of the dissipation rate . . . . .	274
9.12	3-D Taylor-Green vortex flow: Enstrophy field at $t = 0$ for $Re = 200$ . . . . .	277
9.13	3-D Taylor-Green vortex flow: Enstrophy field at $t = 6$ for $Re = 200$ . . . . .	278
9.14	3-D Taylor-Green vortex flow: Convergence of dissipation rate . . . . .	279
10.1	Hierarchical B-spline simulation of lid-driven cavity flow . . . . .	282

# Chapter 1

## Introduction

### 1.1 Motivation

Many systems of differential equations exhibit important mathematical structure, often in the form of topological constraints, conservation or balance laws, symmetries, positivity structures, and maximum principles. Compatible discretizations are defined as numerical methods which preserve such structure. The simplest compatible discretizations appear in the field of Hamiltonian mechanics. These discretizations, known as symplectic integrators, possess as a conserved quantity a discrete Hamiltonian [60]. By virtue of this conservation property, symplectic integrators are well-behaved for long-term evolution of chaotic Hamiltonian systems from the Kepler two-body problem to classical simulations in molecular dynamics.

Recently, compatible spatial discretizations have become popular for the numerical solution of partial differential equations. Such discretizations are especially prevalent in computational electromagnetism. It is well-known that the Maxwell's equations are endowed with beautiful algebraic structure which is encompassed in the classical de Rham complex [70]. Coincidentally, preservation of this structure is vital to the development of stable and convergent approximations of Maxwell's eigenvalue problem [28]. Compatible spatial discretizations are also widely used in the analysis of Darcy flow [5], where it is known that conservation of mass is critical to physically realistic simulation of transport, and in the analysis of convection-diffusion phenomena [76], where discrete approximations are

not always guaranteed to satisfy a very basic positivity principle. These discretizations have even been utilized in the analysis of compressible fluids and solids [112], where satisfaction of the second law of thermodynamics is necessary for physically relevant simulations.

Systems of partial differential equations describing the evolution of viscous incompressible flow are also endowed with vast algebraic and geometric structure. The generalized Stokes equations have a topological structure that can be succinctly described through a cochain complex. The Navier-Stokes equations are infused with even more structure, evidenced by a wide array of balance laws for momentum, angular momentum, energy, vorticity, enstrophy, and helicity. These balance laws are of prime importance in the evolution of laminar and turbulent flow structures [151], and they are even believed to play a role in the regularity of Navier-Stokes solutions, widely considered to be one of the greatest unsolved problems in mathematics.

The key to unlocking much of the structure of the generalized Stokes and Navier-Stokes equations is precisely the volume-preserving nature of incompressible flow, yet most numerical methods only satisfy the incompressibility constraint in an approximate sense. Consequently, such methods do not obey many fundamental laws of physics. In particular, semi-discretizations which conserve momentum are typically guaranteed to balance energy if and only if the incompressibility constraint is satisfied pointwise. This is especially alarming considering the importance of both momentum conservation and energy balance in flow structure development. Moreover, energy balance is inherently linked to the numerical stability of a method [132].

In this dissertation, new B-spline discretizations for viscous incompressible flows are introduced which exactly satisfy the incompressibility constraint. As in-

compressibility is satisfied pointwise, these discretizations replicate the algebraic and geometric structure of the generalized Stokes and Navier-Stokes equations. These attributes in conjunction with the local stability properties and resolution power of B-splines make these discretizations an attractive candidate for reliable numerical simulation of viscous incompressible flows. It is hoped that these discretizations may become useful tools for both engineering analysis as well as the mathematical study of the Navier-Stokes equations.

## **1.2 Accomplishments of the Dissertation**

With the completion of this dissertation, we have accomplished the following tasks.

1. We have constructed divergence-conforming B-spline discretizations for general viscous incompressible flows. We have mapped these discretizations to geometries of scientific and engineering interest using divergence- and integral-preserving transformations, and we have extended our discretizations to flows subject to no-slip boundary conditions as well as to so-called multi-patch configurations by employing tools stemming from the discontinuous Galerkin community.
2. We have successfully proven stability and convergence estimates for our discretization scheme as applied to the generalized Stokes equations, the steady Navier-Stokes equations, the unsteady Stokes equations, and the unsteady Navier-Stokes equations on single-patch configurations. Our convergence estimates are optimal for the velocity field and suboptimal, by one order, for the pressure field. Our theoretical analysis also covers singular solutions typically seen in practice.

3. We have proven that our spatial discretization scheme for the unsteady Navier-Stokes equations satisfies balance laws for momentum, energy, vorticity, enstrophy, and helicity. Additionally, we have proven our scheme satisfies an axial angular momentum balance law on cylindrical domains.
4. To verify our theoretical results, we have numerically simulated a number of flow problems with known analytical solutions on rectilinear and cylindrical domains. These simulations have confirmed our theoretical estimates and further revealed that our discrete pressure fields converge at optimal order, suggesting that our *a priori* estimates may be conservative. These simulations have also indicated that our methodology is robust with respect to the ratio of drag to viscosity in the context of generalized Stokes flow and with respect to the Reynold's number in the context of Navier-Stokes flow. This is in contrast with many traditional finite element and finite difference technologies.
5. We have conducted a full spectrum analysis of our discretization technique as applied to the Stokes eigen-problem. This analysis has revealed that the use of our discretization technique results in dramatically improved accuracy in spectral calculations over traditional finite element and finite difference technologies such as the Taylor-Hood element and the Marker-and-Cell scheme.
6. We have simulated a number of standard benchmark problems using our discretization scheme, including lid-driven cavity flow, creeping flow over a backwards facing step, confined jet impingement, unsteady flow over a cylinder, and three-dimensional Taylor-Green vortex flow. The results of these simulations have indicated the enhanced stability and accuracy properties of our method. For example, the lid-driven cavity results we have obtained using

the lowest-order member of our discretization family are much more accurate than comparative results we have seen in the literature.

In addition to the above, many other projects have been pursued during the course of completing this dissertation, including (i) an analysis of the approximation properties of B-splines via the lens of Kolmogorov  $n$ -widths [73], (ii) the construction of variational methods which automatically satisfy physical constraints such as positivity or monotonicity [74, 76], (iii) the development of stable one-point quadrature elements for the simulation of thin plates [36, 163], (iv) the construction of novel stabilized methods for convection-reaction-diffusion equations, and (v) a variety of projects related to the emerging field of isogeometric analysis [17, 30, 75, 137]. For the sake of brevity, these projects will not be covered in this written dissertation.

### **1.3 Structure of the Dissertation**

This dissertation is organized in a hierarchical manner. The material in later chapters relies heavily on material appearing in earlier chapters. Hence, it is recommended that the dissertation be read in a linear fashion. That being said, we refer back to preceding chapters whenever necessary. For reference, the most common notational conventions are listed in Table 1.1.

An outline of the dissertation is as follows. In Chapter 2, the algebraic structure of Stokes flow is examined and tools from algebraic topology are used to establish existence and uniqueness results. In Chapter 3, the geometric structure of Navier-Stokes flow is studied and balance laws for momentum, energy, vorticity, enstrophy, and helicity are derived. In Chapter 4, we briefly review the construction of B-splines which form the building blocks of our discretization technique. In

$\widehat{\Omega}$	Parametric domain
$\Omega$	Physical domain
$\partial\Omega$	Boundary of the physical domain
$\mathcal{M}_h$	Parametric mesh
$\mathcal{K}_h$	Physical mesh
$\Gamma_h$	Boundary mesh associated with the physical domain
$\mathcal{V}_h$	Space of discrete velocity fields
$\mathcal{Q}_h$	Space of discrete pressure fields
$\mathcal{V}_{0,h}$	Space of discrete velocity fields subject to no-penetration BCs
$\mathcal{Q}_{0,h}$	Space of discrete pressure fields with zero average
$\mathbf{u}$	Exact velocity solution
$p$	Exact pressure solution
$\mathbf{u}_h$	Discrete velocity solution
$p_h$	Discrete pressure solution
$h$	Mesh size
$k'$	Polynomial degree
$\alpha$	Regularity constant
$\mathbf{F}$	Parametric Mapping
$\sigma$	Reaction coefficient
$\nu$	Viscosity coefficient
$C_{pen}$	Nitsche's penalty parameter

Table 1.1: Notational conventions used in this dissertation.

Chapter 5, we introduce the B-spline spaces which we later utilize to discretize velocity and pressure fields. In Chapters 6, 7, 8, and 9, we develop and analyze divergence-conforming discretizations for the generalized Stokes equations, steady Navier-Stokes equations, unsteady Stokes equations, and unsteady Navier-Stokes equations. Finally, in Chapter 10, we draw conclusions and discuss future work.

## Chapter 2

### The Algebraic Structure of Generalized Stokes Flow

While generalized Stokes flow is often analyzed through the lens of partial differential equations and functional analysis, tools from algebraic topology and differential geometry can also be used to establish existence and uniqueness results as well as aid in the development of stable discretization procedures. In Section 2.1, we examine generalized Stokes flow using Hilbert complexes, and in Section 2.2, we use differential geometry to define generalized Stokes solutions in terms of vector potentials and harmonic forms.

#### 2.1 Generalized Stokes Flow and Inf-Sup Stability

Let  $\Omega$  be a bounded, simply connected open domain in  $\mathbb{R}^3$ . Let  $\partial\Omega$  denote the boundary of  $\Omega$  and assume that  $\partial\Omega$  is Lipschitz-continuous. We consider the generalized Stokes problem subject to homogeneous Dirichlet boundary conditions:

$$\left( S \right) \left\{ \begin{array}{l} \text{Given } \sigma : \Omega \rightarrow \mathbb{R}, \nu : \Omega \rightarrow \mathbb{R}, \text{ and } \mathbf{f} : \Omega \rightarrow \mathbb{R}^3, \text{ find } \mathbf{u} : \bar{\Omega} \rightarrow \mathbb{R}^3 \text{ and} \\ p : \Omega \rightarrow \mathbb{R} \text{ such that} \\ \sigma \mathbf{u} - \nabla \cdot (2\nu \nabla^s \mathbf{u}) + \mathbf{grad} p = \mathbf{f} \quad \text{in } \Omega \quad (2.1) \\ \operatorname{div} \mathbf{u} = 0 \quad \text{in } \Omega \quad (2.2) \\ \mathbf{u} = \mathbf{0} \quad \text{on } \partial\Omega \quad (2.3) \\ \text{where} \\ \nabla^s \mathbf{u} = \frac{1}{2} \left( \nabla \mathbf{u} + (\nabla \mathbf{u})^T \right). \quad (2.4) \end{array} \right.$$

Above,  $\mathbf{u}$  denotes the flow velocity of a fluid moving through the domain  $\Omega$ ,  $p$  denotes the pressure acting on the fluid divided by the fluid density,  $\nu$  denotes the kinematic viscosity of the fluid,  $\sigma$  denotes a reaction coefficient which gives the ratio of the viscosity to the permeability of the fluid, and  $\mathbf{f}$  denotes a body force divided by the density. To ensure that the generalized Stokes problem is well-posed, we require that the viscosity be uniformly positive (i.e.,  $\exists \nu_0 > 0$  such that  $\nu \geq \nu_0$ ) and that the reaction coefficient be non-negative (i.e.,  $\sigma \geq 0$ ). Before proceeding, note that the pressure is only determined up to a constant.

We now define a weak formulation for the generalized Stokes problem. Let  $L^2(\Omega)$  denote the space of square integrable functions on  $\Omega$  endowed with the standard  $L^2$ -norm  $\|\cdot\|_{L^2(\Omega)}$ , and let  $\mathbf{L}^2(\Omega) = (L^2(\Omega))^3$ . Let us denote the Hilbert space of  $L^2$  functions with zero average as

$$L_0^2(\Omega) = \left\{ q \in L^2(\Omega) : \int_{\Omega} q dx = 0 \right\}. \quad (2.5)$$

Let us further define the standard Sobolev spaces

$$H^1(\Omega) = \left\{ v \in L^2(\Omega) : \mathbf{grad} v \in (L^2(\Omega))^3 \right\}, \quad (2.6)$$

$$H_0^1(\Omega) = \left\{ v \in H^1(\Omega) : v = 0 \text{ on } \partial\Omega \right\} \quad (2.7)$$

which are endowed with the standard  $H^1$ -norm, and let us denote  $\mathbf{H}^1(\Omega) = (H^1(\Omega))^3$  and  $\mathbf{H}_0^1(\Omega) = (H_0^1(\Omega))^3$ . Assuming that  $\sigma, \nu \in L^\infty(\Omega)$  and  $\mathbf{f} \in \mathbf{L}^2(\Omega)$ , the weak form for the generalized Stokes problem is then written as follows:

$$(W) \left\{ \begin{array}{l} \text{Find } \mathbf{u} \in \mathbf{H}_0^1(\Omega) \text{ and } p \in L_0^2(\Omega) \text{ such that} \\ \qquad \qquad \qquad a(\mathbf{u}, \mathbf{v}) - b(p, \mathbf{v}) + b(q, \mathbf{u}) = (\mathbf{f}, \mathbf{v})_{\mathbf{L}^2(\Omega)} \quad (2.8) \\ \text{for all } \mathbf{v} \in \mathbf{H}_0^1(\Omega) \text{ and } q \in L_0^2(\Omega) \text{ where} \\ \qquad \qquad \qquad a(\mathbf{w}, \mathbf{v}) = (2\nu \nabla^s \mathbf{w}, \nabla^s \mathbf{v})_{(L^2(\Omega))^{3 \times 3}} + (\sigma \mathbf{w}, \mathbf{v})_{\mathbf{L}^2(\Omega)}, \quad (2.9) \\ \qquad \qquad \qquad b(q, \mathbf{v}) = (q, \text{div } \mathbf{v})_{L^2(\Omega)}. \quad (2.10) \end{array} \right.$$

The well-posedness of the above weak formulation is due to the celebrated inf-sup condition. To prove this condition, we will use an algebraic topology result relating the spaces  $\mathbf{H}_0^1(\Omega)$  and  $L_0^2(\Omega)$ . This result invokes the theory of Hilbert complexes, which is elaborated in Chapter 3 of [7].

**Theorem 2.1.1.** *The Hilbert complex*

$$\mathbf{H}_0^1(\Omega) \xrightarrow{\operatorname{div}} L_0^2(\Omega) \quad (2.11)$$

is bounded and exact at  $L_0^2(\Omega)$ . That is, the linear operator  $\operatorname{div} : \mathbf{H}_0^1(\Omega) \rightarrow L_0^2(\Omega)$  satisfies the following properties:

- The operator  $\operatorname{div}$  is continuous.
- The image of  $\operatorname{div}$  is equal to  $L_0^2(\Omega)$  (i.e.,  $\operatorname{div}$  is surjective).

*Proof.* The continuity of  $\operatorname{div}$  follows by direct computation. The surjectivity of  $\operatorname{div}$  is a classical result (see pg. 24 of [86], for example).  $\square$

We immediately have the following result implying the inf-sup stability condition.

**Theorem 2.1.2.** *For each  $q \in L_0^2(\Omega)$ , there exists a  $\mathbf{v} \in \mathbf{H}_0^1(\Omega)$  such that*

$$\operatorname{div} \mathbf{v} = q, \quad (2.12)$$

$$\|\mathbf{v}\|_{\mathbf{H}^1(\Omega)} \leq C \|q\|_{L^2(\Omega)} \quad (2.13)$$

where  $C$  is a positive constant independent of  $q$ .

*Proof.* Let

$$\mathbf{V}_0 = \{ \mathbf{v} \in \mathbf{H}_0^1(\Omega) : \operatorname{div} \mathbf{v} = 0 \}. \quad (2.14)$$

We have that  $\mathbf{V}_0$  and its orthogonal complement  $\mathbf{V}_0^\perp$  are proper closed linear subspaces of  $\mathbf{H}_0^1(\Omega)$ . Furthermore, as the operator  $\operatorname{div}$  is a continuous linear surjection by Theorem 2.1.1, the restriction of  $\operatorname{div}$  to  $\mathbf{V}_0^\perp$  is a bounded linear bijection onto  $L_0^2(\Omega)$ . Hence, by Banach's bounded inverse theorem, there exists a bounded linear operator  $T : L_0^2(\Omega) \rightarrow \mathbf{V}_0^\perp$  such that

$$\operatorname{div} Tq = q, \quad (2.15)$$

$$\|Tq\|_{\mathbf{H}^1(\Omega)} \leq C\|q\|_{L^2(\Omega)} \quad (2.16)$$

for every  $q \in L_0^2(\Omega)$  where  $C > 0$  is the continuity constant of  $T$ . The theorem immediately follows.  $\square$

**Corollary 2.1.1.** *There exists a positive constant  $\beta > 0$  such that*

$$\inf_{q \in L_0^2(\Omega), q \neq 0} \sup_{\mathbf{v} \in \mathbf{H}_0^1(\Omega)} \frac{b(q, \mathbf{v})}{\|q\|_{L^2(\Omega)} \|\mathbf{v}\|_{\mathbf{H}^1(\Omega)}} \geq \beta. \quad (2.17)$$

As a direct consequence of the above inf-sup condition, we can prove existence and uniqueness of weak solutions to the generalized Stokes problem.

**Theorem 2.1.3.** *Problem (W) has a unique weak solution  $(\mathbf{u}, p) \in \mathbf{H}_0^1(\Omega) \times L_0^2(\Omega)$ .*

*Proof.* The result follows from Brezzi's theorem [35], the continuity of the bilinear operators  $a(\cdot, \cdot)$  and  $b(\cdot, \cdot)$ , the coercivity of  $a(\cdot, \cdot)$  provided by Korn's inequality [108], and the inf-sup condition given by Corollary 2.1.1.  $\square$

The algebraic structure of the Hilbert complex presented in Theorem 2.1.1 hints as to how to construct stable finite-dimensional approximation spaces for the generalized Stokes problem. Notably, if one could construct finite-dimensional spaces  $V^h \subset \mathbf{H}_0^1(\Omega)$ ,  $Q^h \subset L_0^2(\Omega)$  and bounded projection operators  $\Pi_V^h : \mathbf{H}_0^1(\Omega) \rightarrow$

$V^h, \Pi_Q^h : L_0^2(\Omega) \rightarrow Q^h$  such that  $\text{div}$  maps  $V^h$  onto  $Q^h$  and the following diagram commutes

$$\begin{array}{ccc} \mathbf{H}_0^1(\Omega) & \xrightarrow{\text{div}} & L_0^2(\Omega) \\ \Pi_V^h \downarrow & & \Pi_Q^h \downarrow \\ V^h & \xrightarrow{\text{div}} & Q^h, \end{array} \quad (2.18)$$

one would immediately obtain a discrete inf-sup condition by Theorem 2.1.2, the commuting property  $\Pi_Q^h \text{div} = \text{div} \Pi_V^h$ , and the continuity of  $\Pi_V^h$  and  $\Pi_Q^h$ . Furthermore, as  $\text{div}$  maps  $V^h$  onto  $Q^h$ , the discrete velocity field resulting from a Galerkin discretization of generalized Stokes flow would be guaranteed pointwise divergence-free. As we will see in the next chapter, this property will be especially important for Navier-Stokes flows.

Let us finish here with one more algebraic result describing the structure of the space  $\mathbf{H}_0^1(\Omega)$  and the maximal inf-sup constant. The result, known as the Velte decomposition, is the equivalent of the Helmholtz decomposition for vector functions in  $\mathbf{L}^2(\Omega)$ . The proof of the result may be found in [184].

**Theorem 2.1.4** (The Velte Decomposition). *The space  $\mathbf{H}_0^1(\Omega)$  admits the orthogonal decomposition*

$$\mathbf{H}_0^1(\Omega) = \mathbf{V}_0 \oplus \mathbf{V}_1 \oplus \mathbf{V}_\beta \quad (2.19)$$

where

$$\mathbf{V}_0 = \{ \mathbf{v} \in \mathbf{H}_0^1(\Omega) : \text{div} \mathbf{v} = 0 \}, \quad (2.20)$$

$$\mathbf{V}_1 = \{ \mathbf{v} \in \mathbf{H}_0^1(\Omega) : \text{curl} \mathbf{v} = \mathbf{0} \}, \quad (2.21)$$

and  $\mathbf{V}_\beta$  consists of solutions  $\mathbf{w} = \mathbf{w}(p)$  of the variational problem

$$a(\mathbf{w}, \mathbf{v}) = b(p, \mathbf{v}), \quad \forall \mathbf{v} \in \mathbf{H}_0^1(\Omega) \quad (2.22)$$

for harmonic  $p \in L_0^2(\Omega)$ . Further, the maximal inf-sup constant

$$\beta_0 = \inf_{p \in L_0^2(\Omega), p \neq 0} \sup_{\mathbf{v} \in \mathbf{H}_0^1(\Omega)} \frac{b(p, \mathbf{v})}{\|p\|_{L^2(\Omega)} \|\mathbf{v}\|_{\mathbf{H}^1(\Omega)}} \quad (2.23)$$

is equal to  $\lambda_1^{-1/2}$  where  $\lambda_1$  is the largest eigenvalue of the variational eigenproblem: find  $(\mathbf{w}, \lambda) \in \mathbf{V}_\beta \times \mathbb{R}^+$  such that

$$a(\mathbf{w}, \mathbf{v}) = \lambda (\operatorname{div} \mathbf{w}, \operatorname{div} \mathbf{v})_{L^2(\Omega)}, \quad \forall \mathbf{v} \in \mathbf{V}_\beta. \quad (2.24)$$

**Remark 2.1.1.** *The results in this section apply to the two-dimensional setting.*

**Remark 2.1.2.** *As a corollary, Theorems 2.1.1 and 2.1.2 extend to the case when  $\mathbf{H}_0^1(\Omega)$  is replaced by the space*

$$\mathbf{H}_n^1(\Omega) = \{\mathbf{v} \in \mathbf{H}^1(\Omega) : \mathbf{v} \cdot \mathbf{n} = 0 \text{ on } \partial\Omega\} \quad (2.25)$$

where  $\mathbf{n}$  denotes the outward pointing normal vector. Similar results also exist for periodic Sobolev spaces, Sobolev spaces without boundary conditions, and Sobolev spaces with boundary conditions along only a subset of the boundary.

**Remark 2.1.3.** *We will later refer to incompressible Darcy flow as a special case of generalized Stokes flow. In this setting, the viscosity coefficient vanishes but the reaction coefficient is taken to be uniformly bounded from below by a positive constant. In addition, the boundary conditions of the velocity field and the function spaces of the variational formulation must be modified to guarantee well-posedness (see, e.g., [142]).*

## 2.2 Vector Potentials and Harmonic Forms

Let us define the following Hilbert spaces:

$$\mathbf{H}(\mathbf{curl}; \Omega) = \{ \mathbf{v} \in \mathbf{L}^2(\Omega) : \mathbf{curl} \mathbf{v} \in \mathbf{L}^2(\Omega) \}, \quad (2.26)$$

$$\mathbf{H}_0(\mathbf{curl}; \Omega) = \{ \mathbf{v} \in \mathbf{H}(\mathbf{curl}; \Omega) : \mathbf{v} \times \mathbf{n} = \mathbf{0} \text{ on } \partial\Omega \}, \quad (2.27)$$

$$\mathbf{H}(\mathbf{div}; \Omega) = \{ \mathbf{v} \in \mathbf{L}^2(\Omega) : \mathbf{div} \mathbf{v} \in L^2(\Omega) \}, \quad (2.28)$$

$$\mathbf{H}_0(\mathbf{div}; \Omega) = \{ \mathbf{v} \in \mathbf{H}(\mathbf{div}; \Omega) : \mathbf{v} \cdot \mathbf{n} = 0 \text{ on } \partial\Omega \}. \quad (2.29)$$

Note that the spaces  $\mathbf{H}(\mathbf{curl}; \Omega)$  and  $\mathbf{H}_0(\mathbf{curl}; \Omega)$  are equipped with the norm

$$\| \mathbf{v} \|_{\mathbf{H}(\mathbf{curl}; \Omega)} = \left( \| \mathbf{v} \|_{\mathbf{L}^2(\Omega)}^2 + \| \mathbf{curl} \mathbf{v} \|_{\mathbf{L}^2(\Omega)}^2 \right)^{1/2} \quad (2.30)$$

and the spaces  $\mathbf{H}(\mathbf{div}; \Omega)$  and  $\mathbf{H}_0(\mathbf{div}; \Omega)$  are equipped with the norm

$$\| \mathbf{v} \|_{\mathbf{H}(\mathbf{div}; \Omega)} = \left( \| \mathbf{v} \|_{\mathbf{L}^2(\Omega)}^2 + \| \mathbf{div} \mathbf{v} \|_{L^2(\Omega)}^2 \right)^{1/2}. \quad (2.31)$$

We have the following classical result concerning the de Rham complex with boundary conditions.

**Theorem 2.2.1** (The de Rham Complex). *Suppose  $\Omega \subset \mathbb{R}^3$  is a bounded, simply connected open domain with connected Lipschitz boundary. Then, the de Rham complex*

$$H_0^1(\Omega) \xrightarrow{\mathbf{grad}} \mathbf{H}_0(\mathbf{curl}; \Omega) \xrightarrow{\mathbf{curl}} \mathbf{H}_0(\mathbf{div}; \Omega) \xrightarrow{\mathbf{div}} L_0^2(\Omega) \quad (2.32)$$

*is bounded and exact.*

For the moment, let the assumptions of Theorem 2.2.1 hold true. Then, as the de Rham complex given by (2.32) is exact at  $\mathbf{H}_0(\mathbf{div}; \Omega)$ , we can write

any divergence-free function  $\mathbf{v} \in \mathbf{H}_0(\text{div}; \Omega)$  in terms of a vector potential  $\boldsymbol{\psi} \in \mathbf{H}_0(\text{curl}; \Omega)$  through the relationship:

$$\mathbf{v} = \text{curl} \boldsymbol{\psi}. \quad (2.33)$$

As the de Rham complex is also exact at  $\mathbf{H}_0(\text{curl}; \Omega)$ , such a vector potential is uniquely defined up to the gradient of a scalar potential  $z \in H_0^1(\Omega)$ . These extra degrees of freedom may be specified by choosing a gauge. For example, a vector potential may be uniquely specified by enforcing the vector potential to lie in the orthogonal complement of the image of  $\mathbf{grad}$ , i.e.,

$$(\boldsymbol{\psi}, \mathbf{grad} w)_{\mathbf{L}^2(\Omega)} = 0, \quad \forall w \in H_0^1(\Omega). \quad (2.34)$$

This gauge, referred to as the Coloumb gauge, enforces the condition  $\text{div} \boldsymbol{\psi} \equiv 0$ . Noting that the restriction of  $\mathbf{curl}$  to the subspace  $\ker(\mathbf{curl})^\perp = \text{im}(\mathbf{grad})^\perp$  is a bounded linear isomorphism onto  $\text{im}(\mathbf{curl})$ , we have the following inequality due to the bounded inverse theorem:

$$\|\boldsymbol{\phi}\|_{\mathbf{H}(\text{curl}; \Omega)} \leq C \|\mathbf{curl} \boldsymbol{\phi}\|_{\mathbf{L}^2(\Omega)}, \quad \forall \boldsymbol{\phi} \in \text{im}(\mathbf{grad})^\perp \quad (2.35)$$

where  $C$  is a positive constant which does not depend on  $\boldsymbol{\phi}$ . Here we have used the standard notation of  $\text{im}(\cdot)$  as the image of an operator and  $\ker(\cdot)$  as the kernel of an operator.

Note that the flow velocity solution of the generalized Stokes problem can be written in terms of a sufficiently smooth vector potential. In fact, by employing a vector potential, the pressure can be eliminated entirely from the generalized Stokes problem. One is then left with a semi-coercive system instead of a mixed variational problem. Proper coercivity can be recovered by restricting the space of admissible vector potentials to the divergence-free Hilbert space

$$\Phi_0 = \{ \boldsymbol{\phi} \in \mathbf{H}_0(\text{curl}; \Omega) : \mathbf{curl} \boldsymbol{\phi} \in \mathbf{H}_0^1(\Omega), \text{div} \boldsymbol{\phi} = 0 \} \quad (2.36)$$

which is equipped with the inner-product

$$(\phi, \varphi)_{\Phi_0} = (\mathbf{curl}\phi, \mathbf{curl}\varphi)_{\mathbf{H}^1(\Omega)}, \quad \forall \phi, \varphi \in \Phi_0 \quad (2.37)$$

due to (2.35). Note that  $\Phi_0$  is a smooth subspace of  $\mathbf{H}_0(\mathbf{curl}; \Omega)$ . If one additionally has an exact de Rham complex at the discrete level, one can develop highly efficient linear solvers by exploiting the existence of a discrete vector potential. This is currently being explored in the context of divergence-free B-splines. For brevity, however, this effort will not be covered in this written dissertation.

The differential structure of the de Rham complex inspires a geometric view of incompressible flow. Notably, it suggests the interpretation of scalar potentials as zero-forms evaluated at points in space, vector potentials as one-forms evaluated along paths, flow velocities as two-forms evaluated on surfaces, and pressures as three-forms evaluated in volumes. This bears obvious similarities to staggered-grid approaches for incompressible flow [97] as well as to conforming finite element discretizations of the mixed Laplacian [159].

Now, let us release the assumption that  $\partial\Omega$  is connected, and let us further allow  $\Omega$  to be multiply connected. In this setting, the de Rham complex given by (2.32) is no longer exact at  $\mathbf{H}_0(\mathbf{curl}; \Omega)$  or  $\mathbf{H}_0(\mathbf{div}; \Omega)$ , and hence a vector potential for the flow velocity may no longer exist. We can, however, specify the flow velocity using an alternative methodology. This methodology is motivated by the diagram in Figure 2.1. Let us define the following spaces of harmonic forms:

$$\mathfrak{h}_0^1 = \ker(\mathbf{curl}) \cap \text{im}(\mathbf{grad})^\perp, \quad (2.38)$$

$$\mathfrak{h}_0^2 = \ker(\mathbf{div}) \cap \text{im}(\mathbf{curl})^\perp. \quad (2.39)$$

With the above notation defined, any divergence-free function  $\mathbf{v} \in \mathbf{H}_0(\mathbf{div}; \Omega)$  can be written as

$$\mathbf{v} = \mathbf{curl}\psi + \mathbf{z} \quad (2.40)$$

$$\begin{array}{ccc}
H_0^1(\Omega) & = & \ker(\mathbf{grad})^\perp \\
\downarrow \mathbf{grad} & & \text{iso} \downarrow \mathbf{grad} \\
\mathbf{H}_0(\mathbf{curl}; \Omega) & = & \text{im}(\mathbf{grad}) \oplus \mathfrak{h}_0^1 \oplus \ker(\mathbf{curl})^\perp \\
\downarrow \mathbf{curl} & & \text{iso} \downarrow \mathbf{curl} \\
\mathbf{H}_0(\mathbf{div}; \Omega) & = & \ker(\mathbf{div})^\perp \oplus \mathfrak{h}_0^2 \oplus \text{im}(\mathbf{curl}) \\
\downarrow \mathbf{div} & & \text{iso} \downarrow \mathbf{div} \\
L_0^2(\Omega) & = & \text{im}(\mathbf{div})
\end{array}$$

Figure 2.1: An alternative view of the de Rham complex with boundary conditions in the general, multiply connected case. Here, we have performed a sum decomposition of the spaces  $H_0^1(\Omega)$ ,  $\mathbf{H}_0(\mathbf{curl}; \Omega)$ ,  $\mathbf{H}_0(\mathbf{div}; \Omega)$ , and  $L_0^2(\Omega)$  into orthogonal subspaces, and we have further illustrated how the mappings  $\mathbf{grad}$ ,  $\mathbf{curl}$ , and  $\mathbf{div}$  can be viewed as isomorphisms by restricting their domains and codomains to selected subspaces. Note the subspaces  $\mathfrak{h}_0^1$  and  $\mathfrak{h}_0^2$  are defined by (2.38) and (2.39) respectively.

where  $\boldsymbol{\psi} \in \mathbf{H}_0(\mathbf{curl}; \Omega)$  and  $\mathbf{z} \in \mathfrak{h}_0^2$  is a uniquely specified harmonic form. As was the case before for simply connected domains and boundaries,  $\boldsymbol{\psi}$  is not unique. However, unlike before, the de Rham complex is not exact at  $\mathbf{H}_0(\mathbf{curl}; \Omega)$ , and the Coloumb gauge is no longer enough to specify the extra degrees of freedom. If we impose one additional set of constraints, we can obtain uniqueness. Specifically, we constrain  $\boldsymbol{\psi}$  to be orthogonal to the set of harmonic functions in  $\mathfrak{h}_0^1$ . Similar to (2.35), we have the following inequality for the newly defined gauged space:

$$\|\boldsymbol{\phi}\|_{\mathbf{H}(\mathbf{curl}; \Omega)} \leq C \|\mathbf{curl} \boldsymbol{\phi}\|_{\mathbf{L}^2(\Omega)}, \quad \forall \boldsymbol{\phi} \in (\text{im}(\mathbf{grad}) \oplus \mathfrak{h}_0^1)^\perp \quad (2.41)$$

where  $C$  is a positive constant which does not depend on  $\boldsymbol{\phi}$ . We can, as before, use the above construction to reduce the generalized Stokes problem to a coercive system in a suitably chosen Sobolev space.

The structure of the spaces  $\mathfrak{h}_0^1$  and  $\mathfrak{h}_0^2$  is well understood (see [89] for example). Notably, it is well-known that the dimensions of the spaces are finite-dimensional and equal to

$$\dim(\mathfrak{h}_0^1) = \beta_2 = \text{number of three-dimensional voids in } \Omega, \quad (2.42)$$

$$\dim(\mathfrak{h}_0^2) = \beta_1 = \text{number of loops or handles in } \Omega \quad (2.43)$$

where  $\beta_i$  is the  $i^{\text{th}}$  Betti number associated with  $\Omega$ . This structure also extends to spaces satisfying a discrete de Rham complex.

We now summarize the main results of this section in the following theorem.

**Theorem 2.2.2.** *Let  $\Omega$  be a multiply connected domain with Lipschitz boundary. Any divergence-free function  $\mathbf{v} \in \mathbf{H}_0(\mathbf{div}; \Omega)$  has the unique representation*

$$\mathbf{v} = \mathbf{curl} \boldsymbol{\psi} + \mathbf{z} \quad (2.44)$$

where  $\mathbf{z} \in \mathfrak{h}_0^2$  and  $\psi \in (\text{im}(\mathbf{grad}) \oplus \mathfrak{h}_0^1)^\perp$ . Furthermore,

$$\|\psi\|_{\mathbf{H}(\text{curl}; \Omega)} \leq C \|\mathbf{v} - \mathbf{z}\|_{\mathbf{L}^2(\Omega)}. \quad (2.45)$$

where  $C$  is a positive constant independent of  $\mathbf{v}$ .

**Remark 2.2.1.** *Many interesting results concerning the vector potential on general domains are presented in the paper [3].*

**Remark 2.2.2.** *There exists a similar de Rham complex for spaces without boundary conditions and an analogous counterpart to Theorem 2.2.2. The resulting spaces of harmonic forms are, of course, different and their dimensionality also differs. However, the cohomologies of the de Rham complexes with and without boundary conditions are related. There also exists a de Rham complex for spaces with periodic boundary conditions or boundary conditions specified only along a subset of  $\partial\Omega$ . For more information on these topics of discussion, see [7].*

**Remark 2.2.3.** *In two dimensions, the notion of a two-dimensional vector potential, the so-called stream function, is utilized instead of a vector potential. The stream function exists and is uniquely specified for simply connected domains. On more complicated domains, an alternative construction may be utilized by invoking the two-dimensional version of harmonic forms.*

## Chapter 3

### The Geometric Structure of Navier-Stokes Flow

An interesting and important aspect of unsteady Navier-Stokes flow is the vast amount of geometry present. Such geometry is most obvious in the inviscid case as incompressible Euler flow may be viewed as a geodesic flow in a suitable infinite-dimensional space when formulated in Lagrangian coordinates. Specifically, Euler flow in a domain  $\Omega$  is described by the geodesics on the group of smooth volume-preserving diffeomorphisms of  $\Omega$  [9]. By employing Lie Algebra methods, it can be shown that Lagrangian formulations of Euler flow have a symplectic structure [141] and various Hamiltonian formulations [10]. The usual conservation properties follow (conservation of linear momentum, angular momentum, vorticity, circulation, energy, enstrophy in  $\mathbb{R}^2$ , and helicity in  $\mathbb{R}^3$ ) and infinite families of symmetries and invariants can be derived [93]. It should be noted that all of these results are largely a consequence of the volume-preserving nature of incompressible Euler flow.

Conservation of enstrophy in two-dimensional Euler flow prevents the formation of singularities in finite time, and global (in time) existence and uniqueness results were proven as early as 1933 for smooth solutions in  $\mathbb{R}^2$  [193]. On the other hand, while local existence and regularity results were obtained in the 1970s for three-dimensional Euler flow [72, 119, 176], global well-posedness remains an open question. Current research is primarily dedicated to the development of non-blowup conditions [23, 50, 126] and the use of computation to investigate possible

Euler singularities [121]. Of particular interest are recently-developed non-blowup conditions due to geometric properties of vortex filaments [62, 63]. Such results attest to the benefit of utilizing a combination of functional analysis and geometry to study the Euler singularity problem. Indeed, a famous result of Lions and DiPerna (see pg. 150-153 of [136]) suggests that functional analysis estimates alone are not enough to answer the three-dimensional well-posedness problem.

The convenient structure of Euler flow unfortunately breaks down when viscosity is introduced. Namely, the symplectic structure is lost and with it the infinite family of symmetries and invariants associated with Euler flow. For example, in a viscous flow, energy is not conserved in the absence of body forces. Rather, it is dissipated. Despite this lack of symplecticity, solutions to the Navier-Stokes equations satisfy a number of important balance laws. These balance laws, in conjunction with the incompressibility constraint, give the Navier-Stokes equations geometric structure and play a vital role in the evolution of flow. In particular, proper balance of momentum, kinetic energy, and helicity are believed to play a critical role in the development of coherent laminar and turbulent flow structures [147–149, 151] and in vortex breakdown [151] in  $\mathbb{R}^3$ . Additionally, if the large scales of a three-dimensional homogeneous turbulent flow are helical, there is a joint cascade of both energy and helicity from large scales down to the dissipative level where they are then destroyed [128], and this joint cascade is dependent on the interaction of helicity and energy as well as the relative magnitude of helicity. In fact, homogeneous flows with large mean-scale helicity have been shown to exhibit a much slower rate of turbulence decay [151].

In light of the above discussion, one may expect a reasonable numerical discretization of the Navier-Stokes equations, in the absence of any turbulence models, to respect balance of momentum, energy, and helicity at least at a global level.

However, semi-discrete formulations of the Navier-Stokes equations which conserve momentum are typically guaranteed to balance energy if and only if incompressibility is satisfied pointwise. Unfortunately, most discretizations do not satisfy this hard constraint.

To illustrate the geometric structure of Navier-Stokes flows, we formally derive various global balance laws in this chapter. For simplicity, we consider the Navier-Stokes equations for a constant-property Newtonian fluid posed on the three-dimensional torus. Denoting our spatial domain as  $\Omega = (0, 2\pi)^3$  and our space-time domain as  $\Omega_T := \Omega \times (0, \infty)$ , our problem of interest is written in conservation form as follows.

$$(S) \left\{ \begin{array}{l} \text{Given } \nu \in \mathbb{R}^+, \mathbf{f} : \Omega_T \rightarrow \mathbb{R}^3, \text{ and } \mathbf{u}_0 : \Omega \rightarrow \mathbb{R}^3, \text{ find } \mathbf{u} : \bar{\Omega}_T \rightarrow \mathbb{R}^3 \text{ and} \\ p : \Omega_T \rightarrow \mathbb{R} \text{ such that } \mathbf{u}(\mathbf{x}, t) \text{ and } p(\mathbf{x}, t) \text{ are periodic in } \mathbf{x} \text{ and} \\ \frac{\partial \mathbf{u}}{\partial t} + \nabla \cdot (\mathbf{u} \otimes \mathbf{u}) - \nabla \cdot (2\nu \nabla^s \mathbf{u}) + \mathbf{grad} p = \mathbf{f} \quad \text{in } \Omega_T, \quad (3.1) \\ \operatorname{div} \mathbf{u} = 0 \quad \text{in } \Omega_T, \quad (3.2) \\ \mathbf{u}(\cdot, 0) = \mathbf{u}_0(\cdot) \quad \text{in } \Omega. \quad (3.3) \end{array} \right.$$

Above,  $\mathbf{u}$  denotes the flow velocity of a fluid moving through the domain  $\Omega$ ,  $p$  denotes the pressure acting on the fluid divided by the density,  $\nu$  denotes the kinematic viscosity of the fluid,  $\mathbf{f}$  denotes an external body force acting on the fluid divided by the density, and  $\mathbf{u}_0$  denotes the initial velocity field. The density of the fluid, denoted as  $\rho$ , is assumed to be constant. The above set of equations accounts for unsteady acceleration, convective acceleration, viscous and normal stresses, and external body forces. Equation (3.1) is a differential statement of momentum balance, and Equation (3.2) is a differential statement of mass conservation. We assume for the remainder of this chapter that  $\mathbf{f}$  is periodic and conservative. That is, we assume there exists a periodic potential  $q : \Omega_T \rightarrow \mathbb{R}$  such that

$$\mathbf{f} = \nabla q.$$

We also assume for the remainder of the chapter that  $\mathbf{u}$  and  $\mathbf{f}$  are smooth and that all derivatives of  $\mathbf{u}$  are periodic in  $\mathbf{x}$ .

### 3.1 Balance of Momentum

Let us now derive a global momentum balance law. To do so, we first multiply (3.1) by  $\rho$  and integrate over  $\Omega$  to obtain

$$\int_{\Omega} \rho \left( \frac{\partial \mathbf{u}}{\partial t} + \nabla \cdot (\mathbf{u} \otimes \mathbf{u}) - \nabla \cdot (2\nu \nabla^s \mathbf{u}) + \mathbf{grad} p - \mathbf{f} \right) d\mathbf{x} = 0.$$

Stoke's theorem gives

$$\int_{\Omega} \rho (\nabla \cdot (\mathbf{u} \otimes \mathbf{u}) - \nabla \cdot (2\nu \nabla^s \mathbf{u}) + \mathbf{grad} p - \mathbf{f}) d\mathbf{x} = 0$$

since  $\mathbf{f}$  is conservative. Hence, we arrive at the following statement dictating the evolution of integrated momentum  $\rho \mathbf{u}$  over time.

***Global balance of linear momentum:***

$$\frac{d}{dt} \int_{\Omega} \rho \mathbf{u} d\mathbf{x} = 0$$

The above balance law states that the global integral of momentum is conserved in time.

### 3.2 Balance of Kinetic Energy

We now seek a balance law for kinetic energy. Begin by considering the integral of the dot-product of (3.1) and the momentum  $\rho \mathbf{u}$  over our domain  $\Omega$ :

$$\int_{\Omega} \left( \frac{\partial \mathbf{u}}{\partial t} + \nabla \cdot (\mathbf{u} \otimes \mathbf{u}) - \nabla \cdot (2\nu \nabla^s \mathbf{u}) + \mathbf{grad} p - \mathbf{f} \right) \cdot \rho \mathbf{u} d\mathbf{x} = 0. \quad (3.4)$$

We analyze the resulting expression term by term. To begin, we write

$$\int \frac{\partial \mathbf{u}}{\partial t} \cdot \rho \mathbf{u} d\mathbf{x} = \frac{d}{dt} \int_{\Omega} e d\mathbf{x} \quad (3.5)$$

where  $e = \frac{1}{2}\rho|\mathbf{u}|^2$  is the kinetic energy of the fluid. A simple calculation gives the following expression for the convection term in (3.4):

$$\int_{\Omega} \nabla \cdot (\mathbf{u} \otimes \mathbf{u}) \cdot \rho \mathbf{u} d\mathbf{x} = \int_{\Omega} (\operatorname{div}(\mathbf{u}e) + e \operatorname{div} \mathbf{u}) d\mathbf{x}.$$

Using Stoke's theorem and incompressibility, we find

$$\int_{\Omega} \nabla \cdot (\mathbf{u} \otimes \mathbf{u}) \cdot \rho \mathbf{u} d\mathbf{x} = 0. \quad (3.6)$$

We use integration by parts to obtain the following expression for the viscous stress, pressure, and body force terms appearing in (3.4):

$$\int_{\Omega} (-\nabla \cdot (2\nu \nabla^s \mathbf{u}) + \mathbf{grad} p - \mathbf{f}) \cdot \rho \mathbf{u} d\mathbf{x} = \int_{\Omega} (2\rho\nu |\nabla^s \mathbf{u}|^2 - \rho(p - q) \operatorname{div} \mathbf{u}) d\mathbf{x}.$$

Invoking the incompressibility constraint again, we arrive at

$$\int_{\Omega} (-\nabla \cdot (2\nu \nabla^s \mathbf{u}) + \mathbf{grad} p - \mathbf{f}) \cdot \rho \mathbf{u} d\mathbf{x} = \int_{\Omega} 2\rho\nu |\nabla^s \mathbf{u}|^2 d\mathbf{x}. \quad (3.7)$$

Combining Equations (3.4), (3.5), (3.6), and (3.7) and letting  $\mu = \rho\nu$  denote the kinematic viscosity, we obtain the following global balance law for kinetic energy.

**Global balance of kinetic energy:**

$$\frac{d}{dt} \int_{\Omega} e d\mathbf{x} = - \int_{\Omega} 2\mu |\nabla^s \mathbf{u}|^2 d\mathbf{x}$$

Hence, kinetic energy is globally dissipated in time.

As we saw, incompressibility had to be invoked on two occasions to derive the kinetic energy balance law. This is the reason semi-discrete formulations

which conserve momentum are typically not guaranteed to properly balance kinetic energy unless incompressibility is satisfied pointwise. Worse yet, semi-discrete formulations which conserve momentum are typically not even guaranteed to dissipate kinetic energy. Alternatively, one can utilize skew-symmetric or rotation formulations of the Navier-Stokes equations in conjunction with discretely divergence-free discretizations to arrive at numerical methods automatically satisfying an energy balance law [100, 194]. However, such formulations then lose the momentum conservation structure of the Navier-Stokes equations unless incompressibility is again satisfied pointwise.

Kinetic energy is a very important quantity in incompressible flows and, as stated earlier, proper balance of energy is believed to be important for flow structure development both at large- and fine-scale levels. Kinetic energy holds yet another meaning in the context of numerical methods. Kinetic energy is inherently related to the stability of a numerical method. Namely, for unsteady viscous flows, a numerical method is said to be stable if the kinetic energy remains bounded in time. Semi-discrete formulations which do not dissipate kinetic energy are typically unstable. The Lax-Milgram theorem [132] suggests that solutions to such formulations may not converge. Even more detrimental is the fact that such solutions may experience catastrophic blowup of error.

### 3.3 Balance of Vorticity

Let  $\boldsymbol{\omega} = \mathbf{curl} \mathbf{u}$  denote the vorticity, a measure of the local angular rate of rotation of the flow field. By taking the  $\mathbf{curl}$  of the linear momentum equation and invoking incompressibility, it can be shown that the vorticity satisfies the following

conservation equation:

$$\frac{\partial \boldsymbol{\omega}}{\partial t} + \nabla \cdot (\mathbf{u} \otimes \boldsymbol{\omega} - \boldsymbol{\omega} \otimes \mathbf{u}) = \nabla \cdot (2\nu \nabla^s \boldsymbol{\omega}). \quad (3.8)$$

Furthermore, the vorticity satisfies a solenoidal constraint:

$$\operatorname{div} \boldsymbol{\omega} = 0. \quad (3.9)$$

Integrating the differential balance law for vorticity over the entire domain and then invoking Stoke's theorem to handle all of the terms except the unsteady term, we arrive at the following global balance law.

***Global balance of vorticity:***

$$\frac{d}{dt} \int_{\Omega} \boldsymbol{\omega} d\mathbf{x} = 0$$

Hence, the global integral of vorticity is conserved in time.

Before proceeding, let us write the differential balance law for vorticity in another form. Let  $\frac{D}{Dt}$  denote the material derivative and let  $\mathbb{D}(\mathbf{u}) = \nabla^s \mathbf{u}$  denote the rate of strain or strain-rate tensor. Then, by virtue of  $\operatorname{div} \mathbf{u} = 0$ ,  $\operatorname{div} \boldsymbol{\omega} = 0$ , and the fact that  $(\nabla \mathbf{u} - \nabla \mathbf{u}^T) \boldsymbol{\omega} = 0$ , we can write (3.8) as

$$\frac{D\boldsymbol{\omega}}{Dt} = \nabla \cdot (2\nu \nabla^s \boldsymbol{\omega}) + \mathbb{D}(\mathbf{u})\boldsymbol{\omega}. \quad (3.10)$$

The above equation indicates that the change of vorticity at a material point is equal to the vorticity diffusion plus a reaction term of the form  $\mathbb{D}(\mathbf{u})\boldsymbol{\omega}$ . This reaction term is responsible for the intensification (or the decrease) of vorticity depending on the alignment of  $\boldsymbol{\omega}$  with eigenvectors corresponding to positive (or negative) eigenvalues of the rate of strain tensor. Since  $\operatorname{tr}(\mathbb{D}(\mathbf{u})) = \operatorname{div} \mathbf{u} = 0$ , the rate of

strain tensor has both positive and negative eigenvalues unless it is identically zero. This results in vortex stretching, a phenomena believed to be of crucial importance in turbulent flow dynamics [12, 67]. It should be noted that vortex stretching is absent in two-dimensional Navier-Stokes flow.

In the discrete setting, it actually proves more natural to represent the vorticity field in terms of a discrete solution of (3.8) rather than as the **curl** of a discrete velocity field. This was the approach taken in [157]. We will later utilize this approach to show that our proposed divergence-free discretization technique satisfies desired balance laws.

### 3.4 Balance of Enstrophy

We now seek a global balance law for enstrophy. Consider the integral of the dot-product of Equation (3.10) and  $\boldsymbol{\omega}$  over  $\Omega$ :

$$\int_{\Omega} \left( \frac{\partial \boldsymbol{\omega}}{\partial t} + (\mathbf{u} \cdot \nabla) \boldsymbol{\omega} - \mathbb{D}(\mathbf{u})\boldsymbol{\omega} - \nabla \cdot (2\nu \nabla^s \boldsymbol{\omega}) \right) \cdot \boldsymbol{\omega} d\mathbf{x} = 0. \quad (3.11)$$

Let us analyze the above expression term by term. To begin, we write

$$\int_{\Omega} \frac{\partial \boldsymbol{\omega}}{\partial t} \cdot \boldsymbol{\omega} d\mathbf{x} = \frac{d}{dt} \int_{\Omega} \gamma d\mathbf{x} \quad (3.12)$$

where  $\gamma = \frac{1}{2}|\boldsymbol{\omega}|^2$  is the enstrophy density of the fluid. Next, invoking incompressibility and Stoke's theorem, we can write

$$\int_{\Omega} ((\mathbf{u} \cdot \nabla) \boldsymbol{\omega}) \cdot \boldsymbol{\omega} d\mathbf{x} = \int_{\Omega} \operatorname{div}(\mathbf{u}\boldsymbol{\nu}) d\mathbf{x} = 0, \quad (3.13)$$

Finally, integration by parts results in

$$- \int_{\Omega} \nabla \cdot (2\nu \nabla^s \boldsymbol{\omega}) d\mathbf{x} = \int_{\Omega} 2\nu |\nabla^s \boldsymbol{\omega}|^2 d\mathbf{x}. \quad (3.14)$$

Combining Equations (3.11)-(3.14), we arrive at the following global balance law.

***Global balance of enstrophy:***

$$\frac{d}{dt} \int_{\Omega} \gamma d\mathbf{x} = - \int_{\Omega} 2\nu |\nabla^s \boldsymbol{\omega}|^2 d\mathbf{x} + \int_{\Omega} \boldsymbol{\omega}^T \mathbb{D}(\mathbf{u}) \boldsymbol{\omega} d\mathbf{x}$$

As  $\mathbb{D}(\mathbf{u})$  is indefinite, the above equation appears to give no real global (in time) control over the behavior of enstrophy. This in turn means we appear to have no global  $L^2$  control over the gradient of  $\mathbf{u}$  or the strain-rate tensor since we have the relationship

$$\int_{\Omega} \gamma d\mathbf{x} = \int_{\Omega} \frac{1}{2} |\nabla \mathbf{u}|^2 d\mathbf{x} = \int_{\Omega} |\mathbb{D}(\mathbf{u})|^2 d\mathbf{x} \quad (3.15)$$

due to periodicity and the incompressibility constraint. Global control of enstrophy is considered very important to the mathematical analysis of the Navier-Stokes equations as it is known that a solution remains smooth as long as the enstrophy is bounded. However, due to the presence of the enstrophy production term

$$\int_{\Omega} \boldsymbol{\omega}^T \mathbb{D}(\mathbf{u}) \boldsymbol{\omega} d\mathbf{x}, \quad (3.16)$$

elementary functional analysis estimates can only be used to establish local (in time) existence of smooth solutions given a smooth initial velocity field [67]. It remains unknown at this time if vorticity dissipation is enough to counterbalance enstrophy production over finite times or if the inherent geometric features of vortex stretching prohibit blowup.

The existence (or lack thereof) of smooth global-in-time Navier-Stokes solutions is considered one of the premier unsolved problems in mathematics, and the problem is even one of the Clay Mathematics Institute's famed Millenium Prize Problems. To date, the best general result in this direction is considered to be that of Caffarelli, Kohn, and Nirenberg which characterizes the potential set of space-time singularities for a space of "suitable weak solutions" [42]. Unfortunately, this result was obtained over 25 years ago, indicating a slow-down of progress. It should

be noted that global existence of weak solutions was obtained as early as 1934 by Leray [134], and global existence and uniqueness for two-dimensional smooth solutions were obtained by Kiselev and Ladyzhenskaya in 1957 [124] by relying on the fact that enstrophy production is absent in two-dimensional flows.

Not unrelated to the Navier-Stokes existence and smoothness problem is the role of enstrophy production in three-dimensional turbulence. Enstrophy production is a fundamental problem in fluid mechanics and has been a focus of attention of the turbulence community for many years [65, 66, 82, 88, 115, 144, 150, 156]. In fact, concentrated vortices characterized by high-enstrophy have been referred to as the “sinews of turbulence” [150]. Formal asymptotics, one of the primary tools of the analytic fluid mechanics community, are rather unreliable in the study of enstrophy production due to the inability to reasonably bound the strain-rate as mentioned above. Numerical simulation [66, 88, 115, 156] and experimentation [66, 144] have been utilized to study enstrophy production and its relationship with energy dissipation rates in a more straight-forward manner.

### 3.5 Balance of Helicity

We finish this chapter by deriving a global balance law for helicity. Let us begin by considering the integral of the dot-product of Equation (3.8) and  $\mathbf{u}$  over  $\Omega$ :

$$\int_{\Omega} \left( \frac{\partial \boldsymbol{\omega}}{\partial t} + \nabla \cdot (\mathbf{u} \otimes \boldsymbol{\omega} - \boldsymbol{\omega} \otimes \mathbf{u}) - \nabla \cdot (2\nu \nabla^s \boldsymbol{\omega}) \right) \cdot \mathbf{u} d\mathbf{x} = 0$$

and the integral of the dot-product of Equation (3.1) and  $\boldsymbol{\omega}$  over  $\Omega$ :

$$\int_{\Omega} \left( \frac{\partial \mathbf{u}}{\partial t} + \nabla \cdot (\mathbf{u} \otimes \mathbf{u}) - \nabla \cdot (2\nu \nabla^s \mathbf{u}) + \mathbf{grad} p - \mathbf{f} \right) \cdot \boldsymbol{\omega} d\mathbf{x} = 0.$$

Adding the two integrals gives

$$\begin{aligned} \int_{\Omega} \left( \frac{\partial \boldsymbol{\omega}}{\partial t} \cdot \mathbf{u} + \frac{\partial \mathbf{u}}{\partial t} \cdot \boldsymbol{\omega} + \nabla \cdot (\mathbf{u} \otimes \boldsymbol{\omega} - \boldsymbol{\omega} \otimes \mathbf{u}) \cdot \mathbf{u} + \nabla \cdot (\mathbf{u} \otimes \mathbf{u}) \cdot \boldsymbol{\omega} \right) d\mathbf{x} \\ + \int_{\Omega} (-\nabla \cdot (2\nu \nabla^s \boldsymbol{\omega}) \cdot \mathbf{u} - \nabla \cdot (2\nu \nabla^s \mathbf{u}) \cdot \boldsymbol{\omega}) d\mathbf{x} \\ + \int_{\Omega} (\mathbf{grad} p \cdot \boldsymbol{\omega} - \mathbf{f} \cdot \boldsymbol{\omega}) d\mathbf{x} = 0. \end{aligned} \quad (3.17)$$

We now analyze the above expression piece by piece. First, for the terms in (3.17) involving time derivatives, we write

$$\int_{\Omega} \left( \frac{\partial \boldsymbol{\omega}}{\partial t} \cdot \mathbf{u} + \frac{\partial \mathbf{u}}{\partial t} \cdot \boldsymbol{\omega} \right) d\mathbf{x} = \frac{d}{dt} \int_{\Omega} \varrho d\mathbf{x} \quad (3.18)$$

where  $\varrho = \boldsymbol{\omega} \cdot \mathbf{u}$  is the helical density, a measure of the helical or corkscrew-like motion of the flow field. Next, for the term in (3.17) involving the convective acceleration of vorticity, we use integration by parts to write

$$\begin{aligned} \int_{\Omega} \nabla \cdot (\mathbf{u} \otimes \boldsymbol{\omega}) \cdot \mathbf{u} d\mathbf{x} &= - \int_{\Omega} (\mathbf{u} \otimes \boldsymbol{\omega}) : (\nabla \mathbf{u}) d\mathbf{x} \\ &= - \int_{\Omega} ((\mathbf{u} \cdot \nabla) \mathbf{u}) \cdot \boldsymbol{\omega} d\mathbf{x}. \end{aligned}$$

We invoke incompressibility to obtain

$$\int_{\Omega} \nabla \cdot (\mathbf{u} \otimes \boldsymbol{\omega}) \cdot \mathbf{u} d\mathbf{x} = - \int_{\Omega} \nabla \cdot (\mathbf{u} \otimes \mathbf{u}) \cdot \boldsymbol{\omega} d\mathbf{x}. \quad (3.19)$$

Proceeding forward to the term in (3.17) involving vortex stretching, we use the product rule to write

$$\int_{\Omega} \nabla \cdot (\boldsymbol{\omega} \otimes \mathbf{u}) \cdot \mathbf{u} d\mathbf{x} = \int_{\Omega} \nabla \cdot (\mathbf{u} \nu) d\mathbf{x}.$$

Stoke's theorem then gives

$$\int_{\Omega} \nabla \cdot (\boldsymbol{\omega} \otimes \mathbf{u}) \cdot \mathbf{u} d\mathbf{x} = 0. \quad (3.20)$$

We now proceed to the terms in (3.17) involving viscous and pressure terms. Simple application of integration by parts and the condition  $\text{div } \boldsymbol{\omega} = 0$  results in

$$\int_{\Omega} (-\nabla \cdot (2\nu \nabla^s \boldsymbol{\omega}) \cdot \mathbf{u} - \nabla \cdot (2\nu \nabla^s \mathbf{u}) \cdot \boldsymbol{\omega} + \mathbf{grad} p \cdot \boldsymbol{\omega}) d\mathbf{x} = \int_{\Omega} 4\nu (\nabla^s \mathbf{u}) : (\nabla^s \boldsymbol{\omega}) d\mathbf{x}. \quad (3.21)$$

Finally, the observation that  $\mathbf{f}$  is conservative gives the following expression for the term in (3.17) involving body forces after an application of integration by parts:

$$\int_{\Omega} \mathbf{f} \cdot \boldsymbol{\omega} d\mathbf{x} = \int_{\Omega} q \text{div } \boldsymbol{\omega} d\mathbf{x} = 0. \quad (3.22)$$

Combining Equations (3.17), (3.18), (3.19), (3.20), (3.21), and (3.22), we obtain the following global balance law.

***Global balance of helicity:***

$$\frac{d}{dt} \int_{\Omega} \varrho d\mathbf{x} = - \int_{\Omega} 4\nu (\nabla^s \mathbf{u}) : (\nabla^s \boldsymbol{\omega}) d\mathbf{x}$$

Note that in the absence of viscosity, global helicity is conserved. This is in opposition with the global enstrophy.

Helicity is a fundamental quantity in laminar and turbulent flow. It can be interpreted topologically as the degree to which a flow's vortex tubes are tangled and intertwined (see Figure 3.1 above and the discussion in [160]). As mentioned earlier, helicity cascades over the inertial range jointly with kinetic energy [128] and may actually impede the energy cascade [2], and helicity is also believed to be closely related to vortex breakdown [151]. Furthermore, results in mathematics indicate a potential role of helicity for the regularity of Navier-Stokes solutions [26]. Strangely, the concept of helicity is relatively recent in fluid mechanics [146, 152],

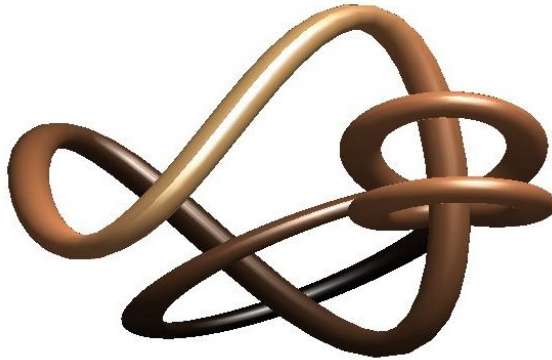


Figure 3.1: Tangling of vortex tubes, tubes with contours of axial vorticity.

but its roots date back to seminal contributions of Kelvin [120]. Kelvin recognized that, in an inviscid flow, vortex lines behave like material lines. This implies the inviscid invariance of helicity, giving helicity a status comparable to energy. As such, one may expect a reasonable discretization of the Navier-Stokes equations to respect helicity balance. However, for the same reasons as were discussed in Section 3.2, conservative semi-discrete formulations are typically not guaranteed to properly balance helicity unless incompressibility is satisfied exactly. Moreover, even when incompressibility holds pointwise, discrete vorticity must be appropriately defined to ensure helicity balance. This will be explored in more depth in Chapter 9.

**Remark 3.5.1.** *All of the balance laws derived here can be extended to general choices of boundary conditions provided appropriate boundary terms are included. It should be noted that such boundary terms are often non-trivial. For example, a flow subject to traction boundary conditions will be characterized by energy, enstrophy, and helicity production on the boundary of the domain. To avoid these complications, we restricted our discussion here to that of an unphysical three-dimensional closed manifold.*

## Chapter 4

### B-splines and Geometrical Mappings

B-splines were first introduced by Schoenberg in 1946 [166] in the attempt to develop piecewise polynomials with prescribed smoothness properties. In his 1972 paper, de Boor [58] introduced a simple and stable recursion formula for evaluating them, and since then, B-splines have been a standard in the numerical analysis and computer-aided geometric design communities. For an overview of splines, their properties, and robust algorithms for evaluating their values and derivatives, see de Boor [59] and Schumaker [169].

B-splines have been employed in the numerical analysis of differential equations for several decades. In 1972, de Boor introduced an orthogonal collocation method using B-splines to solve arbitrary-order differential equations [58], and B-spline collocation and Galerkin methods have since been utilized in a variety of complex flow applications [129–131, 171] where it has been shown that the resolution power of B-splines of maximum continuity allows the representation of a broad range of scales of turbulent flow. Of particular interest is the stable staggered grid approach introduced by Botella [31] which bears some semblance to the discretization schemes introduced in this dissertation. Inspired by the prevalence of Non-Uniform Rational B-Splines (NURBS) in computer aided design (CAD), isogeometric analysis was proposed in [109] by Hughes, Cottrell, and Bazilevs as a means of uniting CAD and computer aided engineering. In isogeometric analysis, the same basis for the geometry as defined in a CAD package is also utilized in finite

element analysis. The original instantiation was based on NURBS, but other isogeometric analysis techniques have since been developed [17, 68]. NURBS-based isogeometric analysis has been applied to a number of applications, including turbulent flow simulation [1, 16, 18], fluid-structure interaction [19], and structural analysis [53, 54, 137]. In many of these papers, it was shown that splines have superior stability and approximation properties as compared to standard finite elements. For an introductory text on isogeometric analysis, see Cottrell, Hughes, and Bazilevs [52].

In this chapter, we briefly review the construction of univariate and multivariate B-splines which form the building blocks of our discretization technique. We also introduce parametric mappings which will allow us to map B-splines to general geometries of interest, and we define various notation which will be utilized throughout the remainder of this dissertation.

## 4.1 Univariate B-splines

For two positive integers  $k$  and  $n$ , representing degree and dimensionality respectively, let us introduce the ordered knot vector

$$\Xi := \{0 = \xi_1, \xi_2, \dots, \xi_{n+k+1} = 1\} \quad (4.1)$$

where

$$\xi_1 \leq \xi_2 \leq \dots \leq \xi_{n+k+1}.$$

Given  $\Xi$  and  $k$ , univariate B-spline basis functions are constructed recursively starting with piecewise constants ( $k = 0$ ):

$$B_i^0(\xi) = \begin{cases} 1 & \text{if } \xi_i \leq \xi < \xi_{i+1} \\ 0 & \text{otherwise.} \end{cases} \quad (4.2)$$

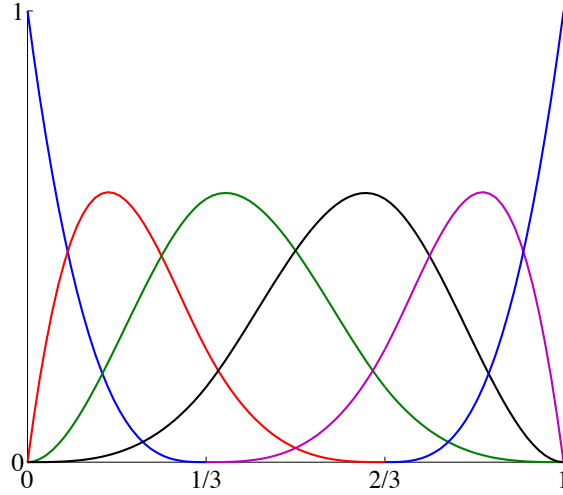


Figure 4.1: Cubic B-spline basis functions for open, non-uniform knot vector  $\Xi = \{0, 0, 0, 0, 1/3, 2/3, 1, 1, 1, 1\}$ . Note the basis is  $C^2$  everywhere in the interval  $(0, 1)$ .

For  $k = 1, 2, 3, \dots$ , they are defined by

$$B_i^k(\xi) = \frac{\xi - \xi_i}{\xi_{i+k} - \xi_i} B_i^{k-1}(\xi) + \frac{\xi_{i+k+1} - \xi}{\xi_{i+k+1} - \xi_{i+1}} B_{i+1}^{k-1}(\xi). \quad (4.3)$$

When  $\xi_{i+k} - \xi_i = 0$ ,  $\frac{\xi - \xi_i}{\xi_{i+k} - \xi_i}$  is taken to be zero, and similarly, when  $\xi_{i+k+1} - \xi_{i+1} = 0$ ,  $\frac{\xi_{i+k+1} - \xi}{\xi_{i+k+1} - \xi_{i+1}}$  is taken to be zero. B-spline basis functions are piecewise polynomials of degree  $k$ , form a partition of unity, have local support, and are non-negative. An example of a cubic B-spline basis is shown in Figure 4.1. Note the basis is  $C^2$  everywhere in the interval  $(0, 1)$ . Enhanced smoothness is one of the defining features of B-splines. We refer to linear combinations of B-spline basis functions as B-splines or simply splines.

Let us now introduce the vector  $\zeta = \{\zeta_1, \dots, \zeta_m\}$  of knots without repetitions and a corresponding vector  $\{r_1, \dots, r_m\}$  of knot multiplicities. That is,  $r_i$  is defined to be the multiplicity of the knot  $\zeta_i$  in  $\Xi$ . By construction,  $\sum_{i=1}^m r_i =$

$n + k + 1$ . We assume that  $r_i \leq k + 1$ . Let us further assume throughout that  $r_1 = r_m = k + 1$ , *i.e.*, that  $\Xi$  is an open knot vector. This allows us to easily prescribe Dirichlet boundary conditions. At the point  $\zeta_i$ , B-spline basis functions have  $\alpha_i := k - r_i$  continuous derivatives. Therefore,  $-1 \leq \alpha_i \leq k - 1$ , and the maximum multiplicity allowed,  $r_i = k + 1$ , gives a discontinuity at  $\zeta_i$ . We define the regularity vector  $\alpha$  by  $\alpha := \{\alpha_1, \dots, \alpha_m\}$ . By construction,  $\alpha_1 = \alpha_m = -1$ . In what follows, we utilize the notation

$$|\alpha| = \min\{\alpha_i : 2 \leq i \leq m - 1\} \quad (4.4)$$

and  $\alpha - 1 := \{-1, \alpha_2 - 1, \dots, \alpha_{m-1} - 1, -1\}$  when  $\alpha_i \geq 0$  for  $2 \leq i \leq m - 1$ .

We denote the space of B-splines spanned by the basis functions  $B_i^k$  as

$$S_\alpha^k := \text{span} \{B_i^k\}_{i=1}^n. \quad (4.5)$$

When  $k \geq 1$  and  $\alpha_i \geq 0$  for  $2 \leq i \leq m - 1$ , the derivatives of functions in  $S_\alpha^k$  are splines as well. In fact, we have the stronger relationship

$$\left\{ \frac{d}{dx} v : v \in S_\alpha^k \right\} \equiv S_{\alpha-1}^{k-1}. \quad (4.6)$$

That is, the derivative operator  $\partial_x : S_\alpha^k \rightarrow S_{\alpha-1}^{k-1}$  is surjective. One of the most important properties of univariate B-splines is refinement and, perhaps more importantly, nestedness of refinement. Notably, knot insertion and degree elevation allow one to define a sequence of nested, refined B-spline spaces. Knot insertion and degree elevation algorithms are described in detail in Chapter 2 of [52].

## 4.2 Multivariate B-splines

The definition of multivariate B-splines follows easily through a tensor-product construction. For  $d$  a positive integer, let us consider the unit cube  $\widehat{\Omega} =$

$(0, 1)^d \subset \mathbb{R}^d$ , which we will henceforth refer to as the parametric domain. Mimicking the one-dimensional case, given integers  $k_l$  and  $n_l$  for  $l = 1, \dots, d$ , let us introduce open knot vectors  $\Xi_l = \{\xi_{1,l}, \dots, \xi_{n_l+k_l+1,l}\}$  and the associated vectors  $\zeta_l = \{\zeta_{1,l}, \dots, \zeta_{m_l,l}\}$ ,  $\{r_{1,l}, \dots, r_{m_l,l}\}$ , and  $\alpha_l = \{\alpha_{1,l}, \dots, \alpha_{m_l,l}\}$ . There is a parametric Cartesian mesh  $\mathcal{M}_h$  associated with these knot vectors partitioning the parametric domain into rectangular parallelepipeds. Visually,

$$\mathcal{M}_h = \{Q = \otimes_{l=1,\dots,d} (\zeta_{i_l,l}, \zeta_{i_l+1,l}), 1 \leq i_l \leq m_l - 1\}. \quad (4.7)$$

For each element  $Q \in \mathcal{M}_h$  we associate a parametric mesh size  $h_Q = \text{diam}(Q)$ . We also define a shape regularity constant  $\lambda$  which satisfies the inequality

$$\lambda^{-1} \leq \frac{h_{Q,\min}}{h_Q} \leq \lambda, \quad \forall Q \in \mathcal{M}_h, \quad (4.8)$$

where  $h_{Q,\min}$  denotes the length of the smallest edge of  $Q$ . A sequence of parametric meshes that satisfy the above inequality for an identical shape regularity constant is said to be locally quasi-uniform.

We associate with each knot vector  $\Xi_l$  ( $l = 1, \dots, d$ ) univariate B-spline basis functions  $B_{i_l,l}^{k_l}$  of degree  $k_l$  for  $i_l = 1, \dots, n_l$ . On the mesh  $\mathcal{M}_h$ , we define the tensor-product B-spline basis functions as

$$B_{i_1,\dots,i_d}^{k_1,\dots,k_d} := B_{i_1,1}^{k_1} \otimes \dots \otimes B_{i_d,d}^{k_d}, \quad i_1 = 1, \dots, n_1, \dots, i_d = 1, \dots, n_d. \quad (4.9)$$

We then accordingly define the tensor-product B-spline space as

$$S_{\alpha_1,\dots,\alpha_d}^{k_1,\dots,k_d} \equiv S_{\alpha_1,\dots,\alpha_d}^{k_1,\dots,k_d}(\mathcal{M}_h) := \text{span} \left\{ B_{i_1,\dots,i_d}^{k_1,\dots,k_d} \right\}_{i_1=1,\dots,i_d=1}^{n_1,\dots,n_d}. \quad (4.10)$$

The space is fully characterized by the mesh  $\mathcal{M}_h$ , the degrees  $k_l$ , and the regularity vectors  $\alpha_l$ , as the notation reflects. Like their univariate counterparts, multivariate

B-spline basis functions are piecewise polynomial, form a partition of unity, have local support, and are non-negative. Defining the regularity constant

$$\alpha := \min_{l=1,\dots,d} \min_{2 \leq i_l \leq m_l - 1} \{\alpha_{i_l, l}\} \quad (4.11)$$

we see that our B-splines are  $C^\alpha$ -continuous throughout the domain  $\widehat{\Omega}$ . Refinement of multivariate B-spline bases is obtained by applying knot insertion and degree elevation in tensor-product fashion. In the remainder of the text, we consider a family of nested meshes  $\{\mathcal{M}_h\}_{h \leq h_0}$  and associated B-spline spaces  $\{S_{\alpha_1, \dots, \alpha_d}^{k_1, \dots, k_d}(\mathcal{M}_h)\}_{h \leq h_0}$  that have been obtained by successive applications of knot refinement. Furthermore, we assume throughout that the mesh family  $\{\mathcal{M}_h\}_{h \leq h_0}$  is locally quasi-uniform.

Note that each element  $Q = \otimes_{l=1, \dots, d} (\zeta_{i_l, l}, \zeta_{i_l+1, l})$  has the equivalent representation  $Q = \otimes_{l=1, \dots, d} (\xi_{j_l, l}, \xi_{j_l+1, l})$  for some index  $j_l$ . With this in mind, we associate with each element a support extension  $\tilde{Q}$ , defined as

$$\tilde{Q} := \otimes_{l=1, \dots, d} (\xi_{j_l - p_l, l}, \xi_{j_l + p_l + 1, l}). \quad (4.12)$$

The support extension is the interior of the set formed by the union of the supports of all B-spline basis functions whose support intersects  $Q$ . Note that each element belongs to the support extension of at most  $\prod_{l=1, \dots, d} (2p_l + 1)$  elements. The support extension is a natural object to consider when examining the local approximation properties of a B-spline space.

### 4.3 Piecewise Smooth Functions, Geometrical Mappings, and Physical Mesh Entities

On the parametric mesh  $\mathcal{M}_h$ , we define the space of piecewise smooth functions with interelement regularity given by the vectors  $\alpha_1, \dots, \alpha_d$  as

$$C_{\alpha_1, \dots, \alpha_d}^\infty = C_{\alpha_1, \dots, \alpha_d}^\infty(\mathcal{M}_h). \quad (4.13)$$

Precisely, a function in  $C_{\alpha_1, \dots, \alpha_d}^\infty$  is a function whose restriction to an element  $Q \in \mathcal{M}_h$  admits a  $C^\infty$  extension in the closure of that element and which has  $\alpha_{i,l}$  continuous derivatives with respect to the  $l$ th coordinate along the internal mesh faces  $\{(x_1, \dots, x_d) : x_l = \zeta_{i,l}, \zeta_{j',l'} < x_{l'} < \zeta_{j'+1,l'}, l' \neq l\}$  for all  $i_l = 2, \dots, m_l - 1$  and  $j_{l'} = 1, \dots, m_{l'} - 1$ . Note immediately that any function lying in the B-spline space  $S_{\alpha_1, \dots, \alpha_d}^{k_1, \dots, k_d}$  also lies in  $C_{\alpha_1, \dots, \alpha_d}^\infty$ .

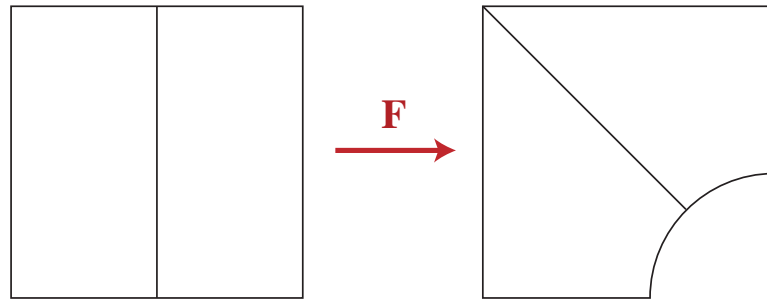
Unless specified otherwise, we assume throughout the rest of the dissertation that the physical domain  $\Omega \subset \mathbb{R}^d$  can be exactly parametrized by a geometrical mapping  $\mathbf{F} : \widehat{\Omega} \rightarrow \Omega$  belonging to  $(C_{\alpha_1, \dots, \alpha_d}^\infty)^d$  with piecewise smooth inverse. We further assume that  $d = 2$  or  $3$ , the physical domain  $\Omega$  is simply connected with connected boundary  $\partial\Omega$ , and the geometrical mapping is independent of the mesh family index  $h$ . See, for example, the sequence of mapped meshes depicted in Figure 4.2. A geometrical mapping meeting our criteria could be defined utilizing B-splines or Non-Uniform Rational B-Splines (NURBS) on the coarsest mesh  $\mathcal{M}_{h_0}$ . NURBS mappings are especially useful as they can represent many geometries of scientific and engineering interest and are the main tools employed in Computer Aided Design (CAD) software. Later in this dissertation, we will additionally utilize polar mappings to solve flow problems on cylindrical geometries in order to preserve symmetries.

The geometrical mapping  $\mathbf{F}$  naturally induces a mesh

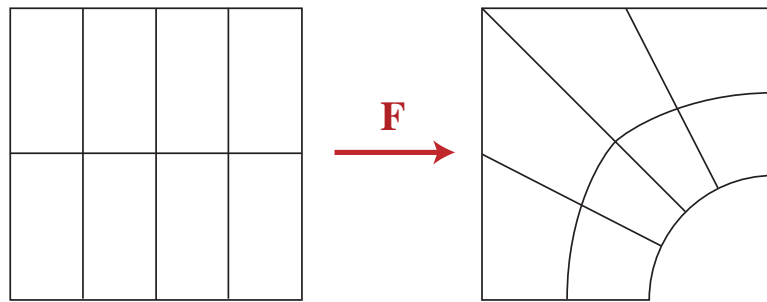
$$\mathcal{K}_h = \{K : K = \mathbf{F}(Q), Q \in \mathcal{M}_h\} \quad (4.14)$$

on the physical domain  $\Omega$ . We define for each element  $K \in \mathcal{K}_h$  a physical mesh size

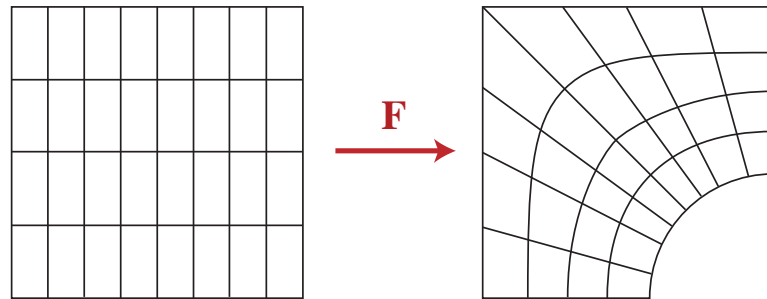
$$h_K = \|D\mathbf{F}\|_{L^\infty(Q)} h_Q \quad (4.15)$$



Coarse Mesh



First Refinement



Second Refinement

Figure 4.2: Illustration in the two-dimensional setting of how the parametric mapping  $\mathbf{F}$  is independent of the mesh family index  $h$ .

where  $Q$  is the inverse image of  $K$ , and we also define the support extension  $\tilde{K} = \mathbf{F}(\tilde{Q})$ . We define for a given mesh the global mesh size

$$h = \max \{h_K, K \in \mathcal{K}_h\}.$$

Note that as the parametric mesh family  $\{\mathcal{M}_h\}_{h \leq h_0}$  is locally quasi-uniform and the geometrical mapping  $\mathbf{F}$  is independent of the mesh family index  $h$ , the physical mesh family  $\{\mathcal{K}_h\}_{h \leq h_0}$  is also locally quasi-uniform. We refer to the physical domain  $\Omega$  and its pre-image  $\hat{\Omega}$  interchangeably as the patch. It should be noted that, in general, the domain  $\Omega$  cannot be represented using just a single patch. Instead, multiple patches must be employed. We will discuss further the multi-patch setting in Section 6.5.

We define on the parametric mesh a set of mesh faces  $\hat{\mathcal{F}}_h = \{\hat{F}\}$  where  $\hat{F}$  is a face of one or more elements in  $\mathcal{M}_h$ . We define the physical set of mesh faces as

$$\mathcal{F}_h = \{F = \mathbf{F}(\hat{F}) : \hat{F} \in \hat{\mathcal{F}}_h\}$$

and we define the boundary mesh to be

$$\Gamma_h = \{F \in \mathcal{F}_h : F \subset \partial\Omega\}.$$

By construction,

$$\partial\Omega = \cup_{F \in \Gamma_h} \overline{F}.$$

Note that for each face  $F \in \Gamma_h$  there is a unique  $K \in \mathcal{K}_h$  such that  $F$  is a “face” of  $K$  (in the sense that  $F$  is the image of a face of  $Q$ , the pre-image of  $K$ ). We hence define for such a face the mesh size

$$h_F := h_K.$$

One may also define  $h_F$  to be the wall-normal mesh-size as is done in [21]. Such a definition is more appropriate for stretched meshes.

Throughout the text, we will utilize the terminology “a constant independent of  $h$ ”. When we employ such terminology, we simply indicate that the constant will not depend on the given mesh and, in particular, its size. The constant may, however, depend on the domain, the shape regularity of the parametric mesh family, the polynomial degrees of the employed B-spline spaces, and mesh-invariant measures of the parametric mapping.

## Chapter 5

### Discretization of Velocity and Pressure Fields

In this chapter, we define the B-spline spaces which we will later utilize to discretize the velocity and pressure fields appearing in the generalized Stokes and Navier-Stokes problems. These spaces are motivated by the recent theory of isogeometric discrete differential forms [40, 41] and can be interpreted as smooth generalizations of Raviart-Thomas-Nédélec elements [153, 159]. We start this chapter by establishing preliminary notation. Then, we recall the construction of compatible B-spline discretizations which conform to a commuting de Rham diagram. Following this effort, we reveal a new Hilbert complex for the study of Stokes flow, and we demonstrate that compatible B-spline discretizations also conform to a commuting Stokes complex provided the discretizations are sufficiently smooth. This conformity results in methods which automatically satisfy the inf-sup condition and provide divergence-free velocity fields. We finish this chapter by presenting interpolation estimates, inverse inequalities, and trace inequalities.

#### 5.1 Notation: Sobolev Spaces

Let us begin with some standard notation. Let  $D \subset \mathbb{R}^d$  denote an arbitrary bounded Lipschitz domain with boundary  $\partial D$ . As usual, let  $L^2(D)$  denote the space of square integrable functions on  $D$  and define  $\mathbf{L}^2(D) = (L^2(D))^d$ . Let  $H^k(D)$  denote the space of functions in  $L^2(D)$  whose  $k^{\text{th}}$ -order derivatives belong to  $L^2(D)$  and define  $\mathbf{H}^k(D) = (H^k(D))^d$ . We identify with  $H^k(D)$  the standard Sobolev

norm  $\|\cdot\|_{H^k(D)}$  and semi-norm  $|\cdot|_{H^k(D)}$ . We employ the convention  $H^0(D) = L^2(D)$ . Throughout, Sobolev spaces of fractional order are defined using function space interpolation (see, e.g., Chapter 1 of [181]). As in Chapter 2, we define  $H_0^1(D) \subset H^1(D)$  to be the subspace of functions with homogeneous boundary conditions,  $\mathbf{H}_0^1(D)$  to be the vectorial counterpart of  $H_0^1(D)$ , and  $L_0^2(D) \subset L^2(D)$  to be the space of square-integrable functions with zero average on  $D$ . We will also utilize the more general Lebesgue spaces  $L^p(D)$  where  $1 \leq p \leq \infty$  and their vectorial counterpart  $\mathbf{L}^p(D)$ .

For  $D \subset \mathbb{R}^3$ , we define  $\mathbf{H}^s(\mathbf{curl}; D)$  to be the Sobolev space of all functions in  $\mathbf{H}^s(D)$  whose  $\mathbf{curl}$  also belongs to  $\mathbf{H}^s(D)$  and  $\mathbf{H}^s(\mathbf{div}; D)$  to be the Sobolev space of all functions in  $\mathbf{H}^s(\Omega)$  whose divergence belongs to  $H^s(D)$ . These two spaces are equipped with the norms

$$\|\mathbf{v}\|_{\mathbf{H}^s(\mathbf{curl}; D)} = \left( \|\mathbf{v}\|_{\mathbf{H}^s(D)}^2 + \|\mathbf{curl}\mathbf{v}\|_{\mathbf{H}^s(D)}^2 \right)^{1/2}$$

and

$$\|\mathbf{v}\|_{\mathbf{H}^s(\mathbf{div}; D)} = \left( \|\mathbf{v}\|_{\mathbf{H}^s(D)}^2 + \|\mathbf{div}\mathbf{v}\|_{H^s(D)}^2 \right)^{1/2}$$

respectively. When  $s = 0$ , we will drop the index. As in Chapter 2, we define

$$\mathbf{H}_0(\mathbf{curl}; D) = \{\mathbf{v} \in \mathbf{H}(\mathbf{curl}; D) : \mathbf{v} \times \mathbf{n} = \mathbf{0} \text{ on } \partial D\}$$

$$\mathbf{H}_0(\mathbf{div}; D) = \{\mathbf{v} \in \mathbf{H}(\mathbf{div}; D) : \mathbf{v} \cdot \mathbf{n} = 0 \text{ on } \partial D\}$$

where  $\mathbf{n}$  denotes the outward pointing unit normal. These definitions naturally extend to the two-dimensional setting, with the vector  $\mathbf{curl}$  operator being replaced with the scalar rotor operator  $\mathbf{rot} \mathbf{u} = \partial_{x_2} u_1 - \partial_{x_1} u_2$ . Furthermore, in two-dimensions, the space  $\mathbf{H}_0(\mathbf{div}; D)$  can be obtained by rotating the space  $\mathbf{H}_0(\mathbf{rot}; D)$ .

Recall that  $\widehat{\Omega} = (0, 1)^d$  denotes the parametric domain. As discussed in Section 4.3, we assume that the physical domain  $\Omega$  is defined through a piecewise smooth parametrization with piecewise smooth inverse which we denote as

$\mathbf{F} : \widehat{\Omega} \rightarrow \Omega$ . We further assume unless otherwise specified that  $\Omega$  is simply connected with connected boundary  $\partial\Omega$ . From this point forward, we will utilize the notation  $\widehat{\text{grad}}, \widehat{\text{curl}}, \widehat{\text{div}}$  to distinguish differentiation in parametric space from differentiation in physical space. Since  $\mathbf{F}$  and its inverse are piecewise smooth, we can define the pullbacks relating these spaces as

$$\begin{aligned}
\iota_S(\phi) &:= \phi \circ \mathbf{F}, & \phi &\in H^1(\Omega) \\
\iota_N(\mathbf{u}) &:= (D\mathbf{F})^T (\mathbf{u} \circ \mathbf{F}), & \mathbf{u} &\in \mathbf{H}(\text{curl}; \Omega) \\
\iota_{\mathcal{RT}}(\mathbf{v}) &:= \det(D\mathbf{F}) (D\mathbf{F})^{-1} (\mathbf{v} \circ \mathbf{F}), & \mathbf{v} &\in \mathbf{H}(\text{div}; \Omega) \\
\iota_W(\psi) &:= \det(D\mathbf{F}) (\psi \circ \mathbf{F}), & \psi &\in L^2(\Omega)
\end{aligned} \tag{5.1}$$

where  $D\mathbf{F}$  is the Jacobian matrix of the parametric mapping  $\mathbf{F}$ . We would like to note at this point that  $\iota_{\mathcal{RT}}$  is the classical Piola transform. Due to the **curl** and divergence preserving properties of  $\iota_N$  and  $\iota_{\mathcal{RT}}$  respectively, we have the following commuting de Rham diagram for  $\Omega \subset \mathbb{R}^3$ :

$$\begin{array}{ccccccc}
H^1(\widehat{\Omega}) & \xrightarrow{\widehat{\text{grad}}} & \mathbf{H}(\widehat{\text{curl}}; \widehat{\Omega}) & \xrightarrow{\widehat{\text{curl}}} & \mathbf{H}(\widehat{\text{div}}; \widehat{\Omega}) & \xrightarrow{\widehat{\text{div}}} & L^2(\widehat{\Omega}) \\
\iota_S \uparrow & & \iota_N \uparrow & & \iota_{\mathcal{RT}} \uparrow & & \iota_W \uparrow \\
H^1(\Omega) & \xrightarrow{\text{grad}} & \mathbf{H}(\text{curl}; \Omega) & \xrightarrow{\text{curl}} & \mathbf{H}(\text{div}; \Omega) & \xrightarrow{\text{div}} & L^2(\Omega).
\end{array} \tag{5.2}$$

We also have the commuting diagram

$$\begin{array}{ccccccc}
H_0^1(\widehat{\Omega}) & \xrightarrow{\widehat{\text{grad}}} & \mathbf{H}_0(\widehat{\text{curl}}; \widehat{\Omega}) & \xrightarrow{\widehat{\text{curl}}} & \mathbf{H}_0(\widehat{\text{div}}; \widehat{\Omega}) & \xrightarrow{\widehat{\text{div}}} & L_0^2(\widehat{\Omega}) \\
\iota_S \uparrow & & \iota_N \uparrow & & \iota_{\mathcal{RT}} \uparrow & & \iota_W \uparrow \\
H_0^1(\Omega) & \xrightarrow{\text{grad}} & \mathbf{H}_0(\text{curl}; \Omega) & \xrightarrow{\text{curl}} & \mathbf{H}_0(\text{div}; \Omega) & \xrightarrow{\text{div}} & L_0^2(\Omega)
\end{array} \tag{5.3}$$

which exploits the integral-preserving property of  $\iota_W$ . For  $\Omega \subset \mathbb{R}^2$ , we have the two commuting diagrams

$$\begin{array}{ccccccc}
H^1(\widehat{\Omega}) & \xrightarrow{\widehat{\text{curl}}} & \mathbf{H}(\widehat{\text{div}}; \widehat{\Omega}) & \xrightarrow{\widehat{\text{div}}} & L^2(\widehat{\Omega}) & & \\
\iota_S \uparrow & & \iota_{\mathcal{RT}} \uparrow & & \iota_W \uparrow & & \\
H^1(\Omega) & \xrightarrow{\text{curl}} & \mathbf{H}(\text{div}; \Omega) & \xrightarrow{\text{div}} & L^2(\Omega). & & 
\end{array} \tag{5.4}$$

and

$$\begin{array}{ccccc}
H_0^1(\widehat{\Omega}) & \xrightarrow{\widehat{\mathbf{curl}}} & \mathbf{H}_0(\widehat{\mathbf{div}}; \widehat{\Omega}) & \xrightarrow{\widehat{\mathbf{div}}} & L_0^2(\widehat{\Omega}) \\
\iota_S \uparrow & & \iota_{\mathcal{RT}} \uparrow & & \iota_W \uparrow \\
H_0^1(\Omega) & \xrightarrow{\mathbf{curl}} & \mathbf{H}_0(\mathbf{div}; \Omega) & \xrightarrow{\mathbf{div}} & L_0^2(\Omega)
\end{array} \tag{5.5}$$

where  $\mathbf{curl}$  and  $\widehat{\mathbf{curl}}$  are the standard two-dimensional vector operators

$$\mathbf{curl} = \{\partial/\partial x_2, -\partial/\partial x_1\}^T$$

and

$$\widehat{\mathbf{curl}} = \{\partial/\partial \xi_2, -\partial/\partial \xi_1\}^T.$$

## 5.2 B-spline Spaces Satisfying the de Rham Diagram

The de Rham complex was originally introduced to study the algebraic topology of differential manifolds. The existence of a commuting de Rham diagram [70] has since played a large role in the mathematical study of finite element discretizations of the Maxwell's equations and mixed methods for the Hodge Laplacian. The de Rham complex has especially played a critical role in the study of numerical methods for the Maxwell eigenproblem where it has been shown a commuting diagram is a necessary requirement for proper convergence [28]. B-splines satisfying a discrete de Rham complex were first introduced by Buffa *et al.* [41] in order to solve two-dimensional Maxwell's problems using isogeometric analysis. In [40], commuting projection operators were introduced in order to study the three-dimensional Maxwell's eigenproblem and spectral correctness of the B-spline discretization technique was proven by exploiting these operators.

In this section, we briefly review the construction of B-splines satisfying a discrete de Rham complex. Restricting first to the three-dimensional setting, let us

introduce the following spaces of B-splines:

$$\begin{aligned}
\widehat{\mathcal{S}}_h &:= S_{\alpha_1, \alpha_2, \alpha_3}^{k_1, k_2, k_3}(\mathcal{M}_h) \\
\widehat{\mathcal{N}}_h &:= S_{\alpha_1-1, \alpha_2, \alpha_3}^{k_1-1, k_2, k_3}(\mathcal{M}_h) \times S_{\alpha_1, \alpha_2-1, \alpha_3}^{k_1, k_2-1, k_3}(\mathcal{M}_h) \times S_{\alpha_1, \alpha_2, \alpha_3-1}^{k_1, k_2, k_3-1}(\mathcal{M}_h) \\
\widehat{\mathcal{RT}}_h &:= S_{\alpha_1, \alpha_2-1, \alpha_3-1}^{k_1, k_2-1, k_3-1}(\mathcal{M}_h) \times S_{\alpha_1-1, \alpha_2, \alpha_3-1}^{k_1-1, k_2, k_3-1}(\mathcal{M}_h) \times S_{\alpha_1-1, \alpha_2-1, \alpha_3}^{k_1-1, k_2-1, k_3}(\mathcal{M}_h) \\
\widehat{\mathcal{W}}_h &:= S_{\alpha_1-1, \alpha_2-1, \alpha_3-1}^{k_1-1, k_2-1, k_3-1}(\mathcal{M}_h).
\end{aligned}$$

We refer to the above set of spaces as compatible B-spline spaces. The meaning of this terminology will become more clear in a moment. It should be noted that standard tensor-product Raviart-Thomas-Nédélec discretizations [153, 159] can actually be written in terms of compatible B-spline spaces. In this sense, we interpret compatible B-splines as generalizations of Raviart-Thomas-Nédélec elements. Specifically, we refer to functions in  $\widehat{\mathcal{N}}_h$  as B-splines of Nédélec type and ones in  $\widehat{\mathcal{RT}}_h$  as B-splines of Raviart-Thomas type. We also refer to functions in  $\widehat{\mathcal{N}}_h$  as curl-conforming B-splines and functions in  $\widehat{\mathcal{RT}}_h$  as divergence-conforming B-splines.

In order for the spaces of compatible B-splines to be meaningful, we require that  $\alpha \geq 0$  where  $\alpha$  is the continuity constant

$$\alpha = \min_{l=1, \dots, d} \min_{2 \leq i_l \leq m_l-1} \{\alpha_{i_l, l}\}.$$

This means that the functions in  $\widehat{\mathcal{S}}_h$  are at least continuous, the vector functions in  $\widehat{\mathcal{N}}_h$  are at least tangential continuous, and the vector functions in  $\widehat{\mathcal{RT}}_h$  are at least normal continuous. In order to deal with boundary conditions, we define the following constrained spaces:

$$\begin{aligned}
\widehat{\mathcal{S}}_{0,h} &:= \widehat{\mathcal{S}}_h \cap H_0^1(\widehat{\Omega}) \\
\widehat{\mathcal{N}}_{0,h} &:= \widehat{\mathcal{N}}_h \cap \mathbf{H}_0(\mathbf{curl}; \widehat{\Omega}) \\
\widehat{\mathcal{RT}}_{0,h} &:= \widehat{\mathcal{RT}}_h \cap \mathbf{H}_0(\mathbf{div}; \widehat{\Omega}) \\
\widehat{\mathcal{W}}_{0,h} &:= \widehat{\mathcal{W}}_h \cap L_0^2(\widehat{\Omega}).
\end{aligned}$$

Due to the special relationship given by (4.6), it is easily seen that the above spaces satisfy the discrete de Rham complex

$$\widehat{\mathcal{S}}_{0,h} \xrightarrow{\widehat{\mathbf{grad}}} \widehat{\mathcal{N}}_{0,h} \xrightarrow{\widehat{\mathbf{curl}}} \widehat{\mathcal{RT}}_{0,h} \xrightarrow{\widehat{\mathbf{div}}} \widehat{\mathcal{W}}_{0,h}. \quad (5.6)$$

In fact, we have a much stronger result which was proven in [40].

**Proposition 5.2.1.** *For  $\Omega \subset \mathbb{R}^3$ , there exist  $L^2$ -stable projection operators  $\widehat{\Pi}_{\mathcal{S}_h}^0 : L^2(\widehat{\Omega}) \rightarrow \widehat{\mathcal{S}}_{0,h}$ ,  $\widehat{\Pi}_{\mathcal{N}_h}^0 : \mathbf{L}^2(\widehat{\Omega}) \rightarrow \widehat{\mathcal{N}}_{0,h}$ ,  $\widehat{\Pi}_{\mathcal{RT}_h}^0 : \mathbf{L}^2(\widehat{\Omega}) \rightarrow \widehat{\mathcal{RT}}_{0,h}$ , and  $\widehat{\Pi}_{\mathcal{W}_h}^0 : L_0^2(\widehat{\Omega}) \rightarrow \widehat{\mathcal{W}}_{0,h}$  such that the following diagram commutes:*

$$\begin{array}{ccccccc}
H_0^1(\widehat{\Omega}) & \xrightarrow{\widehat{\text{grad}}} & \mathbf{H}_0(\widehat{\text{curl}}; \widehat{\Omega}) & \xrightarrow{\widehat{\text{curl}}} & \mathbf{H}_0(\widehat{\text{div}}; \widehat{\Omega}) & \xrightarrow{\widehat{\text{div}}} & L_0^2(\widehat{\Omega}) \\
\widehat{\Pi}_{\mathcal{S}_h}^0 \downarrow & & \widehat{\Pi}_{\mathcal{N}_h}^0 \downarrow & & \widehat{\Pi}_{\mathcal{RT}_h}^0 \downarrow & & \widehat{\Pi}_{\mathcal{W}_h}^0 \downarrow \\
\widehat{\mathcal{S}}_{0,h} & \xrightarrow{\widehat{\text{grad}}} & \widehat{\mathcal{N}}_{0,h} & \xrightarrow{\widehat{\text{curl}}} & \widehat{\mathcal{RT}}_{0,h} & \xrightarrow{\widehat{\text{div}}} & \widehat{\mathcal{W}}_{0,h}.
\end{array} \tag{5.7}$$

Furthermore, the continuity constants associated with the commuting projection operators only depend on the polynomial degrees of the B-spline discretization and the shape regularity of the mesh family  $\{\mathcal{M}_h\}_{h \leq h_0}$ .

For spaces not subject to boundary conditions, we have the following result.

**Proposition 5.2.2.** *For  $\Omega \subset \mathbb{R}^3$ , there exist  $L^2$ -stable projection operators such that the following diagram holds:*

$$\begin{array}{ccccccc}
H^1(\widehat{\Omega}) & \xrightarrow{\widehat{\text{grad}}} & \mathbf{H}(\widehat{\text{curl}}; \widehat{\Omega}) & \xrightarrow{\widehat{\text{curl}}} & \mathbf{H}(\widehat{\text{div}}; \widehat{\Omega}) & \xrightarrow{\widehat{\text{div}}} & L^2(\widehat{\Omega}) \\
\widehat{\Pi}_{\mathcal{S}_h} \downarrow & & \widehat{\Pi}_{\mathcal{N}_h} \downarrow & & \widehat{\Pi}_{\mathcal{RT}_h} \downarrow & & \widehat{\Pi}_{\mathcal{W}_h} \downarrow \\
\widehat{\mathcal{S}}_h & \xrightarrow{\widehat{\text{grad}}} & \widehat{\mathcal{N}}_h & \xrightarrow{\widehat{\text{curl}}} & \widehat{\mathcal{RT}}_h & \xrightarrow{\widehat{\text{div}}} & \widehat{\mathcal{W}}_h.
\end{array} \tag{5.8}$$

Furthermore, the continuity constants of the projection operators only depend on polynomial degree and shape regularity.

Hence, the spaces of compatible B-splines, in conjunction with the commuting projection operators defined in the preceding two propositions, conform to a commuting de Rham diagram. This is the reason we refer to the B-spline spaces introduced in this section as being compatible. Due to this conformity, compatible B-spline spaces mimic intrinsic properties of the continuous de Rham complex.

This is especially important, say, for discretization of electromagnetic eigenproblems. If compatible B-splines are utilized to approximate Maxwell's eigenproblem, one obtains a discretization procedure which inherits underlying properties of the underlying partial differential eigensystem. The result is a method free of spurious modes [28, 44].

Compatible B-spline spaces in the physical domain  $\Omega$  are simply defined through a push forward of the spaces in the parametric domain  $\widehat{\Omega}$ . Recall the pullbacks given by (5.1). The discrete spaces in the physical domain corresponding to the de Rham complex with homogeneous boundary conditions are then defined as

$$\begin{aligned} \mathcal{S}_{0,h} &:= \left\{ \phi_h : \iota_{\mathcal{S}}(\phi_h) \in \widehat{\mathcal{S}}_{0,h} \right\} \\ \mathcal{N}_{0,h} &:= \left\{ \mathbf{u}_h : \iota_{\mathcal{N}}(\mathbf{u}_h) \in \widehat{\mathcal{N}}_{0,h} \right\} \\ \mathcal{RT}_{0,h} &:= \left\{ \mathbf{v}_h : \iota_{\mathcal{RT}}(\mathbf{v}_h) \in \widehat{\mathcal{RT}}_{0,h} \right\} \\ \mathcal{W}_{0,h} &:= \left\{ \psi_h : \iota_{\mathcal{W}}(\psi_h) \in \widehat{\mathcal{W}}_{0,h} \right\} \end{aligned} \quad (5.9)$$

while the discrete spaces  $\mathcal{S}_h$ ,  $\mathcal{N}_h$ ,  $\mathcal{RT}_h$ , and  $\mathcal{W}_h$  are defined in an identical fashion. Similarly, we define projection operators for the de Rham complex with homogeneous boundary conditions as

$$\iota_{\mathcal{S}}(\Pi_{\mathcal{S}_h}^0 \phi) := \widehat{\Pi}_{\mathcal{S}_h}^0(\iota_{\mathcal{S}}(\phi)), \quad \forall \phi \in H_0^1(\Omega) \quad (5.10)$$

$$\iota_{\mathcal{N}}(\Pi_{\mathcal{N}_h}^0 \mathbf{u}) := \widehat{\Pi}_{\mathcal{N}_h}^0(\iota_{\mathcal{N}}(\mathbf{u})), \quad \forall \mathbf{u} \in \mathbf{H}_0(\mathbf{curl}; \Omega) \quad (5.11)$$

$$\iota_{\mathcal{RT}}(\Pi_{\mathcal{RT}_h}^0 \mathbf{v}) := \widehat{\Pi}_{\mathcal{RT}_h}^0(\iota_{\mathcal{RT}}(\mathbf{v})), \quad \forall \mathbf{v} \in \mathbf{H}_0(\mathbf{div}; \Omega) \quad (5.12)$$

$$\iota_{\mathcal{W}}(\Pi_{\mathcal{W}_h}^0 \psi) := \widehat{\Pi}_{\mathcal{W}_h}^0(\iota_{\mathcal{W}}(\psi)), \quad \forall \psi \in L_0^2(\Omega). \quad (5.13)$$

and projection operators  $\Pi_{\mathcal{S}_h}$ ,  $\Pi_{\mathcal{N}_h}$ ,  $\Pi_{\mathcal{RT}_h}$ , and  $\Pi_{\mathcal{W}_h}$  using the same prescription. Then, from the commuting and stability properties of the parametric projection operators, the pullbacks, and the push forwards, we immediately have the following proposition (see Proposition 4.5 of [40]).

**Proposition 5.2.3.** For  $\Omega \subset \mathbb{R}^3$ , we have the commuting de Rham diagrams

$$\begin{array}{ccccccc}
H_0^1(\Omega) & \xrightarrow{\text{grad}} & \mathbf{H}_0(\mathbf{curl}; \Omega) & \xrightarrow{\text{curl}} & \mathbf{H}_0(\text{div}; \Omega) & \xrightarrow{\text{div}} & L_0^2(\Omega) \\
\Pi_{\mathcal{S}_h}^0 \downarrow & & \Pi_{\mathcal{N}_h}^0 \downarrow & & \Pi_{\mathcal{RT}_h}^0 \downarrow & & \Pi_{\mathcal{W}_h}^0 \downarrow \\
\mathcal{S}_{0,h} & \xrightarrow{\text{grad}} & \mathcal{N}_{0,h} & \xrightarrow{\text{curl}} & \mathcal{RT}_{0,h} & \xrightarrow{\text{div}} & \mathcal{W}_{0,h}
\end{array} \tag{5.14}$$

and

$$\begin{array}{ccccccc}
H^1(\Omega) & \xrightarrow{\text{grad}} & \mathbf{H}(\mathbf{curl}; \Omega) & \xrightarrow{\text{curl}} & \mathbf{H}(\text{div}; \Omega) & \xrightarrow{\text{div}} & L^2(\Omega) \\
\Pi_{\mathcal{S}_h} \downarrow & & \Pi_{\mathcal{N}_h} \downarrow & & \Pi_{\mathcal{RT}_h} \downarrow & & \Pi_{\mathcal{W}_h} \downarrow \\
\mathcal{S}_h & \xrightarrow{\text{grad}} & \mathcal{N}_h & \xrightarrow{\text{curl}} & \mathcal{RT}_h & \xrightarrow{\text{div}} & \mathcal{W}_h.
\end{array} \tag{5.15}$$

Furthermore, the continuity constants associated with the commuting projection operators only depend on polynomial degree, shape regularity, and mesh-invariant measures of the parametric mapping.

In previous works, compatible B-splines were mapped to physical space using NURBS and were referred to as isogeometric discrete differential forms [40,41]. However, other mappings such as the polar map can be employed. We believe polar mappings are especially useful for cylindrical problems as they preserve important symmetries.

We now introduce compatible B-splines for the two-dimensional setting. Let us define the following spaces of B-splines:

$$\begin{aligned}
\widehat{\mathcal{S}}_h &:= S_{\alpha_1, \alpha_2}^{k_1, k_2}(\mathcal{M}_h) \\
\widehat{\mathcal{RT}}_h &:= S_{\alpha_1, \alpha_2 - 1}^{k_1, k_2 - 1}(\mathcal{M}_h) \times S_{\alpha_1 - 1, \alpha_2}^{k_1 - 1, k_2}(\mathcal{M}_h) \\
\widehat{\mathcal{W}}_h &:= S_{\alpha_1 - 1, \alpha_2 - 1}^{k_1 - 1, k_2 - 1}(\mathcal{M}_h).
\end{aligned} \tag{5.16}$$

We have re-utilized the notation  $\widehat{\mathcal{S}}_h$ ,  $\widehat{\mathcal{RT}}_h$ , and  $\widehat{\mathcal{W}}_h$  as the spaces above are simply the two-dimensional counterparts of the three-dimensional spaces discussed previously. Again, in order for the spaces of compatible B-splines to be meaningful, we

require that  $\alpha \geq 0$ , and we define

$$\begin{aligned}\widehat{\mathcal{S}}_{0,h} &:= \widehat{\mathcal{S}}_h \cap H_0^1(\widehat{\Omega}) \\ \widehat{\mathcal{RT}}_{0,h} &:= \widehat{\mathcal{RT}}_h \cap \mathbf{H}_0(\widehat{\text{div}}; \widehat{\Omega}) \\ \widehat{\mathcal{W}}_{0,h} &:= \widehat{\mathcal{W}}_h \cap L_0^2(\widehat{\Omega}).\end{aligned}\tag{5.17}$$

Defining our two-dimensional compatible B-spline spaces in physical space as

$$\begin{aligned}\mathcal{S}_{0,h} &:= \left\{ \phi_h : \iota_{\mathcal{S}}(\phi_h) \in \widehat{\mathcal{S}}_{0,h} \right\} \\ \mathcal{RT}_{0,h} &:= \left\{ \mathbf{v}_h : \iota_{\mathcal{RT}}(\mathbf{v}_h) \in \widehat{\mathcal{RT}}_{0,h} \right\} \\ \mathcal{W}_{0,h} &:= \left\{ \psi_h : \iota_{\mathcal{W}}(\psi_h) \in \widehat{\mathcal{W}}_{0,h} \right\} \\ \mathcal{S}_h &:= \left\{ \phi_h : \iota_{\mathcal{S}}(\phi_h) \in \widehat{\mathcal{S}}_h \right\} \\ \mathcal{RT}_h &:= \left\{ \mathbf{v}_h : \iota_{\mathcal{RT}}(\mathbf{v}_h) \in \widehat{\mathcal{RT}}_h \right\} \\ \mathcal{W}_h &:= \left\{ \psi_h : \iota_{\mathcal{W}}(\psi_h) \in \widehat{\mathcal{W}}_h \right\},\end{aligned}\tag{5.18}$$

we have the following proposition which results from generalizing in a straightforward manner the three-dimensional results of [40] to the two-dimensional setting.

**Proposition 5.2.4.** *For  $\Omega \subset \mathbb{R}^2$ , there exist  $L^2$ -stable projection operators such that the following diagrams commute:*

$$\begin{array}{ccccc} H_0^1(\Omega) & \xrightarrow{\text{curl}} & \mathbf{H}_0(\text{div}; \Omega) & \xrightarrow{\text{div}} & L_0^2(\Omega) \\ \Pi_{\mathcal{S}_h}^0 \downarrow & & \Pi_{\mathcal{RT}_h}^0 \downarrow & & \Pi_{\mathcal{W}_h}^0 \downarrow \\ \mathcal{S}_{0,h} & \xrightarrow{\text{curl}} & \mathcal{RT}_{0,h} & \xrightarrow{\text{div}} & \mathcal{W}_{0,h} \end{array}\tag{5.19}$$

and

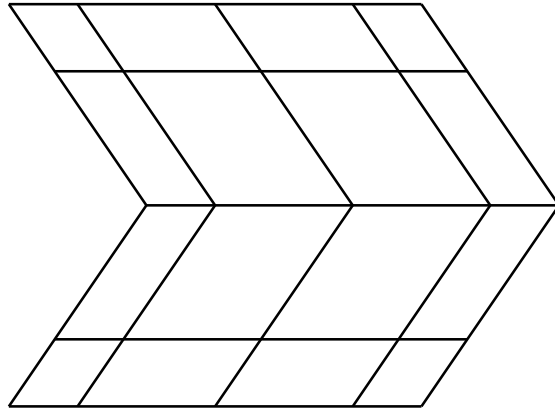
$$\begin{array}{ccccc} H^1(\Omega) & \xrightarrow{\text{curl}} & \mathbf{H}(\text{div}; \Omega) & \xrightarrow{\text{div}} & L^2(\Omega) \\ \Pi_{\mathcal{S}_h} \downarrow & & \Pi_{\mathcal{RT}_h} \downarrow & & \Pi_{\mathcal{W}_h} \downarrow \\ \mathcal{S}_h & \xrightarrow{\text{curl}} & \mathcal{RT}_h & \xrightarrow{\text{div}} & \mathcal{W}_h. \end{array}\tag{5.20}$$

Furthermore, the continuity constants associated with the commuting projection operators only depend on polynomial degree, shape regularity, and mesh-invariant measures of the parametric mapping.

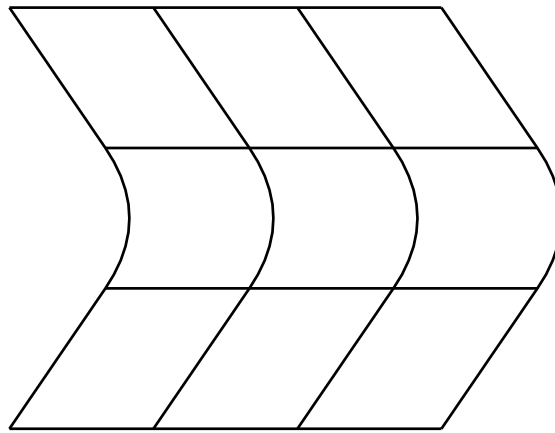
We now visualize some of the basis functions associated with these compatible B-spline spaces. For ease of presentation, we confine ourselves to the two-dimensional setting. Let  $k_1 = k_2 = 2$ , and let  $\Xi_1$  and  $\Xi_2$  be equal to

$$\Xi_1 := \Xi_2 := \{0, 0, 0, 1/3, 2/3, 1, 1, 1\}. \quad (5.21)$$

These polynomial degrees and knot vectors define a parametric mesh  $\mathcal{M}_h$  and B-spline spaces  $\widehat{\mathcal{S}}_h$ ,  $\widehat{\mathcal{RT}}_h$ , and  $\widehat{\mathcal{W}}_h$  over  $\mathcal{M}_h$ . To define the physical domain, we employ a biquadratic B-spline mapping. The control net defining this mapping (see Chapter 2 of [52]) and the resulting physical mesh  $\mathcal{K}_h$  are illustrated in Figure 5.1. In Figure 5.2, we have depicted a representative basis function of  $\mathcal{S}_h$  in both parametric and physical space. Note the basis function is  $C^1$ -continuous. In Figure 5.3, we have depicted a “first-component” vector basis function of  $\mathcal{RT}_h$ . Note that the basis function is  $C^1$ -continuous along horizontal parametric lines and  $C^0$ -continuous along vertical parametric lines. Further note that the directionality of the basis function is preserved under the map  $\iota_{\mathcal{RT}}$  in the sense that the function is oriented in the direction of horizontal parametric lines in both parametric and physical space. In Figure 5.4, we have depicted a typical “second-component” vector basis function of  $\mathcal{RT}_h$ . Note that the basis function is  $C^0$ -continuous along horizontal parametric lines and  $C^1$ -continuous along vertical parametric lines, and the directionality of the basis function is preserved under the map  $\iota_{\mathcal{RT}}$  in the sense that the function is oriented in the direction of vertical parametric lines in both parametric and physical space. Finally, in Figure 5.5, we have depicted a representative basis function of  $\mathcal{W}_h$  which is  $C^0$ -continuous in both parametric and physical space. To further highlight why we have mapped functions in  $\widehat{\mathcal{RT}}_h$  using the Piola transform, we have illustrated a divergence-free member of  $\widehat{\mathcal{RT}}_h$  and its image under the Piola transform in Figure 5.6. Note that the B-spline is divergence-free in both parametric and physical space.

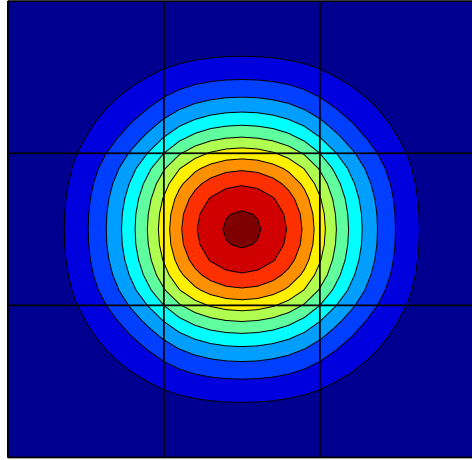


Control Mesh

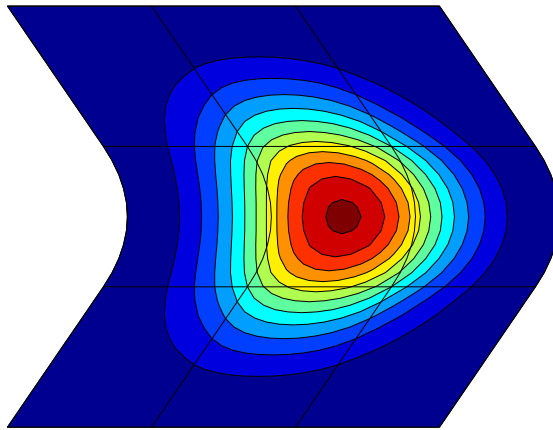


Physical Mesh

Figure 5.1: The control net and physical mesh for the biquadratic B-spline surface with  $\Xi_1 := \Xi_2 := \{0, 0, 0, 1/3, 2/3, 1, 1, 1\}$ .

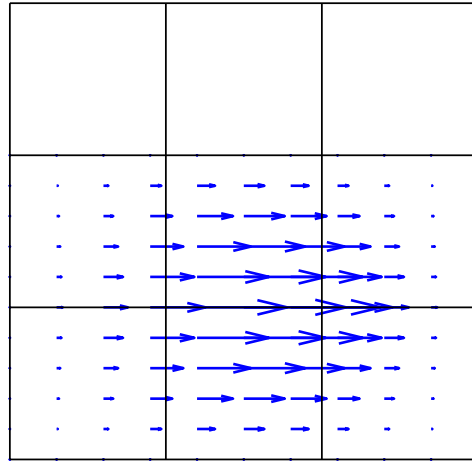


Parametric Space

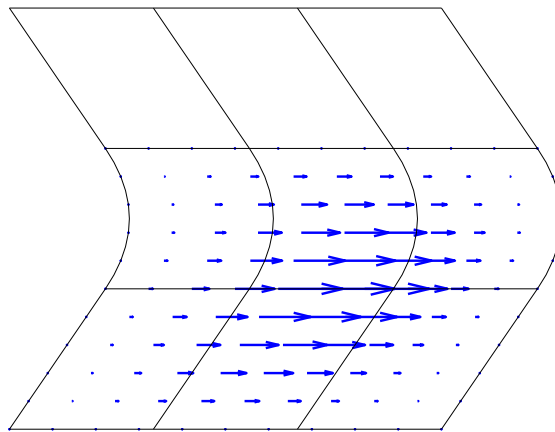


Physical Space

Figure 5.2: Contour plots of a representative basis function of  $\mathcal{S}_h$  in both parametric and physical space.

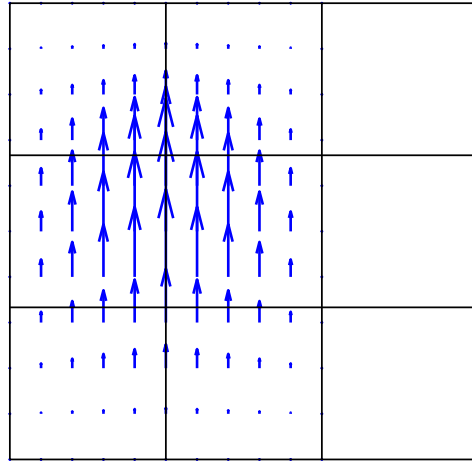


Parametric Space

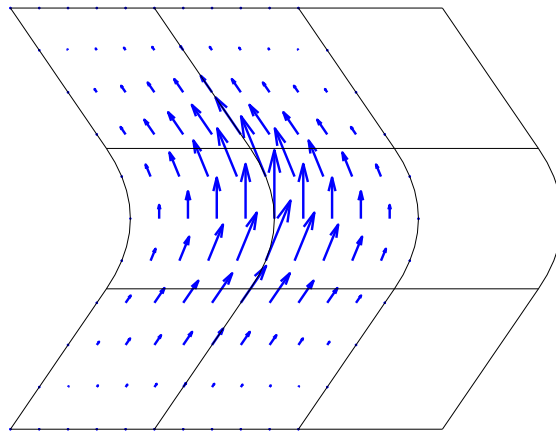


Physical Space

Figure 5.3: Vector plots of a representative first-component vector basis function of  $\mathcal{RT}_h$  in both parametric and physical space.

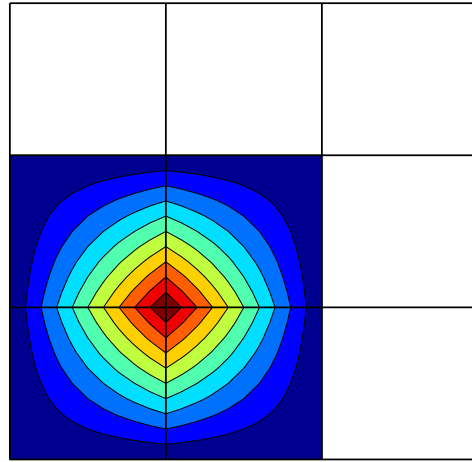


Parametric Space

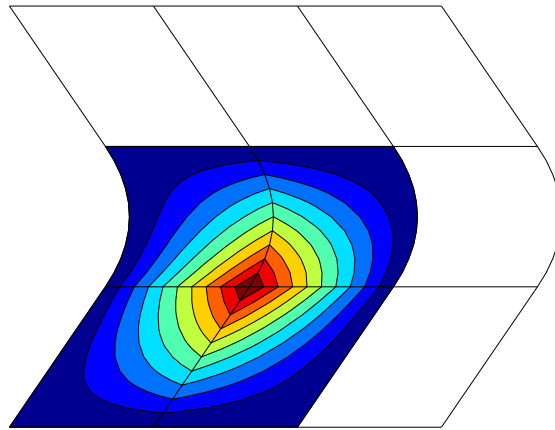


Physical Space

Figure 5.4: Vector plots of a representative second-component vector basis function of  $\mathcal{RT}_h$  in both parametric and physical space.



Parametric Space



Physical Space

Figure 5.5: Contour plots of a representative basis function of  $\mathcal{W}_h$  in both parametric and physical space.

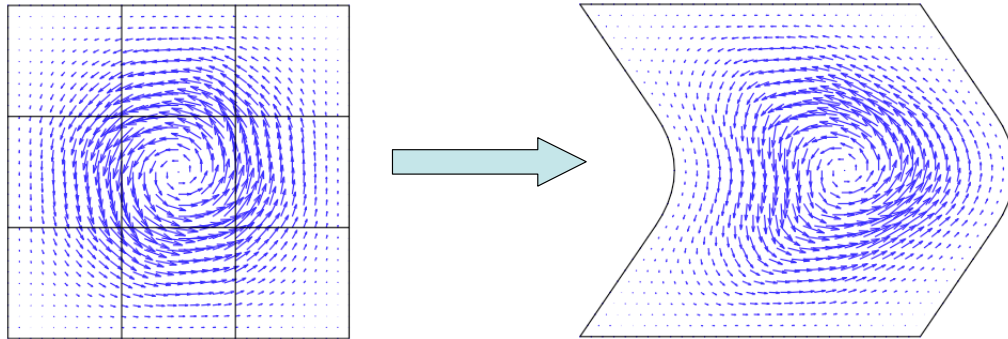


Figure 5.6: The Piola transform maps divergence-free fields in parametric space to divergence-free fields in physical space, as shown here for the case of a divergence-free B-spline.

**Remark 5.2.1.** *The results stated here can be extended to the case with mixed boundary conditions assuming that each type of boundary condition is imposed on a set formed by the union of faces of the cube  $\widehat{\Omega}$  as shown in [40]. The results can also be extended to cases with periodicity.*

**Remark 5.2.2.** *It should be emphasized that, unlike the finite element setting, no regularization (see, for example, [61]) was necessary in order to establish commuting diagrams. In this sense, the projection operators introduced in [40] are similar in nature to those presented in [87] for spectral mixed methods. This is not surprising as B-spline discretizations may be interpreted as lying somewhere between finite element and spectral techniques.*

### 5.3 The Stokes Hilbert Complex

A Hilbert complex extends the notion of a cochain complex to the Hilbert space setting. In fact, a bounded Hilbert complex is simply a cochain complex in the category of Hilbert spaces. The most famous (and common) Hilbert complex is the

de Rham complex that was the focus of the preceding section. However, the concept of a Hilbert complex allows for much more generality. For example, there exists a Hilbert complex for linear elasticity [6]. Here, we introduce Hilbert complexes for Stokes flow comprising of Hilbert spaces for scalar potentials, vector potentials, flow velocities, and pressures. They are a generalization of the Hilbert complex introduced in Section 2.1. As we shall see, the Hilbert complex is a valuable tool for the study of mixed discretizations of the Stokes equations. It should be mentioned that the Hilbert complexes introduced here are not higher-order analogues of the de Rham complex [177] and are characterized by a reduction in smoothness when compared with such high-order complexes.

In [7], Arnold *et al.* presented an abstract framework through which one can analyze the stability of discrete subcomplexes of Hilbert complexes. The framework invokes the existence of bounded cochain projection operators which commute with a given Hilbert complex. The work presented here can be thought of as a specific application of this framework. However, the applicability of a discrete subcomplex goes beyond just the design and analysis of stable discretizations. While not covered in this written dissertation, we can actually use the discrete subcomplex to develop optimal linear solvers. Likewise, Hiptmair developed optimal solvers in [104] and [103] for  $\mathbf{H}(\mathbf{curl}; \Omega)$ - and  $\mathbf{H}(\mathbf{div}; \Omega)$ -elliptic problems respectively using the Hodge decomposition associated with the de Rham cohomology.

Restricting initially to the three-dimensional setting, let us define the following Hilbert spaces:

$$\begin{aligned}\mathbf{H}_n^1(\Omega) &:= \{ \mathbf{v} \in \mathbf{H}^1(\Omega) : \mathbf{v} \cdot \mathbf{n} = 0 \text{ on } \partial\Omega \} \\ \Phi(\Omega) &:= \{ \phi \in \mathbf{L}^2(\Omega) : \mathbf{curl} \phi \in \mathbf{H}^1(\Omega) \} \\ \Phi_n(\Omega) &:= \Phi(\Omega) \cap \mathbf{H}_0(\mathbf{curl}; \Omega).\end{aligned}$$

The space  $\mathbf{H}_n^1(\Omega)$  is endowed with the standard  $\mathbf{H}^1$ -norm and the spaces  $\Phi(\Omega)$  and  $\Phi_n(\Omega)$  are endowed with the inner-product

$$(\cdot, \cdot)_{\Phi(\Omega)} := (\cdot, \cdot)_{L^2(\Omega)} + (\mathbf{curl} \cdot, \mathbf{curl} \cdot)_{\mathbf{H}^1(\Omega)}$$

and induced norm  $\|\cdot\|_{\Phi(\Omega)} = (\cdot, \cdot)_{\Phi(\Omega)}^{1/2}$ . By the exact sequence property of the de Rham diagram

$$\mathbf{grad} (H_0^1(\Omega)) = \{\mathbf{u} \in \mathbf{H}_0(\mathbf{curl}; \Omega) : \mathbf{curl} \mathbf{u} = \mathbf{0}\}.$$

It follows that

$$\mathbf{grad} (H_0^1(\Omega)) = \{\mathbf{u} \in \Phi_n(\Omega) : \mathbf{curl} \mathbf{u} = \mathbf{0}\}.$$

It is easily shown that  $\mathbf{curl} (\Phi_n(\Omega)) \subset \mathbf{H}_n^1(\Omega)$ . Furthermore, we know  $\mathbf{div} \mathbf{curl} = 0$ . Now, suppose  $\mathbf{v} \in \mathbf{H}_n^1(\Omega)$  such that  $\mathbf{div} \mathbf{v} = 0$ . By the exact sequence property of the de Rham diagram, we know that there exists a  $\mathbf{u} \in \mathbf{H}_0(\mathbf{curl}; \Omega)$  such that  $\mathbf{curl} \mathbf{u} = \mathbf{v}$ . Furthermore, as  $\mathbf{v} \in \mathbf{H}_n^1(\Omega)$ , it follows that  $\mathbf{u} \in \Phi_n(\Omega)$ . Thus, we have:

$$\mathbf{curl} (\Phi_n(\Omega)) = \{\mathbf{v} \in \mathbf{H}_n^1(\Omega) : \mathbf{div} \mathbf{v} = 0\}.$$

Finally, by the results of Section 2.1, we know that:

$$\mathbf{div} (\mathbf{H}_n^1(\Omega)) = L_0^2(\Omega).$$

Then, by coupling the above discussion with the trivial inequalities

$$\|\mathbf{grad} \phi\|_{\Phi(\Omega)} \leq \|\phi\|_{\mathbf{H}^1(\Omega)}, \quad \forall \phi \in H_0^1(\Omega) \quad (5.22)$$

$$\|\mathbf{curl} \phi\|_{\mathbf{H}^1(\Omega)} \leq \|\phi\|_{\Phi(\Omega)}, \quad \forall \phi \in \Phi_n(\Omega) \quad (5.23)$$

$$\|\mathbf{div} \mathbf{v}\|_{L^2(\Omega)} \leq \|\mathbf{v}\|_{\mathbf{H}^1(\Omega)}, \quad \forall \mathbf{v} \in \mathbf{H}_n^1(\Omega) \quad (5.24)$$

we obtain the following proposition.

**Proposition 5.3.1.** For  $\Omega \subset \mathbb{R}^3$ , the following

$$H_0^1(\Omega) \xrightarrow{\text{grad}} \Phi_n(\Omega) \xrightarrow{\text{curl}} \mathbf{H}_n^1(\Omega) \xrightarrow{\text{div}} L_0^2(\Omega) \quad (5.25)$$

is a bounded and exact Hilbert complex.

By utilizing a similar argument, we obtain an analagous proposition for spaces without boundary conditions.

**Proposition 5.3.2.** For  $\Omega \subset \mathbb{R}^3$ , the following

$$\mathbb{R} \longrightarrow H^1(\Omega) \xrightarrow{\text{grad}} \Phi(\Omega) \xrightarrow{\text{curl}} \mathbf{H}^1(\Omega) \xrightarrow{\text{div}} L^2(\Omega) \quad (5.26)$$

is a bounded and exact Hilbert complex.

Finally, if we define the space

$$\Phi_0(\Omega) := \{ \phi \in \mathbf{H}_0(\text{curl}; \Omega) : \text{curl} \phi \in \mathbf{H}_0^1(\Omega) \}$$

which is endowed with the  $\Phi$ -norm, we have one more result.

**Proposition 5.3.3.** For  $\Omega \subset \mathbb{R}^3$ , the following

$$H_0^1(\Omega) \xrightarrow{\text{grad}} \Phi_0(\Omega) \xrightarrow{\text{curl}} \mathbf{H}_0^1(\Omega) \xrightarrow{\text{div}} L_0^2(\Omega) \quad (5.27)$$

is a bounded and exact Hilbert complex.

As illustrated in Section 2.1, the Hilbert complexes given by the above three propositions provide a natural setting through which one can study Stokes flow. Indeed, Proposition 5.3.3 applies to the most common case, that of normal and tangential Dirichlet boundary conditions. Proposition 5.3.2 applies to the case of traction boundary conditions, and, finally, Proposition 5.3.1 applies to the case of

normal Dirichlet and tangential traction boundary conditions. The spaces appearing in the Hilbert complexes correspond to those of (from left to right) scalar potentials, vector potentials, flow velocities, and pressures.

The Stokes complex takes a much simpler form in the two-dimensional setting. Defining

$$H_{\mathbf{n}}^2(\Omega) := H^2(\Omega) \cap H_0^1(\Omega),$$

we have the following proposition.

**Proposition 5.3.4.** *For  $\Omega \subset \mathbb{R}^2$ , the following*

$$H_{\mathbf{n}}^2(\Omega) \xrightarrow{\text{curl}} \mathbf{H}_{\mathbf{n}}^1(\Omega) \xrightarrow{\text{div}} L_0^2(\Omega) \quad (5.28)$$

$$\mathbb{R} \longrightarrow H^2(\Omega) \xrightarrow{\text{curl}} \mathbf{H}^1(\Omega) \xrightarrow{\text{div}} L^2(\Omega) \quad (5.29)$$

$$H_0^2(\Omega) \xrightarrow{\text{curl}} \mathbf{H}_0^1(\Omega) \xrightarrow{\text{div}} L_0^2(\Omega) \quad (5.30)$$

*are bounded and exact Hilbert complexes.*

The spaces appearing in the two-dimensional Hilbert complexes above correspond to those of (from left to right) stream functions, flow velocities, and pressures.

## 5.4 B-spline Spaces Satisfying the Stokes Diagram

While we presented the Hilbert complex given by Proposition 5.3.3 for the sake of completeness, the development of a discrete subcomplex and corresponding projection operators which commute with the Hilbert complex has proven to be quite difficult and rather unsuccessful. On the other hand, using the compatible B-spline spaces and projection operators introduced in the Section 5.2, the development of subcomplexes and commuting diagrams for the other Hilbert complexes appearing in the previous section is quite straight-forward. Key to this development is the following proposition which was proven in [40].

**Proposition 5.4.1.** *The following inequalities hold for  $j \leq \alpha$ :*

$$\|\Pi_{\mathcal{S}_h}^0 \phi\|_{H^{j+1}(\Omega)} \leq C \|\phi\|_{H^{j+1}(\Omega)}, \quad \forall \phi \in H_0^1(\Omega) \cap H^{j+1}(\Omega) \quad (5.31)$$

$$\|\Pi_{\mathcal{N}_h}^0 \mathbf{u}\|_{\mathbf{H}^j(\Omega)} \leq C \|\mathbf{u}\|_{\mathbf{H}^j(\Omega)}, \quad \forall \mathbf{u} \in \mathbf{H}_0(\mathbf{curl}; \Omega) \cap \mathbf{H}^j(\Omega) \quad (5.32)$$

$$\|\Pi_{\mathcal{RT}_h}^0 \mathbf{v}\|_{\mathbf{H}^j(\Omega)} \leq C \|\mathbf{v}\|_{\mathbf{H}^j(\Omega)}, \quad \forall \mathbf{v} \in \mathbf{H}_0(\text{div}; \Omega) \cap \mathbf{H}^j(\Omega) \quad (5.33)$$

$$\|\Pi_{\mathcal{W}_h}^0 \psi\|_{H^j(\Omega)} \leq C \|\psi\|_{H^j(\Omega)}, \quad \forall \psi \in L_0^2(\Omega) \cap H^j(\Omega) \quad (5.34)$$

$$\|\Pi_{\mathcal{S}_h} \phi\|_{H^{j+1}(\Omega)} \leq C \|\phi\|_{H^{j+1}(\Omega)}, \quad \forall \phi \in H^{j+1}(\Omega) \quad (5.35)$$

$$\|\Pi_{\mathcal{N}_h} \mathbf{u}\|_{\mathbf{H}^j(\Omega)} \leq C \|\mathbf{u}\|_{\mathbf{H}^j(\Omega)}, \quad \forall \mathbf{u} \in \mathbf{H}^j(\Omega) \quad (5.36)$$

$$\|\Pi_{\mathcal{RT}_h} \mathbf{v}\|_{\mathbf{H}^j(\Omega)} \leq C \|\mathbf{v}\|_{\mathbf{H}^j(\Omega)}, \quad \forall \mathbf{v} \in \mathbf{H}^j(\Omega) \quad (5.37)$$

$$\|\Pi_{\mathcal{W}_h} \psi\|_{H^j(\Omega)} \leq C \|\psi\|_{H^j(\Omega)}, \quad \forall \psi \in H^j(\Omega) \quad (5.38)$$

where  $\alpha$  is the regularity constant and  $C$  denotes a positive constant, possibly different at each appearance, which depends only on shape regularity, polynomial degree, and mesh-invariant measures of the parametric mapping.

As a direct result of the above proposition, the projection operators introduced in Section 5.2 are stable with respect to the norms of the spaces appearing in the Stokes complex provided the smoothness condition  $\alpha \geq 1$  is satisfied. This stability result immediately yields the following theorem.

**Theorem 5.4.1.** *Let  $\alpha \geq 1$ . Then the following commuting diagrams hold for  $\Omega \subset \mathbb{R}^3$ :*

$$\begin{array}{ccccccc} H_0^1(\Omega) & \xrightarrow{\text{grad}} & \Phi_{\mathbf{n}}(\Omega) & \xrightarrow{\text{curl}} & \mathbf{H}_{\mathbf{n}}^1(\Omega) & \xrightarrow{\text{div}} & L_0^2(\Omega) \\ \Pi_{\mathcal{S}_h}^0 \downarrow & & \Pi_{\mathcal{N}_h}^0 \downarrow & & \Pi_{\mathcal{RT}_h}^0 \downarrow & & \Pi_{\mathcal{W}_h}^0 \downarrow \\ \mathcal{S}_{0,h} & \xrightarrow{\text{grad}} & \mathcal{N}_{0,h} & \xrightarrow{\text{curl}} & \mathcal{RT}_{0,h} & \xrightarrow{\text{div}} & \mathcal{W}_{0,h} \end{array} \quad (5.39)$$

and

$$\begin{array}{ccccccc} H^1(\Omega) & \xrightarrow{\text{grad}} & \Phi(\Omega) & \xrightarrow{\text{curl}} & \mathbf{H}^1(\Omega) & \xrightarrow{\text{div}} & L^2(\Omega) \\ \Pi_{\mathcal{S}_h} \downarrow & & \Pi_{\mathcal{N}_h} \downarrow & & \Pi_{\mathcal{RT}_h} \downarrow & & \Pi_{\mathcal{W}_h} \downarrow \\ \mathcal{S}_h & \xrightarrow{\text{grad}} & \mathcal{N}_h & \xrightarrow{\text{curl}} & \mathcal{RT}_h & \xrightarrow{\text{div}} & \mathcal{W}_h, \end{array} \quad (5.40)$$

and the following diagrams hold for  $\Omega \subset \mathbb{R}^2$ :

$$\begin{array}{ccccc}
H_{\mathbf{n}}^2(\Omega) & \xrightarrow{\text{curl}} & \mathbf{H}_{\mathbf{n}}^1(\Omega) & \xrightarrow{\text{div}} & L_0^2(\Omega) \\
\Pi_{\mathcal{S}_h}^0 \downarrow & & \Pi_{\mathcal{RT}_h}^0 \downarrow & & \Pi_{\mathcal{W}_h}^0 \downarrow \\
\mathcal{S}_{0,h} & \xrightarrow{\text{curl}} & \mathcal{RT}_{0,h} & \xrightarrow{\text{div}} & \mathcal{W}_{0,h}
\end{array} \tag{5.41}$$

and

$$\begin{array}{ccccc}
H^2(\Omega) & \xrightarrow{\text{curl}} & \mathbf{H}^1(\Omega) & \xrightarrow{\text{div}} & L^2(\Omega) \\
\Pi_{\mathcal{S}_h} \downarrow & & \Pi_{\mathcal{RT}_h} \downarrow & & \Pi_{\mathcal{W}_h} \downarrow \\
\mathcal{S}_h & \xrightarrow{\text{curl}} & \mathcal{RT}_h & \xrightarrow{\text{div}} & \mathcal{W}_h.
\end{array} \tag{5.42}$$

Furthermore, the continuity constants associated with the commuting projection operators only depend on the polynomial degrees of the B-spline discretization, the shape regularity of the mesh family  $\{\mathcal{M}_h\}_{h \leq h_0}$ , and global, mesh-invariant measures of the parametrization  $\mathbf{F}$ .

The above theorem suggests how we should choose our discrete velocity and pressure spaces provided  $\alpha \geq 1$ . In the presence of homogeneous boundary conditions, we should select our velocity and pressure spaces as

$$\mathcal{V}_{0,h} := \mathcal{RT}_{0,h}, \quad \mathcal{Q}_{0,h} := \mathcal{W}_{0,h}.$$

In the absence of boundary conditions, we should select our velocity and pressure spaces as

$$\mathcal{V}_h := \mathcal{RT}_h, \quad \mathcal{Q}_h := \mathcal{W}_h.$$

In light of these selections, we will denote

$$\Pi_{\mathcal{V}_h}^0 := \Pi_{\mathcal{RT}_h}^0, \quad \Pi_{\mathcal{Q}_h}^0 := \Pi_{\mathcal{W}_h}^0, \quad \Pi_{\mathcal{V}_h} := \Pi_{\mathcal{RT}_h}, \quad \Pi_{\mathcal{Q}_h} := \Pi_{\mathcal{W}_h} \tag{5.43}$$

throughout the remainder of the dissertation. The following result shows that the above velocity/pressure pairs are inf-sup stable.

**Theorem 5.4.2.** *There exist positive constant  $\beta_h, \beta_{0,h}$  only dependent on shape regularity, polynomial degree, and the parametric mapping such that the following hold:*

$$\inf_{\substack{\psi_h \in \mathcal{Q}_{0,h} \\ \psi_h \neq 0}} \sup_{\mathbf{v}_h \in \mathcal{V}_{0,h}} \frac{(\operatorname{div} \mathbf{v}_h, \psi_h)}{\|\mathbf{v}_h\|_{\mathbf{H}^1(\Omega)} \|\psi_h\|_{L^2(\Omega)}} \geq \tilde{\beta}_{0,h} \quad (5.44)$$

$$\inf_{\substack{\psi_h \in \mathcal{Q}_h \\ \psi_h \neq 0}} \sup_{\mathbf{v}_h \in \mathcal{V}_h} \frac{(\operatorname{div} \mathbf{v}_h, \psi_h)}{\|\mathbf{v}_h\|_{\mathbf{H}^1(\Omega)} \|\psi_h\|_{L^2(\Omega)}} \geq \tilde{\beta}_h. \quad (5.45)$$

*Proof.* We prove only the first inequality, the proof of the second being identical. Let  $\psi_h \in \mathcal{Q}_{0,h}$  be arbitrary. Then we know by Theorem 2.1.2 that there exists a function  $\mathbf{v} \in \mathbf{H}_n^1(\Omega)$  (in fact,  $\mathbf{v} \in \mathbf{H}_0^1(\Omega)$ ) such that  $\operatorname{div} \mathbf{v} = \psi_h$  and

$$\|\mathbf{v}\|_{\mathbf{H}^1(\Omega)} \leq \beta_0^{-1} \|\psi_h\|_{L^2(\Omega)} \quad (5.46)$$

where  $\beta_0$  is independent of  $\mathbf{v}$ . Let  $\mathbf{v}_h = \Pi_{\mathcal{V}_h}^0 \mathbf{v}$ . Then,  $\operatorname{div} \mathbf{v}_h = \operatorname{div} \Pi_{\mathcal{V}_h}^0 \mathbf{v} = \Pi_{\mathcal{Q}_h}^0 \operatorname{div} \mathbf{v} = \psi_h$  and, by Theorem 5.4.1, there exists a constant  $C_{stab}$  only dependent on shape regularity, polynomial degree, and parametric mapping such that

$$\|\mathbf{v}_h\|_{\mathbf{H}^1(\Omega)} \leq C_{stab} \|\mathbf{v}\|_{\mathbf{H}^1(\Omega)} \leq C_{stab} \beta_0^{-1} \|\psi_h\|_{L^2(\Omega)}. \quad (5.47)$$

Thus the theorem holds with  $\beta_{0,h} = \frac{\beta}{C_{stab}}$ .  $\square$

Note that we did not need to apply any of the standard machinery in order to prove inf-sup stability. We did not need to employ Fortin's trick [80] or Verfürth's trick [185]. We did not need to apply any domain decomposition procedures [86] or any macroelement techniques [174], although admittedly B-spline basis functions do have larger supports than standard finite element basis functions. All that was necessary was a discrete subcomplex with the same cohomology structure as the infinite-dimensional Hilbert complex and bounded commuting projection operators. We believe this is an elegant approach to an age-old problem. However,

as we do not have a discrete subcomplex of the Hilbert complex given in Proposition 5.3.3, an alternative methodology must be utilized in the presence of tangential Dirichlet boundary conditions. For example, in [39], a special discrete pressure space was constructed in the two-dimensional setting by selectively reducing the dimensionality of  $\mathcal{Q}_{0,h}$  using T-splines [17]. However, a proof of mesh-independent discrete stability remains absent with this choice of pressure space, and the convenient tensor-product structure of B-splines is lost. Motivated by the appearance of sharp boundary layers in high Reynolds number flows, we advocate weakly enforcing tangential Dirichlet boundary conditions. This will be illustrated in the next chapter. Through the use of weak boundary conditions, we retain all of the stability and cohomology properties discussed here. Furthermore, by weakly enforcing no-slip boundary conditions, our proposed discretizations for the generalized Stokes and Navier-Stokes equations default to proper discretizations of Darcy and Euler flow in the limit of vanishing viscosity.

We also have the following result.

**Proposition 5.4.2.** *If  $\mathbf{v}_h \in \mathcal{V}_{0,h}$  satisfies*

$$(\operatorname{div} \mathbf{v}_h, \psi_h) = 0, \quad \forall \psi_h \in \mathcal{Q}_{0,h}, \quad (5.48)$$

*then  $\operatorname{div} \mathbf{v}_h \equiv 0$ . Furthermore, if  $\mathbf{v}_h \in \mathcal{V}_h$  satisfies*

$$(\operatorname{div} \mathbf{v}_h, \psi_h) = 0, \quad \forall \psi_h \in \mathcal{Q}_h, \quad (5.49)$$

*then  $\operatorname{div} \mathbf{v}_h \equiv 0$ .*

*Proof.* The proof holds trivially as  $\operatorname{div}$  maps  $\mathcal{V}_{0,h}$  onto  $\mathcal{Q}_{0,h}$  and  $\mathcal{V}_h$  onto  $\mathcal{Q}_h$ .  $\square$

Hence, by choosing  $\mathcal{V}_{0,h}$  and  $\mathcal{Q}_{0,h}$  (or  $\mathcal{V}_h$  and  $\mathcal{Q}_h$ ) as discrete velocity and pressure spaces, we arrive at a discretization that automatically returns velocity

fields that are pointwise divergence-free. Furthermore, corresponding to these velocity and pressure spaces, we have discrete scalar and vector potential spaces. The existence of these spaces is very useful in the development of optimal linear solvers when coupled with the decompositions discussed in Section 2.2.

**Remark 5.4.1.** *If the condition  $\alpha \geq 1$  is not met, the interior penalty method can be utilized to enforce tangential continuity of the flow velocity without upsetting the inf-sup condition. This will also be the approach taken on multi-patch geometries.*

## 5.5 Interpolation Estimates

Let us define

$$k' = \min_{l=1,\dots,d} |k_l - 1|. \quad (5.50)$$

Note that the discrete velocity and pressure spaces  $\mathcal{V}_{0,h}$  and  $\mathcal{Q}_{0,h}$  (and  $\mathcal{V}_h$  and  $\mathcal{Q}_h$ ) consist of mapped piecewise polynomials which are complete up to degree  $k'$ . Hence,  $k'$  may be thought of as the polynomial degree of our discretization technique. The following result details the local approximation properties of our discrete spaces. Its proof may be found in [40].

**Proposition 5.5.1.** *Let  $K \in \mathcal{K}_h$  and  $\tilde{K}$  denote the support extension of  $K$ . For  $0 \leq j \leq s \leq k' + 1$ , we have*

$$|\mathbf{v} - \Pi_{\mathcal{V}_h}^0 \mathbf{v}|_{\mathbf{H}^j(K)} \leq Ch^{s-j} \|\mathbf{v}\|_{\mathbf{H}^s(\tilde{K})}, \quad \forall \mathbf{v} \in \mathbf{H}^s(\tilde{K}) \cap \mathbf{H}_0(\text{div}; \Omega) \quad (5.51)$$

$$|q - \Pi_{\mathcal{Q}_h}^0 q|_{H^j(K)} \leq Ch^{s-j} \|q\|_{H^s(\tilde{K})}, \quad \forall q \in H^s(\tilde{K}) \cap L_0^2(\Omega) \quad (5.52)$$

$$|\mathbf{v} - \Pi_{\mathcal{V}_h} \mathbf{v}|_{\mathbf{H}^j(K)} \leq Ch^{s-j} \|\mathbf{v}\|_{\mathbf{H}^s(\tilde{K})}, \quad \forall \mathbf{v} \in \mathbf{H}^s(\tilde{K}) \cap \mathbf{H}(\text{div}; \Omega) \quad (5.53)$$

$$|q - \Pi_{\mathcal{Q}_h} q|_{H^j(K)} \leq Ch^{s-j} \|q\|_{H^s(\tilde{K})}, \quad \forall q \in H^s(\tilde{K}) \cap L^2(\Omega) \quad (5.54)$$

where  $C$  denotes a positive constant, possibly different at each appearance, independent of  $h$ .

Hence, our discrete spaces deliver optimal rates of convergence from an approximation point of view. This being said, the results of Proposition 5.5.1 are riddled with inconvenient interpolation constants  $C$  which depend on, among other things, the polynomial degree and continuity of our approximation spaces. To attack the question of degree and continuity directly, Beirão da Veiga *et al.* derived interpolation estimates for B-splines with explicit dependence on degree and continuity in [56]. However, the derived estimates are only available for interpolations of Hermite-type. All of this seems to indicate that function analytic estimates have their limitations. Alternatively, one can use numerics to study the approximation properties of discrete spaces using the theory of Kolmogorov  $n$ -widths. This approach allows one to exactly compute the interpolation constants associated with variational projection through the solution of a generalized eigenproblem. The theory of Kolmogorov  $n$ -widths was used to study one-dimensional B-spline discretizations in [73]. This paper revealed that maximal continuity B-spline spaces harbor nearly optimal resolution properties and admit smaller interpolation constants than lower continuity spaces. Recently, the theory of Kolmogorov  $n$ -widths has been used to study multi-dimensional and compatible B-spline discretizations. This study has also revealed the advantage of employing B-splines of maximal continuity in the multi-dimensional setting. The results of this study will be presented in a forthcoming paper.

## 5.6 Inverse and Trace Inequalities

We finish this chapter with inverse and trace inequalities for our discrete velocity spaces. These results will prove useful in our later analysis. The trace inequality will prove particularly useful in the analysis of schemes for weak imposition of boundary conditions. Let us begin with the following lemma.

**Lemma 5.6.1.** *Let  $K \in \mathcal{K}_h$ . Then we have*

$$\|\mathbf{v}_h\|_{\mathbf{H}^2(K)} \leq C_{inverse} h_K^{-1} \|\mathbf{v}_h\|_{\mathbf{H}^1(K)}, \quad \forall \mathbf{v}_h \in \mathcal{V}_h \quad (5.55)$$

where  $C_{inverse}$  is a positive constant independent of  $h$ .

*Proof.* Let  $\mathbf{v}_h \in \mathcal{V}_h$  be arbitrary. By Lemma 5.2 of [40], we have

$$\|\mathbf{v}_h\|_{\mathbf{H}^2(K)} \leq C_{pull} \|\iota_{\mathcal{RT}}(\mathbf{v}_h)\|_{\mathbf{H}^2(Q)} \quad (5.56)$$

where  $Q$  is the inverse image (under  $\mathbf{F}$ ) of  $K$  and  $C_{pull}$  is a positive constant which only depends on shape regularity and the parametric mapping. Since  $\iota_{\mathcal{RT}}(\mathbf{v}_h)$  is a vector whose components are polynomial over  $Q$ , we have the usual inverse inequality

$$\|\iota_{\mathcal{RT}}(\mathbf{v}_h)\|_{\mathbf{H}^2(Q)} \leq C_{inv} h_Q^{-1} \|\iota_{\mathcal{RT}}(\mathbf{v}_h)\|_{\mathbf{H}^1(Q)}. \quad (5.57)$$

where  $C_{inv} > 0$  is an inverse constant only dependent on polynomial degree and parametric shape regularity. Finally, apply Lemma 5.2 of [40] again to obtain

$$\|\iota_{\mathcal{RT}}(\mathbf{v}_h)\|_{\mathbf{H}^1(Q)} \leq C_{push} \|\mathbf{v}_h\|_{\mathbf{H}^1(K)} \quad (5.58)$$

where  $C_{push}$  is a positive constant with the same functional dependencies as  $C_{pull}$ . The result follows by combining the observation that

$$h_Q^{-1} \leq \|D\mathbf{F}\|_{L^\infty(\hat{\Omega})} h_K^{-1}$$

with inequalities (5.56)-(5.58). □

Using the above lemma, we can prove the following trace inequality.

**Lemma 5.6.2.** *Let  $K \in \mathcal{K}_h$ . Then, we have*

$$\|(\nabla^s \mathbf{v}_h) \mathbf{n}\|_{(L^2(\partial K))^3}^2 \leq C_{trace} h_K^{-1} \|\mathbf{v}_h\|_{\mathbf{H}^1(K)}^2, \quad \forall \mathbf{v}_h \in \mathcal{V}_h \quad (5.59)$$

where

$$\nabla^s \mathbf{v}_h = \frac{1}{2} \left( (\nabla \mathbf{v}_h) + (\nabla \mathbf{v}_h)^T \right)$$

and  $C_{trace}$  is a positive constant independent of  $h$ .

*Proof.* Let  $\mathbf{v}_h \in \mathcal{V}_h$ . By the continuous trace inequality (see Theorem 3.2 of [75]) there exists a positive constant  $C_{tr}$  independent of  $h$  (but dependent on shape regularity and the parametric mapping) such that

$$\| (\nabla^s \mathbf{v}_h) \mathbf{n} \|_{(L^2(\partial K))^d}^2 \leq C_{tr} \left( h_K^{-1} \| \nabla^s \mathbf{v}_h \|_{(\mathbf{L}^2(K))^d}^2 + h_K \| \nabla \nabla^s \mathbf{v}_h \|_{(\mathbf{L}^2(K))^{d \times d}}^2 \right).$$

Then, applying Lemma 5.6.1, we obtain

$$\| (\nabla^s \mathbf{v}_h) \mathbf{n} \|_{(L^2(\partial K))^3}^2 \leq (1 + C_{inverse}^2) C_{tr} h_K^{-1} \| \mathbf{v}_h \|_{\mathbf{H}^1(K)}^2.$$

The result follows with  $C_{trace} = (1 + C_{inverse}^2) C_{tr}$ .  $\square$

In [75], it was shown that Lemma 5.6.2 holds for B-splines and parametric hexahedral finite elements with  $C_{trace} \sim (k')^2$ . However, our numerical experience has indicated that the lemma also holds for  $C_{trace} \sim k'$  if B-splines of maximal continuity are utilized. This allows us to select a smaller penalty parameter when employing Nitsche's method. As we will see in the next chapter, our convergence estimates for the generalized Stokes equations scale inversely with the square root of Nitsche's penalty parameter. Hence, we want to select Nitsche's penalty parameter as small as possible. Finally, our numerical experience has also indicated that Lemma 5.6.1 holds for  $C_{inverse} \sim k'$  if B-splines of maximal continuity are employed.

## Chapter 6

### Approximation of the Generalized Stokes Problem

The Stokes equations describe a wide variety of fluid flows where advective inertial forces are so small when compared with viscous forces that they can be neglected altogether. Such flows arise in a large number of applications in nature and technology, from the flow of lava in the Earth's mantle [173] to microfluidic flow in micro-electromechanical devices [123]. The generalized Stokes equations are a simple extension of the Stokes equations which account for Darcy drag forces in highly porous media [37]. These equations, also referred to as the Brinkman or Darcy-Stokes equations, have been used to model groundwater flow [57], heat and mass transfer in pipes [118], and flow in biological tissues [122]. One also obtains a generalized Stokes problem when nonlinear terms are treated explicitly during semi-implicit time-integration of the unsteady Navier-Stokes equations.

Despite their simple appearance, the Stokes and generalized Stokes equations have presented considerable difficulty in their numerical approximation. At the heart of the matter is the celebrated Babuška-Brezzi inf-sup condition [13, 35]. Simply put, the condition states that one must properly select discrete velocity and pressure spaces in order to arrive at a stable and convergent discrete mixed formulation. Since the inception of the Marker-and-Cell scheme in 1965 [97], a large number of finite difference, finite volume, and finite element methods have been devised to address the discrete inf-sup condition in the context of the Stokes equations. For a review, see the treatise by Boffi, Brezzi, and Fortin [29]. Most methods for

Stokes flow only satisfy the incompressibility constraint in an approximate sense. Some bypass the inf-sup condition entirely through the use of a stabilized Petrov-Galerkin method [81]. However, methods which return discretely divergence-free velocity fields are generally not robust in the limit of vanishing viscosity when applied to generalized Stokes flows [140]. Moreover, mass conservation is considered to be of prime importance for coupled flow-transport [143], and it has been demonstrated that methods which fail to exactly satisfy the incompressibility constraint suffer from spurious velocity oscillations when applied to “high pressure, low flow” problems [84, 135]. These issues have motivated the development of discretization procedures which satisfy the incompressibility constraint exactly.

One of the simplest methods returning a divergence-free velocity field is the  $\mathbf{P}^k - P^{k-1}$  triangular element which approximates velocity fields using continuous piecewise polynomials of degree  $k$  and pressure fields using discontinuous polynomials of degree  $k - 1$ . This method satisfies the Babuška-Brezzi condition for meshes containing no nearly-singular vertices provided  $k \geq 4$  [170] and for certain macro-element configurations [8, 195]. Unfortunately, the method is not stable for general meshes and polynomial degrees. Recently, the use of  $\mathbf{H}(\text{div}; \Omega)$  elements has arisen as a new paradigm for the simulation of generalized Stokes flows [117, 125, 189]. As these approximations are typically not members of  $\mathbf{H}^1(\Omega)$ , techniques such as the interior penalty method [4, 69, 191] must be employed to enforce tangential continuity across elements. Alternatively, one can modify divergence-conforming elements to ensure they have some limited tangential continuity [177], and some authors have elected to release continuity entirely in favor of hybridization [46, 47]. In the same vein, divergence-free wavelets have been proposed for the solution of Stokes flows [133, 175, 182, 183], though these discretizations have a complicated construction and are limited to periodic and cuboid domains.

In this chapter, we present divergence-conforming discretizations for the generalized Stokes problem using the B-spline spaces introduced in the preceding chapter. The discretizations are (at least) patch-wise  $C^0$  and hence can be directly utilized in the Galerkin solution of generalized Stokes flow for single-patch configurations. We enforce no-slip boundary conditions weakly by means of Nitsche's method [154], allowing our method to default to a compatible discretization of Darcy flow in the setting of vanishing viscosity. In the presence of multi-patch geometries, we invoke the discontinuous Galerkin framework in order to enforce tangential continuity without upsetting the conservation or stability properties of the method across patch boundaries. For single-patch solutions, we are able to prove *a priori* error estimates which are optimal for the discrete velocity field and suboptimal, by one order, for the discrete pressure field. This is reminiscent of error estimates for stabilized equal-order interpolations [81, 111]. Our derived estimates are also robust with respect to the parameters of generalized Stokes flow. We utilize the methods of exact and manufactured solutions to verify our estimates, and we find that pressure actually converges at optimal order. We further test the effectiveness of our method using a selection of benchmark problems.

## 6.1 The Continuous Problem

Let us recall the generalized Stokes problem subject to homogeneous Dirichlet boundary conditions:

$$(S) \left\{ \begin{array}{l} \text{Given } \sigma : \Omega \rightarrow \mathbb{R}^+ \cup \{0\}, \nu : \Omega \rightarrow \mathbb{R}^+, \text{ and } \mathbf{f} : \Omega \rightarrow \mathbb{R}^d, \text{ find } \mathbf{u} : \bar{\Omega} \rightarrow \mathbb{R}^d \\ \text{and } p : \Omega \rightarrow \mathbb{R} \text{ such that} \\ \sigma \mathbf{u} - \nabla \cdot (2\nu \nabla^s \mathbf{u}) + \mathbf{grad} p = \mathbf{f} \quad \text{in } \Omega \quad (6.1) \\ \operatorname{div} \mathbf{u} = 0 \quad \text{in } \Omega \quad (6.2) \\ \mathbf{u} = \mathbf{0} \quad \text{on } \partial\Omega. \quad (6.3) \end{array} \right.$$

As discussed in Section 4.3,  $\Omega \subset \mathbb{R}^d$  is a domain defined by some piecewise smooth parametric mapping  $\mathbf{F} : (0, 1)^d \rightarrow \mathbb{R}^d$ . Note that the pressure  $p$  is only determined up to an arbitrary constant.

Let us now make an assumption regarding the data of our problem. Notably, let us assume that  $\sigma, \nu \in L^\infty(\Omega)$  and  $\mathbf{f} \in \mathbf{L}^2(\Omega)$ . The weak form for the generalized Stokes problem is then written as follows:

$$(W) \left\{ \begin{array}{l} \text{Find } \mathbf{u} \in \mathbf{H}_0^1(\Omega) \text{ and } p \in L_0^2(\Omega) \text{ such that} \\ \qquad \qquad \qquad a(\mathbf{u}, \mathbf{v}) - b(p, \mathbf{v}) + b(q, \mathbf{u}) = (\mathbf{f}, \mathbf{v})_{\mathbf{L}^2(\Omega)} \qquad (6.4) \\ \text{for all } \mathbf{v} \in \mathbf{H}_0^1(\Omega) \text{ and } q \in L_0^2(\Omega) \text{ where} \\ \qquad \qquad \qquad a(\mathbf{w}, \mathbf{v}) = (2\nu \nabla^s \mathbf{w}, \nabla^s \mathbf{v})_{(L^2(\Omega))^{d \times d}} + (\sigma \mathbf{w}, \mathbf{v})_{\mathbf{L}^2(\Omega)}, \qquad (6.5) \\ \qquad \qquad \qquad b(q, \mathbf{v}) = (q, \operatorname{div} \mathbf{v})_{L^2(\Omega)}. \qquad (6.6) \end{array} \right.$$

We have the following theorem which was proven in Chapter 2 using tools from algebraic topology.

**Theorem 6.1.1.** *Problem (W) has a unique weak solution  $(\mathbf{u}, p) \in \mathbf{H}_0^1(\Omega) \times L_0^2(\Omega)$ .*

## 6.2 The Discretized Problem

We now present a discrete variational formulation for the generalized Stokes problem using the spaces  $\mathcal{V}_{0,h}$  and  $\mathcal{Q}_{0,h}$  defined in Chapter 5. Since members of  $\mathcal{V}_{0,h}$  do not satisfy homogeneous tangential Dirichlet boundary conditions, we resort to Nitsche's method [154] to weakly enforce no-slip boundary conditions. This requires slightly more regularity on our problem data. Specifically, we assume

$$\nu \in W^{1,\infty}(\Omega) := \{w \in L^\infty(\Omega) : \nabla w \in \mathbf{L}^\infty(\Omega)\}.$$

This assumption ensures the trace of  $\nu$  on the boundary  $\partial\Omega$  is well-defined. Now, let us define the following bilinear form:

$$a_h(\mathbf{w}, \mathbf{v}) = a(\mathbf{w}, \mathbf{v}) - \sum_{F \in \Gamma_h} \int_F 2\nu \left( ((\nabla^s \mathbf{v}) \mathbf{n}) \cdot \mathbf{w} + ((\nabla^s \mathbf{w}) \mathbf{n}) \cdot \mathbf{v} - \frac{C_{pen}}{h_F} \mathbf{w} \cdot \mathbf{v} \right) ds. \quad (6.7)$$

In the above equation,  $C_{pen} \geq 1$  denotes a specially chosen positive penalty constant which will be specified in the sequel. Our discrete formulation is written as follows.

$$(G) \left\{ \begin{array}{l} \text{Find } \mathbf{u}_h \in \mathcal{V}_{0,h} \text{ and } p_h \in \mathcal{Q}_{0,h} \text{ such that} \\ a_h(\mathbf{u}_h, \mathbf{v}_h) - b(p_h, \mathbf{v}_h) + b(q_h, \mathbf{u}_h) = (\mathbf{f}, \mathbf{v}_h)_{\mathbf{L}^2(\Omega)}, \\ \forall \mathbf{v}_h \in \mathcal{V}_{0,h}, q_h \in \mathcal{Q}_{0,h}. \end{array} \right. \quad (6.8)$$

Note that the mesh-dependent bilinear form given by (6.7) has three additional terms in comparison with the continuous bilinear form: a penalty term, a consistency term, and a stability term. All three of these terms will prove important in our proceeding mathematical analysis.

We have the following lemma detailing the consistency of our numerical method provided the exact solution satisfies a reasonable regularity condition.

**Lemma 6.2.1.** *Suppose that the unique weak solution  $(\mathbf{u}, p)$  of  $(W)$  satisfies the regularity condition  $\mathbf{u} \in \mathbf{H}^{3/2+\epsilon}(\Omega)$  for some  $\epsilon > 0$ . Then:*

$$a_h(\mathbf{u}, \mathbf{v}_h) - b(p, \mathbf{v}_h) + b(q_h, \mathbf{u}) = (\mathbf{f}, \mathbf{v}_h)_{\mathbf{L}^2(\Omega)} \quad (6.9)$$

for all  $\mathbf{v}_h \in \mathcal{V}_{0,h}$  and  $q_h \in \mathcal{Q}_{0,h}$ .

*Proof.* We trivially have

$$b(q_h, \mathbf{u}) = 0, \quad \forall q_h \in \mathcal{Q}_{0,h}.$$

Now let  $\mathbf{v}_h \in \mathcal{V}_{0,h}$ . By the trace theorem for fractional Sobolev spaces [181], the assumption  $\mathbf{u} \in \mathbf{H}^{3/2+\epsilon}(\Omega)$  guarantees that  $(\nabla^s \mathbf{u}) \mathbf{n}$  is well-defined along  $\partial\Omega$  and  $(\nabla^s \mathbf{u}) \mathbf{n} \in (L^2(\partial\Omega))^d$ . Furthermore,  $(\nabla^s \mathbf{v}_h) \mathbf{n}$  is well-defined along  $\partial\Omega$  and  $(\nabla^s \mathbf{v}_h) \mathbf{n} \in (L^2(\partial\Omega))^d$ . Hence, the quantity  $a_h(\mathbf{u}, \mathbf{v}_h)$  is well-defined. Utilizing integration by parts and the fact that  $\mathbf{u}$  satisfies homogeneous Dirichlet boundary conditions and  $\mathbf{v}_h$  satisfies homogeneous normal Dirichlet boundary conditions, we have

$$\begin{aligned} a_h(\mathbf{u}, \mathbf{v}_h) - b(p, \mathbf{v}_h) &= \int_{\Omega} (\sigma \mathbf{u} - \nabla \cdot (2\nu \nabla^s \mathbf{u}) + \mathbf{grad} p) \cdot \mathbf{v}_h d\mathbf{x} \\ &= \int_{\Omega} \mathbf{f} \cdot \mathbf{v}_h d\mathbf{x} \\ &= (\mathbf{f}, \mathbf{v}_h)_{L^2(\Omega)} \end{aligned}$$

where integration is to be understood in the sense of distributions. This completes the proof of the lemma.  $\square$

Consistency is the primary reason that we employed Nitsche's method instead of a naïve penalty method. Nitsche's method also admits adjoint consistency, and this will allow us to prove optimal  $L^2$  estimates for our numerical method. This is in contrast with some standard discontinuous Galerkin techniques such as the Nonsymmetric Interior Penalty Galerkin (NIPG) method [161]. Furthermore, note that our method is consistent for velocity fields satisfying  $\mathbf{u} \in \mathbf{H}^{3/2+\epsilon}(\Omega)$  for arbitrary  $\epsilon > 0$ . Thus, our method is consistent for such singular problems as flow over a backward facing step. As a direct result of consistency, we have the following orthogonality condition.

**Corollary 6.2.1.** *Let  $(\mathbf{u}_h, p_h)$  denote a solution of (G), and suppose that the unique weak solution  $(\mathbf{u}, p)$  of (W) satisfies the regularity condition  $\mathbf{u} \in \mathbf{H}^{3/2+\epsilon}(\Omega)$  for*

some  $\epsilon > 0$ . Then:

$$a_h(\mathbf{u} - \mathbf{u}_h, \mathbf{v}_h) - b(p - p_h, \mathbf{v}_h) + b(q_h, \mathbf{u} - \mathbf{u}_h) = 0 \quad (6.10)$$

for all  $\mathbf{v}_h \in \mathcal{V}_{0,h}$  and  $q_h \in \mathcal{Q}_{0,h}$ .

Our discretization also enjoys the following pointwise mass conservation property which is a direct consequence of Proposition 5.4.2.

**Corollary 6.2.2.** *Let  $(\mathbf{u}_h, p_h)$  denote a solution of (G). Then:*

$$\operatorname{div} \mathbf{u}_h \equiv 0 \quad (6.11)$$

We would like to note that in the event the viscosity  $\nu$  vanishes for uniformly positive  $\sigma$ , Problem (G) reduces a compatible discretization of incompressible Darcy flow subject to a no-penetration boundary condition. This reduction is contingent upon the weak specification of the no-slip condition. In this sense, weak boundary conditions are essential to the proper behavior of the discrete system under vanishing viscosity. Our proceeding stability and error analysis extends trivially to the case of vanishing viscosity. Furthermore, much like the solutions of Navier-Stokes flows, the generalized Stokes solution is characterized by the presence of a sharp boundary layer for small  $\nu$ . The weak no-slip condition alleviates the necessity of highly-refined boundary layer meshes [20–22].

**Remark 6.2.1.** *If we wish to impose non-homogeneous tangential Dirichlet (e.g., prescribed slip) boundary conditions, we add the following expression to the right hand side of our discrete formulation:*

$$f_{BC}(\mathbf{v}_h) = \sum_{F \in \Gamma_h} \int_F 2\nu \left( -((\nabla^s \mathbf{v}_h) \mathbf{n}) \cdot \mathbf{u}_{BC} + \frac{C_{pen}}{h_F} \mathbf{u}_{BC} \cdot \mathbf{v}_h \right) ds \quad (6.12)$$

where  $\mathbf{u}_{BC}$  is a vector function living on  $\partial\Omega$  with prescribed tangential boundary value and zero normal boundary value. The imposition of non-homogeneous normal Dirichlet boundary conditions is executed strongly in the standard sense.

### 6.3 Continuity and Stability

We now establish continuity and stability estimates for our discrete formulation. Continuity and stability, in conjunction with consistency and regularity, will guarantee convergence. To obtain the estimates in this section, we will need to call upon standard tools from the discontinuous Galerkin community such as trace and inverse estimates, and we will also rely on the results presented in Chapter 5.

Before proceeding, let us assume throughout the remainder of the next two sections that the reaction rate  $\sigma$  and the kinematic viscosity  $\nu$  are constant over  $\Omega$ . This will greatly simplify the presentation of our mathematical analysis. Nonetheless, our results extend to the more general setting of variable reaction and viscosity. Let us define the following weighted mesh-dependent norm:

$$\begin{aligned} \|\mathbf{v}\|_{\mathbb{V}(h)}^2 &:= \sigma \|\mathbf{v}\|_{\mathbf{H}(\text{div};\Omega)}^2 + 2\nu |\mathbf{v}|_{\mathbf{H}^1(\Omega)}^2 \\ &\quad + 2\nu \sum_{F \in \Gamma_h} h_F \|(\nabla^s \mathbf{v}) \mathbf{n}\|_{(L^2(F))^d}^2 + 2\nu \sum_{F \in \Gamma_h} \frac{C_{pen}}{h_F} \|\mathbf{v}\|_{(L^2(F))^d}^2. \end{aligned} \quad (6.13)$$

Note that this is a proper norm over our discrete velocity space due to the Poincaré inequality

$$\|\mathbf{v}\|_{\mathbf{H}^1(\Omega)} \leq C_{poin} |\mathbf{v}|_{\mathbf{H}^1(\Omega)}, \quad \forall \mathbf{v} \in \mathbf{H}^1(\Omega) \cap \mathbf{H}_0(\text{div};\Omega) \quad (6.14)$$

where  $C_{poin}$  is a positive constant which depends only on  $\Omega$ . In fact, by Lemma 5.6.2 and the Poincaré inequality, there exists a positive constant  $C_{inv}$  independent of  $h$ ,  $\sigma$ ,  $\nu$ , and  $C_{pen}$  such that

$$\|\mathbf{v}_h\|_{\mathbb{V}(h)}^2 \leq C_{inv} \left( \sigma \|\mathbf{v}_h\|_{\mathbf{H}(\text{div};\Omega)}^2 + 2\nu |\mathbf{v}_h|_{\mathbf{H}^1(\Omega)}^2 + 2\nu \sum_{F \in \Gamma_h} \frac{C_{pen}}{h_F} \|\mathbf{v}_h\|_{(L^2(F))^d}^2 \right) \quad (6.15)$$

for all  $\mathbf{v}_h \in \mathcal{V}_{0,h}$ . The above inequality dictates that our proposed norm acts as expected on the discrete subspace  $\mathcal{V}_{0,h}$ . That is, it is analogous to a weighted  $\mathbf{H}^1$ -norm coupled with an appropriate penalty term to handle tangential boundary conditions. The use of a mesh-dependent norm is fairly standard in the discontinuous Galerkin community. It is also standard in the stabilized methods community. The use of a weighted norm is motivated by our desire to extract error estimates with an explicit dependence on the problem parameters  $\sigma$  and  $\nu$  as well as the penalty constant  $C_{pen}$ . Let us define the following weighted  $L^2$ -norm for the pressure space

$$\|q\|_{\mathcal{Q}}^2 := \frac{1}{\sigma + 2\nu} \|q\|_{L^2(\Omega)}^2, \quad \forall q \in L_0^2(\Omega). \quad (6.16)$$

Note that when  $\nu = 0$ , our norms reduce to  $\sigma$ -weighted  $\mathbf{H}(\text{div})$ - and  $L^2$ -norms. Hence, we recover the proper norms for Darcy flow in the limit of vanishing viscosity.

We have the following continuity result.

**Lemma 6.3.1.** *The following continuity statements hold:*

$$a_h(\mathbf{w}, \mathbf{v}) \leq C_{cont} \|\mathbf{w}\|_{\mathcal{V}(h)} \|\mathbf{v}\|_{\mathcal{V}(h)}, \quad \forall \mathbf{w}, \mathbf{v} \in \mathcal{V}_{0,h} \oplus (\mathbf{H}_0^1(\Omega) \cap \mathbf{H}^{3/2+\epsilon}(\Omega)) \quad (6.17)$$

$$b(p, \mathbf{v}) \leq \|p\|_{\mathcal{Q}} \|\mathbf{v}\|_{\mathcal{V}(h)}, \quad \forall p \in L_0^2(\Omega), \mathbf{v} \in \mathcal{V}_{0,h} \oplus (\mathbf{H}_0^1(\Omega) \cap \mathbf{H}^{3/2+\epsilon}(\Omega)) \quad (6.18)$$

where  $\epsilon > 0$  is an arbitrary positive number and  $C_{cont}$  is a positive constant independent of  $h$ ,  $\sigma$ ,  $\nu$ ,  $C_{pen}$ , and  $\epsilon$ .

*Proof.* To establish the first estimate, we write

$$a_h(\mathbf{w}, \mathbf{v}) = a(\mathbf{w}, \mathbf{v}) - \sum_{F \in \Gamma_h} \int_F 2\nu \left( ((\nabla^s \mathbf{v}) \mathbf{n}) \cdot \mathbf{w} + ((\nabla^s \mathbf{w}) \mathbf{n}) \cdot \mathbf{v} - \frac{C_{pen}}{h_F} \mathbf{w} \cdot \mathbf{v} \right)$$

for some  $\mathbf{w}, \mathbf{v} \in \mathcal{V}_{0,h} \oplus (\mathbf{H}_0^1(\Omega) \cap \mathbf{H}^{3/2+\epsilon}(\Omega))$ . We now bound  $a_h(\cdot, \cdot)$  term by term.

To begin, note immediately that

$$a(\mathbf{w}, \mathbf{v}) + 2\nu \sum_{F \in \Gamma_h} \int_F \frac{C_{pen}}{h_F} \mathbf{w} \cdot \mathbf{v} \leq \|\mathbf{w}\|_{\mathcal{V}(h)} \|\mathbf{v}\|_{\mathcal{V}(h)}.$$

Next, we write

$$\begin{aligned} \sum_{F \in \Gamma_h} \int_F 2\nu ((\nabla^s \mathbf{v}) \mathbf{n}) \cdot \mathbf{w} &\leq 2\nu \sum_{F \in \Gamma_h} (\|\mathbf{w}\|_{(L^2(F))^d} \|(\nabla^s \mathbf{v}) \mathbf{n}\|_{(L^2(F))^d}) \\ &\leq 2\nu \sqrt{\sum_{F \in \Gamma_h} h_F \|(\nabla^s \mathbf{v}) \mathbf{n}\|_{(L^2(F))^d}^2} \sqrt{\sum_{F \in \Gamma_h} h_F^{-1} \|\mathbf{w}\|_{(L^2(F))^d}^2} \\ &\leq \|\mathbf{w}\|_{\mathcal{V}(h)} \|\mathbf{v}\|_{\mathcal{V}(h)}. \end{aligned}$$

Similarly, we have

$$\sum_{F \in \Gamma_h} \int_F 2\nu ((\nabla^s \mathbf{w}) \mathbf{n}) \cdot \mathbf{v} \leq \|\mathbf{w}\|_{\mathcal{V}(h)} \|\mathbf{v}\|_{\mathcal{V}(h)}.$$

Collecting our bounds, we have

$$a_h(\mathbf{w}, \mathbf{v}) \leq C_{cont} \|\mathbf{w}\|_{\mathcal{V}(h)} \|\mathbf{v}\|_{\mathcal{V}(h)}$$

with  $C_{cont} = 3$ . To establish the second continuity result of the lemma, we first write

$$b(p, \mathbf{v}) \leq \|p\|_{L^2(\Omega)} \|\operatorname{div} \mathbf{v}\|_{L^2(\Omega)}.$$

The result is then a consequence of

$$\|p\|_{L^2(\Omega)} = (\sigma + 2\nu)^{1/2} \|p\|_{\Omega}$$

and

$$\|\operatorname{div} \mathbf{v}\|_{L^2(\Omega)} \leq (\sigma + 2\nu)^{-1/2} \|\mathbf{v}\|_{\mathcal{V}(h)}.$$

□

Now we seek a coercivity estimate for the bilinear form  $a_h(\cdot, \cdot)$ . Note that we cannot obtain a general estimate with respect to the  $\mathcal{V}(h)$ -norm because the bilinear form imposes no gradient control along  $\partial\Omega$ . On the other hand, (6.15) suggests that a coercivity estimate can be achieved if we restrict ourselves to the discrete space  $\mathcal{V}_{0,h}$ . To develop estimates which are independent of the problem parameters  $\sigma$  and  $\nu$ , we further restrict ourselves to the divergence-free space

$$\hat{\mathcal{V}}_{0,h} := \{\mathbf{v}_h \in \mathcal{V}_{0,h} : \operatorname{div} \mathbf{v}_h = 0\}.$$

To proceed, we must make two assumptions regarding the size of  $C_{pen}$ . First, in light of Lemma 5.6.2, we choose  $C_{pen}$  large enough such that

$$C_{pen} \geq 4h_K C_{poin}^2 C_{Korn} \frac{\|(\nabla^s \mathbf{v}_h) \mathbf{n}\|_{(L^2(\partial K))^d}^2}{\|\mathbf{v}_h\|_{\mathbf{H}^1(K)}^2}, \quad \forall K \in \mathcal{K}_h, \mathbf{v}_h \in \mathcal{V}_{0,h} \quad (6.19)$$

where  $C_{poin}$  is the Poincaré constant associated with (6.14) and  $C_{Korn}$  is the positive constant associated with the following Korn's inequality [34]:

$$\|\mathbf{w}\|_{\mathbf{H}^1(\Omega)}^2 \leq C_{Korn} \left( \|\nabla^s \mathbf{w}\|_{(L^2(\Omega))^{d \times d}}^2 + |\partial\Omega|^{-1/(d-1)} \|\mathbf{w}\|_{(L^2(\partial\Omega))^d}^2 \right), \quad \forall \mathbf{w} \in \mathbf{H}^1(\Omega).$$

Second, we assume that

$$C_{pen} \geq 4h_0 |\partial\Omega|^{-1/(d-1)} \quad (6.20)$$

where  $h_0$  is the mesh size of the coarsest mesh  $\mathcal{K}_0$  and  $|\partial\Omega|$  denotes the area of  $\partial\Omega$ . This second assumption is necessary as rotation modes carry zero energy when  $\sigma = 0$ . Hence, weak boundary conditions are needed to control these modes in rotationally symmetric (or near rotationally symmetric) configurations. As such configurations are of significant engineering interest, we believe that any analysis results should cover these situations. Note that a constant  $C_{pen}$  satisfying the above assumption need not depend on  $h$ ,  $\sigma$ , or  $\nu$ . Rather, it only needs to depend on

the size of the domain, the polynomial degree of the discretization, the parametric shape regularity, and global, mesh-invariant measures of the parametric mapping.

We have the following lemma governing the coercivity of our problem.

**Lemma 6.3.2.** *Suppose (6.19) and (6.20) are satisfied. Then we have*

$$a_h(\mathbf{w}_h, \mathbf{w}_h) \geq C_{coerc} \|\mathbf{w}_h\|_{\mathring{V}(h)}^2, \quad \forall \mathbf{w}_h \in \mathring{V}_{0,h} \quad (6.21)$$

where  $C_{coerc}$  is a positive constant independent of  $h$ ,  $\sigma$ ,  $\nu$ , and  $C_{pen}$ .

*Proof.* Let  $\mathbf{w}_h \in \mathring{V}_{0,h}$  be arbitrary. We expand

$$\begin{aligned} a_h(\mathbf{w}_h, \mathbf{w}_h) &= a(\mathbf{w}_h, \mathbf{w}_h) \\ &\quad - \sum_{F \in \Gamma_h} \int_F 2\nu \left( ((\nabla^s \mathbf{w}_h) \mathbf{n}) \cdot \mathbf{w}_h + ((\nabla^s \mathbf{w}_h) \mathbf{n}) \cdot \mathbf{w}_h - \frac{C_{pen}}{h_F} \mathbf{w}_h \cdot \mathbf{w}_h \right) \\ &= \sigma \|\mathbf{w}_h\|_{\mathbf{H}(\text{div}; \Omega)}^2 + 2\nu \|\nabla^s \mathbf{w}_h\|_{(\mathbf{L}(\Omega))^{d \times d}}^2 + 2\nu \sum_{F \in \Gamma_h} \frac{C_{pen}}{h_F} \|\mathbf{w}_h\|_{(L^2(F))^d}^2 \\ &\quad - 4\nu \sum_{F \in \Gamma_h} \int_F ((\nabla^s \mathbf{w}_h) \mathbf{n}) \cdot \mathbf{w}_h \end{aligned} \quad (6.22)$$

where we have used the divergence-free condition on  $\mathbf{w}_h$  to obtain  $\|\mathbf{w}_h\|_{\mathbf{H}(\text{div}; \Omega)} = \|\mathbf{w}_h\|_{\mathbf{L}^2(\Omega)}$ . We now use Cauchy-Schwarz to write

$$\begin{aligned} &4\nu \sum_{F \in \Gamma_h} \int_F ((\nabla^s \mathbf{w}_h) \mathbf{n}) \cdot \mathbf{w}_h \leq \\ &2\nu \sum_{F \in \Gamma_h} \left( \frac{2h_F}{C_{pen}} \|(\nabla^s \mathbf{w}_h) \mathbf{n}\|_{(L^2(F))^d}^2 + \frac{C_{pen}}{2h_F} \|\mathbf{w}_h\|_{(L^2(F))^d}^2 \right). \end{aligned} \quad (6.23)$$

Due to Assumption (6.19) and the Poincaré inequality, we have

$$\sum_{F \in \Gamma_h} \frac{2h_F}{C_{pen}} \|(\nabla^s \mathbf{w}_h) \mathbf{n}\|_{(L^2(F))^d}^2 \leq \sum_{K \in \mathcal{K}_h} \frac{1}{2C_{Korn}} |\mathbf{w}_h|_{\mathbf{H}^1(\Omega)}^2 \quad (6.24)$$

where  $C_{Korn}$  is the positive constant (only dependent on the domain  $\Omega$ ) associated with the Korn's inequality

$$|\mathbf{w}|_{\mathbf{H}^1(\Omega)}^2 \leq C_{Korn} \left( \|\nabla^s \mathbf{w}\|_{(L(\Omega))^{d \times d}}^2 + |\partial\Omega|^{-1/(d-1)} \|\mathbf{w}\|_{(L^2(\partial\Omega))^d}^2 \right), \quad \forall \mathbf{w} \in \mathbf{H}^1(\Omega). \quad (6.25)$$

Inserting (6.24) into (6.23) gives

$$\sum_{F \in \Gamma_h} \int_F 4\nu ((\nabla^s \mathbf{w}_h) \mathbf{n}) \cdot \mathbf{w}_h \leq 2\nu \sum_{F \in \Gamma_h} \left( \frac{1}{2C_{Korn}} |\mathbf{w}_h|_{\mathbf{H}^1(\Omega)}^2 + \frac{C_{pen}}{2h_F} \|\mathbf{w}_h\|_{(L^2(F))^d}^2 \right),$$

and by inserting the above inequality into (6.22) and employing (6.25), we obtain

$$\begin{aligned} a_h(\mathbf{w}_h, \mathbf{w}_h) &\geq \sigma \|\mathbf{w}_h\|_{\mathbf{H}(\text{div}; \Omega)}^2 + \frac{\nu}{C_{Korn}} |\mathbf{w}_h|_{\mathbf{H}^1(\Omega)}^2 \\ &\quad + \sum_{F \in \Gamma_h} \nu \left( \frac{C_{pen}}{h_F} - \frac{2}{|\partial\Omega|^{1/(d-1)}} \right) \|\mathbf{w}_h\|_{(L^2(F))^d}^2. \end{aligned}$$

Invoking Assumption (6.20), we have

$$a_h(\mathbf{w}_h, \mathbf{w}_h) \geq \sigma \|\mathbf{w}_h\|_{\mathbf{H}(\text{div}; \Omega)}^2 + \frac{\nu}{C_{Korn}} |\mathbf{w}_h|_{\mathbf{H}^1(\Omega)}^2 + \sum_{F \in \Gamma_h} \frac{\nu C_{pen}}{2h_F} \|\mathbf{w}_h\|_{(L^2(F))^d}^2$$

as

$$h_F \leq h \leq h_0.$$

The lemma then follows with  $C_{coerc} = C_{inv}^{-1} \min \{0.25, 0.5 (C_{Korn})^{-1}\}$  where  $C_{inv}$  is the constant associated with (6.15).  $\square$

We need one more stability estimate. We need to satisfy the Babuška-Brezzi inf-sup condition. Recall that we already proved an inf-sup condition for our discrete spaces in Section 5.4. However, for that inf-sup condition, we utilized the  $\mathbf{H}^1$ -norm for the velocity space. Here, we must employ the stronger  $\mathcal{V}(h)$ -norm. To arrive at an inf-sup condition for this stronger norm, we will proceed by employing three powerful tools: (1) commuting projectors, (2) trace inequalities, and (3) approximation estimates.

**Lemma 6.3.3.** *There exists a positive constant  $\tilde{\beta}$  independent of  $h$ ,  $\sigma$ , and  $\nu$  such that the following holds: for every  $q_h \in \mathcal{Q}_{0,h}$ , there exists a  $\mathbf{v}_h \in \mathcal{V}_{0,h}$  such that:*

$$\operatorname{div} \mathbf{v}_h = q_h \quad (6.26)$$

and

$$\|\mathbf{v}_h\|_{\mathcal{V}(h)} \leq \frac{\sigma + 2\nu}{\tilde{\beta}} \|q_h\|_{\Omega}. \quad (6.27)$$

Hence,

$$\inf_{q_h \in \mathcal{Q}_{0,h}, q_h \neq 0} \sup_{\mathbf{v}_h \in \mathcal{V}_{0,h}} \frac{(\operatorname{div} \mathbf{v}_h, q_h)}{\|\mathbf{v}_h\|_{\mathcal{V}(h)} \|q_h\|_{\Omega}} \geq \tilde{\beta}. \quad (6.28)$$

Furthermore, the inf-sup constant  $\tilde{\beta}$  asymptotically scales inversely with the square root of  $C_{pen}$ .

*Proof.* Let  $q_h \in \mathcal{Q}_{0,h}$  be arbitrary. Then we know there exists a function  $\mathbf{v} \in \mathbf{H}_0^1(\Omega)$  such that  $\operatorname{div} \mathbf{v} = q_h$  and

$$2\nu \|\mathbf{v}\|_{\mathbf{H}^1(\Omega)}^2 \leq 2\nu\beta^{-2} \|q_h\|_{L^2(\Omega)}^2$$

where  $\beta$  is a positive constant independent of  $\mathbf{v}$ . Let  $\mathbf{v}_h = \Pi_{\mathcal{V}_h}^0 \mathbf{v}$ . Then, by Theorem 5.4.1,  $\operatorname{div} \mathbf{v}_h = \operatorname{div} \Pi_{\mathcal{V}_h}^0 \mathbf{v} = \Pi_{\mathcal{Q}_h}^0 \operatorname{div} \mathbf{v} = q_h$  and

$$2\nu \|\mathbf{v}_h\|_{\mathbf{H}^1(\Omega)}^2 \leq 2\nu C_u^2 \|\mathbf{v}\|_{\mathbf{H}^1(\Omega)}^2 \leq 2\nu C_u^2 \beta^{-2} \|q_h\|_{L^2(\Omega)}^2 \quad (6.29)$$

where  $C_u > 0$  is a positive constant independent of  $h$ ,  $\sigma$ ,  $\eta$ , and  $C_{pen}$ . Similarly, we have

$$\sigma \|\mathbf{v}_h\|_{\mathbf{H}(\operatorname{div}; \Omega)}^2 \leq \sigma C_u^2 \beta^{-2} \|q_h\|_{L^2(\Omega)}^2. \quad (6.30)$$

As  $\mathbf{v}$  satisfies homogeneous Dirichlet boundary conditions, we can apply the continuous trace inequality (see Theorem 3.2 of [75]) to obtain the expression

$$\begin{aligned} \sum_{F \in \Gamma_h} h_F^{-1} \|\mathbf{v}_h\|_{(L^2(F))^d}^2 &= \sum_{F \in \Gamma_h} h_F^{-1} \|\mathbf{v}_h - \mathbf{v}\|_{(L^2(F))^d}^2 \\ &\leq C_{tr}^2 \sum_{K \in \mathcal{K}_h} \left( h_K^{-2} \|\mathbf{v}_h - \mathbf{v}\|_{L^2(K)}^2 + |\mathbf{v}_h - \mathbf{v}|_{\mathbf{H}^1(K)}^2 \right) \end{aligned}$$

where  $C_{tr}$  is a positive constant only dependent on the shape regularity of the mesh family  $\{\mathcal{M}_h\}_{h \leq h_0}$  and global, mesh-invariant measures of the parametric mapping. Proposition 5.5.1 gives

$$\sum_{K \in \mathcal{K}_h} \left( h_K^{-2} \|\mathbf{v}_h - \mathbf{v}\|_{\mathbf{L}^2(K)}^2 + |\mathbf{v}_h - \mathbf{v}|_{\mathbf{H}^1(K)}^2 \right) \leq C_{bound}^2 \|\mathbf{v}\|_{\mathbf{H}^1(\Omega)}^2$$

where  $C_{bound}$  is a positive constant independent of  $h$ ,  $\sigma$ ,  $\nu$ , and  $C_{pen}$ . Thus, we have

$$2\nu \sum_{F \in \Gamma_h} \frac{C_{pen}}{h_F} \|\mathbf{v}_h\|_{(L^2(F))^d}^2 \leq 2\nu C_{bound}^2 C_{tr}^2 C_{pen} \beta^{-2} \|q_h\|_{L^2(\Omega)}^2. \quad (6.31)$$

Combining (6.15), (6.29), (6.30), and (6.31), we have

$$\|\mathbf{v}_h\|_{\mathbb{V}(h)}^2 \leq C_{inv} \beta^{-2} (C_u^2 + C_{bound}^2 C_{tr}^2 C_{pen}) (\sigma + 2\nu) \|q_h\|_{L^2(\Omega)}^2.$$

Hence, (6.27) holds with

$$\tilde{\beta} = C_{inv}^{-1/2} (C_u^2 + C_{bound}^2 C_{tr}^2 C_{pen})^{-1/2} \beta.$$

□

The inverse dependence of the inf-sup constant  $\tilde{\beta}$  on the square root of the penalty constant  $C_{pen}$  suggests that  $C_{pen}$  should be chosen as small as possible to satisfy coercivity. Indeed, we have numerically computed the inf-sup constant  $\tilde{\beta}$  for a wide range of values of  $C_{pen}$  and found that the relationship  $\tilde{\beta} \lesssim C_{pen}^{-1/2}$  is sharp (for reference, see the results listed in Table 6.1). We would like to note that this makes intuitive sense as we lose inf-sup stability entirely if we enforce the no-slip condition strongly.

By Lemmata 6.3.1, 6.3.2, and 6.3.3 and Brezzi's Theorem [35], we immediately have the following theorem establishing well-posedness.

Table 6.1: Dependence of the inf-sup constant  $\tilde{\beta}$  on Nitsche's penalty constant  $C_{pen}$  for  $k' = 1$ ,  $h = 1/16$ , and  $\Omega = (0, 1)^2$ .

$C_{pen}$	1	2	4	8	16	32	64
$\tilde{\beta}$	4.24e-1	3.89e-1	3.29e-1	2.50e-1	1.82e-1	1.30e-1	9.24e-2
order	-	-0.13	-0.24	-0.39	-0.46	-0.48	-0.49

**Theorem 6.3.1.** *Suppose that the assumptions of Lemma 6.3.2 hold true. Then, Problem (G) has a unique weak solution  $(\mathbf{u}_h, p_h) \in \mathcal{V}_{0,h} \times \mathcal{Q}_{0,h}$ . Furthermore,*

$$\|\mathbf{u}_h\|_{\mathcal{V}(h)} \leq \frac{1}{C_{coerc}} (\sigma + 2\nu C_{poin}^{-2})^{-1/2} \|\mathbf{f}\|_{\mathbf{L}^2(\Omega)}, \quad (6.32)$$

$$\|p_h\|_{\mathcal{Q}} \leq \frac{1}{\tilde{\beta}} (\sigma + 2\nu C_{poin}^{-2})^{-1/2} \left(1 + \frac{C_{cont}}{C_{coerc}}\right) \|\mathbf{f}\|_{\mathbf{L}^2(\Omega)}. \quad (6.33)$$

We would like to note that all of the continuity and stability estimates here hold when  $\nu$  is identically zero and  $\sigma$  is positive. Hence, we have a unified stability analysis of Stokes flow and incompressible Darcy flow.

**Remark 6.3.1.** *Note that for the setting of constant viscosity, one has*

$$\nabla \cdot (2\nu \nabla^s \mathbf{u}) = \nu \Delta \mathbf{u}. \quad (6.34)$$

*This inspires a different variational formulation than that presented here which is often the basis for numerical discretization (see, for example, [49]). However, these discretizations (and their accompanying mathematical analysis) are not extendable to the more difficult and physically relevant setting of variable viscosity, and they also cannot easily accommodate traction boundary conditions.*

## 6.4 A Priori Error Estimates

We are now ready to derive *a priori* error estimates for our discrete formulation. We begin with the following lemma.

**Lemma 6.4.1.** *Let  $(\mathbf{u}, p)$  and  $(\mathbf{u}_h, p_h)$  denote the unique solutions of Problems (W) and (G) respectively. Furthermore, assume that  $\mathbf{u} \in \mathbf{H}^{3/2+\epsilon}(\Omega)$  for some  $\epsilon > 0$  and that the assumptions of Lemma 6.3.2 hold true. Then*

$$\|\mathbf{u} - \mathbf{u}_h\|_{\mathcal{V}(h)} \leq \left(1 + \frac{C_{cont}}{C_{coerc}}\right) \inf_{\mathbf{v}_h \in \tilde{\mathcal{V}}_{0,h}} \|\mathbf{u} - \mathbf{v}_h\|_{\mathcal{V}(h)} \quad (6.35)$$

and

$$\|p - p_h\|_{\Omega} \leq \left(1 + \frac{1}{\tilde{\beta}}\right) \inf_{q_h \in \mathcal{Q}_{0,h}} \|p - q_h\|_{\Omega} + \frac{C_{cont}}{\tilde{\beta}} \|\mathbf{u} - \mathbf{u}_h\|_{\mathcal{V}(h)} \quad (6.36)$$

where  $C_{cont}$  is the continuity constants given by Lemma 6.3.1,  $C_{coerc}$  is the coercivity constant given by Lemma 6.3.2, and  $\tilde{\beta}$  is the inf-sup constant given by Lemma 6.3.3.

*Proof.* We first prove (6.35). We have that, for any  $\mathbf{v}_h \in \mathcal{V}_{0,h}$  such that  $\operatorname{div} \mathbf{v}_h = 0$ ,

$$\begin{aligned} \|\mathbf{v}_h - \mathbf{u}_h\|_{\tilde{\mathcal{V}}(h)}^2 &\leq \frac{1}{C_{coerc}} a(\mathbf{v}_h - \mathbf{u}_h, \mathbf{v}_h - \mathbf{u}_h) \\ &= \frac{1}{C_{coerc}} a(\mathbf{v}_h - \mathbf{u}, \mathbf{v}_h - \mathbf{u}_h) \\ &\leq \frac{C_{cont}}{C_{coerc}} \|\mathbf{v}_h - \mathbf{u}\|_{\mathcal{V}(h)} \|\mathbf{v}_h - \mathbf{u}_h\|_{\mathcal{V}(h)} \end{aligned} \quad (6.37)$$

where we employed the orthogonality given by Corollary 6.2.1 and the condition

$$\operatorname{div} (\mathbf{u}_h - \mathbf{v}_h) = 0$$

in the second line of the (6.37). Hence, we can write

$$\begin{aligned} \|\mathbf{u} - \mathbf{u}_h\|_{\mathcal{V}(h)} &\leq \inf_{\mathbf{v}_h \in \tilde{\mathcal{V}}_{0,h}} (\|\mathbf{u} - \mathbf{v}_h\|_{\mathcal{V}(h)} + \|\mathbf{v}_h - \mathbf{u}_h\|_{\mathcal{V}(h)}) \\ &\leq \left(1 + \frac{C_{cont}}{C_{coerc}}\right) \inf_{\mathbf{v}_h \in \tilde{\mathcal{V}}_{0,h}} \|\mathbf{u} - \mathbf{v}_h\|_{\mathcal{V}(h)}. \end{aligned} \quad (6.38)$$

We now prove (6.36). We have that, for any  $q_h \in \mathcal{Q}_{0,h}$ ,

$$\begin{aligned}
\|p_h - q_h\|_{\Omega} &\leq \frac{1}{\tilde{\beta}} \sup_{\mathbf{w}_h \in \mathcal{V}_{0,h}} \frac{b(p_h - q_h, \mathbf{w}_h)}{\|\mathbf{w}_h\|_{\mathcal{V}(h)}} \\
&= \frac{1}{\tilde{\beta}} \sup_{\mathbf{w}_h \in \mathcal{V}_{0,h}} \frac{b(p - q_h, \mathbf{w}_h) - a(\mathbf{u} - \mathbf{u}_h, \mathbf{w}_h)}{\|\mathbf{w}_h\|_{\mathcal{V}(h)}} \\
&\leq \frac{1}{\tilde{\beta}} (\|p - q_h\|_{\Omega} + C_{cont} \|\mathbf{u} - \mathbf{u}_h\|_{\mathcal{V}(h)}) \tag{6.39}
\end{aligned}$$

where we again employed orthogonality in the second line above. Inequality (6.36) then follows in the same manner as (6.38) by a splitting of the pressure error and a usage of (6.39).  $\square$

We have the following theorem giving us *a priori* convergence estimates which are optimal for the discrete velocity field and suboptimal, by one order, for the discrete pressure field.

**Theorem 6.4.1.** *Let  $(\mathbf{u}, p)$  and  $(\mathbf{u}_h, p_h)$  denote the unique solutions of Problems (W) and (G) respectively. Furthermore, assume that  $(\mathbf{u}, p) \in \mathbf{H}^{j+1}(\Omega) \times H^j(\Omega)$  for some  $j > 1/2$  and that the assumptions of Lemma 6.3.2 hold true. Then*

$$\|\mathbf{u} - \mathbf{u}_h\|_{\mathcal{V}(h)} \leq C_{\mathbf{u}} \left( 1 + \frac{C_{cont}}{C_{coerc}} \right) \sqrt{\sigma h^{2s+2} + 2\nu h^{2s}} \|\mathbf{u}\|_{\mathbf{H}^{s+1}(\Omega)} \tag{6.40}$$

and

$$\|p - p_h\|_{\Omega} \leq C_p \left( 1 + \frac{1}{\tilde{\beta}} \right) (\sigma + 2\nu)^{-1/2} h^s \|p\|_{H^s(\Omega)} + \frac{C_{cont}}{\tilde{\beta}} \|\mathbf{u} - \mathbf{u}_h\|_{\mathcal{V}(h)} \tag{6.41}$$

for  $s = \min \{k', j\}$  where  $k'$  is the polynomial degree of our discretization,  $C_{\mathbf{u}}$  is a positive constant independent of  $h$ ,  $\sigma$ , and  $\nu$  which asymptotically scales with the square root of  $C_{pen}$ , and  $C_p$  is a positive constant independent of  $h$ ,  $\sigma$ ,  $\nu$ , and  $C_{pen}$ .

*Proof.* We first prove (6.40). Recall the error estimate given by (6.35):

$$\|\mathbf{u} - \mathbf{u}_h\|_{V(h)} \leq \left(1 + \frac{C_{cont}}{C_{coerc}}\right) \inf_{\mathbf{v}_h \in \hat{V}_{0,h}} \|\mathbf{u} - \mathbf{v}_h\|_{V(h)}.$$

Noting  $\operatorname{div} \Pi_{V_h}^0 \mathbf{u} = \Pi_{Q_h}^0 \operatorname{div} \mathbf{u} = 0$ , we can choose  $\mathbf{v}_h = \Pi_{V_h}^0 \mathbf{u}$  in the above expression to obtain

$$\begin{aligned} \|\mathbf{u} - \mathbf{u}_h\|_{V(h)} &\leq \left(1 + \frac{C_{cont}}{C_{coerc}}\right) \|\mathbf{u} - \Pi_{V_h}^0 \mathbf{u}\|_{V(h)} \\ &= C_{co} \sqrt{T_1 + T_2 + T_3 + T_4} \end{aligned} \quad (6.42)$$

where we have assigned  $C_{co} = \left(1 + \frac{C_{cont}}{C_{coerc}}\right)$  and

$$T_1 = \sigma \|\mathbf{u} - \Pi_{V_h}^0 \mathbf{u}\|_{\mathbf{H}(\operatorname{div}; \Omega)}^2 = \sigma \|\mathbf{u} - \Pi_{V_h}^0 \mathbf{u}\|_{\mathbf{L}^2(\Omega)}^2 \quad (6.43)$$

$$T_2 = 2\nu |\mathbf{u} - \Pi_{V_h}^0 \mathbf{u}|_{\mathbf{H}^1(\Omega)}^2 \quad (6.44)$$

$$T_3 = 2\nu \sum_{F \in \Gamma_h} h_F \|\nabla^s (\mathbf{u} - \Pi_{V_h}^0 \mathbf{u}) \mathbf{n}\|_{(L^2(F))^d}^2 \quad (6.45)$$

$$T_4 = 2\nu \sum_{F \in \Gamma_h} C_{pen} h_F^{-1} \|\mathbf{u} - \Pi_{V_h}^0 \mathbf{u}\|_{(L^2(F))^d}^2. \quad (6.46)$$

To handle the face integral in (6.45), we recruit the multiplicative trace inequality for fractional Sobolev spaces [181] and Young's inequality element-wise to obtain the bound

$$\begin{aligned} &\sum_{F \in \Gamma_h} C_{pen} h_F \|\nabla^s (\mathbf{u} - \Pi_{V_h}^0 \mathbf{u}) \mathbf{n}\|_{(L^2(F))^d}^2 \leq \\ &(C_{trc,1})^2 \sum_{K \in \mathcal{K}_h} \left( |\mathbf{u} - \Pi_{V_h}^0 \mathbf{u}|_{\mathbf{H}^1(K)}^2 + h_K^{2q} |\mathbf{u} - \Pi_{V_h}^0 \mathbf{u}|_{\mathbf{H}^{q+1}(\Omega)}^2 \right) \end{aligned}$$

where  $1/2 < q \leq s$  and  $C_{trc,1}$  is a positive constant independent of  $h$ ,  $\sigma$ ,  $\nu$ , and  $C_{pen}$ . To handle the face integral in (6.46), we recruit the standard continuous trace

inequality element-wise to obtain the bound

$$\sum_{F \in \Gamma_h} C_{pen} h_F^{-1} \|\mathbf{u} - \Pi_{V_h}^0 \mathbf{u}\|_{(L^2(F))^d}^2 \leq (C_{trc,2})^2 \sum_{K \in \mathcal{K}_h} \left( h_K^{-2} \|\mathbf{u} - \Pi_{V_h}^0 \mathbf{u}\|_{\mathbf{L}^2(K)}^2 + \|\mathbf{u} - \Pi_{V_h}^0 \mathbf{u}\|_{\mathbf{H}^1(K)}^2 \right)$$

where  $C_{trc,2}$  is a positive constant independent of  $h$ ,  $\sigma$ , and  $\nu$  which varies linearly with the square root of  $C_{pen}$ . It should be noted the two constants  $C_{trc,1}$  and  $C_{trc,2}$  necessarily depend on the shape regularity of the mesh family  $\{\mathcal{Q}\}_{h \leq h_0}$  and the parametric mapping which together give the shape regularity of the mesh family  $\{\mathcal{K}\}_{h \leq h_0}$ . See [75] for more details. Inserting the above two inequalities into (6.42) and then applying Proposition 5.5.1, we immediately acquire the bound

$$\|\mathbf{u} - \Pi_{V_h}^0 \mathbf{u}\|_{V(h)} \leq C_{\mathbf{u}} C_{co} \sqrt{\sigma h^{2s+2} + 2\nu h^{2s}} \|\mathbf{u}\|_{\mathbf{H}^{s+1}(\Omega)}$$

for  $C_{\mathbf{u}}$  a positive constant independent of  $h$ ,  $\sigma$ , and  $\nu$  with the same functional dependency on the penalty parameter as  $C_{trc,2}$ .

The proof for (6.41) is much more immediate. Choosing  $q_h = \Pi_{Q_h}^0 p$  in the error estimate given by (6.36), one obtains

$$\|p - p_h\|_{\Omega} \leq \left(1 + \frac{1}{\tilde{\beta}}\right) \|p - \Pi_{Q_h}^0 p\|_{\Omega} + \frac{C_{cont}}{\tilde{\beta}} \|\mathbf{u} - \mathbf{u}_h\|_{V(h)}.$$

Inequality (6.41) follows by an application of Proposition 5.5.1 to bound the pressure interpolation error.  $\square$

Since we have the bound

$$2\nu |\cdot|_{\mathbf{H}^1(\Omega)} \lesssim \|\cdot\|_{V(h)},$$

the above theorem also provides optimal convergence rates for the velocity field in the  $\mathbf{H}^1$ -norm. If we assume slightly more regularity for the pressure space, we have the following proposition.

**Proposition 6.4.1.** *Let  $(\mathbf{u}, p)$  and  $(\mathbf{u}_h, p_h)$  denote the unique solutions of Problems (W) and (G) respectively. Furthermore, assume that  $(\mathbf{u}, p) \in \mathbf{H}^{j+1}(\Omega) \times H^{j+1}(\Omega)$  for some  $j > 1/2$  and that the assumptions of Lemma 6.3.2 hold true. Then*

$$\|p - p_h\|_{\Omega} \leq C_{p,e} \left(1 + \frac{1}{\tilde{\beta}}\right) (\sigma + 2\nu)^{-1/2} h^{s+1} \|p\|_{H^{s+1}(\Omega)} + \frac{C_{cont}}{\tilde{\beta}} \|\mathbf{u} - \mathbf{u}_h\|_{V(h)} \quad (6.47)$$

for  $s = \min\{k', j\}$  where  $C_{p,e}$  is a positive constant independent of  $h$ ,  $\sigma$ ,  $\nu$ , and  $C_{pen}$ .

Observe that the pressure error estimate given by the above proposition is still suboptimal due to the presence of the velocity error, which converges with order  $s$  for general viscous flows. Let us further note that the preceding theorem and proposition are trivially extended to the setting of vanishing viscosity. In this case, the velocity error actually converges with order  $s + 1$ , giving optimal *a priori* error estimates for both the discrete pressure field and discrete velocity field for incompressible Darcy flow.

Under an elliptic regularity assumption, we can obtain optimal estimates for the velocity field in the  $\mathbf{L}^2$ -norm by utilizing a standard duality argument. Given the unique solutions  $(\mathbf{u}, p)$  and  $(\mathbf{u}_h, p_h)$  of Problems (W) and (G), let us consider the following ancillary problem, written in strong form.

$$(A) \left\{ \begin{array}{l} \text{Find } (\boldsymbol{\psi}, r) \in \mathbf{H}_0^1(\Omega) \times L_0^2(\Omega) \text{ such that} \\ \sigma \boldsymbol{\psi} - \nabla \cdot (2\nu \nabla^s \boldsymbol{\psi}) + \mathbf{grad} r = \mathbf{u} - \mathbf{u}_h \quad \text{in } \Omega \quad (6.48) \\ \operatorname{div} \boldsymbol{\psi} = 0 \quad \text{in } \Omega \quad (6.49) \\ \boldsymbol{\psi} = \mathbf{0} \quad \text{on } \partial\Omega. \quad (6.50) \end{array} \right.$$

The above problem has a unique weak solution  $(\boldsymbol{\psi}, r)$ . Before proceeding, note that we can formally take the divergence of (6.48) to obtain

$$\Delta r = 0, \quad \text{in } \Omega. \quad (6.51)$$

Since  $r$  has zero average, it follows, at least from our formal argument, that  $r = 0$ . This argument can be made rigorous by a suitable use of convolutions and passing to the limit. Now suppose that  $\boldsymbol{\psi} \in \mathbf{H}^2(\Omega)$ . We can then multiply the left and right hand sides of (6.48) by  $\sigma\boldsymbol{\psi} + \nabla \cdot (2\nu\nabla^s\boldsymbol{\psi})$  to acquire the result

$$\|\sigma\boldsymbol{\psi}\|_{\mathbf{L}^2(\Omega)}^2 + \|\nabla \cdot (2\nu\nabla^s\boldsymbol{\psi})\|_{\mathbf{L}^2(\Omega)}^2 = (\mathbf{u} - \mathbf{u}_h, \sigma\boldsymbol{\psi} + \nabla \cdot (2\nu\nabla^s\boldsymbol{\psi}))_{\mathbf{L}^2(\Omega)}. \quad (6.52)$$

A simple application of Cauchy-Schwarz and the triangle inequality gives

$$\begin{aligned} & \|\sigma\boldsymbol{\psi}\|_{\mathbf{L}^2(\Omega)}^2 + \|\nabla \cdot (2\nu\nabla^s\boldsymbol{\psi})\|_{\mathbf{L}^2(\Omega)}^2 = \\ & \|\mathbf{u} - \mathbf{u}_h\|_{\mathbf{L}^2(\Omega)} (\|\sigma\boldsymbol{\psi}\|_{\mathbf{L}^2(\Omega)} + \|\nabla \cdot (2\nu\nabla^s\boldsymbol{\psi})\|_{\mathbf{L}^2(\Omega)}) \end{aligned} \quad (6.53)$$

Since  $x^2 + y^2 \geq \frac{1}{2}(x + y)^2$ , we can divide both sides by  $\|\sigma\boldsymbol{\psi}\|_{\mathbf{L}^2(\Omega)} + \|\nabla \cdot (2\nu\nabla^s\boldsymbol{\psi})\|_{\mathbf{L}^2(\Omega)}$  to obtain

$$\frac{1}{2} (\|\sigma\boldsymbol{\psi}\|_{\mathbf{L}^2(\Omega)} + \|\nabla \cdot (2\nu\nabla^s\boldsymbol{\psi})\|_{\mathbf{L}^2(\Omega)}) \leq \|\mathbf{u} - \mathbf{u}_h\|_{\mathbf{L}^2(\Omega)}. \quad (6.54)$$

As  $\boldsymbol{\psi}$  satisfies normal and tangential homogeneous Dirichlet boundary conditions and  $\nu$  is assumed positive, we can employ a combination of Korn's inequalities and Poincaré inequalities to obtain a standard elliptic regularity result of the form

$$\|\boldsymbol{\psi}\|_{\mathbf{H}^2(\Omega)} \leq C_A \nu^{-1} \|\mathbf{u} - \mathbf{u}_h\|_{\mathbf{L}^2(\Omega)}. \quad (6.55)$$

where  $C_A$  is a positive constant which only depends on the domain  $\Omega$ . In view of the above discussion, we have the following theorem.

**Theorem 6.4.2.** *Let  $(\mathbf{u}, p)$  and  $(\mathbf{u}_h, p_h)$  denote the unique solutions of Problems (W) and (G) respectively, and let  $(\boldsymbol{\psi}, r)$  denote the unique solution of Problem (A). Furthermore, assume that  $(\mathbf{u}, p) \in \mathbf{H}^{j+1}(\Omega) \times H^j(\Omega)$  for some  $j \geq 1$ , that  $\boldsymbol{\psi} \in \mathbf{H}^2(\Omega)$ , and that the assumptions of Lemma 6.3.2 hold true. Then*

$$\|\mathbf{u} - \mathbf{u}_h\|_{\mathbf{L}^2(\Omega)} \leq C_l h^{s+1} \|\mathbf{u}\|_{\mathbf{H}^{s+1}(\Omega)} \quad (6.56)$$

for  $s = \min \{k', j\}$  where  $C_1$  is a positive constant independent of  $h$ ,  $\sigma$ , and  $\nu$  which asymptotically scales with the square root of  $C_{pen}$ .

*Proof.* Since by assumption  $(\boldsymbol{\psi}, r) \in \mathbf{H}^2(\Omega) \times H^1(\Omega)$ , consistency and symmetry give

$$a_h(\mathbf{v}, \boldsymbol{\psi}) - b(r, \mathbf{v}) = (\mathbf{u} - \mathbf{u}_h, \mathbf{v})_{\mathbf{L}^2(\Omega)}$$

for all  $\mathbf{v} \in \mathcal{V}_h$ . Let us take  $\mathbf{v} = \mathbf{u} - \mathbf{u}_h$ . We then have

$$\|\mathbf{u} - \mathbf{u}_h\|_{\mathbf{L}^2(\Omega)}^2 = a_h(\mathbf{u} - \mathbf{u}_h, \boldsymbol{\psi}).$$

as  $\operatorname{div}(\mathbf{u} - \mathbf{u}_h) = 0$  (or  $r = 0$  by our preceding discussion). By using the orthogonality given by Corollary 6.2.1, we can write

$$\begin{aligned} \|\mathbf{u} - \mathbf{u}_h\|_{\mathbf{L}^2(\Omega)}^2 &= a_h(\mathbf{u} - \mathbf{u}_h, \boldsymbol{\psi} - \Pi_{\mathcal{V}_h}^0 \boldsymbol{\psi}) \\ &\leq C_{cont} \|\mathbf{u} - \mathbf{u}_h\|_{\mathcal{V}(h)} \|\boldsymbol{\psi} - \Pi_{\mathcal{V}_h}^0 \boldsymbol{\psi}\|_{\mathcal{V}(h)}. \end{aligned} \quad (6.57)$$

We bound the interpolation error by utilizing a similar argument to that used to prove (6.47), obtaining

$$\|\boldsymbol{\psi} - \Pi_{\mathcal{V}_h}^0 \boldsymbol{\psi}\|_{\mathcal{V}(h)} \leq C_{interp} (\sigma^{1/2} h^2 + \nu^{1/2} h) \|\boldsymbol{\psi}\|_{\mathbf{H}^2(\Omega)}$$

for  $C_{interp}$  a positive constant independent of  $h$ ,  $\sigma$ , and  $\nu$  which asymptotically scales with the the square root of  $C_{pen}$ . We can now employ the elliptic regularity condition (6.55) to arrive at

$$\|\boldsymbol{\psi} - \Pi_{\mathcal{V}_h}^0 \boldsymbol{\psi}\|_{\mathcal{V}(h)} \leq C_A C_{interp} (\sigma^{1/2} \nu^{-1} h^2 + \nu^{-1/2} h) \|\mathbf{u} - \mathbf{u}_h\|_{\mathbf{L}^2(\Omega)}. \quad (6.58)$$

Inserting (6.58) into (6.57) results in

$$\|\mathbf{u} - \mathbf{u}_h\|_{\mathbf{L}^2(\Omega)} \leq C_A C_{interp} C_{cont} (\sigma^{1/2} \nu^{-1} h^2 + \nu^{-1/2} h) \|\mathbf{u} - \mathbf{u}_h\|_{\mathcal{V}(h)}.$$

Immediately invoking the error estimate given by Theorem 6.4.1, we obtain

$$\|\mathbf{u} - \mathbf{u}_h\|_{\mathbf{L}^2(\Omega)} \leq C_{temp} \left(1 + \sqrt{Da_h}\right)^2 h^{s+1} \|\mathbf{u}\|_{\mathbf{H}^{s+1}(\Omega)} \quad (6.59)$$

where  $C_{temp}$  is a positive constant independent of  $h$ ,  $\sigma$ , and  $\nu$  which asymptotically scales with the square root of  $C_{pen}$  and

$$Da_h = \frac{\sigma h^2}{\nu}.$$

However, we also have the following estimate due to Theorem 6.4.1:

$$\|\mathbf{u} - \mathbf{u}_h\|_{\mathbf{L}^2(\Omega)} \leq C_{\mathbf{u}} \left(1 + \frac{C_{cont}}{C_{coerc}}\right) \left(1 + (Da_h)^{-1}\right)^{1/2} h^{s+1} \|\mathbf{u}\|_{\mathbf{H}^{s+1}(\Omega)}. \quad (6.60)$$

The desired result follows by taking the minimum of (6.59) and (6.60).  $\square$

This concludes our *a priori* error analysis. Note that, for reasonably regular exact solutions, we have obtained optimal estimates for the velocity field in both the strong  $\mathcal{V}(h)$ -norm as well as the weaker  $\mathbf{H}^1$ - and  $\mathbf{L}^2$ -norms. The estimates are additionally robust with respect to the fluid coefficients  $\sigma$  and  $\nu$ . On the other hand, we have obtained pressure error estimates which are suboptimal by one order. This is reminiscent of error estimates for stabilized equal-order interpolations of the Stokes equations and is not unexpected as both our discrete velocity and pressure spaces consist of mapped piecewise polynomials which are only complete up to degree  $k'$ . However, our later numerical studies suggest the conservative nature of these estimates by revealing, for simple model problems, optimal convergence rates for the pressure field. Ongoing work is being dedicated to the theoretical confirmation of these convergence rates. Note that our analysis covers typical singular solutions of the generalized Stokes equations. Later in this chapter, we will numerically study the effectiveness of our method for a selection of singular Stokes problems. Finally,

we would like to mention that our velocity error estimates are completely independent of the pressure field. This property does not hold for discretizations which preserve the incompressibility in only a discrete sense.

**Remark 6.4.1.** *In opposition to standard Bubnov-Galerkin methods, the constant*

$$(1 + C_{cont} (C_{coerc})^{-1})$$

*appearing in (6.35) cannot be reduced to just  $C_{cont} (C_{coerc})^{-1}$ .*

**Remark 6.4.2.** *At this point, suitable requirements guaranteeing elliptic regularity for domains obtained by NURBS mappings are unknown. One anticipates that such requirements should be less stringent than those associated with polyhedral domains (namely, convexity) because of enhanced smoothness. In our view, this is an interesting area of research.*

## 6.5 Extension to Multi-Patch Domains

As was mentioned previously in Section 4.3, most geometries of scientific and engineering interest cannot be represented by a single patch. Instead, the multi-patch concept must be invoked. We assume that there exist  $n_p$  sufficiently smooth parametric mappings  $\mathbf{F}_i : (0, 1)^d \rightarrow \mathbb{R}^d$  such that the subdomains

$$\Omega_i = \mathbf{F}_i \left( \widehat{\Omega} \right), \quad i = 1, \dots, n_p$$

are non-overlapping and

$$\overline{\Omega} = \cup_{i=1}^{n_p} \overline{\Omega}_i.$$

We refer to each subdomain  $\Omega_i$  (and its inverse image) as a patch. For a visual depiction of a multi-patch construction in  $\mathbb{R}^2$ , see Figure 6.1. We build discrete velocity and pressure spaces over each patch  $\Omega_i$ ,  $i = 1, \dots, n_p$  in the same manner

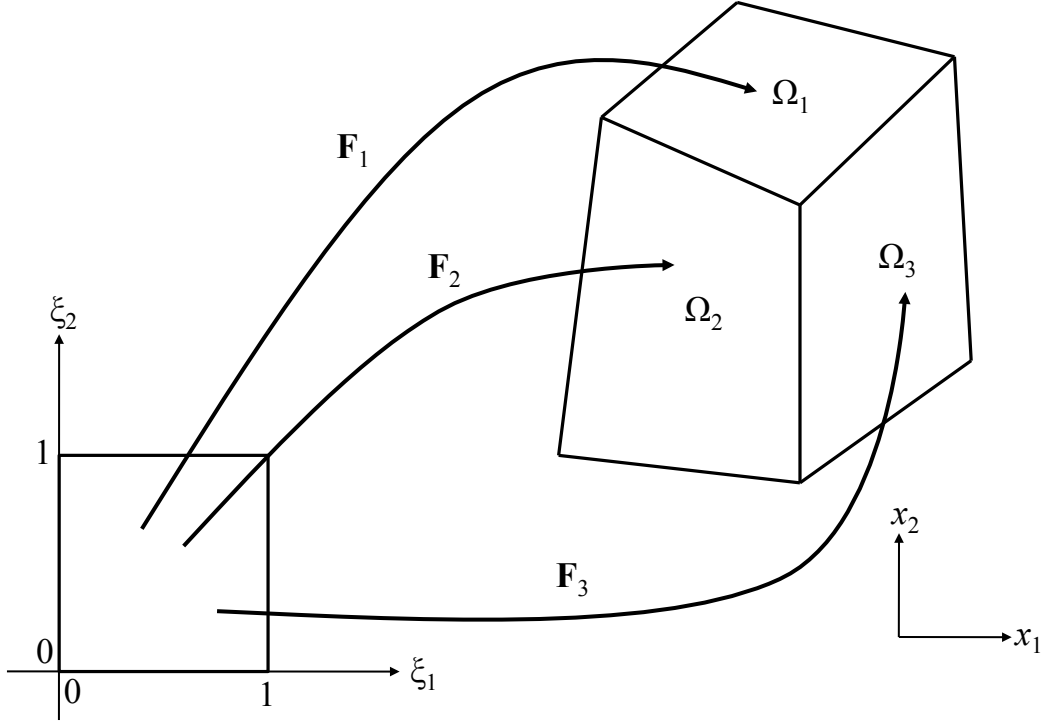


Figure 6.1: Example multi-patch construction in  $\mathbb{R}^2$ .

as in Chapter 5 except that we do not yet enforce boundary conditions, and we denote these spaces as  $\mathcal{V}_h(\Omega_i)$  and  $\mathcal{Q}_h(\Omega_i)$ .

To proceed further, we must make some assumptions. First of all, we assume that if two disjoint patches  $\Omega_i$  and  $\Omega_j$  have the property that  $\partial\Omega_i \cap \partial\Omega_j \neq \emptyset$ , then this intersection consists strictly of patch faces, edges, and corners. More succinctly, two patches cannot intersect along an isolated portion of a face (or edge) interior. Second, we assume that the mappings  $\{\mathbf{F}_i\}_{i=1}^{n_p}$  are compatible in the following sense: if two patches  $\Omega_i$  and  $\Omega_j$  share a face, then  $\mathbf{F}_i$  and  $\mathbf{F}_j$  parametrize that face identically up to changes in orientation. Third, we assume that if two patches  $\Omega_i$  and  $\Omega_j$  share a face, the B-spline meshes associated with the patches are identi-

cal along that face. This guarantees our mesh is conforming. Finally, we assume for simplicity that  $k_1 = \dots = k_d = k^*$  for all patches. The mixed polynomial degree case introduces additional complications that are beyond the scope of this work. We would like to note that all four assumptions hold if we employ a conforming NURBS multi-patch construction. See, for example, Chapter 2 of [52].

We define our global discrete velocity and pressure spaces as follows:

$$\mathcal{V}_{0,h} := \{\mathbf{v}_h \in \mathbf{H}_0(\operatorname{div}; \Omega) : \mathbf{v}_h|_{\Omega_i} \in \mathcal{V}_h(\Omega_i), \forall i = 1, \dots, n_p\}, \quad (6.61)$$

$$\mathcal{Q}_{0,h} := \{q_h \in L_0^2(\Omega) : q_h|_{\Omega_i} \in \mathcal{Q}_h(\Omega_i), \forall i = 1, \dots, n_p\}. \quad (6.62)$$

The space  $\mathcal{V}_{0,h}$  is easily constructed due to our preceding four assumptions and use of open knot vectors. Specifically, we set to zero the coefficient of any basis function whose normal is nonzero along  $\partial\Omega$ , and along shared faces between patches, we (i) equivalence the coefficients of any basis functions whose normal values are nonzero and equal in magnitude and direction and (ii) set opposite the coefficients of any basis functions whose normal values are nonzero, equal in magnitude, and opposite in direction. We note that this is precisely the same procedure as is used to construct Raviart-Thomas spaces on conforming finite element meshes. We simply have patches instead of elements. It is easily shown that the spaces  $\mathcal{V}_{0,h}$  and  $\mathcal{Q}_{0,h}$ , along with the divergence operator, form the bounded discrete cochain complex

$$\mathcal{V}_{0,h} \xrightarrow{\operatorname{div}} \mathcal{Q}_{0,h}.$$

However, functions in  $\mathcal{V}_{0,h}$  do not necessarily lie in  $\mathbf{H}^1(\Omega)$  as tangential continuity is not enforced across patch interfaces. Hence, we need to account for this lack of continuity when designing a discretization scheme for the generalized Stokes equations. We employ the symmetric interior penalty method [4,69,191], a standard technique in the discontinuous Galerkin community, to weakly enforce tangential continuity between adjacent patches.

We now establish some preliminary notation. Let  $\mathcal{K}_h(\Omega_i)$  and  $\mathcal{F}_h(\Omega_i)$  denote the sets of physical mesh elements and faces associated with patch  $\Omega_i$ . We denote the global set of mesh elements as  $\mathcal{K}_h$  and the global set of mesh faces as  $\mathcal{F}_h$ . As in the single patch setting, we define the boundary mesh to be

$$\Gamma_h = \{F \in \mathcal{F}_h(\Omega_i), i = 1, \dots, n_p : F \subset \partial\Omega\}, \quad (6.63)$$

and we define the interface mesh to be

$$\mathcal{J}_h = \{F \in \mathcal{F}_h(\Omega_i), i = 1, \dots, n_p : F \in \mathcal{F}_h(\Omega_j), i \neq j \text{ and } F \notin \Gamma_h\}. \quad (6.64)$$

For each face  $F \in \mathcal{J}_h$  belonging to the interface mesh, there exist two unique adjacent elements  $K^+, K^- \in \mathcal{K}_h$  such that  $F \in \partial K^+$  and  $F \in \partial K^-$ . We define for such a face the mesh size

$$h_F := \frac{1}{2} (h_{K^+} + h_{K^-}). \quad (6.65)$$

Let  $\phi$  be an arbitrary scalar-, vector-, or matrix-valued piecewise smooth function, and let us denote by  $\phi^+$  and  $\phi^-$  the traces of  $\phi$  on  $F$  as taken from within the interior of  $K^+$  and  $K^-$  respectively. We define the mean value of  $\phi$  at  $\mathbf{x} \in F$  as

$$\{\{\phi\}\} := \frac{1}{2} (\phi^+ + \phi^-). \quad (6.66)$$

Further, for a generic multiplication operator  $\odot$ , we define the jump of  $\phi \odot \mathbf{n}$  at  $\mathbf{x} \in F$  as

$$\llbracket \phi \odot \mathbf{n} \rrbracket := \phi^+ \odot \mathbf{n}_{K^+} + \phi^- \odot \mathbf{n}_{K^-} \quad (6.67)$$

where  $\mathbf{n}_{K^{+/-}}$  denotes the outward facing normal on the boundary  $\partial K^{+/-}$  of element  $K^{+/-}$ .

With the above notation established, let us define the following bilinear form:

$$\begin{aligned}
a_h^*(\mathbf{w}, \mathbf{v}) &= \sum_{i=1}^{n_p} \left( (2\nu \nabla^s \mathbf{w}, \nabla^s \mathbf{v})_{(L^2(\Omega_i))^{d \times d}} + (\sigma \mathbf{w}, \mathbf{v})_{\mathbf{L}^2(\Omega_i)} \right) \\
&\quad - \sum_{F \in \mathcal{J}_h} \int_F 2\nu (\{\{\nabla^s \mathbf{v}\}\} : [\mathbf{w} \otimes \mathbf{n}] + \{\{\nabla^s \mathbf{w}\}\} : [\mathbf{v} \otimes \mathbf{n}]) \, ds \\
&\quad + \sum_{F \in \mathcal{J}_h} \int_F 2\nu \left( \frac{2C_{pen}}{h_F} [\mathbf{w} \otimes \mathbf{n}] : [\mathbf{v} \otimes \mathbf{n}] \right) \, ds \\
&\quad - \sum_{F \in \Gamma_h} \int_F 2\nu \left( ((\nabla^s \mathbf{v}) \mathbf{n}) \cdot \mathbf{w} + ((\nabla^s \mathbf{w}) \mathbf{n}) \cdot \mathbf{v} - \frac{C_{pen}}{h_F} \mathbf{w} \cdot \mathbf{v} \right) \, ds.
\end{aligned} \tag{6.68}$$

Above,  $C_{pen} > 0$  denotes the same positive penalty constant as before. Our discrete formulation over the multi-patch domain then reads as follows.

$$(MP) \begin{cases} \text{Find } \mathbf{u}_h \in \mathcal{V}_{0,h} \text{ and } p_h \in \mathcal{Q}_{0,h} \text{ such that} \\ \qquad \qquad \qquad a_h^*(\mathbf{u}_h, \mathbf{v}_h) - b(p_h, \mathbf{v}_h) + b(q_h, \mathbf{u}_h) = (\mathbf{f}, \mathbf{v}_h)_{\mathbf{L}^2(\Omega)} \\ \text{for all } \mathbf{v}_h \in \mathcal{V}_{0,h} \text{ and } q_h \in \mathcal{Q}_{0,h}. \end{cases} \tag{6.69}$$

As in the single patch setting, the discrete formulation detailed above returns a pointwise divergence-free velocity field. However, we do not have a convergence analysis available as we do not yet have a multi-patch analogue of Theorem 5.4.1. We anticipate this will take new theoretical developments. Nonetheless, we have utilized the above formulation in practice and observed it returns optimal convergence rates for both velocity and pressure fields.

## 6.6 Numerical Verification of Convergence Estimates

In this section, we numerically verify our convergence estimates using a collection of problems with exact solutions. Throughout, we choose Nitsche's penalty

constant as

$$C_{pen} = 5(k' + 1)$$

where  $k'$  is the polynomial degree of a given discretization. We have found that this choice leads to stable numerical formulations for the generalized Stokes equations. Furthermore, unless otherwise specified, we employ uniform parametric meshes, linear parametric mappings, and B-spline spaces of maximal continuity.

### 6.6.1 Two-Dimensional Manufactured Solution

As a first numerical experiment, we consider a two-dimensional manufactured solution that was originally presented in [39]. Let

$$\Omega \equiv (0, 1)^2$$

and

$$\mathbf{f} \equiv \sigma \bar{\mathbf{u}} - \nabla \cdot (2\nu \nabla^s \bar{\mathbf{u}}) + \nabla \bar{p}$$

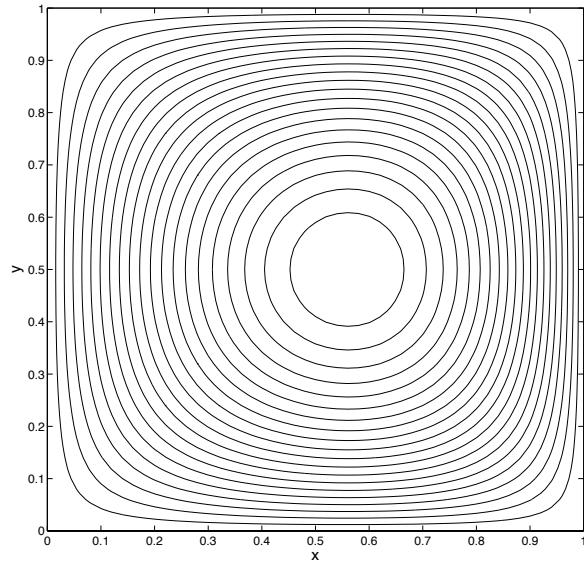
with

$$\bar{\mathbf{u}} = \begin{bmatrix} 2e^x(-1+x)^2x^2(y^2-y)(-1+2y) \\ (-e^x(-1+x)x(-2+x(3+x))(-1+y)^2y^2) \end{bmatrix}$$

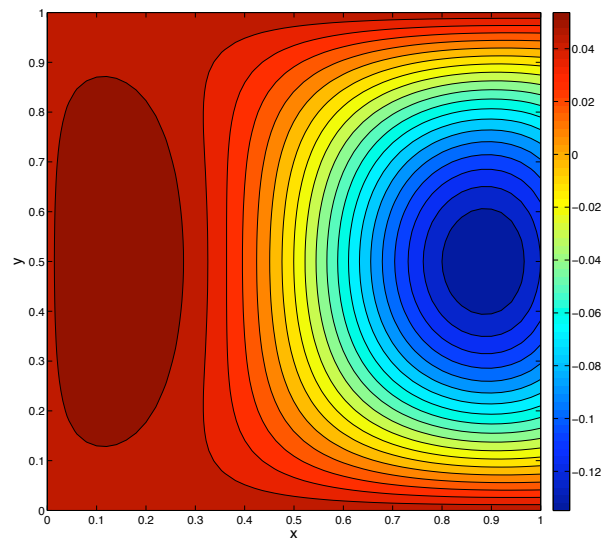
and

$$\bar{p} = (-424 + 156e + (y^2 - y)(-456 + e^x(456 + x^2(228 - 5(y^2 - y))) + 2x(-228 + (y^2 - y)) + 2x^3(-36 + (y^2 - y)) + x^4(12 + (y^2 - y))))).$$

Homogeneous boundary conditions are applied along the boundary  $\partial\Omega$ , and the pressure is enforced to satisfy  $\int_{\Omega} p d\mathbf{x} = 0$ . The unique solution to the generalized Stokes equation with the prescribed forcing is then clearly  $(\mathbf{u}, p) = (\bar{\mathbf{u}}, \bar{p})$ . The streamlines and pressure contours associated with the exact solution are plotted in Figure 6.2. Note from the streamline plot that the velocity solution has a simple vortex structure.



(a)



(b)

Figure 6.2: Generalized Stokes manufactured solution in 2-D: (a) Flow velocity streamlines, (b) Pressure contours.

Table 6.2: Generalized Stokes convergence rates in 2-D:  $Da = 0$

Polynomial degree  $k' = 1$

$h$	1/4	1/8	1/16	1/32	1/64
$\ \mathbf{u} - \mathbf{u}_h\ _{\mathcal{V}(h)}$	7.75e-2	3.96e-2	1.98e-2	9.90e-3	4.95e-3
order	-	0.97	1.00	1.00	1.00
$ \mathbf{u} - \mathbf{u}_h _{\mathbf{H}^1(\Omega)}$	5.48e-2	2.80e-2	1.40e-2	7.00e-3	3.50e-3
order	-	0.97	1.00	1.00	1.00
$\ \mathbf{u} - \mathbf{u}_h\ _{\mathbf{L}^2(\Omega)}$	2.77e-3	8.16e-4	2.28e-4	6.10e-5	1.58e-5
order	-	1.76	1.84	1.90	1.95
$\ p - p_h\ _{L^2(\Omega)}$	5.04e-3	1.38e-3	3.49e-4	8.72e-5	2.18e-5
order	-	1.87	1.98	2.00	2.00

Polynomial degree  $k' = 2$

$h$	1/4	1/8	1/16	1/32	1/64
$\ \mathbf{u} - \mathbf{u}_h\ _{\mathcal{V}(h)}$	1.37e-2	3.30e-3	8.03e-4	1.98e-4	4.92e-5
order	-	2.06	2.04	2.02	2.01
$ \mathbf{u} - \mathbf{u}_h _{\mathbf{H}^1(\Omega)}$	9.70e-3	2.33e-3	5.68e-4	1.40e-4	3.48e-5
order	-	2.06	2.04	2.02	2.01
$\ \mathbf{u} - \mathbf{u}_h\ _{\mathbf{L}^2(\Omega)}$	2.94e-4	3.84e-5	5.03e-6	6.47e-7	8.21e-8
order	-	2.94	2.93	2.96	2.98
$\ p - p_h\ _{L^2(\Omega)}$	1.18e-3	1.19e-4	1.17e-5	1.19e-6	1.27e-7
order	-	3.31	3.35	3.30	3.23

Polynomial degree  $k' = 3$

$h$	1/4	1/8	1/16	1/32	1/64
$\ \mathbf{u} - \mathbf{u}_h\ _{\mathcal{V}(h)}$	1.39e-3	1.81e-4	2.33e-5	3.01e-6	3.85e-7
order	-	2.94	2.96	2.95	2.97
$ \mathbf{u} - \mathbf{u}_h _{\mathbf{H}^1(\Omega)}$	9.83e-4	1.28e-4	1.65e-5	2.10e-6	2.66e-7
order	-	2.94	2.96	2.97	2.98
$\ \mathbf{u} - \mathbf{u}_h\ _{\mathbf{L}^2(\Omega)}$	3.05e-5	2.34e-6	1.59e-7	1.03e-8	6.55e-10
order	-	3.70	3.88	3.95	3.98
$\ p - p_h\ _{L^2(\Omega)}$	1.10e-4	5.64e-6	3.45e-7	2.19e-8	1.39e-9
order	-	4.29	4.03	3.98	3.98

Table 6.3: Generalized Stokes convergence rates in 2-D:  $Da = 1$

Polynomial degree  $k' = 1$

$h$	1/4	1/8	1/16	1/32	1/64
$\ \mathbf{u} - \mathbf{u}_h\ _{\mathcal{V}(h)}$	7.75e-2	3.96e-2	1.98e-2	9.90e-3	4.95e-3
order	-	0.97	1.00	1.00	1.00
$ \mathbf{u} - \mathbf{u}_h _{\mathbf{H}^1(\Omega)}$	5.47e-2	2.80e-2	1.40e-2	7.00e-3	3.50e-3
order	-	0.97	1.00	1.00	1.00
$\ \mathbf{u} - \mathbf{u}_h\ _{\mathbf{L}^2(\Omega)}$	2.75e-3	8.09e-4	2.26e-4	6.05e-5	1.57e-5
order	-	1.76	1.84	1.90	1.95
$\ p - p_h\ _{L^2(\Omega)}$	5.04e-3	1.37e-3	3.48e-4	8.72e-5	2.18e-5
order	-	1.88	1.98	2.00	2.00

Polynomial degree  $k' = 2$

$h$	1/4	1/8	1/16	1/32	1/64
$\ \mathbf{u} - \mathbf{u}_h\ _{\mathcal{V}(h)}$	1.37e-2	3.30e-3	8.03e-4	1.98e-4	4.92e-5
order	-	2.06	2.04	2.02	2.01
$ \mathbf{u} - \mathbf{u}_h _{\mathbf{H}^1(\Omega)}$	9.70e-3	2.33e-3	5.68e-4	1.40e-4	3.48e-5
order	-	2.06	2.04	2.02	2.01
$\ \mathbf{u} - \mathbf{u}_h\ _{\mathbf{L}^2(\Omega)}$	2.94e-4	3.84e-5	5.03e-6	6.47e-7	8.21e-8
order	-	2.94	2.93	2.96	2.98
$\ p - p_h\ _{L^2(\Omega)}$	1.18e-3	1.19e-4	1.17e-5	1.19e-6	1.27e-7
order	-	3.31	3.35	3.30	3.23

Polynomial degree  $k' = 3$

$h$	1/4	1/8	1/16	1/32	1/64
$\ \mathbf{u} - \mathbf{u}_h\ _{\mathcal{V}(h)}$	1.39e-3	1.81e-4	2.35e-5	3.01e-6	3.85e-7
order	-	2.94	2.95	2.96	2.97
$ \mathbf{u} - \mathbf{u}_h _{\mathbf{H}^1(\Omega)}$	9.83e-4	1.28e-4	1.65e-5	2.10e-6	2.66e-7
order	-	2.94	2.96	2.97	2.98
$\ \mathbf{u} - \mathbf{u}_h\ _{\mathbf{L}^2(\Omega)}$	3.05e-5	2.34e-6	1.59e-7	1.03e-8	6.55e-10
order	-	3.70	3.88	3.95	3.98
$\ p - p_h\ _{L^2(\Omega)}$	1.10e-4	5.64e-6	3.45e-7	2.19e-8	1.39e-9
order	-	4.29	4.03	3.98	3.98

Table 6.4: Generalized Stokes convergence rates in 2-D:  $Da = 1000$

Polynomial degree  $k' = 1$

$h$	1/4	1/8	1/16	1/32	1/64
$\ \mathbf{u} - \mathbf{u}_h\ _{\mathcal{V}(h)}$	3.13e-3	1.33e-3	6.36e-4	3.14e-4	1.57e-4
order	-	1.23	1.06	1.02	1.00
$ \mathbf{u} - \mathbf{u}_h _{\mathbf{H}^1(\Omega)}$	5.50e-2	2.78e-2	1.39e-2	6.98e-3	3.49e-3
order	-	0.98	1.00	0.99	1.00
$\ \mathbf{u} - \mathbf{u}_h\ _{\mathbf{L}^2(\Omega)}$	1.93e-3	4.79e-4	1.22e-4	3.20e-5	8.38e-6
order	-	2.01	1.97	1.93	1.93
$\ p - p_h\ _{L^2(\Omega)}$	3.37e-3	7.97e-4	1.96e-4	4.89e-5	1.22e-5
order	-	2.08	2.02	2.00	2.00

Polynomial degree  $k' = 2$

$h$	1/4	1/8	1/16	1/32	1/64
$\ \mathbf{u} - \mathbf{u}_h\ _{\mathcal{V}(h)}$	5.24e-4	1.11e-4	2.58e-5	6.30e-6	1.55e-6
order	-	2.24	2.11	2.03	2.02
$ \mathbf{u} - \mathbf{u}_h _{\mathbf{H}^1(\Omega)}$	9.85e-3	2.32e-3	5.67e-4	1.40e-4	3.48e-5
order	-	2.08	2.03	2.02	2.01
$\ \mathbf{u} - \mathbf{u}_h\ _{\mathbf{L}^2(\Omega)}$	2.83e-4	3.80e-5	5.01e-6	6.46e-7	8.21e-8
order	-	2.90	2.92	2.96	2.98
$\ p - p_h\ _{L^2(\Omega)}$	4.69e-4	5.36e-5	6.42e-6	7.97e-7	9.98e-8
order	-	3.13	3.06	3.01	3.00

Polynomial degree  $k' = 3$

$h$	1/4	1/8	1/16	1/32	1/64
$\ \mathbf{u} - \mathbf{u}_h\ _{\mathcal{V}(h)}$	5.31e-5	6.12e-6	7.57e-7	9.56e-8	1.22e-8
order	-	3.12	3.02	2.99	2.97
$ \mathbf{u} - \mathbf{u}_h _{\mathbf{H}^1(\Omega)}$	9.74e-4	1.26e-4	1.64e-5	2.10e-6	2.66e-7
order	-	2.95	2.94	2.97	2.98
$\ \mathbf{u} - \mathbf{u}_h\ _{\mathbf{L}^2(\Omega)}$	3.04e-5	2.33e-6	1.59e-7	1.03e-8	6.55e-10
order	-	3.71	3.89	3.95	3.98
$\ p - p_h\ _{L^2(\Omega)}$	7.56e-5	4.60e-6	3.19e-7	2.12e-8	1.37e-9
order	-	4.04	3.89	3.91	3.95

For the above constructed solution, we have computed convergence rates for divergence-conforming B-spline discretizations of varying mesh size and polynomial degree. Furthermore, we have computed convergence rates for a variety of Damköhler numbers

$$Da = \frac{\sigma L^2}{\nu}$$

where  $L$  is a length parameter which we henceforth specify as one. These convergence rates are provided in Tables 6.2, 6.3, and 6.4. Note immediately from the tables that our theoretically derived error estimates are confirmed. Second, note that the  $L^2$ -norm of the pressure error optimally converges like  $O(h^{k'+1})$ , which is an improvement over our theoretically derived estimate. Third, note that our methodology is robust with respect to the Damköhler number. That is, the errors for our discretization are virtually independent of the Damköhler number. In fact, our pressure error decreases with increasing Damköhler number. Finally, it should be mentioned that (a) the  $\mathbf{H}^1$  error of the velocity field approaches the  $\mathbf{H}^1$  best approximation error as  $k'$  is increased, and (b) the  $L^2$  error of the pressure field approaches the  $L^2$  best approximation error as  $k'$  is increased.

### 6.6.2 Three-Dimensional Manufactured Solution

As a second numerical experiment, we consider a three-dimensional manufactured solution representing a vortical filament. Let

$$\Omega \equiv (0, 1)^3$$

and

$$\mathbf{f} \equiv \sigma \bar{\mathbf{u}} - \nabla \cdot (2\nu \nabla^s \bar{\mathbf{u}}) + \nabla \bar{p}$$

with

$$\bar{\mathbf{u}} = \text{curl} \bar{\phi},$$

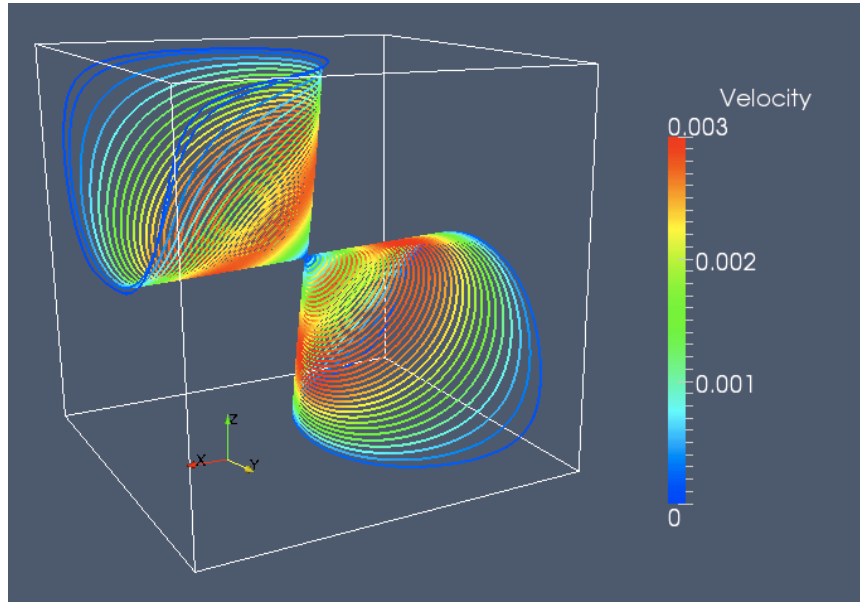


Figure 6.3: Generalized Stokes manufactured solution in 3-D: Flow velocity streamlines colored by velocity magnitude.

$$\bar{\phi} = \begin{bmatrix} x(x-1)y^2(y-1)^2z^2(z-1)^2 \\ 0 \\ x^2(x-1)^2y^2(y-1)^2z(z-1) \end{bmatrix},$$

and

$$\bar{p} = \sin(\pi x) \sin(\pi y) - \frac{4}{\pi^2}.$$

Again, homogeneous boundary conditions are applied along the boundary  $\partial\Omega$ , and the pressure is enforced to satisfy  $\int_{\Omega} p d\mathbf{x} = 0$ . The unique solution to the generalized Stokes equation with the prescribed forcing is then  $(\mathbf{u}, p) = (\bar{\mathbf{u}}, \bar{p})$ . Streamlines associated with the exact solution are plotted in Figure 6.3. Note that the streamlines wrap around a single diagonal vortex filament.

As in the two-dimensional setting, we have computed convergence rates for a variety of divergence-conforming B-spline discretizations and Damköhler num-

Table 6.5: Generalized Stokes convergence rates in 3-D:  $Da = 0$

Polynomial degree  $k' = 1$

$h$	1/2	1/4	1/8	1/16	1/32
$\ \mathbf{u} - \mathbf{u}_h\ _{\mathcal{V}(h)}$	2.59e-2	1.27e-2	5.91e-3	2.81e-3	1.36e-3
order	-	1.03	1.10	1.07	1.05
$\ \mathbf{u} - \mathbf{u}_h\ _{\mathbf{H}^1(\Omega)}$	1.51e-2	7.64e-3	3.77e-3	1.87e-3	9.34e-4
order	-	0.98	1.02	1.01	1.00
$\ \mathbf{u} - \mathbf{u}_h\ _{\mathbf{L}^2(\Omega)}$	1.35e-3	3.68e-4	1.03e-4	2.81e-5	7.40e-6
order	-	1.88	1.84	1.87	1.93
$\ p - p_h\ _{L^2(\Omega)}$	5.41e-2	1.48e-2	3.58e-3	8.85e-4	2.26e-4
order	-	1.87	2.05	2.02	1.97

Polynomial degree  $k' = 2$

$h$	1/2	1/4	1/8	1/16	1/32
$\ \mathbf{u} - \mathbf{u}_h\ _{\mathcal{V}(h)}$	6.50e-3	1.54e-3	4.10e-4	9.51e-5	2.15e-5
order	-	2.08	1.91	2.11	2.15
$\ \mathbf{u} - \mathbf{u}_h\ _{\mathbf{H}^1(\Omega)}$	3.71e-3	9.90e-4	2.79e-4	6.59e-5	1.50e-5
order	-	1.91	1.83	2.08	2.14
$\ \mathbf{u} - \mathbf{u}_h\ _{\mathbf{L}^2(\Omega)}$	1.97e-4	4.25e-5	7.38e-6	8.67e-7	9.18e-8
order	-	2.21	2.53	3.09	3.23
$\ p - p_h\ _{L^2(\Omega)}$	1.50e-2	1.59e-3	2.00e-4	2.56e-5	3.26e-6
order	-	3.24	2.99	2.97	2.97

Table 6.6: Generalized Stokes convergence rates in 3-D:  $Da = 1$

Polynomial degree  $k' = 1$

$h$	1/2	1/4	1/8	1/16	1/32
$\ \mathbf{u} - \mathbf{u}_h\ _{\mathcal{V}(h)}$	2.59e-2	1.28e-2	5.91e-3	2.81e-3	1.36e-3
order	-	1.02	1.11	1.07	1.05
$\ \mathbf{u} - \mathbf{u}_h\ _{\mathbf{H}^1(\Omega)}$	1.51e-2	7.64e-3	3.77e-3	1.87e-3	9.33e-4
order	-	0.98	1.02	1.01	1.00
$\ \mathbf{u} - \mathbf{u}_h\ _{\mathbf{L}^2(\Omega)}$	1.34e-3	3.66e-4	1.02e-4	2.79e-5	7.34e-6
order	-	1.87	1.84	1.87	1.93
$\ p - p_h\ _{L^2(\Omega)}$	5.41e-2	1.48e-2	3.58e-3	8.85e-4	2.21e-4
order	-	1.87	2.05	2.02	2.00

Polynomial degree  $k' = 2$

$h$	1/2	1/4	1/8	1/16	1/32
$\ \mathbf{u} - \mathbf{u}_h\ _{\mathcal{V}(h)}$	6.50e-3	1.54e-3	4.10e-4	9.50e-5	2.15e-5
order	-	2.08	1.91	2.11	2.14
$\ \mathbf{u} - \mathbf{u}_h\ _{\mathbf{H}^1(\Omega)}$	3.71e-3	9.89e-4	2.79e-4	6.59e-5	1.50e-5
order	-	1.91	1.83	2.08	2.14
$\ \mathbf{u} - \mathbf{u}_h\ _{\mathbf{L}^2(\Omega)}$	1.97e-4	4.24e-5	7.38e-6	8.64e-7	9.18e-8
order	-	2.22	2.52	3.09	3.23
$\ p - p_h\ _{L^2(\Omega)}$	1.50e-2	1.59e-3	2.00e-4	2.56e-5	3.26e-6
order	-	3.24	2.99	2.97	2.97

Table 6.7: Generalized Stokes convergence rates in 3-D:  $Da = 1000$

Polynomial degree  $k' = 1$

$h$	1/2	1/4	1/8	1/16	1/32
$\ \mathbf{u} - \mathbf{u}_h\ _{\mathcal{V}(h)}$	1.55e-3	5.16e-4	2.04e-4	9.07e-5	4.32e-5
order	-	1.59	1.34	1.17	1.07
$\ \mathbf{u} - \mathbf{u}_h\ _{\mathbf{H}^1(\Omega)}$	1.56e-2	7.57e-3	3.74e-3	1.86e-3	9.31e-4
order	-	1.04	1.02	1.01	1.00
$\ \mathbf{u} - \mathbf{u}_h\ _{\mathbf{L}^2(\Omega)}$	1.16e-3	2.58e-4	6.29e-5	1.59e-5	4.11e-6
order	-	2.17	2.04	1.98	1.95
$\ p - p_h\ _{L^2(\Omega)}$	5.41e-2	1.48e-2	3.57e-3	8.84e-4	2.20e-4
order	-	1.87	2.05	2.01	2.01

Polynomial degree  $k' = 2$

$h$	1/2	1/4	1/8	1/16	1/32
$\ \mathbf{u} - \mathbf{u}_h\ _{\mathcal{V}(h)}$	2.98e-4	5.25e-5	1.06e-5	2.42e-6	5.84e-7
order	-	2.50	2.31	2.13	2.05
$\ \mathbf{u} - \mathbf{u}_h\ _{\mathbf{H}^1(\Omega)}$	3.79e-3	8.56e-4	2.08e-4	5.14e-5	1.28e-5
order	-	2.15	2.04	2.02	2.01
$\ \mathbf{u} - \mathbf{u}_h\ _{\mathbf{L}^2(\Omega)}$	1.88e-4	2.84e-5	3.74e-6	4.97e-7	6.06e-8
order	-	2.73	2.93	2.91	3.04
$\ p - p_h\ _{L^2(\Omega)}$	1.50e-2	1.59e-3	2.00e-4	2.56e-5	3.26e-6
order	-	3.24	2.99	2.97	2.97

bers

$$Da = \frac{\sigma L^2}{\nu}$$

where  $L$  is a length parameter which we again specify as equal to one. These convergence rates are summarized in Tables 6.5, 6.6, and 6.7. Note immediately from the tables that our theoretically derived error estimates are confirmed. Second, note that the  $L^2$ -norm of the pressure error optimally converges like  $O(h^{k'+1})$ , which is an improvement over our theoretically derived estimate. Third, note that our method is robust with respect to the Damköhler number. Finally, let us remark the exact velocity field is recovered for discretizations of degree  $k' \geq 3$ .

### 6.6.3 Two-Dimensional Problem with a Singular Solution

To examine how our discretization performs in the presence of singularities, we consider Stokes flow in the L-shaped domain  $\Omega = (-1, 1)^2 \setminus ([0, 1) \times (-1, 0])$ . The flow problem in consideration is depicted in Figure 6.4(a). Homogeneous Dirichlet boundary conditions are applied along  $\Gamma_D = \{(0, y) : y \in (-1, 0)\} \cup \{(x, 0) : x \in (0, 1)\}$ , Neumann boundary conditions are applied along  $\Gamma_N = \partial\Omega \setminus \Gamma_D$ , and we set  $\sigma = 0$ ,  $\nu = 1$ , and  $\mathbf{f} = \mathbf{0}$ . As in [186], the Neumann boundary conditions are chosen such that the exact solution is

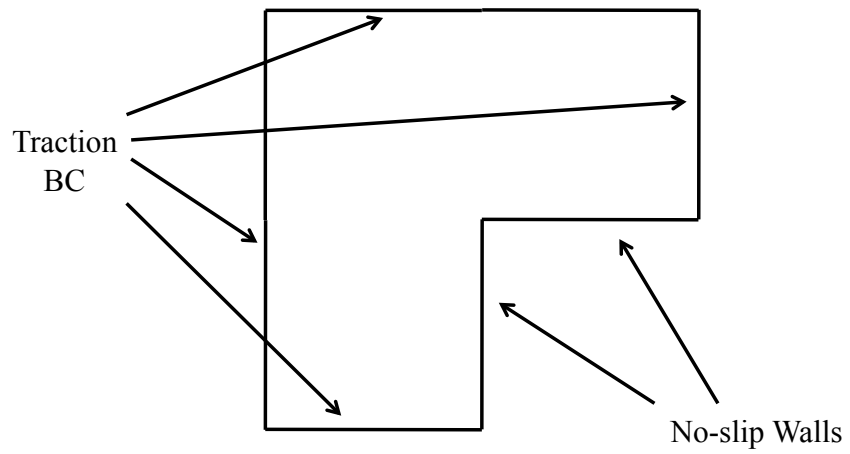
$$\mathbf{u} = \begin{bmatrix} r^\lambda((1 + \lambda) \sin(\theta)\psi(\theta) + \cos(\theta)\psi'(\theta)) \\ r^\lambda(-(1 + \lambda) \cos(\theta)\psi(\theta) + \sin(\theta)\psi'(\theta)) \end{bmatrix}$$

and

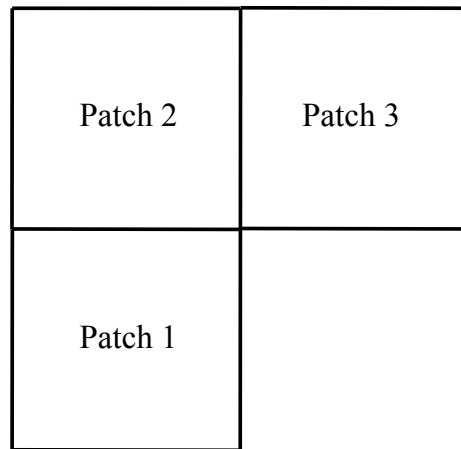
$$p = -r^{\lambda-1} ((1 + \lambda)^2 \phi'(\theta) + \phi'''(\theta)) / (1 - \lambda)$$

where  $(r, \theta)$  are polar coordinates with respect to the origin  $(0, 0)$ ,

$$\begin{aligned} \phi = & \sin((1 + \lambda)\theta) \cos(\lambda\omega) / (1 + \lambda) - \cos((1 + \lambda)\theta) \\ & - \sin((1 - \lambda)\theta) \cos(\lambda\omega) / (1 - \lambda) + \cos((1 - \lambda)\theta), \end{aligned}$$

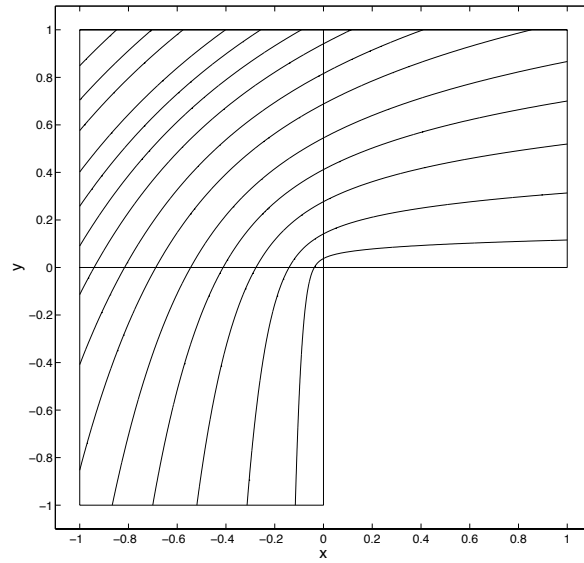


(a)

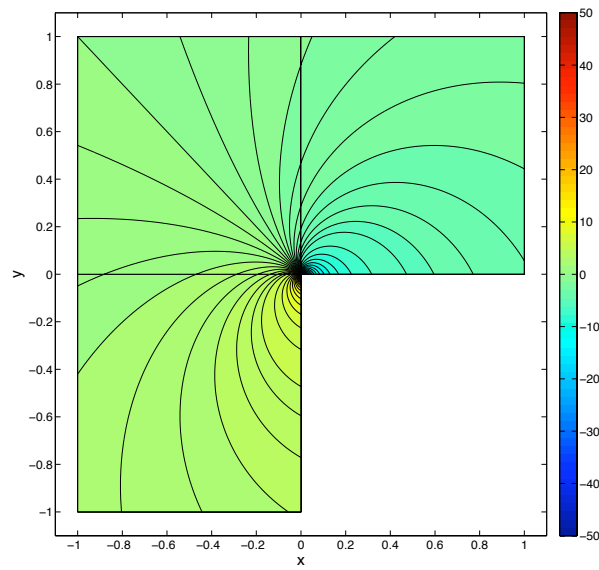


(b)

Figure 6.4: Singular Stokes solution in 2-D: (a) Problem setup, (b) Multi-patch construction.



(a)



(b)

Figure 6.5: Singular Stokes solution in 2-D: (a) Flow velocity streamlines, (b) Pressure contours.

Table 6.8: Singular Stokes convergence rates in 2-D

Polynomial degree  $k' = 1$

$h$	1/2	1/4	1/8	1/16	1/32
$\ \mathbf{u} - \mathbf{u}_h\ _{\mathcal{V}(h)}$	2.29e0	1.61e0	1.13e0	7.73e-1	5.33e-1
order	-	0.51	0.51	0.55	0.54
$\ p - p_h\ _{L^2(\Omega)}$	1.30e0	9.40e-1	6.62e-1	4.66e-1	3.32e-1
order	-	0.47	0.51	0.51	0.49

Polynomial degree  $k' = 2$

$h$	1/2	1/4	1/8	1/16	1/32
$\ \mathbf{u} - \mathbf{u}_h\ _{\mathcal{V}(h)}$	1.50e0	1.05e0	7.25e-1	5.00e-1	3.46e-1
order	-	0.51	0.53	0.54	0.53
$\ p - p_h\ _{L^2(\Omega)}$	8.56e-1	6.39e-1	4.50e-1	3.20e-1	2.36e-1
order	-	0.42	0.51	0.49	0.44

Polynomial degree  $k' = 3$

$h$	1/2	1/4	1/8	1/16	1/32
$\ \mathbf{u} - \mathbf{u}_h\ _{\mathcal{V}(h)}$	1.15e0	8.36e-1	5.79e-1	4.00e-1	2.78e-1
order	-	0.46	0.53	0.53	0.52
$\ p - p_h\ _{L^2(\Omega)}$	6.05e-1	4.90e-1	3.54e-1	2.57e-1	1.91e-1
order	-	0.30	0.47	0.46	0.43

$\omega = \frac{3}{2}\phi$ , and  $\lambda \approx 0.54448373678246$  is the smallest positive root of

$$\sin(\lambda\omega) + \lambda \sin(\omega) = 0.$$

This singular solution is illustrated in Figure 6.5. Note that  $(\mathbf{u}, p) \in \mathbf{H}^{1+\lambda}(\Omega) \times H^\lambda(\Omega)$ . This is the strongest corner singularity for the Stokes operator in the L-shaped domain, and, as such, this numerical example models typical singular behavior observed in the vicinity of reentrant corners.

To compute this flow example using our discretization technique, we must resort to a multi-patch construction. We utilize the three-patch construction illustrated in Figure 6.4(b). Each patch is mapped from the parametric domain using an affine parametrization. As discussed in Section 6.5, we impose normal continuity strongly between patches and tangential continuity weakly using the symmetric interior penalty method. We have computed convergence rates for a variety of divergence-conforming B-spline discretizations and reported our results in Table 6.8. Note from the table that the energy norm of the velocity field and the  $L^2$ -norm of the pressure field are approaching the optimal convergence rates of  $O(h^\lambda)$  as  $h \rightarrow 0$ . Furthermore, note the velocity and pressure errors improve with increasing polynomial degree. This is somewhat counterintuitive as we also increase smoothness with polynomial degree. This being said, such a property has also been observed in the context of Maxwell’s equations [40]. While we only employed uniform meshes for the computations reported here, one could of course obtain more satisfactory results with geometrically graded meshes [92, 94].

#### 6.6.4 Cylindrical Couette Flow

Couette flow is often used as a “sanity check” for Stokes and Navier-Stokes discretizations. Cylindrical Couette flow is a more realistic problem which de-

scribes the flow between two concentric rotating cylinders. Here, we consider generalized Stokes flow between a fixed outer cylinder and a rotating inner cylinder. The problem setup is illustrated in Figure 6.6. No external forcing is applied. In the absence of Darcy drag forces (*i.e.*,  $\sigma = 0$ ), the velocity field for this flow assumes the form

$$\mathbf{u} = \begin{bmatrix} u_\theta(r) \sin(\theta) \\ u_\theta(r) \cos(\theta) \end{bmatrix}$$

where

$$u_\theta(r) = Ar + \frac{B}{r},$$

$(r, \theta)$  are polar coordinates with respect to the center of the cylinders, and

$$A = -\Omega_{in} \frac{\delta^2}{1 - \delta^2}, \quad B = \Omega_{in} \frac{r_{in}^2}{(1 - \delta^2)}, \quad \Omega_{in} = \frac{U}{r_{in}}, \quad \delta = \frac{r_{in}}{r_{out}}.$$

We have depicted this velocity field in Figure 6.7(a). In the presence of Darcy drag forces, the character of the flow field changes considerably. Notably, the motion of the fluid is confined to a small boundary layer attached to the inner cylinder. This motion explicitly takes the form

$$\mathbf{u} = \begin{bmatrix} u_\theta(r) \sin(\theta) \\ u_\theta(r) \cos(\theta) \end{bmatrix}$$

where

$$u_\theta(r) = U \frac{I_1(\gamma r) K_1(\gamma r_{out}) - I_1(\gamma r_{out}) K_1(\gamma r)}{I_1(\gamma r_{in}) K_1(\gamma r_{out}) - I_1(\gamma r_{out}) K_1(\gamma r_{in})},$$

$\gamma = \sqrt{\sigma/\nu}$ , and  $I_1$  and  $K_1$  are modified Bessel functions of the first and second kind respectively. Note that  $\gamma^{-1}$  acts as a length scale, and the width of the boundary layer attached to the inner cylinder is proportional to  $\gamma^{-1}$ . We have depicted a velocity field corresponding to  $\gamma = \sqrt{50}$  in Figure 6.7(b). Finally, under the constraint that

$$\int_{\Omega} p d\mathbf{x} = 0,$$

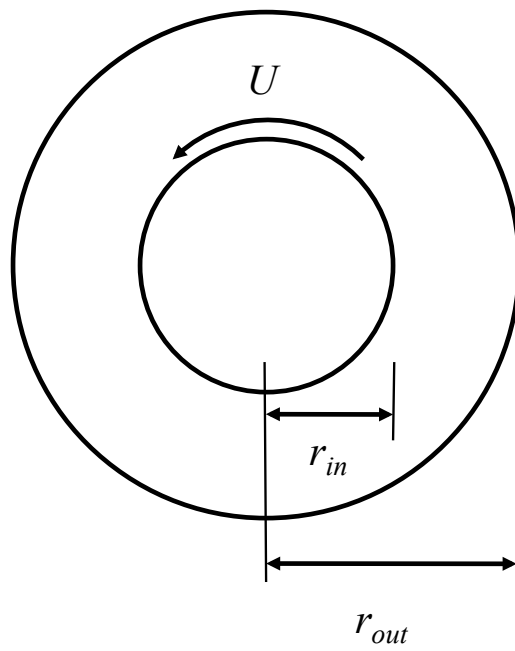
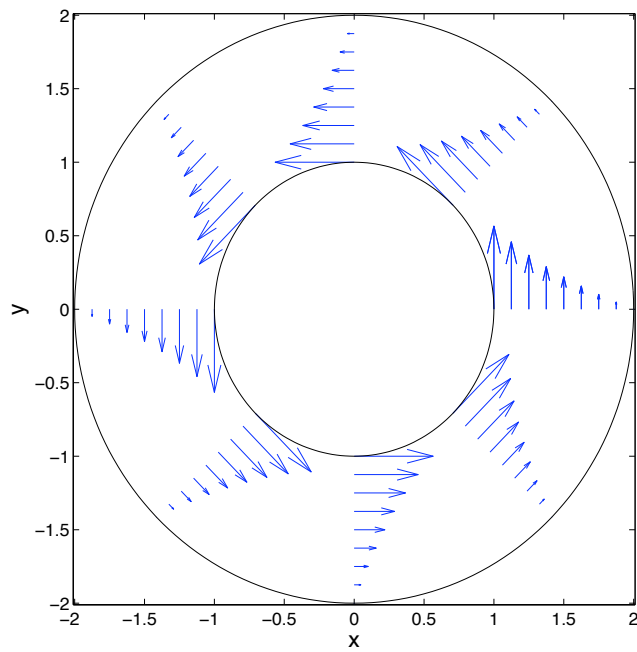
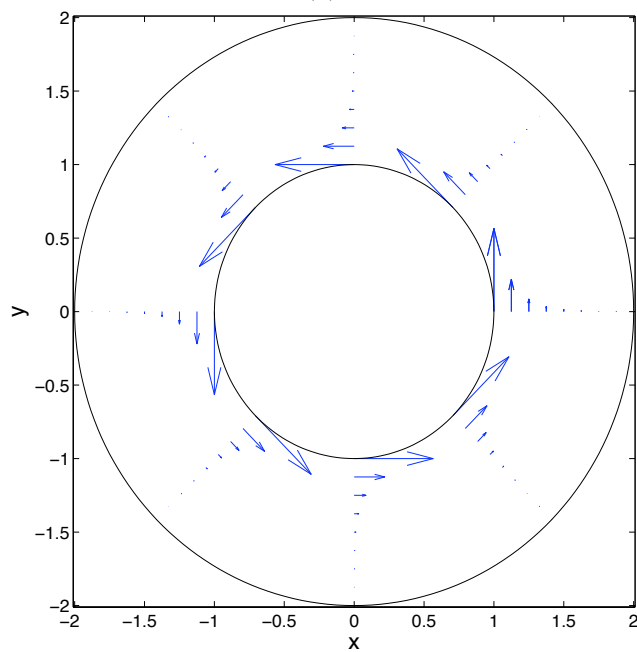


Figure 6.6: Cylindrical Couette flow: Problem setup.

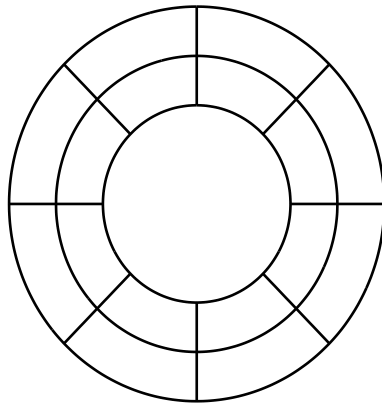


(a)

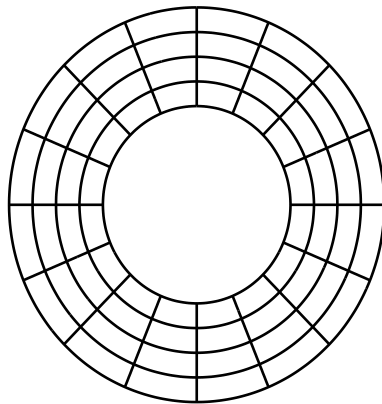


(b)

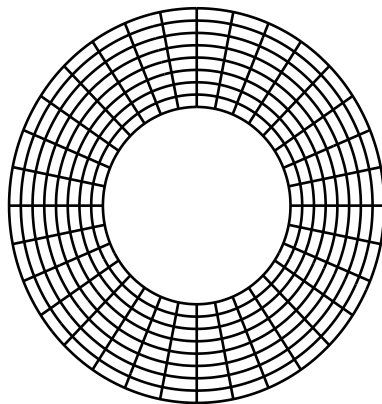
Figure 6.7: Cylindrical Couette flow: (a) Flow velocity arrows for  $\gamma = 0$ , (b) Flow velocity arrows for  $\gamma = \sqrt{50}$ .



$$h/h_0 = 1/2$$



$$h/h_0 = 1/4$$



$$h/h_0 = 1/8$$

Figure 6.8: Cylindrical Couette flow: Sequence of polar meshes.

the pressure field is identically zero for both the Stokes limit as well as the generalized Stokes setting. In what follows, we assume  $r_{in} = 1$ ,  $r_{out} = 2$ , and  $U = 1$ .

We have computed convergence rates for a variety of divergence-conforming B-spline discretizations and for  $\gamma = 0$  and  $\gamma = \sqrt{50}$ . To represent the annular domain in our computations, we employed the polar mapping

$$\mathbf{F}(\xi_1, \xi_2) = \begin{bmatrix} ((r_{out} - r_{in})\xi_2 + r_{in}) \sin(2\pi\xi_1) \\ ((r_{out} - r_{in})\xi_2 + r_{in}) \cos(2\pi\xi_1) \end{bmatrix}, \forall (\xi_1, \xi_2) \in (0, 1)^2 \quad (6.70)$$

and periodic B-splines of maximal continuity in the  $\xi_1$ -direction (see Section 2 of [73]). It should be emphasized that we do not use the polar form of the generalized Stokes equations. Rather, we utilize the polar mapping to define our divergence-conforming B-splines in physical space and then employ the Cartesian-based variational formulation discussed in this chapter. The results of our computations are summarized in Tables 6.9 and 6.10. Note from the tables that all of our theoretically derived error estimates are confirmed, though the results corresponding to  $\gamma = \sqrt{50}$  have a more substantial pre-asymptotic range due to the presence of a boundary layer. Additionally, note that we obtain null pressure fields and axisymmetric velocity fields with null radial component.

We repeated our computations using the multi-patch NURBS construction illustrated in Figure 6.9. Each of the four patches are built through a sufficient rotation of the canonical quadratic single-element NURBS patch described in Figure 6.10, and we have tabulated the location and weights of the control points of the canonical quadratic patch in Figure 6.11. The resulting NURBS parametrization is identical to the polar parametrization in the radial direction and different in the angular direction. We define our B-spline discretization scheme on the multi-patch NURBS construction using the procedure outlined in Section 6.5 with normal continuity being enforced strongly between patches and tangential continuity being

Table 6.9: Cylindrical Couette flow convergence rates:  $\gamma = 0$

Polynomial degree  $k' = 1$

$h/h_0$	1/2	1/4	1/8	1/16	1/32
$\ \mathbf{u} - \mathbf{u}_h\ _{\mathcal{V}(h)}$	5.42e-1	2.63e-1	1.26e-1	6.12e-2	2.99e-2
order	-	1.04	1.06	1.04	1.03
$\ \mathbf{u} - \mathbf{u}_h\ _{\mathbf{H}^1(\Omega)}$	4.48e-1	2.32e-1	1.17e-1	5.86e-2	2.93e-2
order	-	0.95	0.99	1.00	1.00
$\ \mathbf{u} - \mathbf{u}_h\ _{\mathbf{L}^2(\Omega)}$	5.00e-2	1.53e-2	4.28e-3	1.14e-3	2.94e-4
order	-	1.71	1.84	1.91	1.96
$\ u_r - (u_r)_h\ _{L^2(\Omega)}$	0	0	0	0	0
$\ p - p_h\ _{L^2(\Omega)}$	0	0	0	0	0

Polynomial degree  $k' = 2$

$h/h_0$	1/2	1/4	1/8	1/16	1/32
$\ \mathbf{u} - \mathbf{u}_h\ _{\mathcal{V}(h)}$	9.77e-2	2.42e-2	5.64e-3	1.32e-3	3.14e-4
order	-	2.01	2.10	2.10	2.07
$\ \mathbf{u} - \mathbf{u}_h\ _{\mathbf{H}^1(\Omega)}$	7.68e-2	2.00e-2	4.92e-3	1.21e-3	2.99e-4
order	-	1.94	2.02	2.02	2.02
$\ \mathbf{u} - \mathbf{u}_h\ _{\mathbf{L}^2(\Omega)}$	4.43e-3	6.03e-4	8.13e-5	1.07e-5	1.38e-6
order	-	2.88	2.89	2.93	2.95
$\ u_r - (u_r)_h\ _{L^2(\Omega)}$	0	0	0	0	0
$\ p - p_h\ _{L^2(\Omega)}$	0	0	0	0	0

Polynomial degree  $k' = 3$

$h/h_0$	1/2	1/4	1/8	1/16	1/32
$\ \mathbf{u} - \mathbf{u}_h\ _{\mathcal{V}(h)}$	2.01e-2	2.67e-3	3.27e-4	4.01e-5	4.98e-6
order	-	2.91	3.03	3.03	3.01
$\ \mathbf{u} - \mathbf{u}_h\ _{\mathbf{H}^1(\Omega)}$	1.52e-2	2.13e-3	2.84e-4	3.72e-5	4.80e-6
order	-	2.84	2.91	2.93	2.95
$\ \mathbf{u} - \mathbf{u}_h\ _{\mathbf{L}^2(\Omega)}$	6.59e-4	5.69e-5	4.82e-6	3.50e-7	2.33e-8
order	-	3.53	3.56	3.78	3.91
$\ u_r - (u_r)_h\ _{L^2(\Omega)}$	0	0	0	0	0
$\ p - p_h\ _{L^2(\Omega)}$	0	0	0	0	0

Table 6.10: Cylindrical Couette flow convergence rates:  $\gamma = \sqrt{50}$

Polynomial degree  $k' = 1$

$h/h_0$	1/2	1/4	1/8	1/16	1/32
$\ \mathbf{u} - \mathbf{u}_h\ _{\mathcal{V}(h)}$	8.06e-1	4.59e-1	2.30e-1	1.10e-1	5.28e-2
order	-	0.81	1.00	1.06	1.06
$\ \mathbf{u} - \mathbf{u}_h\ _{\mathbf{H}^1(\Omega)}$	3.75e0	2.44e0	1.35e0	6.93e-1	3.49e-1
order	-	0.62	0.85	0.96	0.99
$\ \mathbf{u} - \mathbf{u}_h\ _{\mathbf{L}^2(\Omega)}$	2.43e-1	9.90e-2	3.16e-2	9.24e-3	2.56e-3
order	-	1.30	1.65	1.77	1.85
$\ u_r - (u_r)_h\ _{L^2(\Omega)}$	0	0	0	0	0
$\ p - p_h\ _{L^2(\Omega)}$	0	0	0	0	0

Polynomial degree  $k' = 2$

$h/h_0$	1/2	1/4	1/8	1/16	1/32
$\ \mathbf{u} - \mathbf{u}_h\ _{\mathcal{V}(h)}$	3.97e-1	1.30e-1	3.28e-2	7.56e-3	1.74e-3
order	-	1.61	1.99	2.12	2.12
$\ \mathbf{u} - \mathbf{u}_h\ _{\mathbf{H}^1(\Omega)}$	1.96e0	6.99e-1	1.86e-1	4.57e-2	1.12e-2
order	-	1.49	1.91	2.03	2.03
$\ \mathbf{u} - \mathbf{u}_h\ _{\mathbf{L}^2(\Omega)}$	9.86e-2	2.00e-2	2.73e-3	3.66e-4	4.86e-5
order	-	2.30	2.87	2.90	2.91
$\ u_r - (u_r)_h\ _{L^2(\Omega)}$	0	0	0	0	0
$\ p - p_h\ _{L^2(\Omega)}$	0	0	0	0	0

Polynomial degree  $k' = 3$

$h/h_0$	1/2	1/4	1/8	1/16	1/32
$\ \mathbf{u} - \mathbf{u}_h\ _{\mathcal{V}(h)}$	1.69e-1	3.15e-2	4.01e-3	4.80e-4	5.86e-5
order	-	2.42	2.97	3.06	3.03
$\ \mathbf{u} - \mathbf{u}_h\ _{\mathbf{H}^1(\Omega)}$	8.54e-1	1.67e-1	2.25e-2	2.95e-3	3.86e-4
order	-	2.35	2.89	2.93	2.93
$\ \mathbf{u} - \mathbf{u}_h\ _{\mathbf{L}^2(\Omega)}$	3.31e-2	3.56e-3	3.03e-4	2.55e-5	1.83e-6
order	-	3.22	3.55	3.57	3.80
$\ u_r - (u_r)_h\ _{L^2(\Omega)}$	0	0	0	0	0
$\ p - p_h\ _{L^2(\Omega)}$	0	0	0	0	0

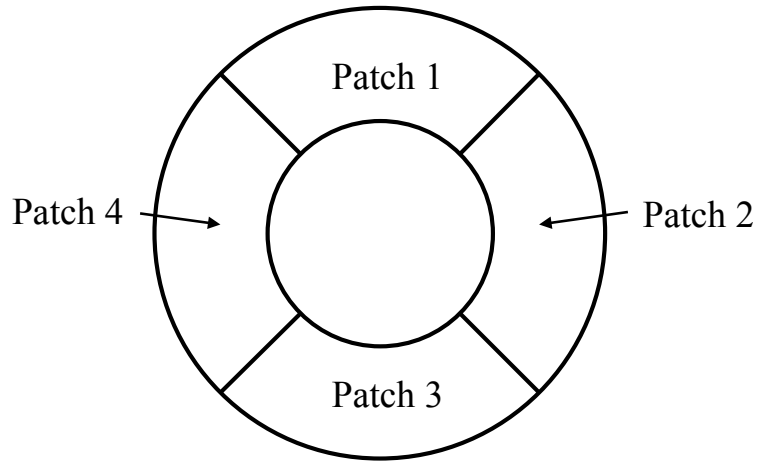


Figure 6.9: Cylindrical Couette flow: NURBS multi-patch construction

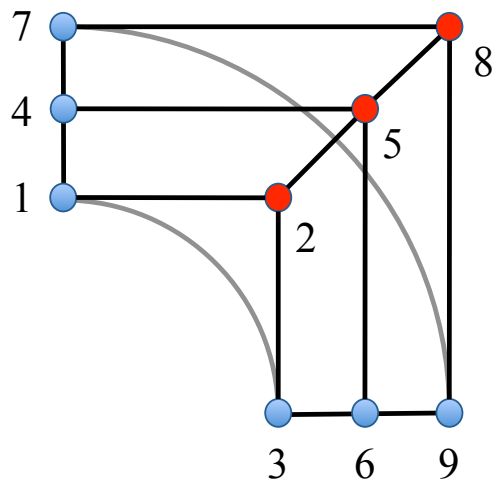


Figure 6.10: Cylindrical Couette flow: Patch template control points

Table 6.11: Cylindrical Couette flow: Patch template control points.

Control Point	$x$	$y$	$w$
1	0	1	1
2	1	1	$1/\sqrt{2}$
3	1	0	1
4	0	$3/2$	1
5	$3/2$	$3/2$	$1/\sqrt{2}$
6	$3/2$	0	1
7	0	2	1
8	2	2	$1/\sqrt{2}$
9	2	0	1

enforced weakly. Surprisingly, we found we obtained exactly the same velocity and pressure fields using the multi-patch NURBS construction as we did with the polar mapping. This property is purely a consequence of the Piola transform. To shed some light on this observation, let us consider a parametric velocity field of the form  $\widehat{\mathbf{v}} = \{v(\xi_2), 0\}^T$ . Then, the image of this velocity field under the Piola transform, denoted as  $\mathbf{v}$ , has the property that

$$\operatorname{div} \mathbf{v} = \frac{1}{J} \widehat{\operatorname{div}} \widehat{\mathbf{v}} = 0$$

where  $J$  is the determinant of the Jacobian matrix  $D\mathbf{F}$ . Moreover, the vector  $\mathbf{v}$  is oriented in the direction of parametric lines defined by  $\xi_2 = C$  where  $C$  is an arbitrary constant. Hence, if  $\xi_1$  represents the angular direction and  $\xi_2$  represents the radial direction, this implies that divergence-free lateral velocity fields in parametric space are mapped to axisymmetric angular velocity fields in physical space regardless of the specification of  $\mathbf{F}$ . Unfortunately, this argument applies only to angular velocity fields and we are not generally able to obtain axisymmetric pressure and radial velocity fields using the multi-patch NURBS construction.

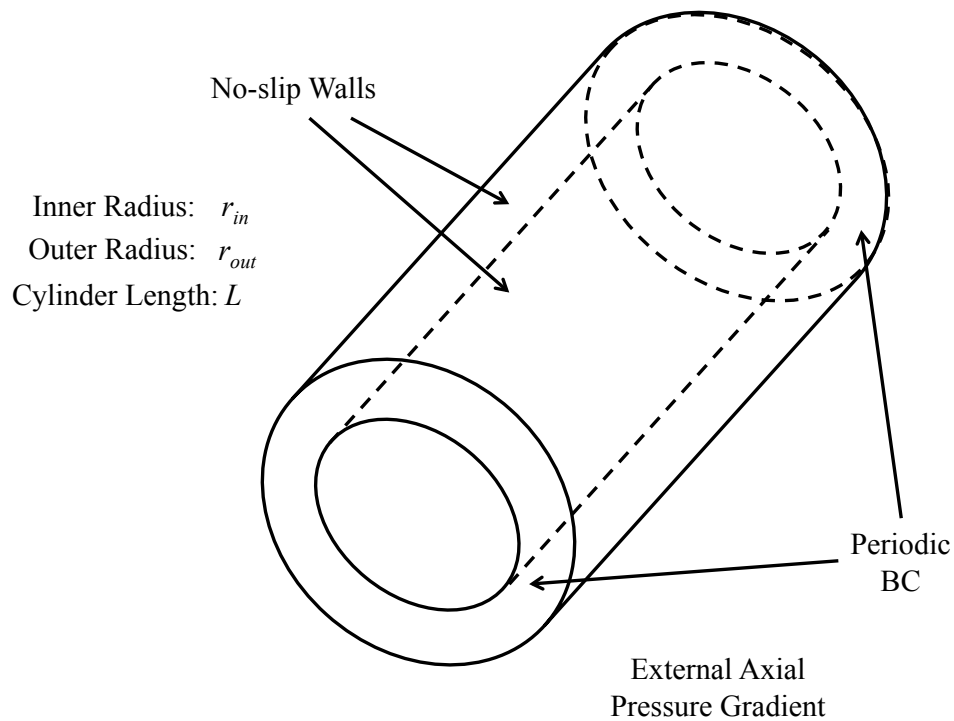


Figure 6.11: Annular Poiseuille flow: Problem setup.

### 6.6.5 Annular Poiseuille Flow

Poiseuille flow is another problem which is often utilized as a “sanity check” for Stokes and Navier-Stokes discretizations. Here, we consider generalized Stokes Poiseuille flow of a viscous fluid between two concentric cylinders. The problem setup is illustrated in Figure 6.11. No-slip and no-penetration boundary conditions are imposed along the cylinder surfaces, and periodic boundary conditions are imposed along the axial direction. An external axial pressure gradient is applied to drive the fluid. In the absence of Darcy drag forces, the velocity field for annular

Poiseuille flow assumes the form

$$\mathbf{u} = \begin{bmatrix} 0 \\ 0 \\ u_z(r) \end{bmatrix}$$

where

$$u_z(r) = -\frac{\Delta p}{4\nu L} \left( r_{in}^2 - r^2 + \frac{r_{out}^2 - r_{in}^2}{\ln(r_{out}/r_{in})} \ln(r/r_{in}) \right)$$

$(r, \theta)$  are polar coordinates with respect to the center of the cylinders, and  $-\Delta p/L$  is the applied pressure gradient. In the presence of Darcy drag, the velocity field takes the form

$$\mathbf{u} = \begin{bmatrix} 0 \\ 0 \\ u_z(r) \end{bmatrix}$$

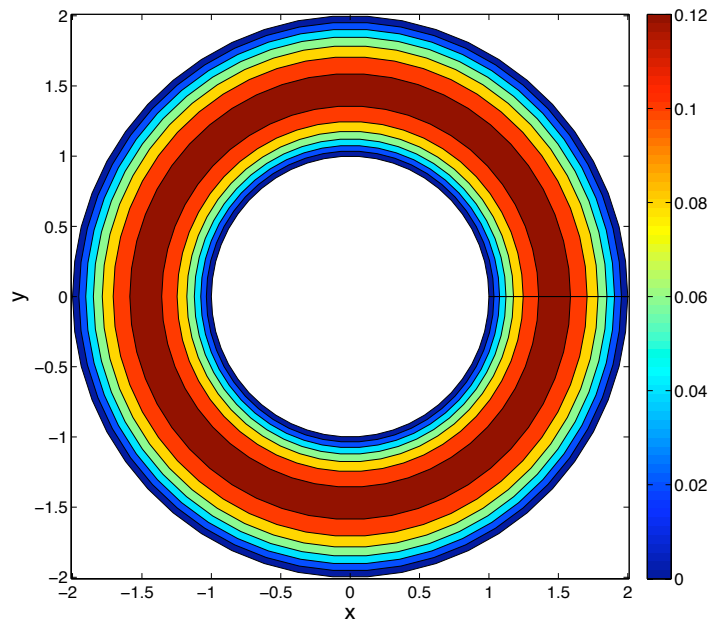
where

$$u_z(r) = -\frac{\Delta p}{\sigma L} \left( \frac{K_0(\gamma r) (I_0(\gamma r_{out}) - I_0(\gamma r_{in})) - I_0(\gamma r) (K_0(\gamma r_{out}) - K_0(\gamma r_{in}))}{K_0(\gamma r_{out})I_0(\gamma r_{in}) - K_0(\gamma r_{in})I_0(\gamma r_{out})} \right) - \frac{\Delta p}{\sigma L},$$

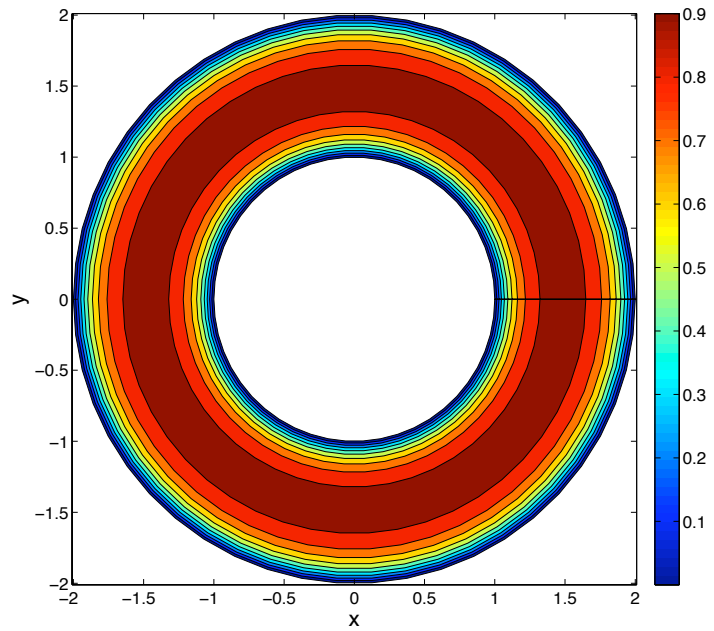
$\gamma = \sqrt{\sigma/\nu}$ , and  $I_0$  and  $K_0$  are modified Bessel functions of the first and second kind respectively. We have illustrated velocity fields corresponding to  $\gamma = 0$  and  $\gamma = \sqrt{50}$  in Figure 6.12. As was the case for cylindrical Couette flow,  $\gamma^{-1}$  acts as a length scale, and there is a boundary layer attached to the inner cylinder with width proportional to  $\gamma^{-1}$ . Finally, under the constraint that

$$\int_{\Omega} p d\mathbf{x} = 0,$$

the pressure field is identically zero for both the Stokes limit as well as the generalized Stokes setting. In what follows, we assume  $r_{in} = 1$ ,  $r_{out} = 2$ ,  $L = 1$ , and  $\Delta p = -1$ .



(a)



(b)

Figure 6.12: Annular Poiseuille flow: Axial velocity contours along an axial slice for (a)  $\gamma = 0$  and (b)  $\gamma = \sqrt{50}$ .

We have computed convergence rates for a variety of divergence-conforming B-spline discretizations and for  $\gamma = 0$  and  $\gamma = \sqrt{50}$ . We have employed both the polar mapping and the NURBS multi-patch construction described in the previous subsection to represent the annular domain in our computations with the axial direction parametrized using a simple linear mapping. Periodic B-splines of maximal continuity were employed in the axial direction. The results of our computations for  $\gamma = 0$  are summarized in Tables 6.12 and 6.13. Note immediately that all of our theoretically derived error estimates are confirmed. Additionally, note that we obtain null pressure fields, radial velocity fields, and angular velocity fields for all cases considered. This being said, observe that we obtain slightly smaller axial velocity errors with the polar mapping than we do with the NURBS multi-patch construction. This is because we maintain exact axisymmetry with the polar mapping but not with the NURBS multi-patch construction. The results of our computations for  $\gamma = \sqrt{50}$  are summarized in Tables 6.14 and 6.15. Again, note that our theoretically derived error estimates are confirmed, and our results for the polar mapping induce slightly smaller axial velocity errors than our results for the NURBS multi-patch construction.

## 6.7 Benchmark Problems

In this section, we investigate the effectiveness of our methodology as applied to a collection of Stokes benchmark problems: two-dimensional lid-driven cavity flow, three-dimensional lid-driven cavity flow, and flow over a backwards-facing step. In addition, we investigate the effectiveness of our methodology for a Darcy-dominated generalized Stokes flow problem characterized by sharp boundary layers. As in the last subsection, we choose Nitsche's penalty constant as  $C_{pen} = 5(k' + 1)$  in all of the following numerical tests, and we employ uniform

Table 6.12: Annular Poiseuille flow convergence rates for  $\gamma = 0$ : Polar meshes

Polynomial degree  $k' = 1$

$h/h_0$	1/2	1/4	1/8	1/16	1/32
$\ \mathbf{u} - \mathbf{u}_h\ _{\mathcal{V}(h)}$	5.30e-1	2.47e-1	1.19e-1	5.80e-2	2.86e-2
order	-	1.10	1.05	1.04	1.02
$\ \mathbf{u} - \mathbf{u}_h\ _{\mathbf{H}^1(\Omega)}$	4.56e-1	2.28e-1	1.14e-1	5.67e-2	2.83e-2
order	-	1.00	1.00	1.01	1.00
$\ \mathbf{u} - \mathbf{u}_h\ _{L^2(\Omega)}$	5.49e-2	1.62e-2	4.34e-3	1.12e-3	2.84e-4
order	-	1.76	1.90	1.95	1.98
$\ u_r - (u_r)_h\ _{L^2(\Omega)}$	0	0	0	0	0
$\ u_\theta - (u_\theta)_h\ _{L^2(\Omega)}$	0	0	0	0	0
$\ p - p_h\ _{L^2(\Omega)}$	0	0	0	0	0

Polynomial degree  $k' = 2$

$h/h_0$	1/2	1/4	1/8	1/16	1/32
$\ \mathbf{u} - \mathbf{u}_h\ _{\mathcal{V}(h)}$	5.67e-2	1.23e-2	2.83e-3	6.73e-4	1.64e-4
order	-	2.20	2.12	2.07	2.04
$\ \mathbf{u} - \mathbf{u}_h\ _{\mathbf{H}^1(\Omega)}$	4.49e-2	1.07e-2	2.61e-3	6.45e-4	1.60e-4
order	-	2.07	2.04	2.02	2.01
$\ \mathbf{u} - \mathbf{u}_h\ _{L^2(\Omega)}$	2.41e-3	3.49e-4	4.64e-5	5.97e-6	7.58e-7
order	-	2.79	2.91	2.96	2.98
$\ u_r - (u_r)_h\ _{L^2(\Omega)}$	0	0	0	0	0
$\ u_\theta - (u_\theta)_h\ _{L^2(\Omega)}$	0	0	0	0	0
$\ p - p_h\ _{L^2(\Omega)}$	0	0	0	0	0

Polynomial degree  $k' = 3$

$h/h_0$	1/2	1/4	1/8	1/16	1/32
$\ \mathbf{u} - \mathbf{u}_h\ _{\mathcal{V}(h)}$	1.86e-3	2.14e-4	2.54e-5	3.11e-6	3.87e-7
order	-	3.12	3.07	3.03	3.01
$\ \mathbf{u} - \mathbf{u}_h\ _{\mathbf{H}^1(\Omega)}$	1.37e-3	1.74e-4	2.26e-5	2.93e-6	3.75e-7
order	-	2.98	2.94	2.95	2.97
$\ \mathbf{u} - \mathbf{u}_h\ _{L^2(\Omega)}$	5.38e-5	5.05e-6	4.03e-7	2.80e-8	1.83e-9
order	-	3.41	3.65	3.85	3.94
$\ u_r - (u_r)_h\ _{L^2(\Omega)}$	0	0	0	0	0
$\ u_\theta - (u_\theta)_h\ _{L^2(\Omega)}$	0	0	0	0	0
$\ p - p_h\ _{L^2(\Omega)}$	0	0	0	0	0

Table 6.13: Annular Poiseuille flow convergence rates for  $\gamma = 0$ : NURBS

Polynomial degree  $k' = 1$

$h/h_0$	1/2	1/4	1/8	1/16	1/32
$\ \mathbf{u} - \mathbf{u}_h\ _{\mathcal{V}(h)}$	5.30e-1	2.47e-1	1.19e-1	5.80e-2	2.86e-2
order	-	1.10	1.05	1.04	1.02
$ \mathbf{u} - \mathbf{u}_h _{\mathbf{H}^1(\mathcal{K}_h)}$	4.57e-1	2.28e-1	1.14e-1	5.67e-2	2.83e-2
order	-	1.00	1.00	1.01	1.00
$\ \mathbf{u} - \mathbf{u}_h\ _{L^2(\Omega)}$	5.51e-2	1.63e-2	4.35e-3	1.12e-3	2.84e-4
order	-	1.76	1.91	1.96	1.98
$\ u_r - (u_r)_h\ _{L^2(\Omega)}$	0	0	0	0	0
$\ u_\theta - (u_\theta)_h\ _{L^2(\Omega)}$	0	0	0	0	0
$\ p - p_h\ _{L^2(\Omega)}$	0	0	0	0	0

Polynomial degree  $k' = 2$

$h/h_0$	1/2	1/4	1/8	1/16	1/32
$\ \mathbf{u} - \mathbf{u}_h\ _{\mathcal{V}(h)}$	5.69e-2	1.23e-2	2.83e-3	6.75e-4	1.64e-4
order	-	2.21	2.12	2.07	2.04
$ \mathbf{u} - \mathbf{u}_h _{\mathbf{H}^1(\mathcal{K}_h)}$	4.51e-2	1.07e-2	2.61e-3	6.46e-4	1.61e-4
order	-	2.08	2.04	2.01	2.00
$\ \mathbf{u} - \mathbf{u}_h\ _{L^2(\Omega)}$	2.52e-3	3.55e-4	4.70e-5	6.04e-6	7.66e-7
order	-	2.83	2.92	2.96	2.98
$\ u_r - (u_r)_h\ _{L^2(\Omega)}$	0	0	0	0	0
$\ u_\theta - (u_\theta)_h\ _{L^2(\Omega)}$	0	0	0	0	0
$\ p - p_h\ _{L^2(\Omega)}$	0	0	0	0	0

Polynomial degree  $k' = 3$

$h/h_0$	1/2	1/4	1/8	1/16	1/32
$\ \mathbf{u} - \mathbf{u}_h\ _{\mathcal{V}(h)}$	1.91e-3	2.38e-4	2.73e-5	3.33e-6	4.13e-7
order	-	3.00	3.12	3.04	3.01
$ \mathbf{u} - \mathbf{u}_h _{\mathbf{H}^1(\mathcal{K}_h)}$	1.44e-3	2.03e-4	2.48e-5	3.16e-6	4.03e-7
order	-	2.83	3.03	2.97	2.97
$\ \mathbf{u} - \mathbf{u}_h\ _{L^2(\Omega)}$	8.00e-5	1.21e-5	6.41e-7	4.00e-8	2.53e-9
order	-	2.72	4.24	4.00	3.98
$\ u_r - (u_r)_h\ _{L^2(\Omega)}$	0	0	0	0	0
$\ u_\theta - (u_\theta)_h\ _{L^2(\Omega)}$	0	0	0	0	0
$\ p - p_h\ _{L^2(\Omega)}$	0	0	0	0	0

Table 6.14: Annular Poiseuille flow convergence rates for  $\gamma = \sqrt{50}$ : Polar meshes

Polynomial degree  $k' = 1$

$h/h_0$	1/2	1/4	1/8	1/16	1/32
$\ \mathbf{u} - \mathbf{u}_h\ _{\mathcal{V}(h)}$	1.73e-1	9.88e-2	4.91e-2	2.35e-2	1.13e-2
order	-	0.81	1.01	1.06	1.06
$ \mathbf{u} - \mathbf{u}_h _{\mathbf{H}^1(\Omega)}$	8.20e-1	5.29e-1	2.90e-1	1.48e-1	7.46e-2
order	-	0.65	0.87	0.97	0.99
$\ \mathbf{u} - \mathbf{u}_h\ _{\mathbf{L}^2(\Omega)}$	4.88e-2	2.12e-2	6.69e-3	1.94e-3	5.37e-4
order	-	1.20	1.66	1.79	1.85
$\ u_r - (u_r)_h\ _{L^2(\Omega)}$	0	0	0	0	0
$\ u_\theta - (u_\theta)_h\ _{L^2(\Omega)}$	0	0	0	0	0
$\ p - p_h\ _{L^2(\Omega)}$	0	0	0	0	0

Polynomial degree  $k' = 2$

$h/h_0$	1/2	1/4	1/8	1/16	1/32
$\ \mathbf{u} - \mathbf{u}_h\ _{\mathcal{V}(h)}$	8.77e-2	2.59e-2	6.37e-3	1.46e-3	3.37e-4
order	-	1.76	2.02	2.13	2.12
$ \mathbf{u} - \mathbf{u}_h _{\mathbf{H}^1(\Omega)}$	4.34e-1	1.39e-1	3.63e-2	8.86e-3	2.16e-3
order	-	1.64	1.94	2.03	2.04
$\ \mathbf{u} - \mathbf{u}_h\ _{\mathbf{L}^2(\Omega)}$	2.32e-2	3.98e-3	5.33e-4	7.14e-5	9.46e-6
order	-	2.54	2.90	2.90	2.92
$\ u_r - (u_r)_h\ _{L^2(\Omega)}$	0	0	0	0	0
$\ u_\theta - (u_\theta)_h\ _{L^2(\Omega)}$	0	0	0	0	0
$\ p - p_h\ _{L^2(\Omega)}$	0	0	0	0	0

Polynomial degree  $k' = 3$

$h/h_0$	1/2	1/4	1/8	1/16	1/32
$\ \mathbf{u} - \mathbf{u}_h\ _{\mathcal{V}(h)}$	2.95e-2	5.72e-3	7.10e-4	8.48e-5	1.04e-5
order	-	2.37	3.01	3.07	3.03
$ \mathbf{u} - \mathbf{u}_h _{\mathbf{H}^1(\Omega)}$	1.48e-1	3.03e-2	4.02e-3	5.27e-4	6.88e-5
order	-	2.29	2.91	2.93	2.94
$\ \mathbf{u} - \mathbf{u}_h\ _{\mathbf{L}^2(\Omega)}$	5.23e-3	6.40e-4	5.59e-5	4.63e-6	3.27e-7
order	-	3.03	3.52	3.59	3.82
$\ u_r - (u_r)_h\ _{L^2(\Omega)}$	0	0	0	0	0
$\ u_\theta - (u_\theta)_h\ _{L^2(\Omega)}$	0	0	0	0	0
$\ p - p_h\ _{L^2(\Omega)}$	0	0	0	0	0

Table 6.15: Annular Poiseuille flow convergence rates for  $\gamma = \sqrt{50}$ : NURBS

Polynomial degree  $k' = 1$

$h/h_0$	1/2	1/4	1/8	1/16	1/32
$\ \mathbf{u} - \mathbf{u}_h\ _{\mathcal{V}(h)}$	1.73e-1	9.88e-2	4.91e-2	2.35e-2	1.13e-2
order	-	0.81	1.01	1.06	1.06
$ \mathbf{u} - \mathbf{u}_h _{\mathbf{H}^1(\Omega)}$	8.20e-1	5.29e-1	2.90e-1	1.49e-1	7.46e-2
order	-	0.65	0.87	0.96	1.00
$\ \mathbf{u} - \mathbf{u}_h\ _{\mathbf{L}^2(\Omega)}$	4.89e-2	2.12e-2	6.70e-3	1.95e-3	5.37e-4
order	-	1.21	1.66	1.78	1.86
$\ u_r - (u_r)_h\ _{L^2(\Omega)}$	0	0	0	0	0
$\ u_\theta - (u_\theta)_h\ _{L^2(\Omega)}$	0	0	0	0	0
$\ p - p_h\ _{L^2(\Omega)}$	0	0	0	0	0

Polynomial degree  $k' = 2$

$h/h_0$	1/2	1/4	1/8	1/16	1/32
$\ \mathbf{u} - \mathbf{u}_h\ _{\mathcal{V}(h)}$	8.77e-2	2.59e-2	6.38e-3	1.46e-3	3.37e-4
order	-	1.76	2.02	2.13	2.12
$ \mathbf{u} - \mathbf{u}_h _{\mathbf{H}^1(\Omega)}$	4.34e-1	1.39e-1	3.63e-2	8.86e-3	2.16e-3
order	-	1.64	1.94	2.03	2.04
$\ \mathbf{u} - \mathbf{u}_h\ _{\mathbf{L}^2(\Omega)}$	2.32e-2	3.98e-3	5.33e-4	7.14e-5	9.46e-6
order	-	2.54	2.90	2.90	2.92
$\ u_r - (u_r)_h\ _{L^2(\Omega)}$	0	0	0	0	0
$\ u_\theta - (u_\theta)_h\ _{L^2(\Omega)}$	0	0	0	0	0
$\ p - p_h\ _{L^2(\Omega)}$	0	0	0	0	0

Polynomial degree  $k' = 3$

$h/h_0$	1/2	1/4	1/8	1/16	1/32
$\ \mathbf{u} - \mathbf{u}_h\ _{\mathcal{V}(h)}$	2.95e-2	5.72e-3	7.10e-4	8.48e-5	1.04e-5
order	-	2.37	3.01	3.07	3.03
$ \mathbf{u} - \mathbf{u}_h _{\mathbf{H}^1(\Omega)}$	1.48e-1	3.03e-2	4.02e-3	5.27e-4	6.88e-5
order	-	2.29	2.91	2.93	2.94
$\ \mathbf{u} - \mathbf{u}_h\ _{\mathbf{L}^2(\Omega)}$	5.23e-3	6.40e-4	5.59e-5	4.63e-6	3.27e-7
order	-	3.03	3.52	3.59	3.82
$\ u_r - (u_r)_h\ _{L^2(\Omega)}$	0	0	0	0	0
$\ u_\theta - (u_\theta)_h\ _{L^2(\Omega)}$	0	0	0	0	0
$\ p - p_h\ _{L^2(\Omega)}$	0	0	0	0	0

parametric meshes, linear parametric mappings, and B-spline spaces of maximal continuity.

### 6.7.1 Two-Dimensional Lid-Driven Cavity Flow

Two-dimensional lid-driven cavity flow is one of the classical verification tests for numerical discretizations of incompressible flow. The setup for this flow problem is elaborated in Figure 6.13. The reaction coefficient  $\sigma$  and the applied forcing  $\mathbf{f}$  are set to be zero. The left, right, and bottom sides of the cavity are fixed no-slip walls while the top side of the cavity is a wall which slides to the right with velocity magnitude  $U$ . For the computations here,  $H$  and  $U$  are set to be 1. The pressure and stress fields associated with this flow experience corner singularities which impede the convergence of numerical methods and expose unstable velocity/pressure pairs. In fact, the exact velocity solution does not even lie in  $\mathbf{H}^1(\Omega)$ . Instead, it lies in the Sobolev space  $\mathbf{W}^{1,q}(\Omega)$  where  $1 < q < 2$ . The velocity field is additionally characterized by a primary vortex near the center of the cavity and an infinite sequence of so-called Moffatt eddies of decreasing size and intensity in the lower left and right corners of the cavity [145]. Of primary interest is how well our discretization procedure approximates the smooth portions of the flow. Of secondary interest is how well our discretization procedure resolves the corner singularities. We do not, however, employ any special techniques such as singular finite elements to handle the singularities.

We have computed approximations of two-dimensional lid-driven cavity flow using divergence-conforming B-spline discretizations of varying mesh size and polynomial degrees  $k' = 1, 2, 3$ . The computed streamlines for two of these approximations are presented in Figure 6.14. The streamlines corresponding to the approximation defined on the fine mesh ( $k' = 1, h = 1/128$ ) are virtually indis-

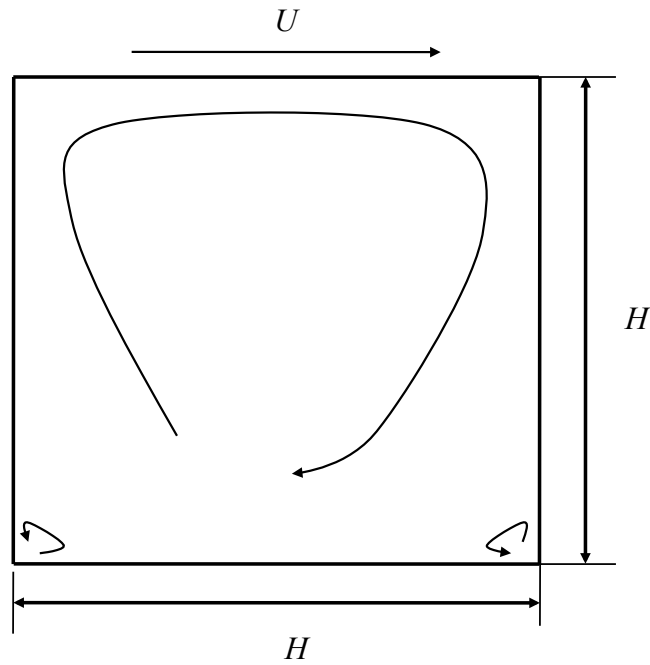
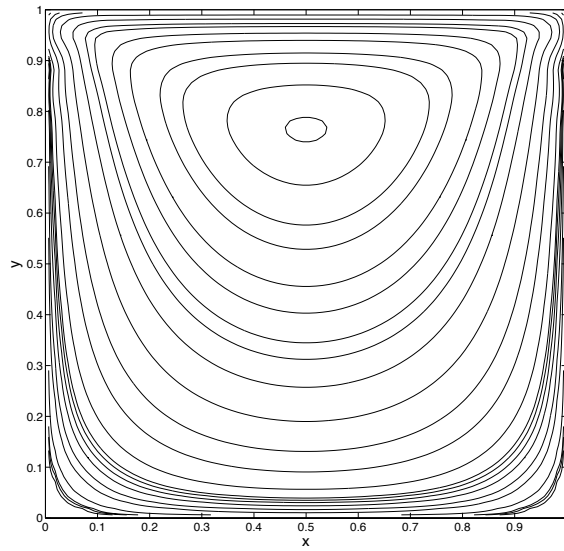
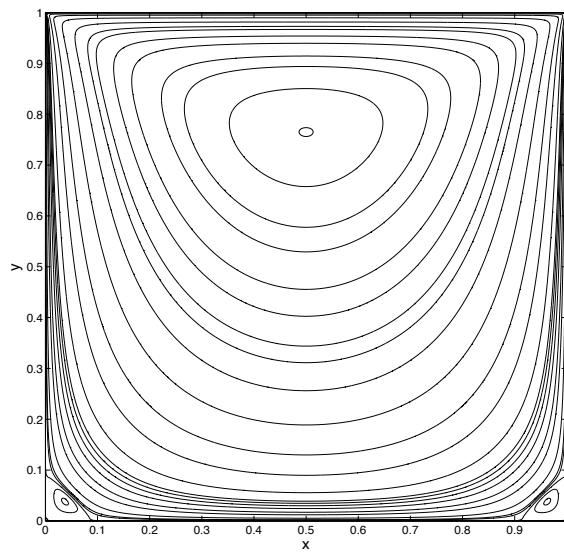


Figure 6.13: Lid-driven Stokes flow in a two-dimensional cavity: Problem setup.

tinguishable from well-accepted benchmark solutions [168]. The streamlines corresponding to the approximation defined on the coarse mesh ( $k' = 1, h = 1/16$ ) closely resemble the fine mesh streamlines in the interior of the domain. In the four corners of the domain, the approximation on the coarse mesh exhibits visible numerical error due to lack of resolution. These results indicate that our methodology suffers from minimal pollution error [14]. It is hypothesized that this is due to the local stability and approximation properties of B-splines. To further highlight how well the approximation on the coarse mesh approximates the solution in the interior of the domain, we have plotted the value of the first component of the velocity field along the vertical center line in Figure 6.15(a) and the value of the second component along the horizontal center line in Figure 6.15(b) for the both the coarse mesh



(a)



(b)

Figure 6.14: Lid-driven Stokes flow in a two-dimensional cavity: (a) Computed flow velocity streamlines for  $k' = 1$  and  $h = 1/16$ , (b) Computed flow velocity streamlines for  $k' = 1$  and  $h = 1/128$ .

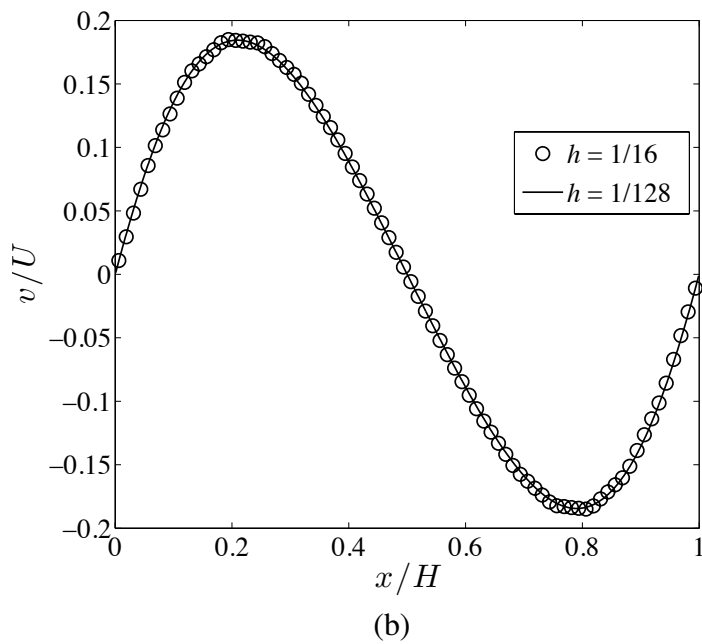
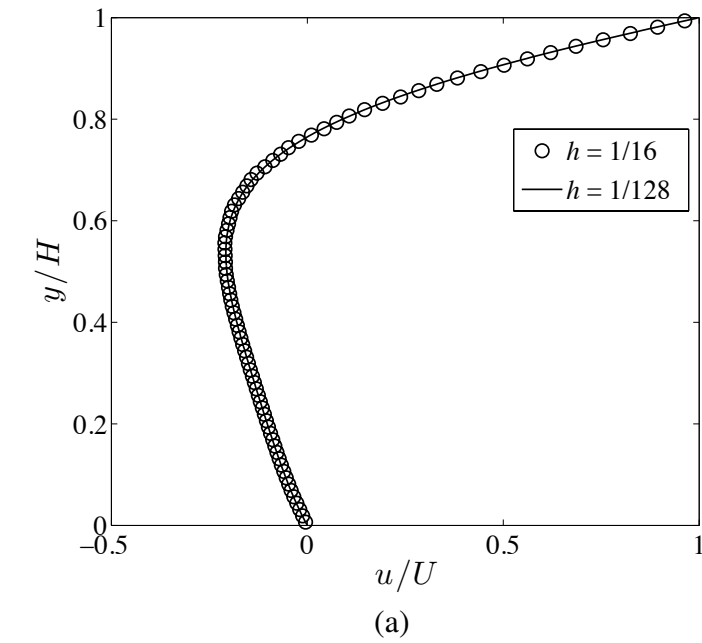


Figure 6.15: Lid-driven Stokes flow in a two-dimensional cavity: (a) Value of the first component of the velocity field along the vertical center line for  $k' = 1$ , (b) Value of the second component of the velocity field along the horizontal center line for  $k' = 1$ .

and fine mesh solutions. It should be mentioned that we have captured the first Moffatt eddy in the two lower corners with both meshes, and we have observed a second Moffatt eddy for meshes of size  $h \leq 1/256$ .

We finish our discussion of the two-dimensional lid-driven cavity problem by analyzing how well our methodology resolves the corner singularities. To do so, we compare the results of our methodology with the highly accurate pseudospectral results given in [32]. These pseudospectral results were obtained using a subtraction of the leading terms of the asymptotic solution of the Stokes equations in the vicinity of the corners in order to exactly represent the corner singularities. In Table 6.16, we compare the vorticity ( $\omega = \text{curl}\mathbf{u}$ ) given by our numerical methodology with the pseudospectral vorticity near the upper right corner of the cavity. We see that the vorticity associated with our numerical methodology slowly converges to the converged pseudospectral solution. We further compare our computed vorticities with the vorticity obtained with a highly-refined finite difference solution [95]. We find that, for  $k' = 1$ , our solutions are more accurate than the finite difference solution for  $h \leq 1/64$ , and for  $k' = 2$ , our solutions are more accurate than the finite difference solution for  $h \leq 1/32$ . For  $k' = 3$ , our solutions are more accurate than the finite difference solution at all resolutions.

### 6.7.2 Three-Dimensional Lid-Driven Cavity Flow

While three-dimensional lid-driven cavity flow is encountered much less often in the literature than its two-dimensional counterpart, we believe it is still an interesting test case for numerical discretizations of incompressible flow. In the three-dimensional setting, cavity flow is characterized by the presence of both edge and corner singularities. The problem setup is illustrated in Figure 6.16. Again, for the computations here,  $\sigma$  and  $\mathbf{f}$  are set to be zero. Every side of the cavity except

Table 6.16: Lid-driven Stokes flow in a two-dimensional cavity: Convergence of vorticity at the point  $(\mathbf{x} = (1, 0.95))$ .

Polynomial degree  $k' = 1$

Method	$\omega$
B-spline, $h = 1/16$	-0.80995
B-spline, $h = 1/32$	14.34482
B-spline, $h = 1/64$	19.04468
B-spline, $h = 1/128$	23.29179
B-spline, $h = 1/256$	25.32238
Pseudospectral (Ref. [32])	27.27901
Finite Difference (Ref. [95])	18.08

Polynomial degree  $k' = 2$

Method	$\omega$
B-spline, $h = 1/16$	11.06384
B-spline, $h = 1/32$	31.81761
B-spline, $h = 1/64$	32.81972
B-spline, $h = 1/128$	26.48645
B-spline, $h = 1/256$	27.34395
Pseudospectral (Ref. [32])	27.27901
Finite Difference (Ref. [95])	18.08

Polynomial degree  $k' = 3$

Method	$\omega$
B-spline, $h = 1/16$	29.86220
B-spline, $h = 1/32$	25.00897
B-spline, $h = 1/64$	29.92944
B-spline, $h = 1/128$	28.75895
B-spline, $h = 1/256$	27.52637
Pseudospectral (Ref. [32])	27.27901
Finite Difference (Ref. [95])	18.08

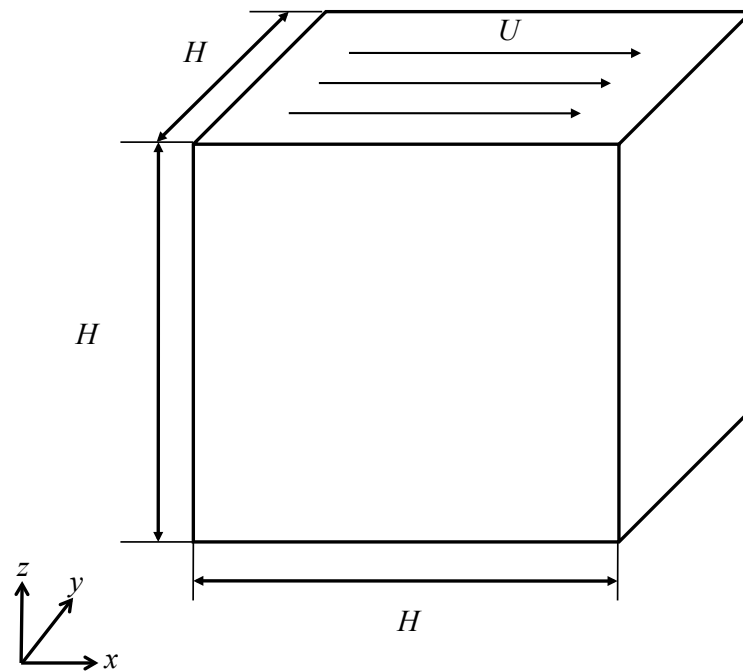


Figure 6.16: Lid-driven Stokes flow in a three-dimensional cavity: Problem setup.

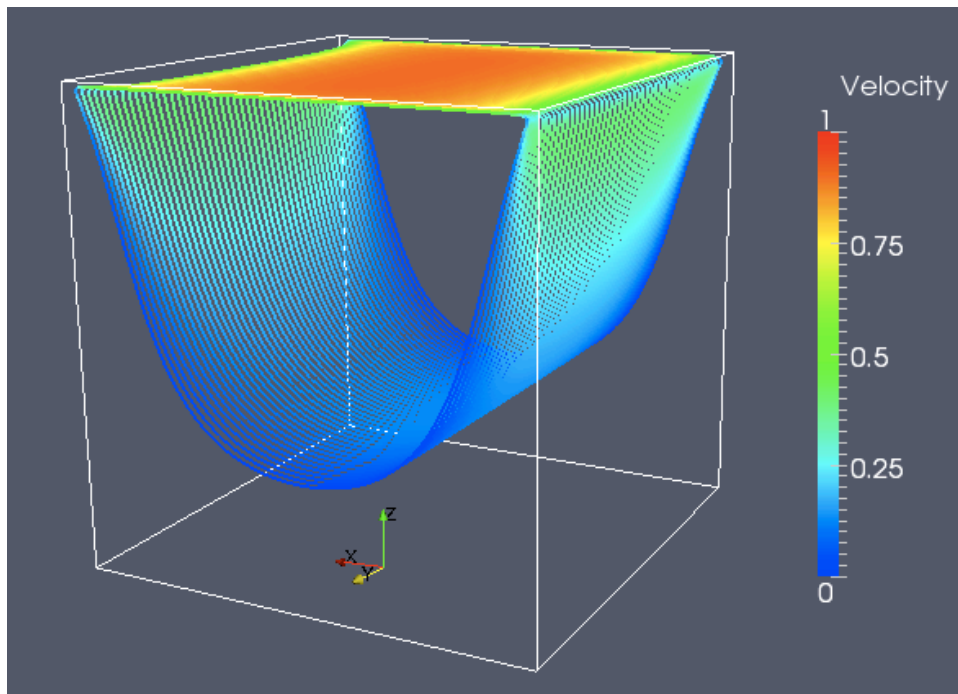


Figure 6.17: Lid-driven Stokes flow in a three-dimensional cavity: Computed flow velocity streamlines for  $k' = 2$  and  $h = 1/32$  colored by velocity magnitude.

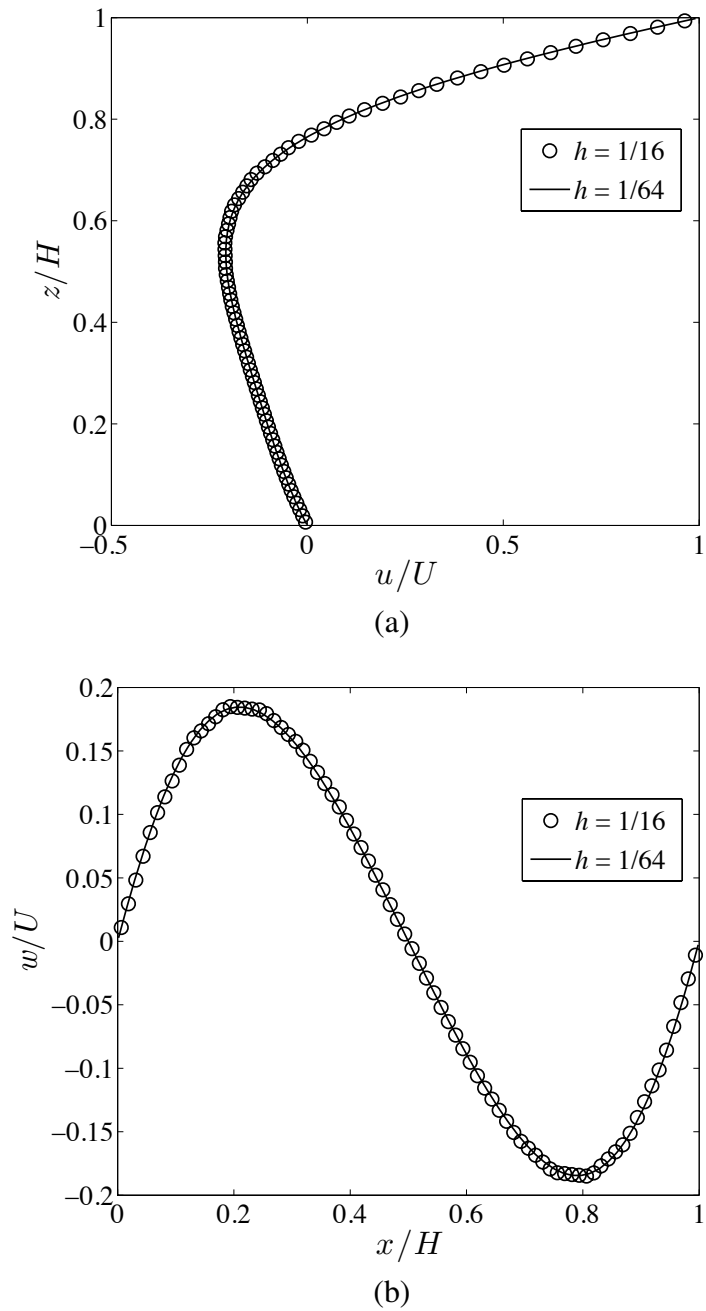
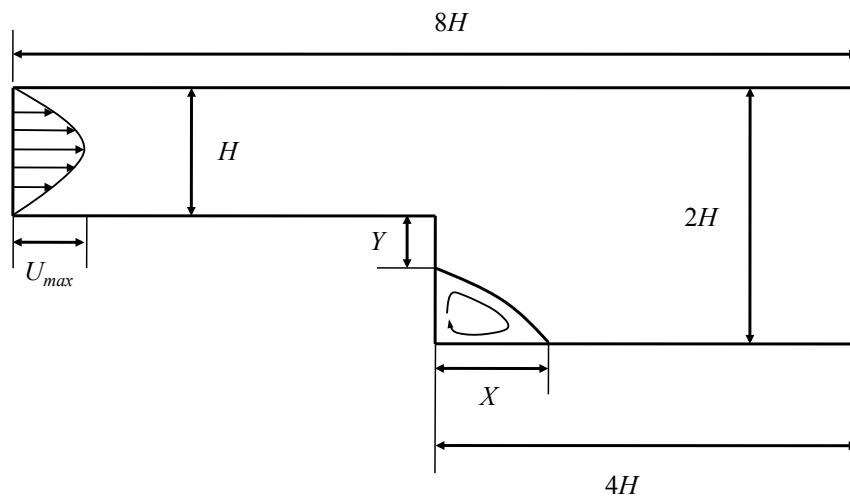


Figure 6.18: Lid-driven Stokes flow in a three-dimensional cavity: (a) Value of the first component of the velocity field along the line  $(x/H, y/H) = (1/2, 1/2)$  for  $k' = 1$ , (b) Value of the third component of the velocity field along the line  $(y/H, z/H) = (1/2, 1/2)$  for  $k' = 1$ .

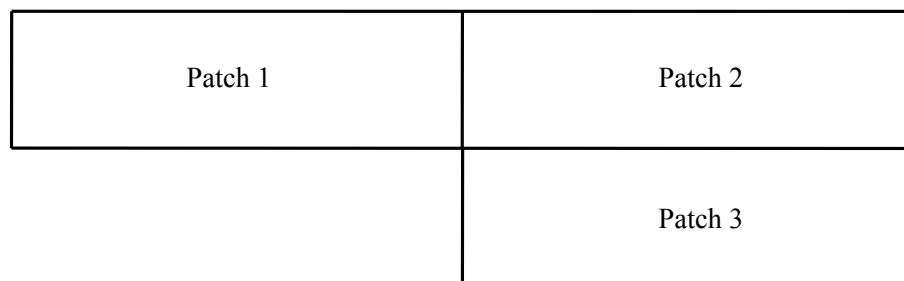
the top is assumed to be a stationary no-slip wall, and the top side of the cavity is assumed to be a wall which slips to the right with velocity magnitude  $U$ . The streamlines resulting from a simulation of three-dimensional lid-driven cavity flow using divergence-conforming B-splines of degree  $k' = 2$  on a mesh with  $32 \times 32$  elements are illustrated in Figure 6.17. Note that the three-dimensional streamlines resemble the two-dimensional streamlines along the slice  $y/H = 1/2$ . To examine how well our discretization technique performs on coarse meshes, we have compared the centerline values of our velocity field along the slice  $y/H = 1/2$  for both a coarse and fine mesh approximation in Figure 6.18. From the figure, we see that the coarse and fine mesh centerline velocity fields are nearly indistinguishable. This indicates that our methodology suffers from minimal pollution error.

### 6.7.3 Flow Over a Backwards Facing Step

Flow over a backwards facing step is another benchmark problem that is often utilized to numerically validate Stokes and Navier-Stokes discretizations. This flow problem is characterized by a collection of interesting properties, including corner singularities, secondary flows, and flow separation. Furthermore, for many flow configurations, flow over a backwards facing step becomes turbulent at a moderate Reynolds number. We consider here two-dimensional Stokes flow over a backwards facing step. The problem description is illustrated in Figure 6.19. No external forcing is applied. The inlet and outlet lengths have been chosen to be sufficiently long so that the flow in the direct vicinity of the step is not affected by their placement. The expansion ratio is chosen to be 2:1. The top and bottom walls are assumed fixed, and a no-slip boundary condition is applied. At the outflow region located at the right hand side of the domain, a zero-traction or “do-nothing” boundary condition is enforced. At the left hand side of the domain, a



(a)



(b)

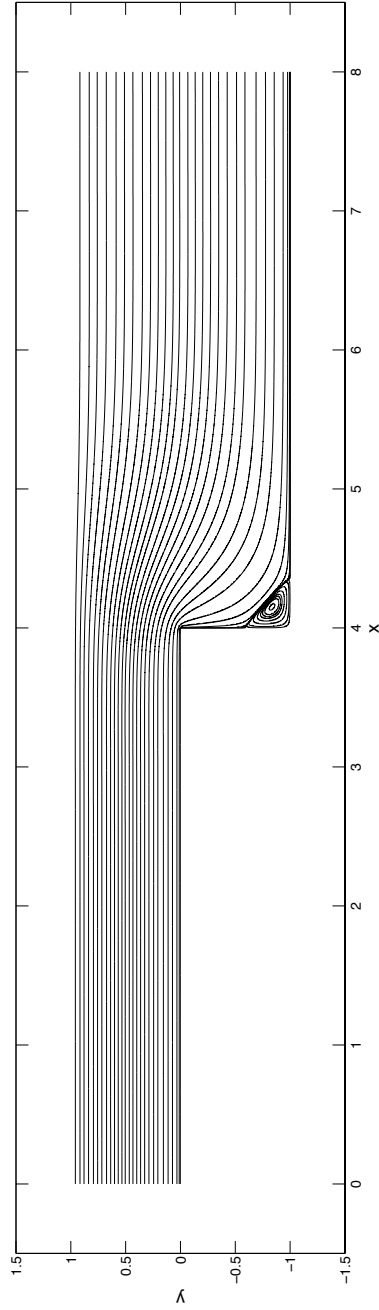
Figure 6.19: Stokes flow over a backward facing step: (a) Problem setup, (b) Multi-patch construction.

Table 6.17: Stokes flow over a backward facing step: Computed sizes of recirculation region.

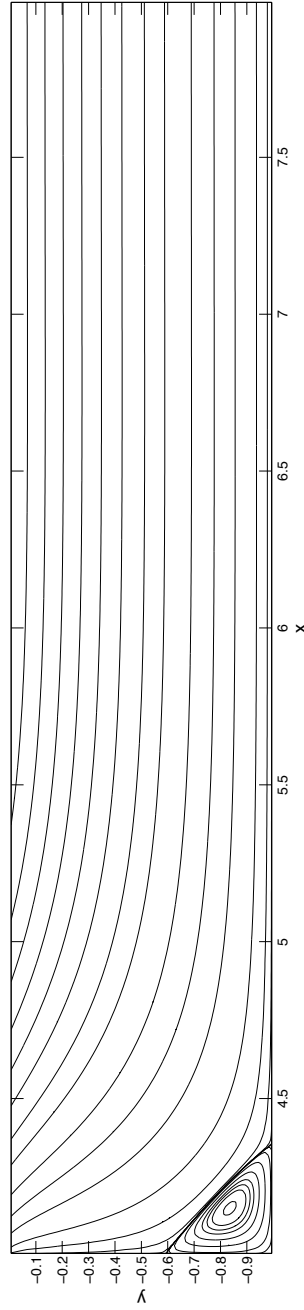
Polynomial degree $k' = 1$				
$h$	1/20	1/40	1/80	1/160
$X$	0.325	0.350	0.351	0.351
$Y$	0.625	0.600	0.597	0.597

parabolic inflow boundary condition is specified with maximum speed  $U_{max}$ . This boundary condition is enforced numerically via  $L^2$ -projection. For the computations presented here, the step height is chosen to be  $H = 1$  and the maximum speed of the inflow is chosen to be  $U_{max} = 3/2$ . Computed streamlines using highly-refined divergence-conforming B-splines of order  $k' = 1$  are illustrated in Figure 6.20. These streamlines are visually indistinguishable from benchmark solutions in the literature.

One of the quantities of interest for this flow problem is the size of the recirculation region illustrated in Figure 6.19(a). Accurate computation of this size is hampered by pollution error introduced by stress singularities at the reentrant corner. To compute the size of the recirculation region, we have employed divergence-conforming B-spline spaces defined via a three-patch construction. This construction is detailed in Figure 6.19(b). In Table 6.17, we have detailed recirculation region sizes that are obtained using patch-wise continuous divergence-conforming B-spline approximations of polynomial degree  $k' = 1$ . Note that the computed sizes quickly converge to  $X = 0.351, Y = 0.597$ . Hence, pollution error has not greatly affected the solution away from the reentrant corner.



(a)



(b)

Figure 6.20: Stokes flow over a backward facing step: (a) Streamlines over the three patches; (b) Third patch zoom in.

**Remark 6.7.1.** *While we enforced the quadratic inflow boundary condition using  $L^2$  projection, there are a variety of other techniques that could be utilized. A local technique would prove especially useful. One possible local technique would be to utilize dual functionals on the boundary of the domain. This has proven to be a satisfactory procedure for “gluing” together non-conforming finite element meshes in a mortar method [192]. We also believe dual mortars is a promising procedure for handling non-matching patches in general engineering geometries.*

#### 6.7.4 Darcy-Dominated Flow with Sharp Boundary Layers

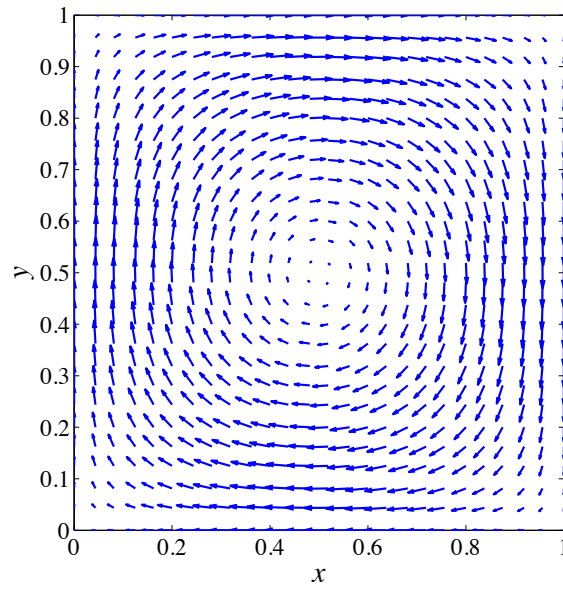
As a final numerical example, we consider a reaction-dominated generalized Stokes problem subject to sharp boundary layers. The problem is posed on the unit square. Homogeneous no-slip and no-penetration boundary conditions are enforced along the boundary of the square, and an external forcing of the form

$$\mathbf{f} = \begin{bmatrix} \sin(\pi x) \cos(\pi y) \\ -\cos(\pi x) \sin(\pi y) \end{bmatrix}$$

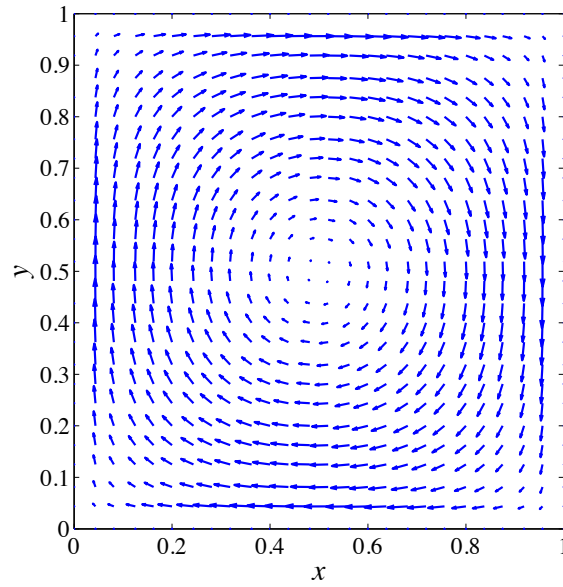
is applied. The reaction term  $\sigma$  is set to be equal to 1 while the viscosity  $\nu$  is set to be equal to  $10^{-6}$ . With these choices, the resulting flow field has a vortical structure in the interior of the domain and sharp boundary layers along the entire boundary of the domain.

We have simulated this flow problem using both our discretization technique as well as the  $\mathbf{Q}_2/Q_1$  Taylor-Hood velocity/pressure pair [106]. The Taylor-Hood velocity/pressure pair is one of the most popular finite elements for generalized Stokes flow, but it is known not to be robust in the Darcy limit. Specifically, the accuracy of the  $\mathbf{Q}_2/Q_1$  Taylor-Hood velocity field reduces to first-order in the Darcy limit [96]. This is due to a lack of strong coercivity (in the kernel) with respect to the  $\mathbf{H}(\text{div}; \Omega)$ -norm. We have visualized the computed velocity vectors corresponding

to divergence-free B-splines of degree  $k' = 1$  and the  $\mathbf{Q}_2/Q_1$  Taylor-Hood velocity-pressure pair on a  $16 \times 16$  element mesh in Figures 6.21(a) and (b). These two quiver plots seem to indicate that the two discrete flow fields are nearly identical except in a small region near the boundary of the domain. However, when we view only the first-component of the velocity field as in Figures 6.22 and 6.23, we see that the divergence-free B-spline solution is monotone while the Taylor-Hood solution suffers from spurious oscillations. Finally, we have visualized the divergence of the discrete flow field corresponding to the Taylor-Hood solution in Figure 6.24. From this figure, we see that the Taylor-Hood solution is characterized by strong expansion and compression in the four corners of the domain. When coupled with a transport solver, this ultimately leads to methods with unphysical species production [143]. On the other hand, the discrete flow field corresponding to the B-spline solution is pointwise divergence-free.

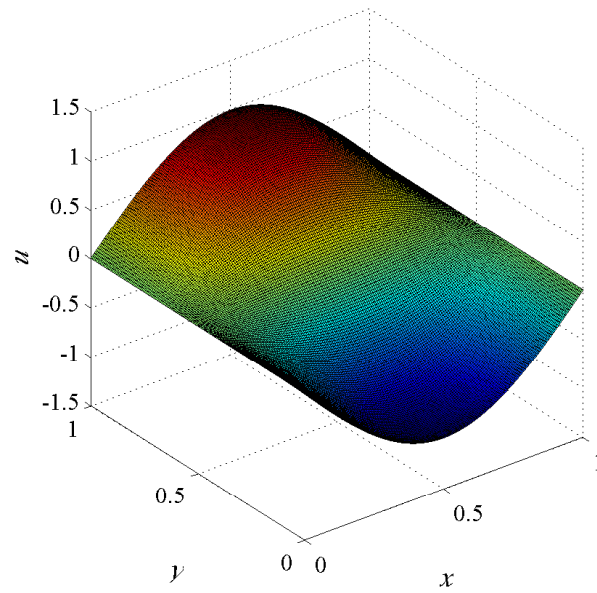


(a)

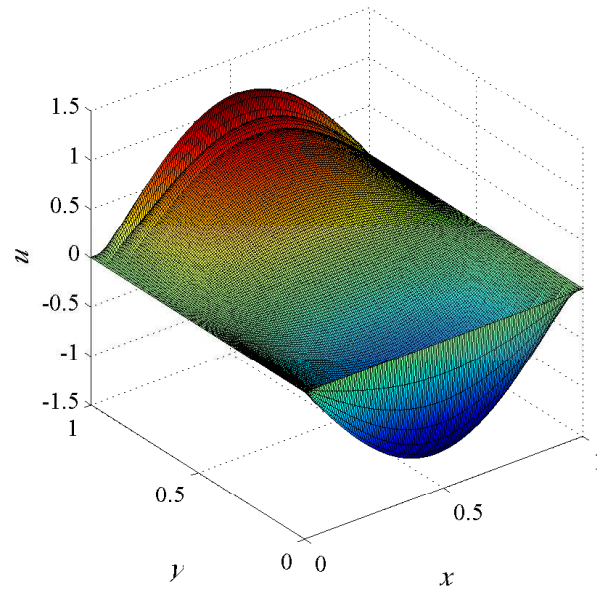


(b)

Figure 6.21: Darcy-dominated flow with boundary layers: Computed velocity fields: (a) Divergence-free B-splines of degree  $k' = 1$ , (b)  $\mathbf{Q}_2/Q_1$  Taylor-Hood velocity/pressure pair.

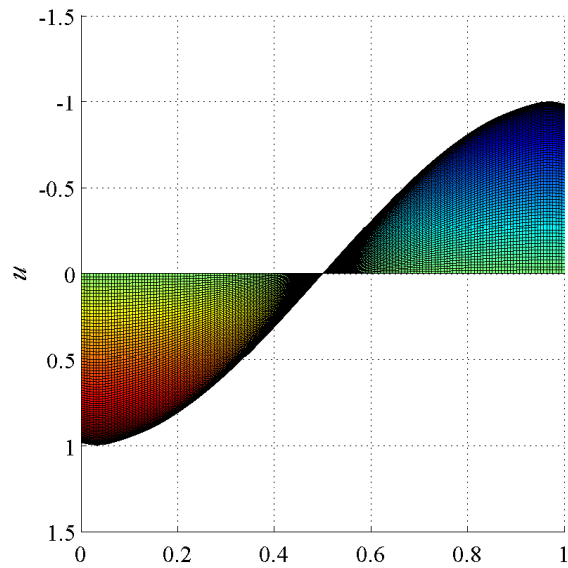


(a)

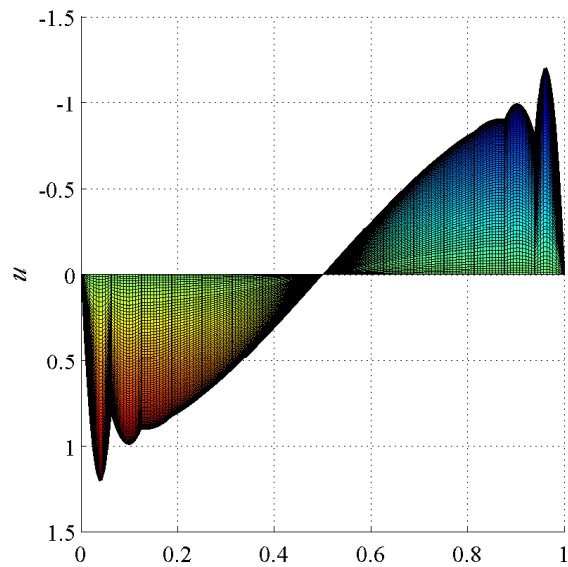


(b)

Figure 6.22: Darcy-dominated flow with boundary layers: First-component of the velocity field: (a) Divergence-free B-splines of degree  $k' = 1$ , (b)  $\mathbf{Q}_2/Q_1$  Taylor-Hood velocity/pressure pair.



(a)



(b)

Figure 6.23: Darcy-dominated flow with boundary layers: Cross-section view of the first velocity component from the  $y = 1$  line: (a) Divergence-free B-splines of degree  $k' = 1$ , (b)  $\mathbf{Q}_2/Q_1$  Taylor-Hood velocity/pressure pair.

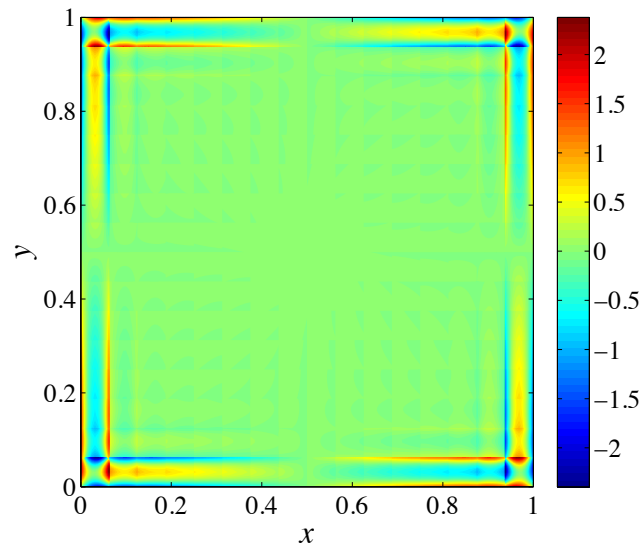


Figure 6.24: Darcy-dominated flow with boundary layers: Divergence of the discrete flow field corresponding to the  $\mathbf{Q}_2/Q_1$  Taylor-Hood velocity/pressure pair.

## Chapter 7

### Approximation of the Steady Navier-Stokes Problem

Steady Navier-Stokes flow is an important simplification of fully unsteady Navier-Stokes flow. Many low speed, laminar fluid flows may be accurately described by the steady Navier-Stokes equations. Additionally, one arrives at a steady Navier-Stokes problem by conducting a Reynolds time-averaging of statistically stationary Navier-Stokes flows (see Chapters 3 and 4 of [158]). Like the generalized Stokes problem, the steady Navier-Stokes problem has presented considerable difficulty in its numerical approximation. It too is subject to the Babuška-Brezzi inf-sup condition. In addition, convection provides a new world of trouble. Namely, on the occasion that the incompressibility constraint is not met exactly, terms corresponding to convection can actually produce energy if written in conservation form. This leads to unstable formulations. Due to this instability, alternative representations of convection operators have been devised. The most popular of these in the finite element community is the skew-symmetric representation [194]. Discretizations of the convection term using the skew-symmetric representation neither produce nor dissipate energy and hence lead to stable numerical methods. Unfortunately, one loses the momentum conservation structure of the Navier-Stokes equations by utilizing such a strategy. Alternatively, provably stable, convergent, and locally-conservative discontinuous Galerkin discretizations have been devised for the steady Navier-Stokes equations in [48, 49], but these discretizations are plagued with a proliferation of degrees of freedom and are thus largely limited to two spatial

dimensions.

Another discretization procedure for the steady Navier-Stokes equations arises through the intelligent choice of weighting function in a Petrov-Galerkin method. Namely, a popular method of choice is the use of an advective formulation in conjunction with the Streamline-Upwind Petrov-Galerkin (SUPG) method [38] to handle convective instabilities and the Pressure-Stabilizing Petrov-Galerkin (PSPG) method [111] to handle pressure instabilities. Unfortunately, the theoretical analysis of this method in the steady regime has been entirely restricted to linearized Oseen problems where the convection velocity is assumed fixed and divergence-free. These linearized model problems are ultimately insufficient as the discrete convection velocity is not, in general, divergence-free. To further control the divergence term, so-called grad-div stabilization techniques [162] have been proposed which add artificial dilatational stresses to the underlying variational formulation. Using a combination of an advective formulation, SUPG, PSPG, and grad-div stabilization, provably convergent numerical methods have been devised for the steady Navier-Stokes equations (see Chapter 3 of [162]). Still, the search for a provably convergent  $\mathbf{H}^1$  finite element discretization of the three-dimensional steady Navier-Stokes equations written in conservation form has largely been for naught.

In this chapter, we present divergence-conforming B-spline discretizations for the steady Navier-Stokes problem using the B-spline spaces introduced in Chapter 5. As our discretizations return pointwise divergence-free velocity fields, we can utilize a variational formulation written in conservation form without being encumbered by instability. As was done for the generalized Stokes problem, we impose the no-penetration condition strongly and the no-slip condition weakly using Nitsche's method. This allows our discretization to naturally default to a conforming approximation of Euler flow in the limit of vanishing viscosity. This also allows our method

to capture boundary layers without resorting to stretched meshes [21,22]. We prove stability and error estimates for single-patch discretizations under a smallness condition. As was the case for the generalized Stokes problem, our error estimates are optimal for the discrete velocity field and suboptimal, by one order, for the discrete pressure field provided that the exact solution is sufficiently regular. We utilize the methods of exact and manufactured solutions to verify our error estimates and, as in the last chapter, find our discrete pressure fields converge at optimal order in contrast with our theoretical estimates. We finish this section by considering the application of our discretization to the analysis of two benchmark problems: lid-driven cavity flow and confined jet impingement. All of our estimates' dependencies on the viscosity and the penalty parameter of Nitsche's method will be made explicit in our analysis.

Before proceeding, note that one might say there is a fundamental issue concerning the fact that our analysis only covers flows subject to "small data". However, well-posedness of the continuous problem is subject to a similar constraint, and we believe the small data assumption is natural as medium- and large-Reynolds number flows are inherently unsteady in both laminar and turbulent regimes.

## 7.1 The Continuous Problem

Let us consider steady Navier-Stokes flow of a constant-property Newtonian fluid subject to homogeneous Dirichlet boundary conditions:

$$(S) \left\{ \begin{array}{l} \text{Given } \nu \in \mathbb{R}^+ \text{ and } \mathbf{f} : \Omega \rightarrow \mathbb{R}^d, \text{ find } \mathbf{u} : \bar{\Omega} \rightarrow \mathbb{R}^d \text{ and } p : \Omega \rightarrow \mathbb{R} \text{ such that} \\ \quad \nabla \cdot (\mathbf{u} \otimes \mathbf{u}) - \nabla \cdot (2\nu \nabla^s \mathbf{u}) + \mathbf{grad} p = \mathbf{f} \quad \text{in } \Omega \quad (7.1) \\ \quad \operatorname{div} \mathbf{u} = 0 \quad \text{in } \Omega \quad (7.2) \\ \quad \mathbf{u} = \mathbf{0} \quad \text{on } \partial\Omega. \quad (7.3) \end{array} \right.$$

Above, as in the generalized Stokes problem,  $\mathbf{u}$  denotes the flow velocity,  $p$  denotes the pressure,  $\nu$  denotes the kinematic viscosity,  $\mathbf{f}$  denotes a body force, and  $\Omega \subset \mathbb{R}^d$  is a domain defined by some piecewise smooth parametric mapping  $\mathbf{F} : (0, 1)^d \rightarrow \mathbb{R}^d$  with  $d = 1, 2$ .

Assuming that  $\mathbf{f} \in \mathbf{L}^2(\Omega)$ , the weak form for the steady Navier-Stokes problem is written as follows:

$$(W) \left\{ \begin{array}{l} \text{Find } \mathbf{u} \in \mathbf{H}_0^1(\Omega) \text{ and } p \in L_0^2(\Omega) \text{ such that} \\ \quad k(\mathbf{u}, \mathbf{v}) + c(\mathbf{u}, \mathbf{u}; \mathbf{v}) - b(p, \mathbf{v}) + b(q, \mathbf{u}) = (\mathbf{f}, \mathbf{v})_{\mathbf{L}^2(\Omega)} \quad (7.4) \\ \text{for all } \mathbf{v} \in \mathbf{H}_0^1(\Omega) \text{ and } q \in L_0^2(\Omega) \text{ where} \\ \quad k(\mathbf{w}, \mathbf{v}) = (2\nu \nabla^s \mathbf{w}, \nabla^s \mathbf{v})_{(L^2(\Omega))^{d \times d}}, \quad \forall \mathbf{w}, \mathbf{v} \in \mathbf{H}_0^1(\Omega), \quad (7.5) \\ \quad b(q, \mathbf{v}) = (q, \operatorname{div} \mathbf{v})_{L^2(\Omega)}, \quad \forall q \in L_0^2(\Omega), \mathbf{v} \in \mathbf{H}_0^1(\Omega), \quad (7.6) \\ \quad c(\mathbf{w}, \mathbf{x}; \mathbf{v}) = -(\mathbf{w} \otimes \mathbf{x}, \nabla \mathbf{v})_{(L^2(\Omega))^{d \times d}}, \quad \forall \mathbf{w}, \mathbf{x}, \mathbf{v} \in \mathbf{H}_0^1(\Omega). \quad (7.7) \end{array} \right.$$

Note that the trilinear form  $c(\cdot, \cdot; \cdot) : \mathbf{H}_0^1(\Omega) \times \mathbf{H}_0^1(\Omega) \times \mathbf{H}_0^1(\Omega) \rightarrow \mathbb{R}$  makes sense due to the continuous Sobolev embedding

$$\mathbf{H}_0^1(\Omega) \hookrightarrow \mathbf{L}^4(\Omega). \quad (7.8)$$

In fact, as  $\partial\Omega$  is Lipschitz, we have the stronger embedding  $\mathbf{H}^1(\Omega) \hookrightarrow \mathbf{L}^4(\Omega)$ . Additionally note that the bilinear form  $k(\cdot, \cdot)$  defined here is equivalent to the bilinear form  $a(\cdot, \cdot)$  defined in Section 6.2 with  $\sigma$  set to zero.

We have the following existence and uniqueness theorem for flows subject to small data whose proof may be found in [86].

**Theorem 7.1.1.** *Problem (W) has a unique weak solution  $(\mathbf{u}, p) \in \mathbf{H}_0^1(\Omega) \times L_0^2(\Omega)$  provided the problem data satisfies an inequality of the form*

$$\frac{C_\Omega C_{\text{poin}}}{\nu^2} \|\mathbf{f}\|_{\mathbf{L}^2(\Omega)} < 1 \quad (7.9)$$

where  $C_\Omega$  is a constant which only depends on  $\Omega$  and  $C_{\text{poin}}$  is the Poincaré constant appearing in (6.14). Furthermore, such a weak solution satisfies the inequality

$$|\mathbf{u}|_{\mathbf{H}^1(\Omega)} \leq \frac{C_{\text{poin}}}{\nu} \|\mathbf{f}\|_{\mathbf{L}^2(\Omega)}. \quad (7.10)$$

**Remark 7.1.1.** In general, we may replace the constant-property Newtonian stress tensor given here,  $\mathbb{T} = 2\nu\nabla^s\mathbf{u}$ , with more suitable choices of stress tensor. Our analysis does not cover this general setting.

## 7.2 The Discretized Problem

We now present a discrete variational formulation for the steady Navier-Stokes problem using the velocity and pressure spaces  $\mathcal{V}_{0,h}$  and  $\mathcal{Q}_{0,h}$  defined in Chapter 5. As in the last chapter, we resort to Nitsche's method to weakly enforce no-slip boundary conditions. Defining the bilinear form

$$k_h(\mathbf{w}, \mathbf{v}) = k(\mathbf{w}, \mathbf{v}) - \sum_{F \in \Gamma_h} \int_F 2\nu \left( ((\nabla^s \mathbf{v}) \mathbf{n}) \cdot \mathbf{w} + ((\nabla^s \mathbf{w}) \mathbf{n}) \cdot \mathbf{v} - \frac{C_{\text{pen}}}{h_F} \mathbf{w} \cdot \mathbf{v} \right) ds \quad (7.11)$$

where  $C_{\text{pen}} \geq 1$  is a chosen positive penalty constant, our discrete formulation is written as follows.

$$(G) \begin{cases} \text{Find } \mathbf{u}_h \in \mathcal{V}_{0,h} \text{ and } p_h \in \mathcal{Q}_{0,h} \text{ such that} \\ k_h(\mathbf{u}_h, \mathbf{v}_h) + c(\mathbf{u}_h, \mathbf{u}_h; \mathbf{v}_h) - b(p_h, \mathbf{v}_h) + b(q_h, \mathbf{u}_h) = (\mathbf{f}, \mathbf{v}_h)_{\mathbf{L}^2(\Omega)} \\ \text{for all } \mathbf{v}_h \in \mathcal{V}_{0,h}, q_h \in \mathcal{Q}_{0,h}. \end{cases} \quad (7.12)$$

We have the following lemma detailing the consistency of our numerical method.

**Lemma 7.2.1.** Suppose that  $(\mathbf{u}, p)$  is a solution of (W) satisfying the regularity condition  $\mathbf{u} \in \mathbf{H}^{3/2+\epsilon}(\Omega)$  for some  $\epsilon > 0$ . Then:

$$k_h(\mathbf{u}, \mathbf{v}_h) + c(\mathbf{u}, \mathbf{u}; \mathbf{v}_h) - b(p, \mathbf{v}_h) + b(q_h, \mathbf{u}) = (\mathbf{f}, \mathbf{v}_h)_{\mathbf{L}^2(\Omega)} \quad (7.13)$$

for all  $\mathbf{v}_h \in \mathcal{V}_{0,h}$  and  $q_h \in \mathcal{Q}_{0,h}$ .

*Proof.* We trivially have

$$b(q_h, \mathbf{u}) = 0, \quad \forall q_h \in \mathcal{Q}_{0,h}.$$

Now let  $\mathbf{v}_h \in \mathcal{V}_{0,h}$ . By the Sobolev trace theorem, the assumption  $\mathbf{u} \in \mathbf{H}^{3/2+\epsilon}(\Omega)$  guarantees that  $(\nabla^s \mathbf{u}) \mathbf{n}$  is well-defined along  $\partial\Omega$  and  $(\nabla^s \mathbf{u}) \mathbf{n} \in (L^2(\partial\Omega))^d$ . Hence, the quantity  $a_h(\mathbf{u}, \mathbf{v}_h)$  is well-defined. Utilizing integration by parts and the fact that  $\mathbf{u}$  satisfies homogeneous Dirichlet boundary conditions and  $\mathbf{v}_h$  satisfies homogeneous normal Dirichlet boundary conditions, we have

$$\begin{aligned} k_h(\mathbf{u}, \mathbf{v}_h) + c(\mathbf{u}, \mathbf{u}; \mathbf{v}_h) - b(p, \mathbf{v}_h) &= \int_{\Omega} (\nabla \cdot (\mathbf{u} \otimes \mathbf{u}) - \nabla \cdot (2\nu \nabla^s \mathbf{u}) + \mathbf{grad} p) \cdot \mathbf{v}_h \\ &= \int_{\Omega} \mathbf{f} \cdot \mathbf{v}_h \\ &= (\mathbf{f}, \mathbf{v}_h)_{\mathbf{L}^2(\Omega)}. \end{aligned}$$

This completes the proof of the lemma.  $\square$

In this nonlinear setting, we do not have an orthogonality condition. Instead, we have the following relationship between the exact solution and a numerical solution.

**Corollary 7.2.1.** *Let  $(\mathbf{u}_h, p_h)$  denote a solution of (G), and let  $(\mathbf{u}, p)$  denote a solution of (W) satisfying the regularity condition  $\mathbf{u} \in \mathbf{H}^{3/2+\epsilon}(\Omega)$  for some  $\epsilon > 0$ . Then:*

$$\begin{aligned} k_h(\mathbf{u} - \mathbf{u}_h, \mathbf{v}_h) + c(\mathbf{u}, \mathbf{u}, \mathbf{v}_h) - c(\mathbf{u}_h, \mathbf{u}_h, \mathbf{v}_h) \\ - b(p - p_h, \mathbf{v}_h) + b(q_h, \mathbf{u} - \mathbf{u}_h) = 0 \end{aligned} \quad (7.14)$$

for all  $\mathbf{v}_h \in \mathcal{V}_{0,h}$  and  $q_h \in \mathcal{Q}_{0,h}$ .

Finally, by Proposition 5.4.2, we have the following lemma.

**Lemma 7.2.2.** *Let  $(\mathbf{u}_h, p_h)$  denote a solution of (G). Then:*

$$\operatorname{div} \mathbf{u}_h \equiv 0 \quad (7.15)$$

Weak imposition of no-slip boundary conditions allows our methodology to default to a compatible discretization of Euler flow in the setting of vanishing viscosity. Moreover, for large Reynold's number flows, there is a sharp boundary layer in the vicinity of walls. Utilizing Nitsche's method allows us to account for these layers in a stable and consistent manner without having to directly resolve them [20–22]. In fact, Nitsche's method can be interpreted as variationally consistent wall model. To better see this interpretation, let us formally rewrite our discrete variational equations as

$$\int_{\Omega} \mathbb{T} : \nabla^s \mathbf{w}_h d\mathbf{x} - \sum_{F \in \Gamma_h} \int_F \mathbb{Q} \cdot \mathbf{w}_h d\mathbf{s} + c(\mathbf{u}_h, \mathbf{u}_h; \mathbf{v}_h) - b(p_h, \mathbf{v}_h) + b(q_h, \mathbf{u}_h) = (\mathbf{f}, \mathbf{v}_h)_{\mathbf{L}^2(\Omega)} \quad (7.16)$$

where  $\mathbb{T}$  is a symmetric tensor satisfying

$$\begin{aligned} \int_{\Omega} \mathbb{T} : \mathbb{W} d\mathbf{x} &= \int_{\Omega} 2\nu \nabla^s \mathbf{u}_h : \mathbb{W} d\mathbf{x} - \sum_{F \in \Gamma_h} \int_F 2\nu \mathbf{u}_h \cdot (\mathbb{W} \mathbf{n}) d\mathbf{s} \\ &= \int_{\Omega} 2\nu \mathbf{u}_h \cdot \operatorname{div} \mathbb{W} d\mathbf{x} \quad (\text{in the sense of distributions}) \end{aligned} \quad (7.17)$$

for symmetric tensors  $\mathbb{W}$  with well-defined normal trace and  $\mathbb{Q}$  is a vector satisfying

$$\mathbb{Q} = 2\nu \left( (\nabla^s \mathbf{u}_h) \mathbf{n} - \frac{C_{pen}}{h} \mathbf{u}_h \right). \quad (7.18)$$

Above,  $\mathbb{T}$  is a weakly defined viscous stress tensor and  $\mathbb{Q}$  is a prescribed normal boundary condition for the viscous stress tensor. In the event that the no-slip boundary condition is met exactly, we recover  $\mathbb{T} \equiv 2\nu \nabla^s \mathbf{u}_h$  and  $\mathbb{Q} \equiv 2\nu (\nabla^s \mathbf{u}_h) \mathbf{n}$ . Otherwise, the definitions of  $\mathbb{T}$  and  $\mathbb{Q}$  are changed accordingly.

As the discrete velocity field satisfies the no-penetration boundary condition strongly, the vector  $\mathbb{Q}$  is equal to the discrete shear stress  $2\nu (\nabla^s \mathbf{u}_h) \mathbf{n}$  plus an additional wall shear stress term  $\mathbb{Q}^+$  in the direction tangent to the wall. Specifically, we have

$$\mathbb{Q}^+ = -u^{*2} \frac{\mathbf{u}_h}{\|\mathbf{u}_h\|} \quad (7.19)$$

where

$$u^{*2} = \frac{2\nu C_{pen} \|\mathbf{u}_h\|}{h}. \quad (7.20)$$

For under-resolved flow simulations, the magnitude of  $(\nabla^s \mathbf{u}_h) \mathbf{n}$  in the direction tangent to the wall is nearly zero and, as such, the tangential component of  $\mathbb{Q}$  is dominated by  $\mathbb{Q}^+$ . In this sense,  $\mathbb{Q}^+$  becomes a model for the wall shear stress. As the mesh is refined and the flow is resolved,  $\mathbb{Q}^+ \rightarrow 0$ . The above interpretation allows us to design physically motivated penalty values for Nitsche's penalty parameter. Notably,  $u^*$  may be interpreted as the friction velocity. By specifying the value of  $u^*$  using Spalding's law of the wall [172], we recover a standard wall model for under-resolved flow simulations. For more on this approach, see Section 3 of [21].

**Remark 7.2.1.** *If we wish to impose non-homogeneous tangential Dirichlet (e.g., prescribed slip) boundary conditions, we must add the following expression to the right hand side of our discrete formulation:*

$$f_N(\mathbf{v}_h) = \sum_{F \in \Gamma_h} \int_F 2\nu \left( -((\nabla^s \mathbf{v}_h) \mathbf{n}) \cdot \mathbf{u}_{BC} + \frac{C_{pen}}{h_F} \mathbf{u}_{BC} \cdot \mathbf{v}_h \right) ds \quad (7.21)$$

where  $\mathbf{u}_{BC}$  is a vector function living on  $\partial\Omega$  with prescribed boundary values. If we also wish to impose non-homogeneous normal Dirichlet (e.g., prescribed penetration) boundary conditions, we must impose these strongly and add the following expression to the left hand side of our discrete formulation:

$$c_{UW}(\mathbf{u}_h, \mathbf{v}_h) = \sum_{F \in \Gamma_h} \int_F (\mathbf{u}_{BC} \cdot \mathbf{n})_+ \mathbf{u}_h \cdot \mathbf{v}_h ds \quad (7.22)$$

and the following expression to the right hand side of our discrete formulation:

$$f_{UW}(\mathbf{v}_h) = - \sum_{F \in \Gamma_h} \int_F (\mathbf{u}_{BC} \cdot \mathbf{n})_- \mathbf{u}_{BC} \cdot \mathbf{v}_h ds \quad (7.23)$$

where

$$(\mathbf{u}_{BC} \cdot \mathbf{n})_+ = \begin{cases} \mathbf{u}_{BC} \cdot \mathbf{n} & \text{if } \mathbf{u}_{BC} \cdot \mathbf{n} > 0 \\ 0 & \text{otherwise} \end{cases}$$

and

$$(\mathbf{u}_{BC} \cdot \mathbf{n})_- = \begin{cases} \mathbf{u}_{BC} \cdot \mathbf{n} & \text{if } \mathbf{u}_{BC} \cdot \mathbf{n} \leq 0 \\ 0 & \text{otherwise.} \end{cases}$$

These additional terms correspond to upwinding.

### 7.3 Well-Posedness for Small Data

We now prove that our discrete formulation is well-posed under a smallness condition. Our method of proof mimics that of the continuous problem (see Theorem 10.1.1 of [86]). To begin, let us define the following mesh-dependent norm:

$$\|\mathbf{v}\|_h^2 := |\mathbf{v}|_{\mathbf{H}^1(\Omega)}^2 + \sum_{F \in \Gamma_h} h_F \|(\nabla^s \mathbf{v}) \mathbf{n}\|_{(L^2(F))^d}^2 + \sum_{F \in \Gamma_h} \frac{C_{pen}}{h_F} \|\mathbf{v}\|_{(L^2(F))^d}^2. \quad (7.24)$$

This norm is simply the unweighted counterpart to the weighted  $\mathcal{V}(h)$ -norm appearing in the previous chapter. We will also denote as in the previous chapter

$$\mathring{\mathcal{V}}_{0,h} := \{\mathbf{v}_h \in \mathcal{V}_{0,h} : \operatorname{div} \mathbf{v}_h = 0\} = \{\mathbf{v}_h \in \mathcal{V}_{0,h} : b(q_h, \mathbf{v}_h) = 0, \forall q_h \in \mathcal{Q}_{0,h}\}.$$

To proceed, we will need to call upon stability and continuity results that were proven in Section 6.3. We summarize these results in the following corollary.

**Corollary 7.3.1.** *Assume (6.19) and (6.20) are satisfied. Then we have*

$$k_h(\mathbf{w}, \mathbf{v}) \leq 2\nu C_{cont} \|\mathbf{w}\|_h \|\mathbf{v}\|_h, \quad \forall \mathbf{w}, \mathbf{v} \in \mathcal{V}_{0,h} \oplus (\mathbf{H}_0^1(\Omega) \cap \mathbf{H}^{3/2+\epsilon}(\Omega)) \quad (7.25)$$

$$b(p, \mathbf{v}) \leq \|p\|_{L^2(\Omega)} \|\mathbf{v}\|_h \quad \forall p \in L_0^2(\Omega), \mathbf{v} \in \mathcal{V}_{0,h} \oplus (\mathbf{H}_0^1(\Omega) \cap \mathbf{H}^{3/2+\epsilon}(\Omega)) \quad (7.26)$$

$$k_h(\mathbf{w}_h, \mathbf{w}_h) \geq 2\nu C_{coerc} \|\mathbf{w}_h\|_h^2, \quad \forall \mathbf{w}_h \in \mathring{\mathcal{V}}_{0,h} \quad (7.27)$$

where  $\epsilon > 0$  is an arbitrary positive number and  $C_{cont}$  and  $C_{coerc}$  are positive constants which are independent of  $h$ ,  $\nu$ ,  $C_{pen}$ , and  $\epsilon$ . Furthermore, we have

$$\inf_{q_h \in \mathcal{Q}_{0,h}, q_h \neq 0} \sup_{\mathbf{v}_h \in \mathcal{V}_{0,h}} \frac{(\operatorname{div} \mathbf{v}_h, q_h)}{\|\mathbf{v}_h\|_{\mathcal{V}(h)} \|q_h\|_{\Omega}} \geq \tilde{\beta}. \quad (7.28)$$

where  $\tilde{\beta}$  is a positive constant independent of  $h$  and  $\nu$  which asymptotically scales inversely with the square root of  $C_{pen}$ .

We will also need the following two lemmas. The first lemma gives a Lipschitz continuity result for the trilinear form  $c(\cdot, \cdot; \cdot)$ . This result hinges upon Sobolev embeddings which exist because our domain is Lipschitz. The second lemma gives a semi-coercivity result for the trilinear form  $c(\cdot, \cdot; \cdot)$ .

**Lemma 7.3.1.** *There exists a constant  $C_0$  only dependent on  $\Omega$  such that*

$$c(\mathbf{w}_1, \mathbf{x}; \mathbf{v}) - c(\mathbf{w}_2, \mathbf{x}; \mathbf{v}) \leq C_0 \|\mathbf{w}_1 - \mathbf{w}_2\|_{\mathbf{H}^1(\Omega)} \|\mathbf{x}\|_{\mathbf{H}^1(\Omega)} \|\mathbf{v}\|_{\mathbf{H}^1(\Omega)} \quad (7.29)$$

for all  $\mathbf{w}_1, \mathbf{w}_2, \mathbf{x}, \mathbf{v} \in \mathbf{H}^1(\Omega) \cap \mathbf{H}_0(\operatorname{div}; \Omega)$ .

*Proof.* Let  $\mathbf{w}_1, \mathbf{w}_2, \mathbf{x}, \mathbf{v} \in \mathbf{H}^1(\Omega) \cap \mathbf{H}_0(\operatorname{div}; \Omega)$  be arbitrary. Note that since  $\partial\Omega$  is Lipschitz, we have the continuous embedding

$$H^1(\Omega) \hookrightarrow L^4(\Omega).$$

By linearity and Hölder's inequality, we can then write

$$\begin{aligned} c(\mathbf{w}_1, \mathbf{x}; \mathbf{v}) - c(\mathbf{w}_2, \mathbf{x}; \mathbf{v}) &= -((\mathbf{w}_1 - \mathbf{w}_2) \otimes \mathbf{x}, \nabla \mathbf{v})_{(L^2(\Omega))^{d \times d}} \\ &\leq \|\mathbf{w}_1 - \mathbf{w}_2\|_{\mathbf{L}^4(\Omega)} \|\mathbf{x}\|_{\mathbf{L}^4(\Omega)} \|\nabla \mathbf{v}\|_{(L^2(\Omega))^{d \times d}}. \end{aligned}$$

Let  $C_{embed}$  denote the positive embedding constant dependent only on the domain  $\Omega$  such that

$$\|\mathbf{y}\|_{\mathbf{L}^4(\Omega)} \leq C_{embed} \|\mathbf{y}\|_{\mathbf{H}^1(\Omega)}, \quad \forall \mathbf{y} \in \mathbf{H}^1(\Omega).$$

Then we have

$$c(\mathbf{w}_1, \mathbf{x}; \mathbf{v}) - c(\mathbf{w}_2, \mathbf{x}; \mathbf{v}) \leq C_{embed}^2 \|\mathbf{w}_1 - \mathbf{w}_2\|_{\mathbf{H}^1(\Omega)} \|\mathbf{x}\|_{\mathbf{H}^1(\Omega)} \|\nabla \mathbf{v}\|_{(L^2(\Omega))^{d \times d}}.$$

The lemma follows with  $C_0 = C_{embed}^2 C_{poin}^2$  where  $C_{poin}$  is the Poincaré constant appearing in (6.14).  $\square$

**Lemma 7.3.2.** *Suppose  $\mathbf{w}, \mathbf{v} \in \mathbf{H}^1(\Omega) \cap \mathbf{H}_0(\text{div}; \Omega)$  such that  $\text{div } \mathbf{w} = 0$ . Then*

$$c(\mathbf{w}, \mathbf{v}; \mathbf{v}) = 0. \quad (7.30)$$

*Proof.* We write

$$c(\mathbf{w}, \mathbf{v}; \mathbf{v}) = - \int_{\Omega} (\mathbf{w} \otimes \mathbf{v}) : \nabla \mathbf{v} d\mathbf{x}.$$

Since  $\text{div } \mathbf{w} = 0$ , we have

$$c(\mathbf{w}, \mathbf{v}; \mathbf{v}) = -\frac{1}{2} \int_{\Omega} \text{div} (\mathbf{w} |\mathbf{v}|^2) d\mathbf{x}.$$

The lemma is then simply a result of Stoke's theorem.  $\square$

With Corollary 7.3.1 and Lemmata 7.3.1 and 7.3.2, we can prove the following proposition which gives the well-posedness of the linearized Oseen problem.

**Proposition 7.3.1.** *Let  $\mathbf{w} \in \mathbf{H}^1(\Omega) \cap \mathbf{H}_0(\text{div}; \Omega)$  such that  $\text{div } \mathbf{w} = 0$ , and assume (6.19) and (6.20) are satisfied. Then the following problem has a unique solution: find  $(\mathbf{x}_h, r_h) \in \mathcal{V}_{0,h} \times \mathcal{Q}_{0,h}$  such that*

$$k_h(\mathbf{x}_h, \mathbf{v}_h) + c(\mathbf{w}, \mathbf{x}_h; \mathbf{v}_h) - b(r_h, \mathbf{v}_h) + b(q_h, \mathbf{x}_h) = (\mathbf{f}, \mathbf{v}_h)_{\mathbf{L}^2(\Omega)} \quad (7.31)$$

for all  $\mathbf{v}_h \in \mathcal{V}_{0,h}$ ,  $q_h \in \mathcal{Q}_{0,h}$ . Furthermore, the unique solution of the linearized Oseen problem satisfies  $\text{div } \mathbf{x}_h = 0$  and the bound

$$\|\mathbf{x}_h\|_h \leq \frac{C_{poin}}{2\nu C_{coerc}} \|\mathbf{f}\|_{\mathbf{L}^2(\Omega)} \quad (7.32)$$

where  $C_{poin}$  is the Poincaré constant appearing in (6.14) and  $C_{coerc}$  is the coercivity constant appearing in Corollary 7.3.1.

*Proof.* Existence and uniqueness are a direct result of Brezzi's theorem, Corollary 7.3.1, and Lemmata 7.3.1 and 7.3.2. Since  $\operatorname{div} \mathcal{V}_{0,h} = \mathcal{Q}_{0,h}$ , we automatically have  $\operatorname{div} \mathbf{x}_h = 0$ . To prove the *a priori* bound, we write using (7.31) and the coercivity of  $k_h(\cdot, \cdot)$

$$\begin{aligned} \|\mathbf{x}_h\|_h^2 &\leq \frac{1}{2\nu C_{\text{coerc}}} k_h(\mathbf{x}_h, \mathbf{x}_h) \\ &= \frac{1}{2\nu C_{\text{coerc}}} \left( (\mathbf{f}, \mathbf{x}_h)_{\mathbf{L}^2(\Omega)} - c(\mathbf{w}, \mathbf{x}_h; \mathbf{x}_h) - b(r_h, \mathbf{x}_h) \right). \end{aligned}$$

Using Lemma 7.3.2 to set  $c(\mathbf{w}, \mathbf{x}_h; \mathbf{x}_h) = 0$  and  $\operatorname{div} \mathbf{x}_h = 0$  to set  $b(r_h, \mathbf{x}_h) = 0$ , we can complete the proof:

$$\begin{aligned} \|\mathbf{x}_h\|_h^2 &\leq \frac{1}{2\nu C_{\text{coerc}}} (\mathbf{f}, \mathbf{x}_h)_{\mathbf{L}^2(\Omega)} \\ &\leq \frac{1}{2\nu C_{\text{coerc}}} \|\mathbf{f}\|_{\mathbf{L}^2(\Omega)} \|\mathbf{x}_h\|_{\mathbf{L}^2(\Omega)} \\ &\leq \frac{C_{\text{poin}}}{2\nu C_{\text{coerc}}} \|\mathbf{f}\|_{\mathbf{L}^2(\Omega)} |\mathbf{x}_h|_{\mathbf{H}^1(\Omega)}. \end{aligned}$$

□

We are now ready to establish well-posedness results for the full-blown Navier-Stokes problem. To do so, we will attempt to obtain the solution to the discrete Navier-Stokes problem through the iterative solution of a sequence of Oseen problems. Notably, given  $\mathbf{u}_0 \in \mathring{\mathcal{V}}_{0,h}$ , we seek the limit of the following iterative solution process: for  $i = 1, 2, 3, \dots$  find  $(\mathbf{u}_i, p_i) \in \mathcal{V}_{0,h} \times \mathcal{Q}_{0,h}$  such that

$$k_h(\mathbf{u}_i, \mathbf{v}_h) + c(\mathbf{u}_{i-1}, \mathbf{u}_i; \mathbf{v}_h) - b(p_i, \mathbf{v}_h) + b(q_h, \mathbf{u}_i) = (\mathbf{f}, \mathbf{v}_h)_{\mathbf{L}^2(\Omega)} \quad (7.33)$$

for all  $\mathbf{v}_h \in \mathcal{V}_{0,h}$ ,  $q_h \in \mathcal{Q}_{0,h}$ . Well-posedness hinges upon the convergence of this iterative solution process, and convergence of this process is further contingent upon a small data constraint.

**Theorem 7.3.1.** Assume (6.19) and (6.20) are satisfied, and further assume that

$$\frac{C_o C_{poin}}{(2\nu)^2 C_{coerc}^2} \|\mathbf{f}\|_{\mathbf{L}^2(\Omega)} < 1 \quad (7.34)$$

where  $C_o$  is the continuity constant appearing in Lemma 7.3.1,  $C_{poin}$  is the Poincaré constant appearing in (6.14), and  $C_{coerc}$  is the coercivity constant appearing in Corollary 7.3.1. Then Problem (G) has a unique solution  $(\mathbf{u}_h, p_h) \in \mathcal{V}_{0,h} \times \mathcal{Q}_{0,h}$ . Furthermore, the unique solution satisfies

$$\|\mathbf{u}_h\|_h \leq \frac{C_{poin}}{2\nu C_{coerc}} \|\mathbf{f}\|_{\mathbf{L}^2(\Omega)} \quad (7.35)$$

$$\|p_h\|_{\mathbf{L}^2(\Omega)} \leq \tilde{\beta}^{-1} \left( \frac{C_o C_{poin}}{(2\nu)^2 C_{coerc}^2} + \frac{C_{cont}}{C_{coerc}} + 1 \right) C_{poin} \|\mathbf{f}\|_{\mathbf{L}^2(\Omega)} \quad (7.36)$$

where  $\tilde{\beta}$  and  $C_{cont}$  are the inf-sup and continuity constants appearing in Corollary 7.3.1.

*Proof.* Begin by defining  $S : \mathring{\mathcal{V}}_{0,h} \rightarrow \mathring{\mathcal{V}}_{0,h}$  to be the nonlinear operator which returns the divergence-free velocity solution of (7.31) given a divergence-free velocity field  $\mathbf{w}_h \in \mathring{\mathcal{V}}_{0,h}$ . Note that by Proposition 7.3.1

$$\|S(\mathbf{w}_h)\|_h \leq \frac{C_{poin}}{2\nu C_{coerc}} \|\mathbf{f}\|_{\mathbf{L}^2(\Omega)}.$$

Therefore, the nonlinear operator  $S$  maps  $\mathring{\mathcal{V}}_{0,h}$  into

$$\mathcal{B}_h := \left\{ \mathbf{w}_h \in \mathring{\mathcal{V}}_{0,h} : \|\mathbf{w}_h\|_h \leq \frac{C_{poin}}{2\nu C_{coerc}} \|\mathbf{f}\|_{\mathbf{L}^2(\Omega)} \right\}.$$

Now, let  $\mathbf{w}_1, \mathbf{w}_2 \in \mathring{\mathcal{V}}_{0,h}$  and  $\bar{\mathbf{w}}_1 = S(\mathbf{w}_1)$ ,  $\bar{\mathbf{w}}_2 = S(\mathbf{w}_2)$ . By using the coercivity of  $k_h(\cdot, \cdot)$  given by Corollary 7.3.1 we have

$$2\nu C_{coerc} \|\bar{\mathbf{w}}_1 - \bar{\mathbf{w}}_2\|_h^2 \leq k_h(\bar{\mathbf{w}}_1 - \bar{\mathbf{w}}_2, \bar{\mathbf{w}}_1 - \bar{\mathbf{w}}_2). \quad (7.37)$$

By (7.31), we have

$$k_h(\bar{\mathbf{w}}_1, \bar{\mathbf{w}}_1 - \bar{\mathbf{w}}_2) = -c(\mathbf{w}_1, \bar{\mathbf{w}}_1, \bar{\mathbf{w}}_1 - \bar{\mathbf{w}}_2) + (\mathbf{f}, \bar{\mathbf{w}}_1 - \bar{\mathbf{w}}_2)_{\mathbf{L}^2(\Omega)}$$

and

$$k_h(\bar{\mathbf{w}}_2, \bar{\mathbf{w}}_1 - \bar{\mathbf{w}}_2) = -c(\mathbf{w}_2, \bar{\mathbf{w}}_2, \bar{\mathbf{w}}_1 - \bar{\mathbf{w}}_2) + (\mathbf{f}, \bar{\mathbf{w}}_1 - \bar{\mathbf{w}}_2)_{\mathbf{L}^2(\Omega)}$$

since  $\operatorname{div}(\bar{\mathbf{w}}_1 - \bar{\mathbf{w}}_2) = 0$ . Hence,

$$\begin{aligned} 2\nu C_{coerc} \|\bar{\mathbf{w}}_1 - \bar{\mathbf{w}}_2\|_h^2 &\leq c(\mathbf{w}_2, \bar{\mathbf{w}}_2, \bar{\mathbf{w}}_1 - \bar{\mathbf{w}}_2) - c(\mathbf{w}_1, \bar{\mathbf{w}}_1, \bar{\mathbf{w}}_1 - \bar{\mathbf{w}}_2) \\ &= -c(\mathbf{w}_2, \bar{\mathbf{w}}_1 - \bar{\mathbf{w}}_2, \bar{\mathbf{w}}_1 - \bar{\mathbf{w}}_2) \\ &\quad + c(\mathbf{w}_2, \bar{\mathbf{w}}_1, \bar{\mathbf{w}}_1 - \bar{\mathbf{w}}_2) - c(\mathbf{w}_1, \bar{\mathbf{w}}_1, \bar{\mathbf{w}}_1 - \bar{\mathbf{w}}_2). \end{aligned}$$

By the continuity and coercivity properties given in Lemmata 7.3.1 and 7.3.2, we can write

$$2\nu C_{coerc} \|\bar{\mathbf{w}}_1 - \bar{\mathbf{w}}_2\|_h^2 \leq C_o \|\mathbf{w}_2 - \mathbf{w}_1\|_h \|\bar{\mathbf{w}}_1\|_h \|\bar{\mathbf{w}}_1 - \bar{\mathbf{w}}_2\|_h.$$

Since  $\bar{\mathbf{w}}_1 \in \mathcal{B}_h$ , we thus have

$$\|\bar{\mathbf{w}}_1 - \bar{\mathbf{w}}_2\|_h \leq \mu \|\mathbf{w}_2 - \mathbf{w}_1\|_h$$

where  $\mu$  is precisely

$$\mu = \frac{C_o C_{poin}}{(2\nu)^2 C_{coerc}^2} \|\mathbf{f}\|_{\mathbf{L}^2(\Omega)}.$$

By assumption  $\mu < 1$ , and we therefore have proved  $S$  is a contractive map. By the Banach fixed point theorem, the nonlinear problem

$$\mathbf{u}_h = S(\mathbf{u}_h)$$

has a unique solution which lies in  $\mathcal{B}_h$  and is precisely the discrete velocity solution (now proven unique) of Problem (G). Given  $\mathbf{u}_h$ , uniqueness of the discrete pressure solution  $p_h$  is a direct result of the inf-sup condition.

We now prove the stability bounds. The bound for  $\mathbf{u}_h$  is straight-forward since  $\mathbf{u}_h \in \mathcal{B}_h$ . To prove the bound for  $p_h$ , we utilize the inf-sup condition, the continuity of  $k_h(\cdot, \cdot)$ , the continuity of  $c(\cdot, \cdot; \cdot)$ , and Poincaré's inequality:

$$\begin{aligned}
\tilde{\beta} \|p_h\|_{\mathbf{L}^2(\Omega)} &\leq \sup_{\mathbf{v}_h \in \mathcal{V}_{0,h}} \frac{b(p_h, \mathbf{v}_h)}{\|\mathbf{v}_h\|_h} \\
&= \sup_{\mathbf{v}_h \in \mathcal{V}_{0,h}} \frac{-(\mathbf{f}, \mathbf{v}_h)_{\mathbf{L}^2(\Omega)} + k_h(\mathbf{u}_h, \mathbf{v}_h) + c(\mathbf{u}_h, \mathbf{u}_h; \mathbf{v}_h)}{\|\mathbf{v}_h\|_h} \\
&\leq \sup_{\mathbf{v}_h \in \mathcal{V}_{0,h}} \frac{\|\mathbf{f}\|_{\mathbf{L}^2(\Omega)} \|\mathbf{v}_h\|_{\mathbf{L}^2(\Omega)} + 2\nu C_{cont} \|\mathbf{u}_h\|_h \|\mathbf{v}_h\|_h + C_o \|\mathbf{u}_h\|_h^2 \|\mathbf{v}_h\|_h}{\|\mathbf{v}_h\|_h} \\
&\leq \sup_{\mathbf{v}_h \in \mathcal{V}_{0,h}} \frac{C_{poin} \|\mathbf{f}\|_{\mathbf{L}^2(\Omega)} \|\mathbf{v}_h\|_h + 2\nu C_{cont} \|\mathbf{u}_h\|_h \|\mathbf{v}_h\|_h + C_o \|\mathbf{u}_h\|_h^2 \|\mathbf{v}_h\|_h}{\|\mathbf{v}_h\|_h}.
\end{aligned}$$

The result then follows by invoking the bound for  $\mathbf{u}_h$ .  $\square$

To the best of our knowledge, the above theorem is the first of its kind for  $\mathbf{H}^1$  hexahedral-based finite element discretizations written in divergence-form. Such a result also hypothetically exists for Scott-Vogelius discretizations on tetrahedra [195], but these discretizations are limited to an extremely restrictive class of macro-element meshes. Well-posedness gives us the confidence that, at the very least, our formulation gives a unique solution under a smallness condition not unlike that for the continuous problem. In the next section, we will show that our discrete solution converges to the exact solution under a slightly more restrictive smallness condition.

It is interesting to note that the proof of Theorem 7.3.1 guarantees that the fixed point iteration given by (7.33) converges to the exact solution for *any* initial divergence-free velocity field. Furthermore, the iterates exhibit the linear convergence rate

$$\|\mathbf{u}_{n+1} - \mathbf{u}_n\|_h \leq \mu^n \|\mathbf{u}_1 - \mathbf{u}_0\|_h$$

for

$$\mu = \frac{C_o C_{poin}}{(2\nu)^2 C_{coerc}^2} \|\mathbf{f}\|_{\mathbf{L}^2(\Omega)} < 1.$$

This fixed-point scheme can be accelerated using a Newton-Raphson procedure.

## 7.4 *A Priori* Error Estimates for Small Data

We are now ready to show that our discrete solution fields converge to the exact solution fields under a smallness and regularity condition. Our method of proof largely mimics that of Theorem 4.8 in [48] for the two-dimensional Navier-Stokes equations. However, our proof is more straight-forward, primarily due to four facts: (1) we employ natively divergence-free discretizations, (2) we employ smooth approximation spaces, (3) we have a simpler treatment of the convection operator, and (4) we do not include stress as an auxiliary variable.

Our first error estimate reads as follows. Note that it is explicit in the mesh-size  $h$ , the diffusivity  $\nu$ , and the penalty parameter  $C_{pen}$ .

**Theorem 7.4.1.** *Assume (6.19) and (6.20) are satisfied, and further assume that*

$$\max \left\{ \frac{C_o C_{poin}}{(2\nu)^2 C_{coerc}^2}, \frac{C_\Omega C_{poin}}{\nu^2}, \frac{C_o C_{poin}}{\nu^2 C_{coerc}} \right\} \|\mathbf{f}\|_{\mathbf{L}^2(\Omega)} < 1 \quad (7.38)$$

where  $C_o$  is the continuity constant appearing in Lemma 7.3.1,  $C_{poin}$  is the Poincaré constant appearing in (6.14),  $C_\Omega$  is the domain-dependent constant appearing in Theorem 7.1.1, and  $C_{coerc}$  is the coercivity constant appearing in Corollary 7.3.1. Let  $(\mathbf{u}, p)$  and  $(\mathbf{u}_h, p_h)$  denote the solutions of Problems (W) and (G) respectively. Under the assumption that  $\mathbf{u} \in \mathbf{H}^{3/2+\epsilon}(\Omega)$  for some  $\epsilon > 0$ , we have

$$\|\mathbf{u} - \mathbf{u}_h\|_h \leq (1 + 2\kappa\gamma) \inf_{\mathbf{v}_h \in \hat{\mathbf{V}}_{0,h}} \|\mathbf{u} - \mathbf{v}_h\|_h \quad (7.39)$$

and

$$\|p - p_h\|_{L^2(\Omega)} \leq \left(1 + \frac{1}{\tilde{\beta}}\right) \inf_{q_h \in \mathcal{Q}_{0,h}} \|p - q_h\|_{L^2(\Omega)} + \frac{\kappa}{\tilde{\beta}} \|\mathbf{u} - \mathbf{u}_h\|_h \quad (7.40)$$

where

$$\kappa = 2\nu C_{cont} + \left(1 + \frac{1}{2C_{coerc}}\right) \frac{C_o C_{poin}}{\nu} \|\mathbf{f}\|_{\mathbf{L}^2(\Omega)} < 2\nu (C_{cont} + 2C_{coerc}^2 + C_{coerc}), \quad (7.41)$$

$$\gamma = \frac{1}{2\nu C_{coerc}}, \quad (7.42)$$

and  $\tilde{\beta}$  and  $C_{cont}$  are the inf-sup and continuity constants appearing in Corollary 7.3.1.

*Proof.* We begin by proving the estimate for the velocity error. Let  $\mathbf{v}_h \in \mathring{\mathcal{V}}_{0,h}$  such that  $\operatorname{div} \mathbf{v}_h = 0$ . By the coercivity of  $k_h(\cdot, \cdot)$  over  $\mathring{\mathcal{V}}_{0,h}$ , we have

$$2\nu C_{coerc} \|\mathbf{v}_h - \mathbf{u}_h\|_h^2 \leq k_h(\mathbf{v}_h - \mathbf{u}_h, \mathbf{v}_h - \mathbf{u}_h).$$

By the consistency given by Corollary 7.2.1 and the divergence-free condition  $\operatorname{div}(\mathbf{v}_h - \mathbf{u}_h) = 0$ , we have

$$\begin{aligned} k_h(\mathbf{v}_h - \mathbf{u}_h, \mathbf{v}_h - \mathbf{u}_h) &= k_h(\mathbf{v}_h - \mathbf{u}, \mathbf{v}_h - \mathbf{u}_h) \\ &\quad - c(\mathbf{u}, \mathbf{u}; \mathbf{v}_h - \mathbf{u}_h) + c(\mathbf{u}_h, \mathbf{u}_h; \mathbf{v}_h - \mathbf{u}_h). \end{aligned}$$

Then, by using the continuity of  $k_h(\cdot, \cdot)$ , we can write

$$\begin{aligned} 2\nu C_{coerc} \|\mathbf{v}_h - \mathbf{u}_h\|_h^2 &\leq k_h(\mathbf{v}_h - \mathbf{u}, \mathbf{v}_h - \mathbf{u}_h) \\ &\quad - c(\mathbf{u}, \mathbf{u}; \mathbf{v}_h - \mathbf{u}_h) + c(\mathbf{u}_h, \mathbf{u}_h; \mathbf{v}_h - \mathbf{u}_h) \\ &\leq 2\nu C_{cont} \|\mathbf{v}_h - \mathbf{u}\|_h \|\mathbf{v}_h - \mathbf{u}_h\|_h + T \end{aligned} \quad (7.43)$$

where

$$T := -c(\mathbf{u}, \mathbf{u}; \mathbf{v}_h - \mathbf{u}_h) + c(\mathbf{u}_h, \mathbf{u}_h; \mathbf{v}_h - \mathbf{u}_h).$$

We now utilize a splitting. Let us decompose

$$T = T_1 + T_2 + T_3 + T_4 \quad (7.44)$$

where

$$T_1 = -c(\mathbf{v}_h, \mathbf{u}; \mathbf{v}_h - \mathbf{u}_h) + c(\mathbf{u}_h, \mathbf{u}; \mathbf{v}_h - \mathbf{u}_h)$$

$$T_2 = -c(\mathbf{u}_h, \mathbf{v}_h - \mathbf{u}_h; \mathbf{v}_h - \mathbf{u}_h)$$

$$T_3 = c(\mathbf{v}_h, \mathbf{u}; \mathbf{v}_h - \mathbf{u}_h) - c(\mathbf{u}, \mathbf{u}; \mathbf{v}_h - \mathbf{u}_h)$$

$$T_4 = c(\mathbf{u}_h, \mathbf{v}_h - \mathbf{u}; \mathbf{v}_h - \mathbf{u}_h).$$

By Lemma 7.3.1, we can write

$$T_1 \leq C_o |\mathbf{u}|_{\mathbf{H}^1(\Omega)} \|\mathbf{v}_h - \mathbf{u}_h\|_h^2$$

$$T_3 \leq C_o |\mathbf{u}|_{\mathbf{H}^1(\Omega)} \|\mathbf{v}_h - \mathbf{u}_h\|_h \|\mathbf{v}_h - \mathbf{u}\|_h$$

$$T_4 \leq C_o \|\mathbf{u}_h\|_h \|\mathbf{v}_h - \mathbf{u}_h\|_h \|\mathbf{v}_h - \mathbf{u}\|_h$$

and by Lemma 7.3.2, we have

$$T_2 = 0. \quad (7.45)$$

Theorems 7.1.1 and 7.3.1 immediately give the bounds

$$T_1 \leq \frac{C_o C_{poin}}{\nu} \|\mathbf{f}\|_{\mathbf{L}^2(\Omega)} \|\mathbf{v}_h - \mathbf{u}_h\|_h^2. \quad (7.46)$$

$$T_3 \leq \frac{C_o C_{poin}}{\nu} \|\mathbf{f}\|_{\mathbf{L}^2(\Omega)} \|\mathbf{v}_h - \mathbf{u}_h\|_h \|\mathbf{v}_h - \mathbf{u}\|_h \quad (7.47)$$

$$T_4 \leq \frac{C_o C_{poin}}{2\nu C_{coerc}} \|\mathbf{f}_h\|_{\mathbf{L}^2(\Omega)} \|\mathbf{v}_h - \mathbf{u}_h\|_h \|\mathbf{v}_h - \mathbf{u}\|_h \quad (7.48)$$

Plugging (7.44), (7.45), (7.46), (7.47), and (7.48) into (7.43), we obtain

$$(1 - \alpha) \|\mathbf{v}_h - \mathbf{u}_h\|_h \leq \kappa \gamma \|\mathbf{v}_h - \mathbf{u}\|_h$$

where

$$\alpha = \frac{C_o C_{poin}}{2\nu^2 C_{coerc}} \|\mathbf{f}\|_{\mathbf{L}^2(\Omega)},$$

$$\gamma = \frac{1}{2\nu C_{coerc}},$$

and

$$\kappa = 2\nu C_{cont} + \left(1 + \frac{1}{2C_{coerc}}\right) \frac{C_o C_{poin}}{\nu} \|\mathbf{f}\|_{\mathbf{L}^2(\Omega)}.$$

By assumption,  $\alpha < 1/2$  and hence

$$\|\mathbf{v}_h - \mathbf{u}_h\|_h \leq 2\kappa\gamma \|\mathbf{v}_h - \mathbf{u}\|_h.$$

To finish the proof for the velocity error, we perform a sum decomposition of the true error as follows:

$$\begin{aligned} \|\mathbf{u} - \mathbf{u}_h\|_h &\leq \inf_{\mathbf{v}_h \in \hat{\mathcal{V}}_{0,h}} (\|\mathbf{u} - \mathbf{v}_h\|_h + \|\mathbf{v}_h - \mathbf{u}_h\|_h) \\ &\leq (1 + 2\kappa\gamma) \inf_{\mathbf{v}_h \in \hat{\mathcal{V}}_{0,h}} \|\mathbf{u} - \mathbf{v}_h\|_h. \end{aligned}$$

We now proceed onto the estimate for the pressure error. Let  $q_h \in \mathcal{Q}_{0,h}$ . By the inf-sup condition, we have

$$\|q_h - p_h\|_{L^2(\Omega)} \leq \frac{1}{\tilde{\beta}} \sup_{\mathbf{v}_h \in \mathcal{V}_{0,h}} \frac{b(q_h - p_h, \mathbf{v}_h)}{\|\mathbf{v}_h\|_h}. \quad (7.49)$$

By the consistency given by Corollary 7.2.1, we have, for any  $\mathbf{v}_h \in \mathcal{V}_{0,h}$ ,

$$\begin{aligned} b(q_h - p_h, \mathbf{v}_h) &= b(q_h - p, \mathbf{v}_h) + k_h(\mathbf{u} - \mathbf{u}_h, \mathbf{v}_h) \\ &\quad + c(\mathbf{u}, \mathbf{u}; \mathbf{v}_h) - c(\mathbf{u}_h, \mathbf{u}_h; \mathbf{v}_h) \\ &= b(q_h - p, \mathbf{v}_h) + k_h(\mathbf{u} - \mathbf{u}_h, \mathbf{v}_h) \\ &\quad + c(\mathbf{u}, \mathbf{u} - \mathbf{u}_h; \mathbf{v}_h) + c(\mathbf{u} - \mathbf{u}_h, \mathbf{u}_h; \mathbf{v}_h). \end{aligned}$$

Our continuity estimates from Corollary 7.3.1 and Lemma 7.3.1 then give the bound

$$b(q_h - p_h, \mathbf{v}_h) \leq \left( \|q_h - p\|_{L^2(\Omega)} + (2\nu C_{cont} + C_0 (\|\mathbf{u}\|_{\mathbf{H}^1(\Omega)} + \|\mathbf{u}_h\|_h)) \|\mathbf{u} - \mathbf{u}_h\|_h \right) \|\mathbf{v}_h\|_h.$$

Theorems 7.1.1 and 7.3.1 give

$$2\nu C_{cont} + C_0 (\|\mathbf{u}\|_{\mathbf{H}^1(\Omega)} + \|\mathbf{u}_h\|_h) \leq \kappa,$$

so we can write

$$b(q_h - p_h, \mathbf{v}_h) \leq \left( \|q_h - p\|_{L^2(\Omega)} + \kappa \|\mathbf{u} - \mathbf{u}_h\|_h \right) \|\mathbf{v}_h\|_h.$$

Plugging the above expression into (7.49), we acquire the estimate

$$\|q_h - p_h\|_{L^2(\Omega)} \leq \frac{1}{\tilde{\beta}} \|q_h - p\|_{L^2(\Omega)} + \frac{\kappa}{\tilde{\beta}} \|\mathbf{u} - \mathbf{u}_h\|_h.$$

To finish the proof for the pressure error, we again perform a sum decomposition of the true error as follows:

$$\begin{aligned} \|p - p_h\|_{L^2(\Omega)} &\leq \inf_{q_h \in \mathcal{Q}_{0,h}} \left( \|p - q_h\|_{L^2(\Omega)} + \|q_h - p_h\|_{L^2(\Omega)} \right) \\ &\leq \left( 1 + \frac{1}{\tilde{\beta}} \right) \inf_{q_h \in \mathcal{Q}_{0,h}} \|p - q_h\|_{L^2(\Omega)} + \frac{\kappa}{\tilde{\beta}} \|\mathbf{u} - \mathbf{u}_h\|_h. \end{aligned}$$

□

Utilizing the same methodology as that used to prove Theorem 6.4.1, we arrive at our second error estimate.

**Theorem 7.4.2.** *Let the assumptions of Theorem 7.4.1 hold true. Furthermore, let  $(\mathbf{u}, p)$  and  $(\mathbf{u}_h, p_h)$  denote the solutions of Problems (W) and (G) respectively.*

Under the assumption that  $\mathbf{u} \in \mathbf{H}^{j+1}(\Omega)$  and  $p \in H^j(\Omega)$  for some  $j > 1/2$ , we have

$$\|\mathbf{u} - \mathbf{u}_h\|_h \leq C_{\mathbf{u}} (1 + 2\kappa\gamma) h^s \|\mathbf{u}\|_{\mathbf{H}^{s+1}(\Omega)} \quad (7.50)$$

and

$$\|p - p_h\|_{L^2(\Omega)} \leq C_p \left(1 + \frac{1}{\tilde{\beta}}\right) h^s \|p\|_{H^s(\Omega)} + \frac{\kappa}{\tilde{\beta}} \|\mathbf{u} - \mathbf{u}_h\|_h \quad (7.51)$$

for  $s = \min\{k', j\}$  where  $\kappa$  is defined by (7.41),  $\gamma$  is defined by (7.42),  $\tilde{\beta}$  is the discrete inf-sup constant,  $C_{\mathbf{u}}$  is a positive constant independent of  $h$  and  $\nu$  which asymptotically scales with the square root of  $C_{pen}$ , and  $C_p$  is a positive constant independent of  $h$ ,  $\nu$ , and  $C_{pen}$ .

Again, to the best of our knowledge, Theorems 7.4.1 and 7.4.2 are the first of their kind for  $\mathbf{H}^1$  hexahedral-based finite element discretizations written in divergence-form. Note that we have obtained error estimates which are optimal for the velocity field and suboptimal, by one order, for the pressure field under a smallness condition not unlike that of the continuous problem. In Section 7.6, we will employ a selection of problems with known analytical solutions to confirm our theoretical convergence rates. As was the case for the generalized Stokes problem, our numerical results will suggest our derived pressure error estimates may be conservative. The analysis presented here also covers singular solutions typically encountered in practice. We will later numerically study the effectiveness of our method for a singular test problem, lid-driven cavity flow.

## 7.5 Extension to Multi-Patch Domains

To extend our discretization to multi-patch domains, we strongly enforce normal continuity of our discrete velocity field between patches and weakly enforce

tangential continuity using a combination of upwinding and the interior penalty method. Invoking the notation set forth in Section 6.5, let us define the bilinear form

$$\begin{aligned}
k_h^*(\mathbf{w}, \mathbf{v}) &= \sum_{i=1}^{n_p} (2\nu \nabla^s \mathbf{w}, \nabla^s \mathbf{v})_{(L^2(\Omega_i))^{d \times d}} \\
&\quad - \sum_{F \in \mathcal{J}_h} \int_F 2\nu (\{\{\nabla^s \mathbf{v}\}\} : [\mathbf{w} \otimes \mathbf{n}] + \{\{\nabla^s \mathbf{w}\}\} : [\mathbf{v} \otimes \mathbf{n}]) \, ds \\
&\quad + \sum_{F \in \mathcal{J}_h} \int_F 2\nu \left( \frac{2C_{pen}}{h_F} [\mathbf{w} \otimes \mathbf{n}] : [\mathbf{v} \otimes \mathbf{n}] \right) \, ds \\
&\quad - \sum_{F \in \Gamma_h} \int_F 2\nu \left( ((\nabla^s \mathbf{v}) \mathbf{n}) \cdot \mathbf{w} + ((\nabla^s \mathbf{w}) \mathbf{n}) \cdot \mathbf{v} - \frac{C_{pen}}{h_F} \mathbf{w} \cdot \mathbf{v} \right) \, ds.
\end{aligned} \tag{7.52}$$

Now, for  $\Omega_i$  an arbitrary patch, let  $\mathbf{n}_i$  denote the outward-facing normal with respect to  $\partial\Omega_i$ . We define the upwind form

$$\begin{aligned}
c_h^*(\mathbf{w}, \mathbf{x}; \mathbf{v}) &= \sum_{i=1}^{n_p} -(\mathbf{w} \otimes \mathbf{x}, \nabla \mathbf{v})_{(L^2(\Omega_i))^{d \times d}} \\
&\quad + \sum_{i=1}^{n_p} \int_{\partial\Omega_i \setminus \partial\Omega} \frac{1}{2} (\mathbf{w} \cdot \mathbf{n}_i + |\mathbf{w} \cdot \mathbf{n}_i|) \mathbf{u} \cdot \mathbf{v} \, ds \\
&\quad + \sum_{i=1}^{n_p} \int_{\partial\Omega_i \setminus \partial\Omega} \frac{1}{2} (\mathbf{w} \cdot \mathbf{n}_i - |\mathbf{w} \cdot \mathbf{n}_i|) \mathbf{u}^e \cdot \mathbf{v} \, ds
\end{aligned}$$

for  $\mathbf{w}, \mathbf{x}, \mathbf{v} \in \mathbf{H}_0(\text{div}; \Omega)$  where  $\mathbf{u}^e$  is the trace of  $\mathbf{u}$  taken from the exterior of  $\Omega_i$ . We would like to remark that the above form is nonlinear in  $\mathbf{w}$ . Furthermore, the form satisfies the semi-coercivity result  $c_h^*(\mathbf{w}, \mathbf{v}; \mathbf{v}) \geq 0$ , and  $c_h^*(\mathbf{w}, \mathbf{x}; \mathbf{v}) = 0$  for constant vector-valued functions  $\mathbf{v} : \Omega \rightarrow \mathbb{R}^d$ . Hence, the upwind form is conservative.

With all the preceding terminology defined, our discrete multi-patch formu-

lation reads as follows.

$$(MP) \left\{ \begin{array}{l} \text{Find } \mathbf{u}_h \in \mathcal{V}_{0,h} \text{ and } p_h \in \mathcal{Q}_{0,h} \text{ such that} \\ k_h^*(\mathbf{u}_h, \mathbf{v}_h) + c^*(\mathbf{u}_h, \mathbf{u}_h; \mathbf{v}_h) - b(p_h, \mathbf{v}_h) + b(q_h, \mathbf{u}_h) = (\mathbf{f}, \mathbf{v}_h)_{\mathbf{L}^2(\Omega)} \\ \text{for all } \mathbf{v}_h \in \mathcal{V}_{0,h} \text{ and } q_h \in \mathcal{Q}_{0,h}. \end{array} \right. \quad (7.53)$$

As in the single patch setting, the discrete formulation detailed above returns a pointwise divergence-free velocity field. However, just as was the case for the generalized Stokes equations, we do not yet have a convergence analysis available. This is a current topic of research.

## 7.6 Numerical Verification of Convergence Estimates

In this section, we numerically verify our convergence estimates using a collection of problems with exact solutions. Throughout, we choose Nitsche's penalty constant as

$$C_{pen} = 5(k' + 1)$$

as was done in the previous chapter. Additionally, we employ uniform parametric meshes, linear parametric mappings, and B-spline spaces of maximal continuity.

### 7.6.1 Two-Dimensional Manufactured Solution

As a first numerical experiment, we consider the two-dimensional vortex solution that was presented in Subsection 6.6.1. Let

$$\Omega \equiv (0, 1)^2$$

and

$$\mathbf{f} \equiv \nabla \cdot (\bar{\mathbf{u}} \otimes \bar{\mathbf{u}}) - \nabla \cdot (2\nu \nabla^s \bar{\mathbf{u}}) + \nabla \bar{p}$$

with

$$\bar{\mathbf{u}} = \begin{bmatrix} 2e^x(-1+x)^2x^2(y^2-y)(-1+2y) \\ (-e^x(-1+x)x(-2+x(3+x))(-1+y)^2y^2) \end{bmatrix}$$

and

$$\bar{p} = (-424 + 156e + (y^2 - y)(-456 + e^x(456 + x^2(228 - 5(y^2 - y))) + 2x(-228 + (y^2 - y)) + 2x^3(-36 + (y^2 - y)) + x^4(12 + (y^2 - y))))).$$

Homogeneous boundary conditions are applied along the boundary  $\partial\Omega$ , and the condition  $\int_{\Omega} p d\mathbf{x} = 0$  is enforced. A solution to the steady Navier-Stokes problem with the prescribed forcing is then clearly  $(\mathbf{u}, p) = (\bar{\mathbf{u}}, \bar{p})$ , and this solution is unique provided a smallness condition is satisfied. The streamlines and pressure contours associated with the solution are plotted in Figure 6.2.

To confirm our theoretically derived error estimates, we have computed convergence rates for divergence-conforming B-spline discretizations of varying mesh size and polynomial degree. Furthermore, we have computed rates for a variety of Reynolds numbers

$$Re = \frac{UL}{\nu}$$

where  $U$  is a velocity scale parameter and  $L$  is a length scale parameter. We take  $U = 1$  and  $L = 1$ . In Table 7.1, we have plotted our numerically computed convergence rates for  $Re = 1$ . For this Reynold's number, the exact and discrete solutions are unique. Note immediately that our theoretically derived error estimates are confirmed. Second, note that the  $L^2$ -norm of the pressure error optimally converges like  $O(h^{k'+1})$ , which is an improvement over our theoretically derived estimate. Third, note that the results in Table 7.1 are identical to the Stokes results appearing in Table 6.2. Hence, the introduction of convection has not affected our numerical error.

While our theoretically derived error estimates only cover flows with “small Reynolds number” (and indeed uniqueness is only guaranteed under a smallness

Table 7.1: Steady vortex flow convergence rates in 2-D:  $Re = 1$

Polynomial degree  $k' = 1$

$h$	1/4	1/8	1/16	1/32	1/64
$\ \mathbf{u} - \mathbf{u}_h\ _h$	5.48e-2	2.80e-2	1.40e-2	7.00e-3	3.50e-3
order	-	0.97	1.00	1.00	1.00
$ \mathbf{u} - \mathbf{u}_h _{\mathbf{H}^1(\Omega)}$	5.48e-2	2.80e-2	1.40e-2	7.00e-3	3.50e-3
order	-	0.97	1.00	1.00	1.00
$\ \mathbf{u} - \mathbf{u}_h\ _{\mathbf{L}^2(\Omega)}$	2.77e-3	8.16e-4	2.28e-4	6.10e-5	1.58e-5
order	-	1.76	1.84	1.90	1.95
$\ p - p_h\ _{L^2(\Omega)}$	5.04e-3	1.38e-3	3.49e-4	8.72e-5	2.18e-5
order	-	1.87	1.98	2.00	2.00

Polynomial degree  $k' = 2$

$h$	1/4	1/8	1/16	1/32	1/64
$\ \mathbf{u} - \mathbf{u}_h\ _h$	9.71e-3	2.33e-3	5.68e-4	1.40e-4	3.48e-5
order	-	2.06	2.04	2.02	2.01
$ \mathbf{u} - \mathbf{u}_h _{\mathbf{H}^1(\Omega)}$	9.70e-3	2.33e-3	5.68e-4	1.40e-4	3.48e-5
order	-	2.06	2.04	2.02	2.01
$\ \mathbf{u} - \mathbf{u}_h\ _{\mathbf{L}^2(\Omega)}$	2.94e-4	3.84e-5	5.03e-6	6.47e-7	8.21e-8
order	-	2.94	2.93	2.96	2.98
$\ p - p_h\ _{L^2(\Omega)}$	1.08e-3	1.12e-4	1.17e-5	1.19e-6	1.27e-7
order	-	3.40	3.26	3.30	3.23

Polynomial degree  $k' = 3$

$h$	1/4	1/8	1/16	1/32	1/64
$\ \mathbf{u} - \mathbf{u}_h\ _h$	9.86e-4	1.28e-4	1.66e-5	2.13e-6	2.72e-7
order	-	2.95	2.95	2.96	2.97
$ \mathbf{u} - \mathbf{u}_h _{\mathbf{H}^1(\Omega)}$	9.83e-4	1.28e-4	1.65e-5	2.10e-6	2.66e-7
order	-	2.94	2.96	2.97	2.98
$\ \mathbf{u} - \mathbf{u}_h\ _{\mathbf{L}^2(\Omega)}$	3.05e-5	2.34e-6	1.59e-7	1.03e-8	6.55e-10
order	-	3.70	3.88	3.95	3.98
$\ p - p_h\ _{L^2(\Omega)}$	1.10e-4	5.64e-6	3.45e-7	2.19e-8	1.39e-9
order	-	4.29	4.03	3.98	3.98

Table 7.2: Robustness of 2-D divergence-free B-spline discretizations as  $Re \rightarrow \infty$

Polynomial degree  $k' = 1, h = 1/16$

$Re$	1	10	100	1000	10000
$\ \mathbf{u} - \mathbf{u}_h\ _h$	1.40e-2	1.40e-2	1.40e-2	1.40e-2	1.40e-2
$ \mathbf{u} - \mathbf{u}_h _{\mathbf{H}^1(\Omega)}$	1.40e-2	1.40e-2	1.40e-2	1.40e-2	1.40e-2
$\ \mathbf{u} - \mathbf{u}_h\ _{\mathbf{L}^2(\Omega)}$	2.28e-4	2.28e-4	2.28e-4	2.28e-4	2.28e-4
$\ p - p_h\ _{L^2(\Omega)}$	3.49e-4	1.98e-4	1.96e-4	1.96e-4	1.96e-4

Polynomial degree  $k' = 2, h = 1/16$

$Re$	1	10	100	1000	10000
$\ \mathbf{u} - \mathbf{u}_h\ _h$	5.68e-4	5.68e-4	5.68e-4	5.68e-4	5.68e-4
$ \mathbf{u} - \mathbf{u}_h _{\mathbf{H}^1(\Omega)}$	5.68e-4	5.68e-4	5.68e-4	5.68e-4	5.68e-4
$\ \mathbf{u} - \mathbf{u}_h\ _{\mathbf{L}^2(\Omega)}$	5.03e-6	5.03e-6	5.03e-6	5.03e-6	5.03e-6
$\ p - p_h\ _{L^2(\Omega)}$	1.17e-5	6.50e-6	6.42e-4	6.42e-6	6.42e-6

Polynomial degree  $k' = 3, h = 1/16$

$Re$	1	10	100	1000	10000
$\ \mathbf{u} - \mathbf{u}_h\ _h$	1.66e-5	1.66e-5	1.66e-5	1.66e-5	1.66e-5
$ \mathbf{u} - \mathbf{u}_h _{\mathbf{H}^1(\Omega)}$	1.66e-5	1.66e-5	1.66e-5	1.66e-5	1.66e-5
$\ \mathbf{u} - \mathbf{u}_h\ _{\mathbf{L}^2(\Omega)}$	1.59e-7	1.59e-7	1.59e-7	1.59e-7	1.59e-7
$\ p - p_h\ _{L^2(\Omega)}$	3.45e-7	3.19e-7	3.19e-7	3.19e-7	3.19e-7

Table 7.3: Instability of conservative 2-D Taylor-Hood discretizations as  $Re \rightarrow \infty$

$\mathbf{Q}_2/Q_1$  velocity/pressure pair,  $h = 1/16$

$Re$	1	10	100	1000	10000
$ \mathbf{u} - \mathbf{u}_h _{\mathbf{H}^1(\Omega)}$	6.77e-4	7.11e-4	2.26e-3	2.16e-2	×
$\ \mathbf{u} - \mathbf{u}_h\ _{\mathbf{L}^2(\Omega)}$	6.54e-6	6.79e-6	1.97e-5	1.86e-4	×
$\ p - p_h\ _{L^2(\Omega)}$	1.96e-4	1.96e-4	1.96e-4	1.96e-4	×

condition), we have investigated the effectiveness of our discretization for larger Reynolds number flows and the two-dimensional forcing prescribed above. To compute these flow solutions, we used a Newton-Raphson nonlinear solver in conjunction with continuation. The results of this investigation are included in Table 7.2 for meshes with  $16 \times 16$  elements. Note that the velocity numerical errors in the tables appear independent of the Reynolds number. Moreover, the pressure numerical errors seem to improve with increasing Reynolds number. Hence, we are able to recover the desired flow solution  $(\mathbf{u}, p)$  for arbitrary Reynolds number. This observation attests to the enhanced stability properties of our discretization for nonlinear flow problems even in the absence of any external stabilization mechanisms. To contrast our methodology with standard mixed flow discretizations, we have repeated the above computations for conservative Taylor-Hood [106] finite element approximations, using again a continuation method in conjunction with a Newton-Raphson nonlinear solver. The results of these computations are included in Table 7.3. Note that the velocity error diverges with increasing Reynolds number. In fact, we were unable to compute a steady solution for  $Re = 10000$ , even when employing a damped Newton-Raphson method with line search. We believe that this divergence is inherently tied to the fact the Taylor-Hood approximations only satisfy the divergence-free constraint approximately.

### 7.6.2 Three-Dimensional Manufactured Solution

As a second numerical experiment, we consider the three-dimensional vortical solution that was presented in Subsection 6.6.2. Let

$$\Omega \equiv (0, 1)^3$$

and

$$\mathbf{f} \equiv \sigma \bar{\mathbf{u}} - \nabla \cdot (2\nu \nabla^s \bar{\mathbf{u}}) + \nabla \bar{p}$$

with

$$\bar{\mathbf{u}} = \mathbf{curl} \bar{\boldsymbol{\phi}},$$

$$\bar{\boldsymbol{\phi}} = \begin{bmatrix} x(x-1)y^2(y-1)^2z^2(z-1)^2 \\ 0 \\ x^2(x-1)^2y^2(y-1)^2z(z-1) \end{bmatrix},$$

and

$$\bar{p} = \sin(\pi x) \sin(\pi y) - \frac{4}{\pi^2}.$$

Again, homogeneous boundary conditions are applied along the boundary  $\partial\Omega$ , and the pressure is enforced to satisfy  $\int_{\Omega} p d\mathbf{x} = 0$ . A solution to the steady Navier-Stokes equations with the prescribed forcing is then clearly  $(\mathbf{u}, p) = (\bar{\mathbf{u}}, \bar{p})$ , and for sufficiently small data, this solution is unique. Streamlines associated with the exact solution are plotted in Figure 6.3.

For  $Re = 1$  flow (with  $Re = 1/\nu$ ), we have computed convergence rates for divergence-conforming B-spline discretizations of varying mesh size and polynomial degree. In Table 7.4, we have listed our numerically computed convergence rates. Note immediately that our theoretically derived error estimates are confirmed. Second, note that the  $L^2$ -norm of the pressure error optimally converges like  $O(h^{k'+1})$ , which is an improvement over our theoretically derived estimate. Third, note that, as in the two-dimensional setting, the results in Table 7.4 are identical to the Stokes results appearing in Table 6.5. Hence, the introduction of convection has not affected our numerical error.

Again, while our theoretically derived error estimates only cover flows with “small Reynolds number”, we have investigated the effectiveness of our discretization for larger Reynolds number flows and the three-dimensional forcing prescribed above. We used a Newton-Raphson nonlinear solver in conjunction with continuation. The results of this investigation are included in Table 7.5 for meshes with

Table 7.4: Steady vortex flow convergence rates in 3-D:  $Re = 1$ .

Polynomial degree $k' = 1$					
$h$	1/2	1/4	1/8	1/16	1/32
$\ \mathbf{u} - \mathbf{u}_h\ _h$	1.83e-2	8.98e-3	4.18e-3	1.99e-3	9.62e-4
order	-	1.03	1.10	1.07	1.05
$ \mathbf{u} - \mathbf{u}_h _{\mathbf{H}^1(\Omega)}$	1.51e-2	7.64e-3	3.77e-3	1.87e-3	9.34e-4
order	-	0.98	1.02	1.01	1.00
$\ \mathbf{u} - \mathbf{u}_h\ _{\mathbf{L}^2(\Omega)}$	1.35e-3	3.68e-4	1.03e-4	2.81e-5	7.40e-6
order	-	1.88	1.84	1.87	1.93
$\ p - p_h\ _{L^2(\Omega)}$	5.41e-2	1.48e-2	3.58e-3	8.85e-4	2.26e-4
order	-	1.87	2.05	2.02	1.97

Polynomial degree $k' = 2$					
$h$	1/2	1/4	1/8	1/16	1/32
$\ \mathbf{u} - \mathbf{u}_h\ _h$	6.50e-3	1.54e-3	4.10e-4	9.51e-5	2.15e-5
order	-	2.08	1.91	2.11	2.15
$ \mathbf{u} - \mathbf{u}_h _{\mathbf{H}^1(\Omega)}$	3.71e-3	9.90e-4	2.79e-4	6.59e-5	1.50e-5
order	-	1.91	1.83	2.08	2.14
$\ \mathbf{u} - \mathbf{u}_h\ _{\mathbf{L}^2(\Omega)}$	1.97e-4	4.25e-5	7.38e-6	8.67e-7	9.18e-8
order	-	2.21	2.53	3.09	3.23
$\ p - p_h\ _{L^2(\Omega)}$	1.50e-2	1.59e-3	2.00e-4	2.56e-5	3.26e-6
order	-	3.24	2.99	2.97	2.97

Table 7.5: Robustness of 3-D divergence-free B-spline discretizations as  $Re \rightarrow \infty$

Polynomial degree  $k' = 1, h = 1/16$

$Re$	1	10	100	1000	10000
$\ \mathbf{u} - \mathbf{u}_h\ _h$	1.99e-3	1.99e-3	1.99e-3	1.99e-3	1.99e-3
$\ \mathbf{u} - \mathbf{u}_h\ _{\mathbf{H}^1(\Omega)}$	1.87e-3	1.87e-3	1.87e-3	1.87e-3	1.87e-3
$\ \mathbf{u} - \mathbf{u}_h\ _{\mathbf{L}^2(\Omega)}$	2.81e-5	2.81e-5	2.81e-5	2.81e-5	2.81e-5
$\ p - p_h\ _{L^2(\Omega)}$	8.84e-4	8.84e-4	8.84e-4	8.84e-4	8.84e-4

Polynomial degree  $k' = 2, h = 1/16$

$Re$	1	10	100	1000	10000
$\ \mathbf{u} - \mathbf{u}_h\ _h$	9.51e-5	9.51e-5	9.51e-5	9.51e-5	9.51e-5
$\ \mathbf{u} - \mathbf{u}_h\ _{\mathbf{H}^1(\Omega)}$	6.59e-5	6.59e-5	6.59e-5	6.59e-5	6.59e-5
$\ \mathbf{u} - \mathbf{u}_h\ _{\mathbf{L}^2(\Omega)}$	8.67e-7	8.67e-7	8.67e-7	8.67e-7	8.67e-7
$\ p - p_h\ _{L^2(\Omega)}$	2.56e-5	2.56e-5	2.56e-5	2.56e-5	2.56e-5

$16 \times 16$  elements. Note that the velocity and pressure numerical errors appearing in the tables are independent of the Reynolds number. Hence, we are able to recover the desired flow solution  $(\mathbf{u}, p)$  for arbitrary Reynolds number.

### 7.6.3 Kovasznay Flow

As a final numerical experiment, we consider Kovasznay flow. Kovasznay flow refers to the flow behind an infinite two-dimensional grid, and it is often utilized as a convergence test for Navier-Stokes discretizations. The flow pattern is periodic and can be analytically derived [127]. Indeed, denoting  $Re = \frac{1}{\nu}$ , the flow solution satisfies

$$\mathbf{u} = \begin{bmatrix} 1 - e^{\lambda x} \cos(2\pi y) \\ \frac{\lambda}{2\pi} e^{\lambda x} \cos(2\pi y) \end{bmatrix}$$

and

$$p = \frac{1 - e^{2\lambda x}}{2}.$$

where

$$\lambda = \frac{\text{Re}}{2} - \sqrt{\frac{\text{Re}^2}{4} + 4\pi^2}.$$

The streamlines and pressure contours associated with the Kovasznay flow solution at  $Re = 40$  are plotted in Figure 7.1. Note that the streamlines closely resemble the streamlines associated with steady flow behind a cylinder.

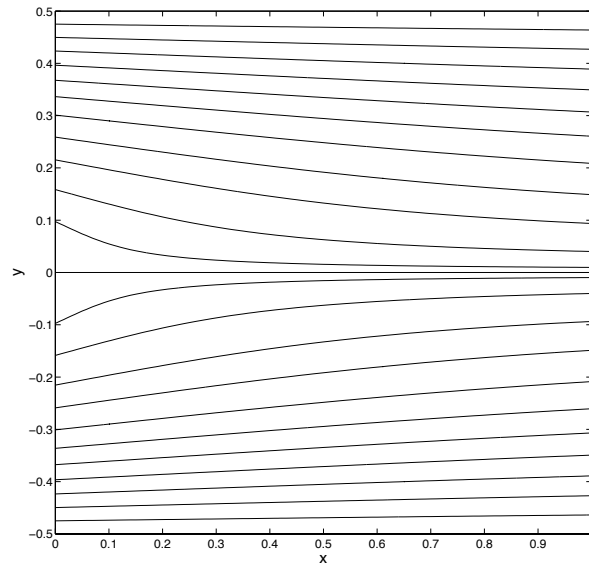
To solve the Kovasznay flow problem numerically, we restrict ourselves to the domain  $\Omega = (0, 1) \times (-1/2, 1/2)$ . On the left, bottom, and top sides of the domain, we enforce Dirichlet boundary conditions. On the right side of the domain, we enforce a traction boundary condition. On the interior of the domain, we apply the usual forcing

$$\mathbf{f} \equiv \nabla \cdot (\mathbf{u} \otimes \mathbf{u}) - \nabla \cdot (2\nu \nabla^s \mathbf{u}) + \nabla p.$$

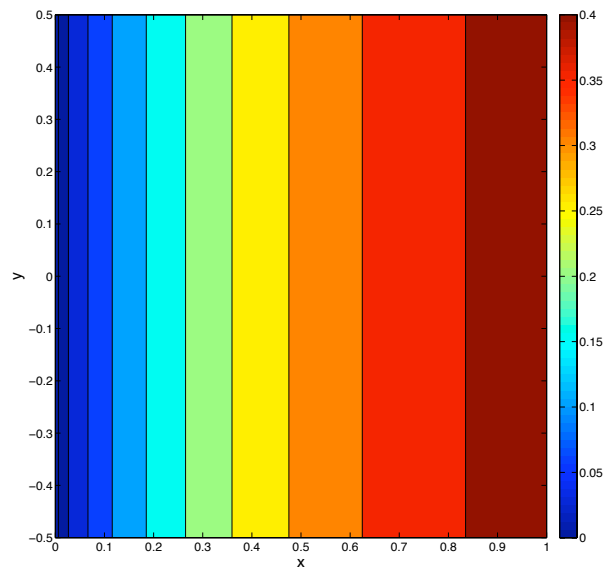
We have computed  $Re = 40$  flow convergence rates for a wide variety of divergence-conforming B-spline discretizations. These rates are summarized in Table 7.6. Note that the convergence rates are approaching the optimal rates as  $h \rightarrow 0$  for both the velocity and pressure field. However, it is apparent that even for  $h = 1/64$  our computations still lie in the pre-asymptotic range.

## 7.7 Benchmark Problems

In this section, we investigate the effectiveness of our methodology as applied to two benchmark problems: two-dimensional lid-driven cavity flow and confined jet impingement. As previously, we choose Nitsche's penalty constant as  $C_{pen} = 5(k' + 1)$  for all of the following examples, and we employ uniform parametric meshes, linear parametric mappings, and B-spline spaces of maximal continuity.



(a)



(b)

Figure 7.1: Steady Kovaszny flow: (a) Streamlines for  $Re = 40$ , (b) Pressure contours for  $Re = 40$ .

Table 7.6: Steady Kovasznay flow convergence rates:  $Re = 40$

Polynomial degree  $k' = 1$

$h$	1/4	1/8	1/16	1/32	1/64
$ \mathbf{u} - \mathbf{u}_h _{\mathbf{H}^1(\Omega)}$	1.39e0	7.31e-1	3.69e-1	1.84e-1	9.19e-2
order	-	0.93	0.99	1.00	1.00
$\ \mathbf{u} - \mathbf{u}_h\ _{\mathbf{L}^2(\Omega)}$	5.31e-2	1.98e-2	6.78e-3	2.15e-3	6.34e-4
order	-	1.43	1.54	1.66	1.76
$\ p - p_h\ _{L^2(\Omega)}$	3.98e-2	1.49e-2	4.73e-3	1.35e-3	3.75e-4
order	-	1.42	1.65	1.81	1.85

Polynomial degree  $k' = 2$

$h$	1/4	1/8	1/16	1/32	1/64
$ \mathbf{u} - \mathbf{u}_h _{\mathbf{H}^1(\Omega)}$	4.59e-1	1.17e-1	2.78e-2	6.69e-3	1.64e-3
order	-	1.97	2.08	2.05	2.03
$\ \mathbf{u} - \mathbf{u}_h\ _{\mathbf{L}^2(\Omega)}$	1.44e-2	1.96e-3	2.41e-4	3.04e-5	2.83e-6
order	-	2.88	3.02	2.99	2.99
$\ p - p_h\ _{L^2(\Omega)}$	1.65e-2	3.55e-3	5.14e-4	7.05e-5	9.56e-6
order	-	2.22	2.79	2.87	2.88

Polynomial degree  $k' = 3$

$h$	1/4	1/8	1/16	1/32	1/64
$ \mathbf{u} - \mathbf{u}_h _{\mathbf{H}^1(\Omega)}$	1.29e-1	1.52e-2	1.94e-3	2.55e-4	3.31e-5
order	-	3.08	2.98	2.92	2.95
$\ \mathbf{u} - \mathbf{u}_h\ _{\mathbf{L}^2(\Omega)}$	2.95e-3	1.97e-4	1.64e-5	1.20e-6	8.51e-8
order	-	3.91	3.59	3.77	3.81
$\ p - p_h\ _{L^2(\Omega)}$	5.59e-3	6.48e-4	5.75e-5	5.28e-6	4.00e-7
order	-	3.11	3.49	3.45	3.72

### 7.7.1 Two-Dimensional Lid-Driven Cavity Flow

As mentioned in the last chapter on generalized Stokes flow, two-dimensional lid-driven cavity flow is widely considered to be one of the classical test problems for the validation of numerical discretizations for incompressible flow simulation. In the presence of increasing Reynolds number, lid-driven cavity flow loses its symmetry and eventually becomes unsteady. The problem setup for lid-driven cavity flow is elaborated in Figure 6.13. For the computations here,  $H$  and  $U$  are defined to be 1. The Reynolds number associated with the flow is defined to be

$$Re = \frac{UH}{\nu}.$$

The left, right, and bottom sides of the cavity are fixed no-slip walls while the top side of the cavity is a wall which slides to the right with velocity magnitude  $U$ . The forcing  $\mathbf{f}$  is defined to be zero.

We have numerically simulated lid-driven cavity flow at  $Re = 100$ ,  $Re = 400$ , and  $Re = 1000$  using a variety of divergence-conforming B-spline discretizations. Streamlines computed using a mesh of degree  $k' = 1$  and size  $h = 1/128$  are plotted in Figures 7.2, 7.3, and 7.4 for  $Re = 100$ ,  $Re = 400$ , and  $Re = 1000$  respectively. These computed streamlines are visually indistinguishable from benchmark streamlines appearing in the literature. Note that as the Reynolds number increases, the solution loses symmetry.

We have compared our numerical results with the classical benchmarks results of Ghia *et al.* [85] for three different polynomial degrees ( $k' = 1$ ,  $k' = 2$ ,  $k' = 3$ ), three different mesh sizes ( $h = 1/32$ ,  $h = 1/64$ , and  $h = 1/128$ ), and the selected Reynolds numbers. The results of Ghia were obtained using a second-order upwind finite difference method on a stretched mesh with  $129^2$  grid points. In Figures 7.5(a), 7.6(a), and 7.7(a), we have compared our  $k' = 1$ ,  $Re = 100$  values

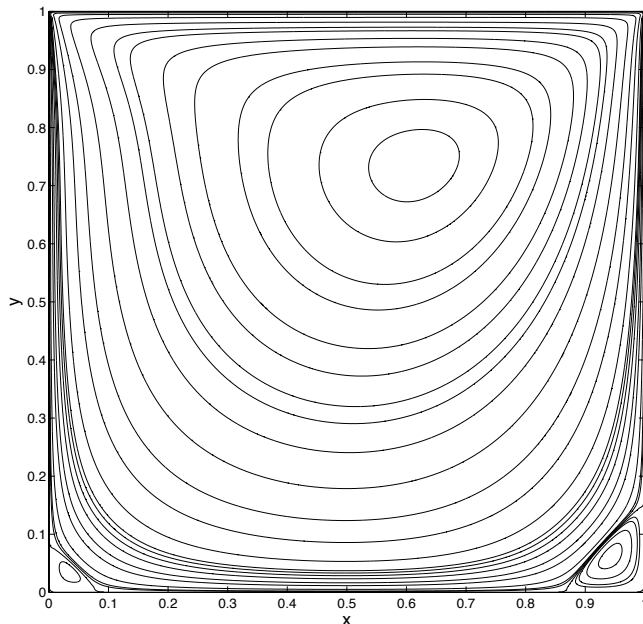


Figure 7.2: Lid-driven cavity flow: Streamlines for  $Re = 100$ .

for the first component of the velocity field along the vertical center line with those of Ghia, and in Figures 7.5(b), 7.6(b), and 7.7(b), we have compared our  $k' = 1$ ,  $Re = 100$  values for the second component of the velocity field along the horizontal center line. Note that our centerline velocity results are roughly independent of the mesh size. Second, note that while our results roughly match those of Ghia, there are discernible differences between the two sets of results even for our finest mesh. To investigate these differences further, we have invoked a set of converged pseudospectral results that were obtained via a subtraction method to remove the leading terms of the corner singularities [32]. In Table 7.7, we have compared our centerline results with these converged results as well as the results of Ghia. Note that our results are much more accurate than the results of Ghia for all mesh sizes and poly-

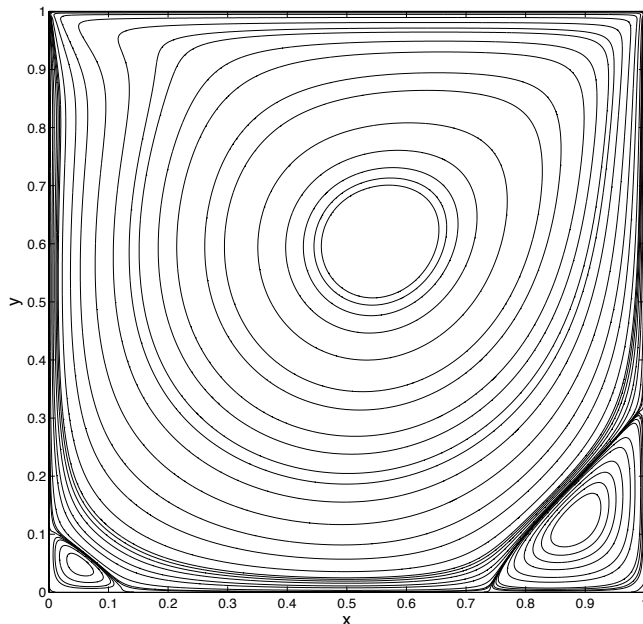


Figure 7.3: Lid-driven cavity flow: Streamlines for  $Re = 400$ .

nomial degrees. Furthermore, our results for  $k' = 2$  and  $k' = 3$  on a  $64 \times 64$  element mesh are indistinguishable from the converged pseudospectral results. This attests to the effectiveness of our discretization with increasing  $k'$ , even in the presence of singularities. We should also again remark that these results were obtained without stretched meshes and without stabilization. We believe that the combination of exact mass conservation and weak enforcement of the no-slip condition plays a pivotal role in the enhanced accuracy of our discretization scheme.

In Figures 7.8(a), 7.9(a), and 7.10(a), we have compared our  $k' = 1$ ,  $Re = 400$  values for the first component of the velocity field along the vertical center line with those of Ghia, and in Figures 7.8(b), 7.9(b), and 7.10(b), we have compared our  $k' = 1$ ,  $Re = 400$  values for the second component of the velocity field along

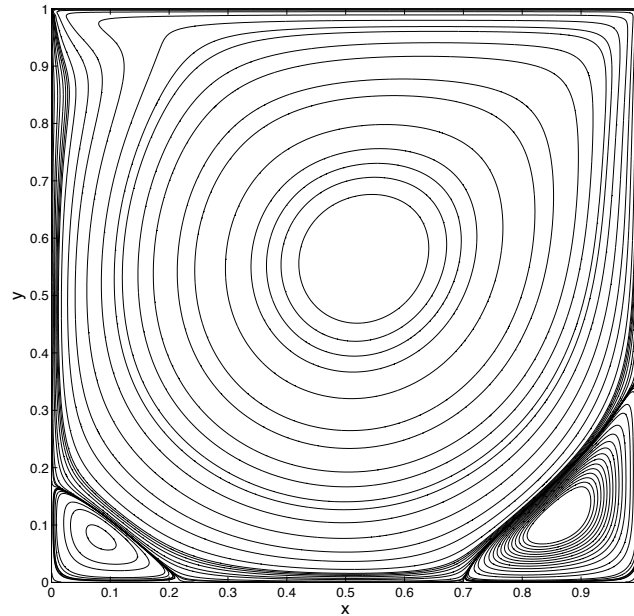


Figure 7.4: Lid-driven cavity flow: Streamlines for  $Re = 1000$ .

the horizontal center line. Note that our  $Re = 400$  results better match the results of Ghia than the  $Re = 100$  results. In fact, our  $Re = 400$  results are nearly indistinguishable from the benchmark results on the finest mesh. This is encouraging as the Ghia  $Re = 400$  results match well with highly-accurate extrapolated results in the literature [167]. Moreover, our results for the coarsest mesh better match the results of Ghia than any comparable second-order results we have seen in the literature. In Table 7.7, we have compared our centerline results with the results of Ghia along with our results for  $k' = 2$  and  $k' = 3$  on a  $64 \times 64$  element mesh. Note that our results appear to converge quickly with increasing  $k'$ , despite the increased smoothness of our discrete spaces. By using our  $k' = 3$  results as a benchmark, we see our  $k' = 1$  results are considerably more accurate than Ghia's results for  $h \leq 1/64$ .

Unfortunately, no pseudospectral results are available to use as comparison.

In Figures 7.11(a), 7.12(a), and 7.13(a), we have compared our  $k' = 1$ ,  $Re = 1000$  values for the first component of the velocity field along the vertical center line with those of Ghia, and in Figures 7.11(b), 7.12(b), and 7.13(b), we have compared our  $k' = 1$ ,  $Re = 1000$  values for the second component of the velocity field along the horizontal center line. This is a more challenging test case than either the  $Re = 100$  or  $Re = 400$  flows, and the coarse  $32 \times 32$  element mesh is not nearly fine enough to resolve the flow features. Nonetheless, our results for this coarse mesh better match the results of Ghia than any comparable second-order results we have seen in the literature. Our results for the  $64 \times 64$  and  $128 \times 128$  element meshes match Ghia's results even better. In Table 7.7, we have compared our centerline results with the results of Ghia along with a set of converged pseudospectral results with singularity subtraction [32]. As expected, the results of Ghia are more accurate than our coarse mesh results, but our results for the  $64 \times 64$  element mesh are comparable in accuracy and our results for the  $128 \times 128$  element mesh are considerably more accurate. We also computed results for the  $64 \times 64$  element mesh for polynomial degrees  $k' = 2$  and  $k' = 3$  and found our results quickly improved with increasing polynomial degree. Indeed, our results for  $k' = 3$  are nearly indistinguishable from the converged pseudospectral results.

To compute all of these flow examples, we utilized the Newton-Raphson method in conjunction with continuation. Specifically, for the  $Re = 100$  simulations, we employed Newton-Raphson using the results of a corresponding Stokes simulation as an initial guess. For the  $Re = 400$  simulations, we employed Newton-Raphson using the results of the  $Re = 100$  simulations as an initial guess, and so on. We found a maximum of four Newton-Raphson steps were required to achieve a sufficiently accurate solution for each nonlinear solve. Using this procedure, we

Table 7.7: Two-dimensional lid-driven cavity flow: Extrema of the velocity through the centerlines of the cavity.

$Re = 100$

Method	$u_{min}$	$v_{max}$	$v_{min}$
B-spline, $k' = 1$ and $h = 1/32$	-0.21551	0.18054	-0.25472
B-spline, $k' = 1$ and $h = 1/64$	-0.21443	0.17991	-0.25409
B-spline, $k' = 1$ and $h = 1/128$	-0.21414	0.17966	-0.25387
B-spline, $k' = 2$ and $h = 1/64$	-0.21404	0.17957	-0.25379
B-spline, $k' = 3$ and $h = 1/64$	-0.21404	0.17957	-0.25380
Pseudospectral (Ref. [32])	-0.21404	0.17957	-0.25380
Ghia <i>et al.</i> (Ref. [85])	-0.21090	0.17527	-0.24533

$Re = 400$

Method	$u_{min}$	$v_{max}$	$v_{min}$
B-spline, $k' = 1$ and $h = 1/32$	-0.33651	0.31039	-0.45768
B-spline, $k' = 1$ and $h = 1/64$	-0.33150	0.30605	-0.45659
B-spline, $k' = 1$ and $h = 1/128$	-0.32989	0.30471	-0.45470
B-spline, $k' = 2$ and $h = 1/64$	-0.32927	0.30415	-0.45406
B-spline, $k' = 3$ and $h = 1/64$	-0.32925	0.30413	-0.45401
Ghia <i>et al.</i> (Ref. [85])	-0.32376	0.30203	-0.44993

$Re = 1000$

Method	$u_{min}$	$v_{max}$	$v_{min}$
B-spline, $k' = 1$ and $h = 1/32$	-0.40140	0.39132	-0.54261
B-spline, $k' = 1$ and $h = 1/64$	-0.39399	0.38229	-0.53353
B-spline, $k' = 1$ and $h = 1/128$	-0.39021	0.37856	-0.52884
B-spline, $k' = 2$ and $h = 1/64$	-0.38874	0.37715	-0.52726
B-spline, $k' = 3$ and $h = 1/64$	-0.38857	0.37698	-0.52696
Pseudospectral (Ref. [32])	-0.38857	0.37694	-0.52707
Ghia <i>et al.</i> (Ref. [85])	-0.38289	0.37095	-0.51550

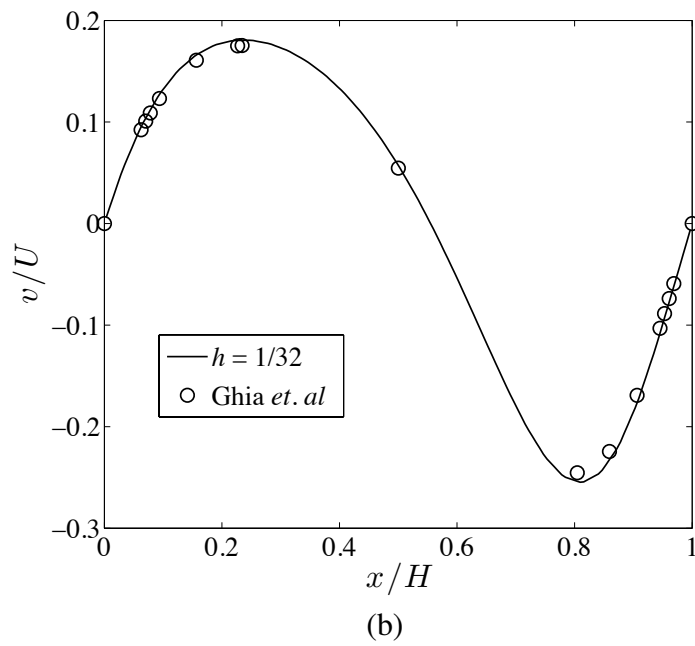
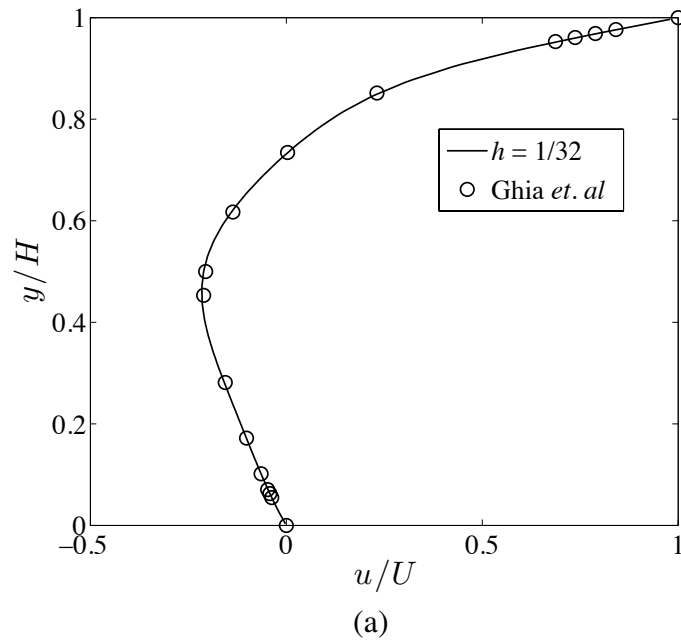


Figure 7.5: Lid-driven cavity flow: Velocity field for  $k' = 1$ ,  $h = 1/32$ , and  $Re = 100$ . (a) Value of the first component of the velocity field along the vertical center line, (b) Value of the second component of the velocity field along the horizontal center line.

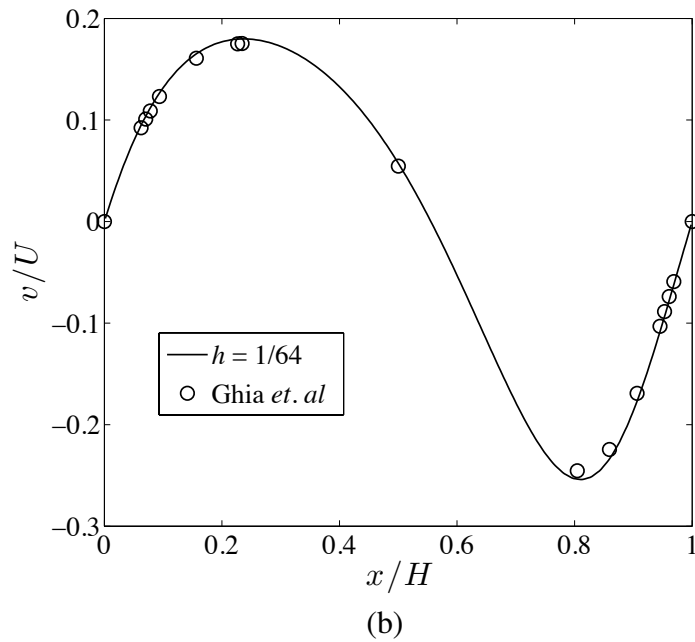
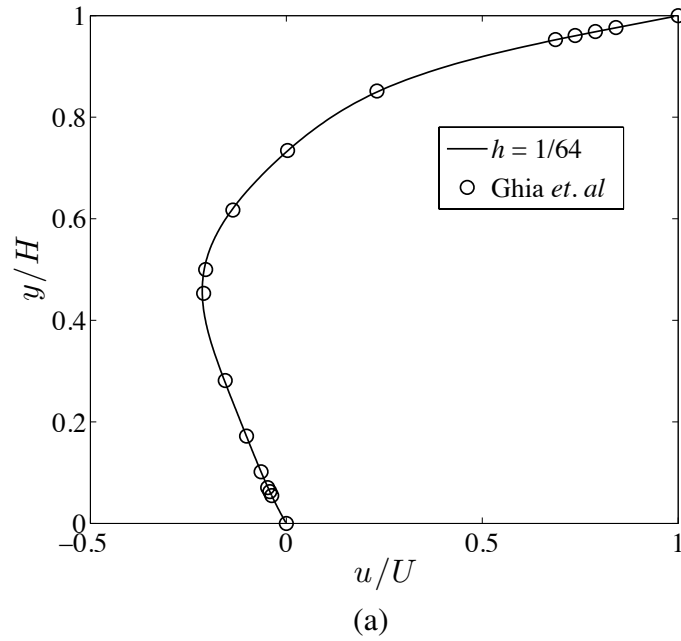


Figure 7.6: Lid-driven cavity flow: Velocity field for  $k' = 1$ ,  $h = 1/64$ , and  $Re = 100$ . (a) Value of the first component of the velocity field along the vertical center line, (b) Value of the second component of the velocity field along the horizontal center line.

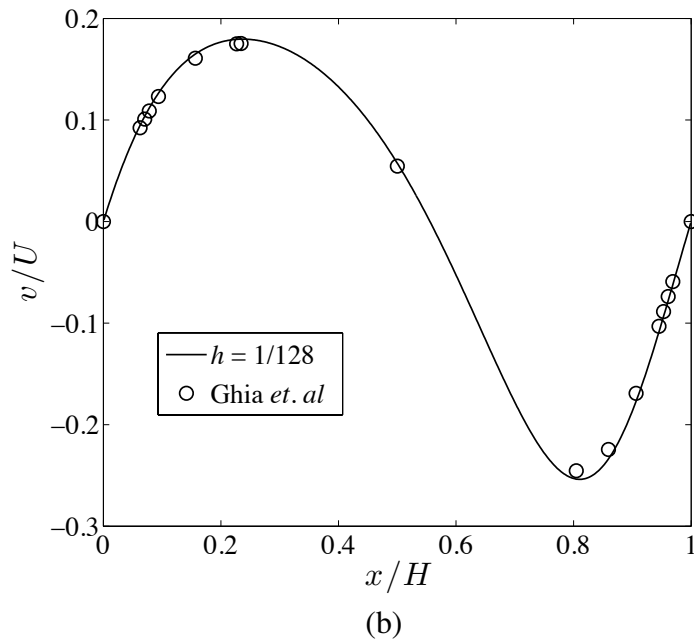
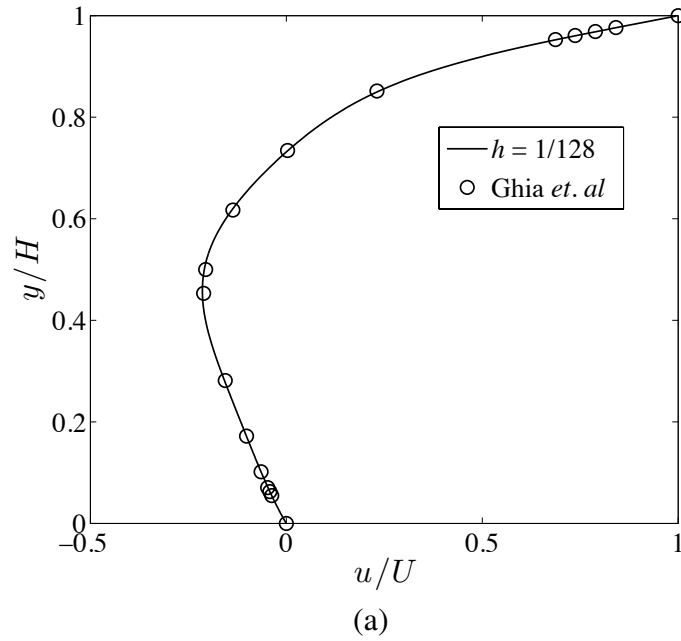


Figure 7.7: Lid-driven cavity flow: Velocity field for  $k' = 1$ ,  $h = 1/128$ , and  $Re = 100$ . (a) Value of the first component of the velocity field along the vertical center line, (b) Value of the second component of the velocity field along the horizontal center line.

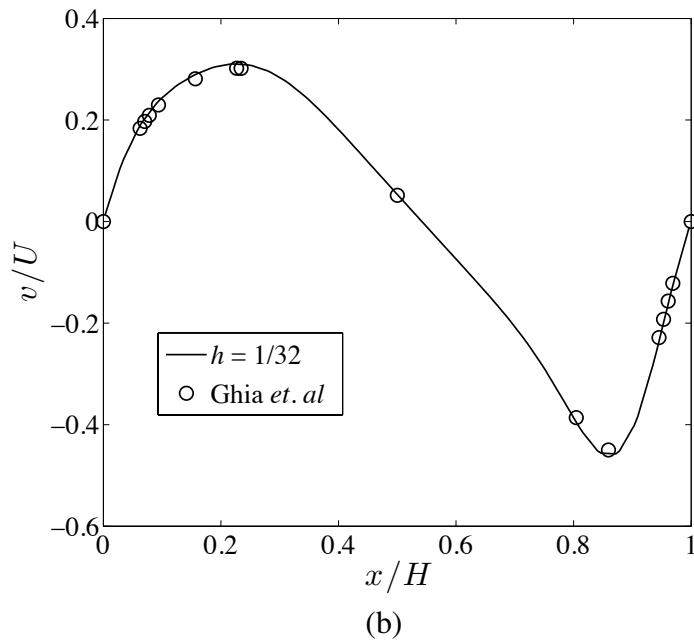
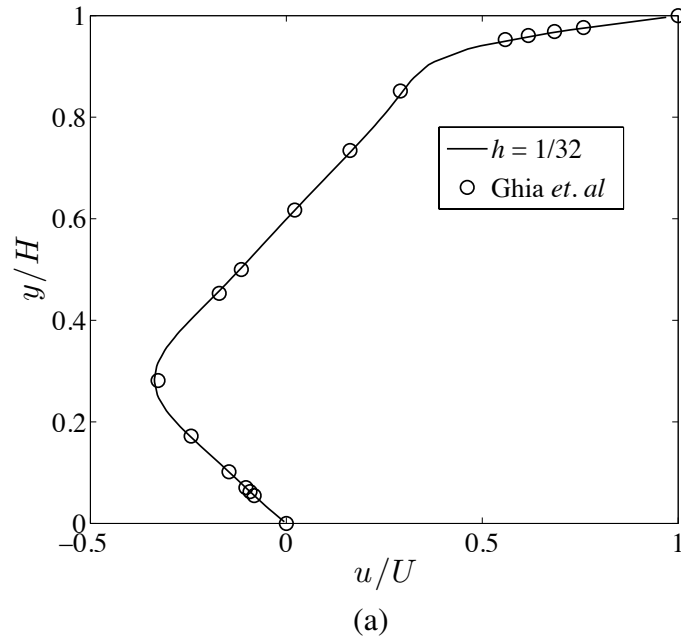
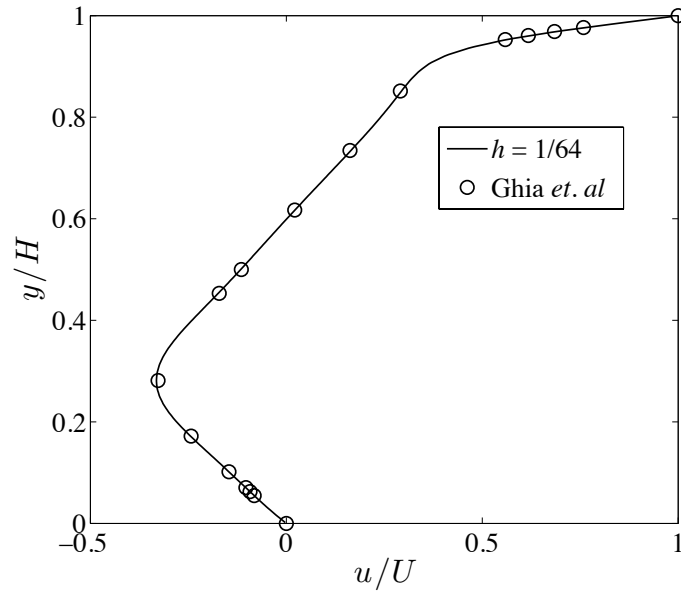
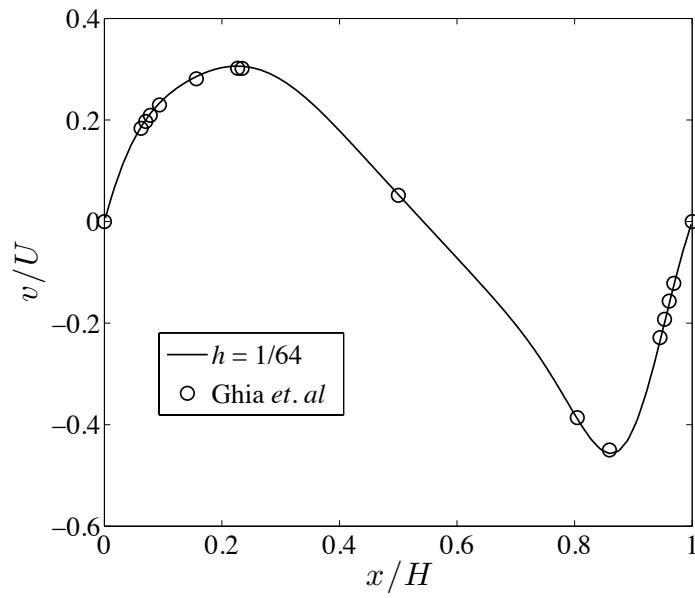


Figure 7.8: Lid-driven cavity flow: Velocity field for  $k' = 1$ ,  $h = 1/32$ , and  $Re = 400$ . (a) Value of the first component of the velocity field along the vertical center line, (b) Value of the second component of the velocity field along the horizontal center line.



(a)



(b)

Figure 7.9: Lid-driven cavity flow: Velocity field for  $k' = 1$ ,  $h = 1/64$ , and  $Re = 400$ . (a) Value of the first component of the velocity field along the vertical center line, (b) Value of the second component of the velocity field along the horizontal center line.

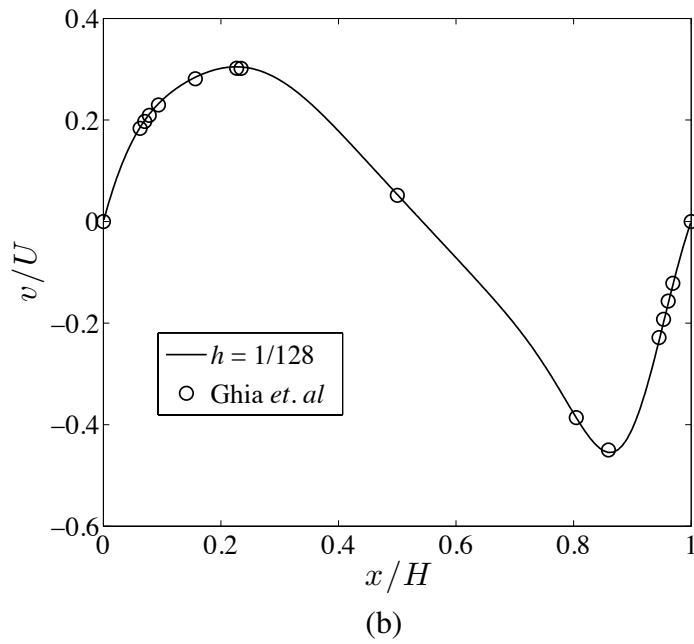
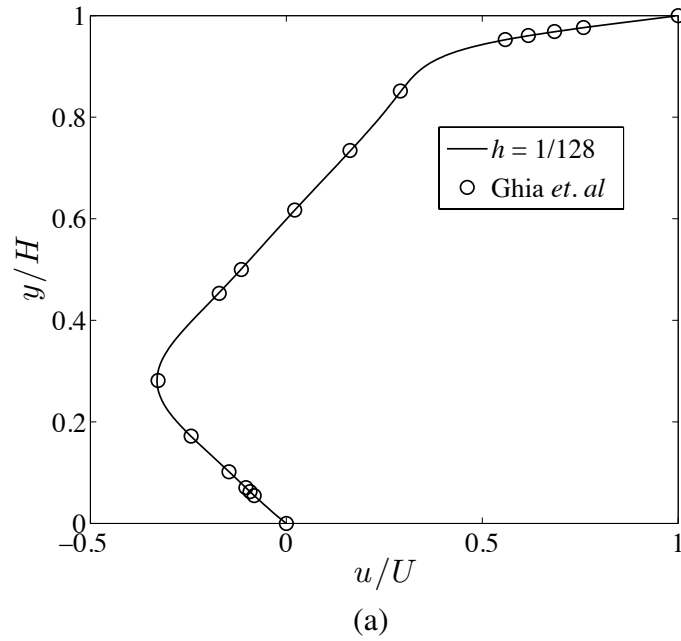


Figure 7.10: Lid-driven cavity flow: Velocity field for  $k' = 1$ ,  $h = 1/128$ , and  $Re = 400$ . (a) Value of the first component of the velocity field along the vertical center line, (b) Value of the second component of the velocity field along the horizontal center line.

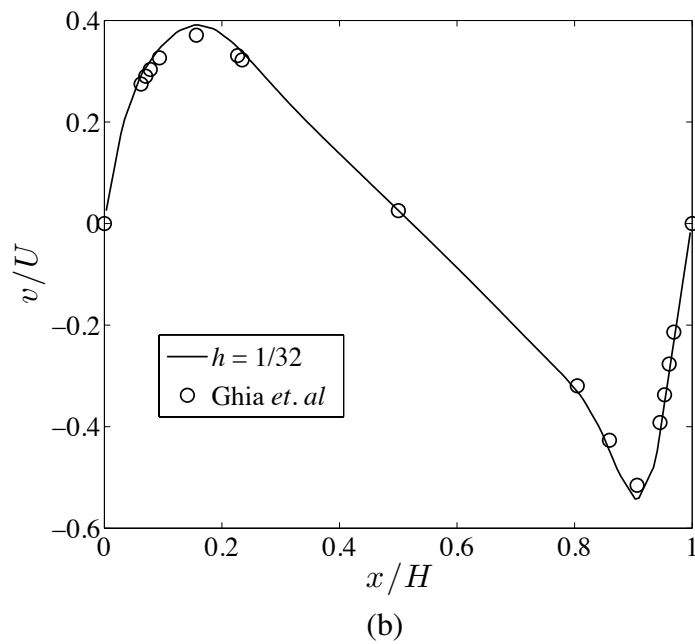
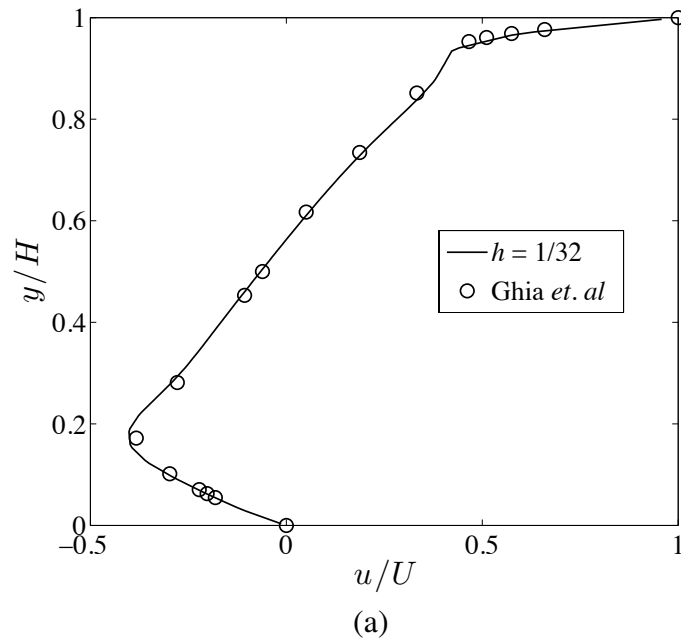


Figure 7.11: Lid-driven cavity flow: Velocity field for  $k' = 1$ ,  $h = 1/32$ , and  $Re = 1000$ . (a) Value of the first component of the velocity field along the vertical center line, (b) Value of the second component of the velocity field along the horizontal center line.

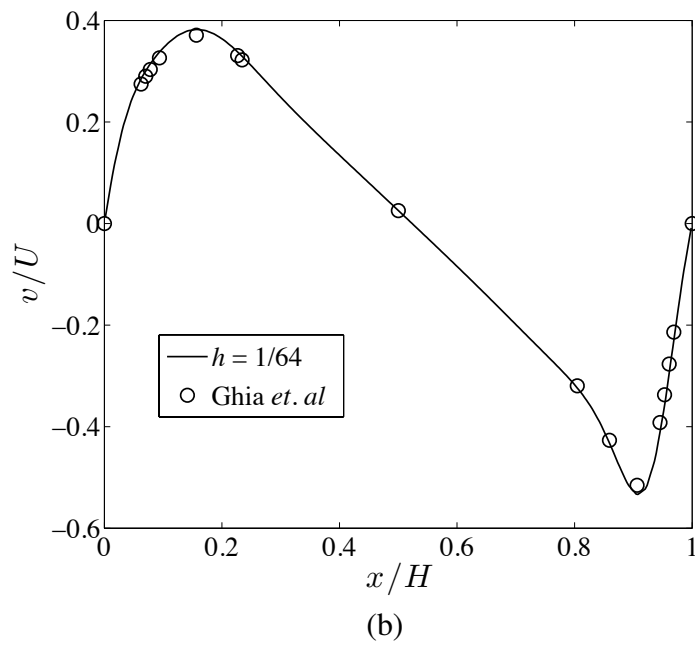
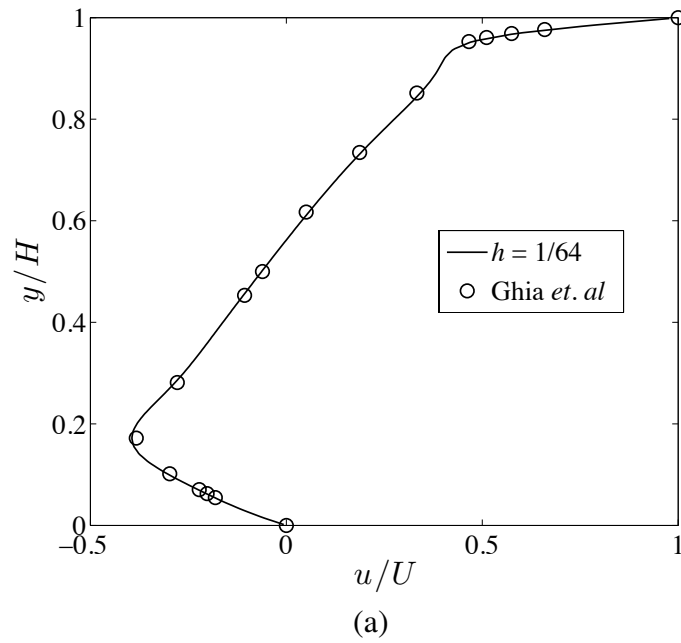


Figure 7.12: Lid-driven cavity flow: Velocity field for  $k' = 1$ ,  $h = 1/64$ , and  $Re = 1000$ . (a) Value of the first component of the velocity field along the vertical center line, (b) Value of the second component of the velocity field along the horizontal center line.

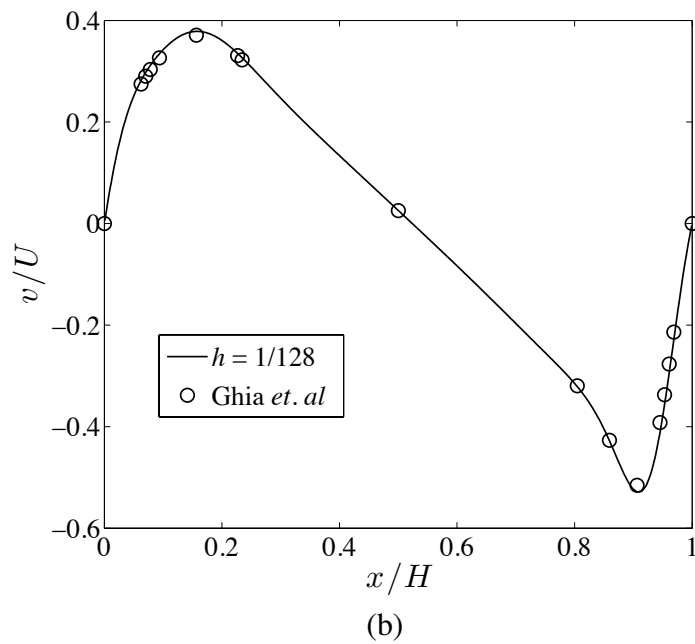
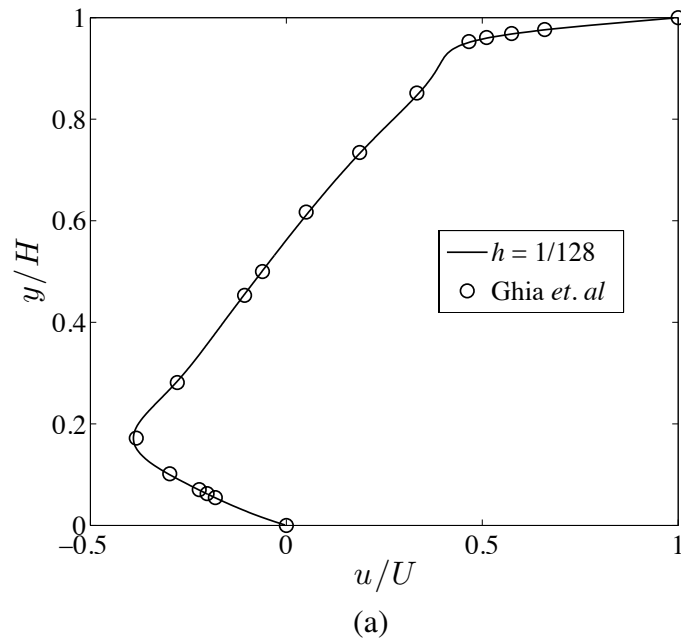


Figure 7.13: Lid-driven cavity flow: Velocity field for  $k' = 1$ ,  $h = 1/128$ , and  $Re = 1000$ . (a) Value of the first component of the velocity field along the vertical center line, (b) Value of the second component of the velocity field along the horizontal center line.

have been able to successfully simulate flows upwards of  $Re = 3200$  on relatively coarse meshes. We have also been able to reproduce all of the results presented here via a more expensive dynamic approach in which the solution is evolved from an initial condition via the unsteady Navier-Stokes equations.

### 7.7.2 Confined Jet Impingement

Impinging jets are commonly used in engineering applications due to their enhanced heat and mass transfer characteristics. Impinging jets even occur in blood vessels and are believed to play a role in atherogenesis [83]. Incompressible jet impingement is considered a difficult numerical benchmark problem because most discretizations return a velocity field with spurious nonzero divergence near the stagnation region, even for flows with small or moderate Reynolds numbers. As our proposed discretization satisfies the divergence-free constraint exactly, it does not suffer from this spurious behavior.

The physical problem of confined jet impingement is illustrated in Figure 7.14. Fluid flows from one pipe into a second pipe lying perpendicular to the first. To simulate this flow, we use a two-dimensional mathematical idealization which is illustrated in Figure 7.15. Along the left hand side of the domain, a symmetry condition is applied as we only model half of the jet system. Along the bottom side of the domain, no-slip and no-penetration boundary conditions are enforced. Along the top side of the domain, two different sets of boundary conditions are applied. Along the first  $D/2$  length of the top side, an inflow boundary condition is applied. Along the remainder of the top side, no-slip and no-penetration boundary conditions are enforced. Along the right hand side of the domain, a zero-traction boundary condition is enforced. The height of the domain is set as  $H$ , and the length of the domain,  $L$ , is chosen long enough such that the flow exiting the pipe

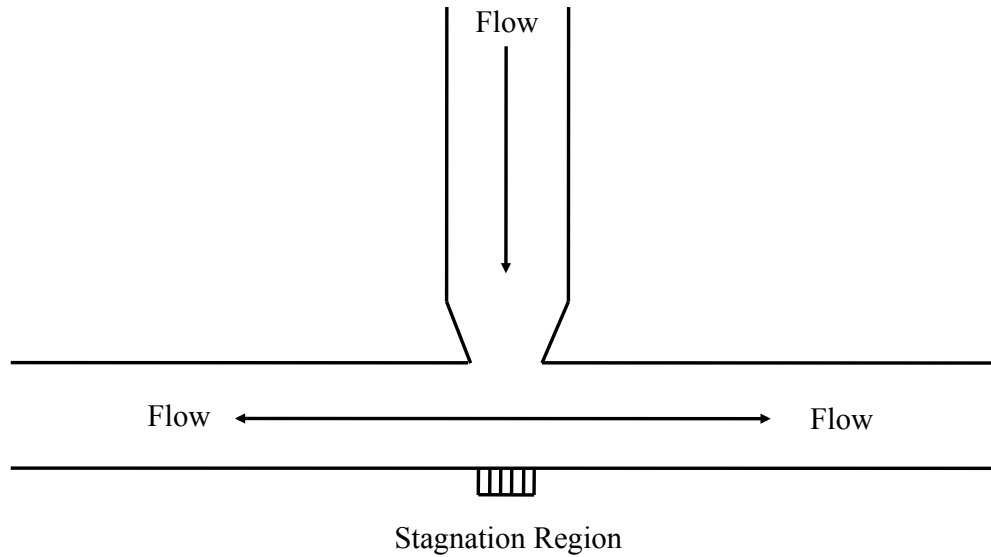


Figure 7.14: Confined jet impingement: Physical setup.

is parallel to the outflow plane. For the computations here,  $H = 1$  and  $L = 8$ . The inflow flow speed is set to be  $U = 1$ . The Reynolds number for the flow is defined as  $Re = UH/\nu$ .

We have simulated  $Re = 50$  confined jet impingement for two divergence-conforming B-spline discretizations of polynomial degree  $k' = 1$  corresponding to mesh lengths of  $h = 1/16$  and  $h = 1/32$ . The resulting velocity fields are plotted in Figures 7.16 and 7.17. First, note that the computed streamlines for the two meshes are indistinguishable. Second, note that the velocity fields are smooth and free from spurious oscillations. Finally, it should be noted we have conducted numerical investigations of confined jet impingement at other Reynolds numbers and obtained similar results.

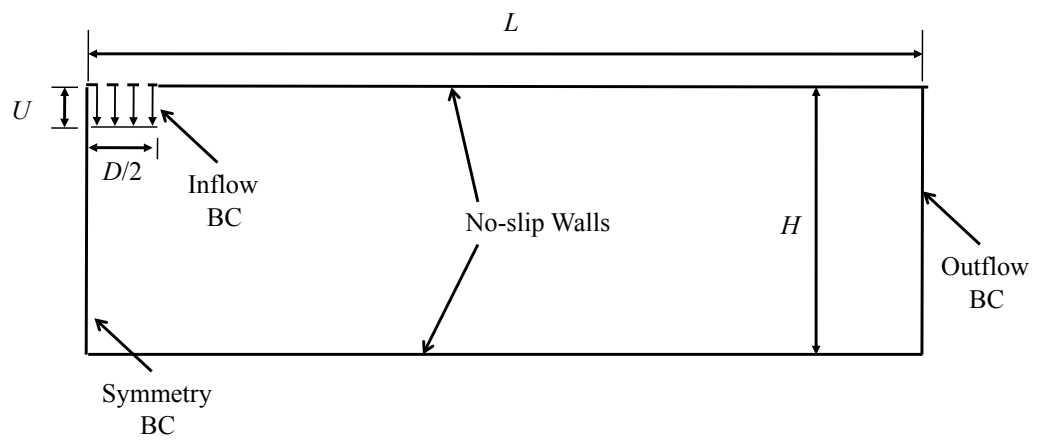


Figure 7.15: Confined jet impingement: Model problem description.

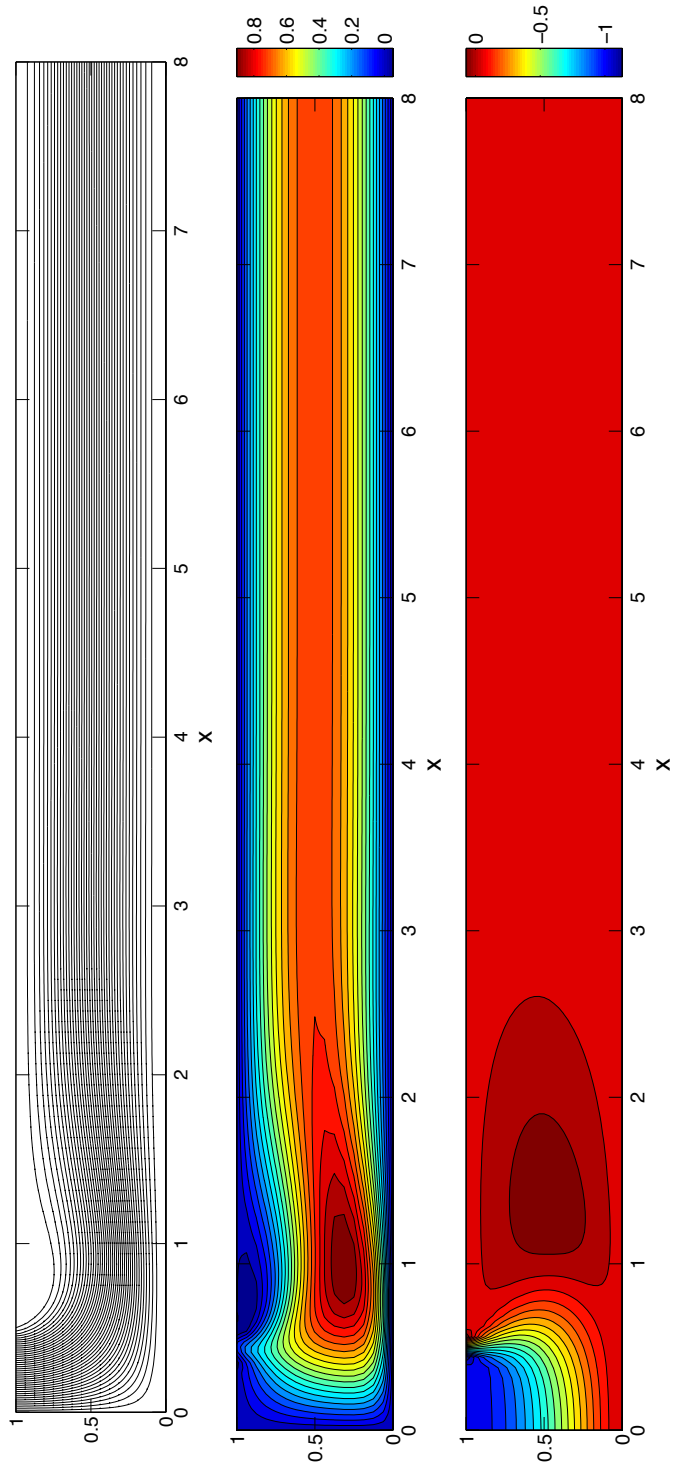


Figure 7.16: Confined jet impingement at  $Re = 50$ : Results for a coarse mesh. Top: Streamlines; Middle: Contours of  $u_1$ ; Bottom: Contours of  $u_2$ .

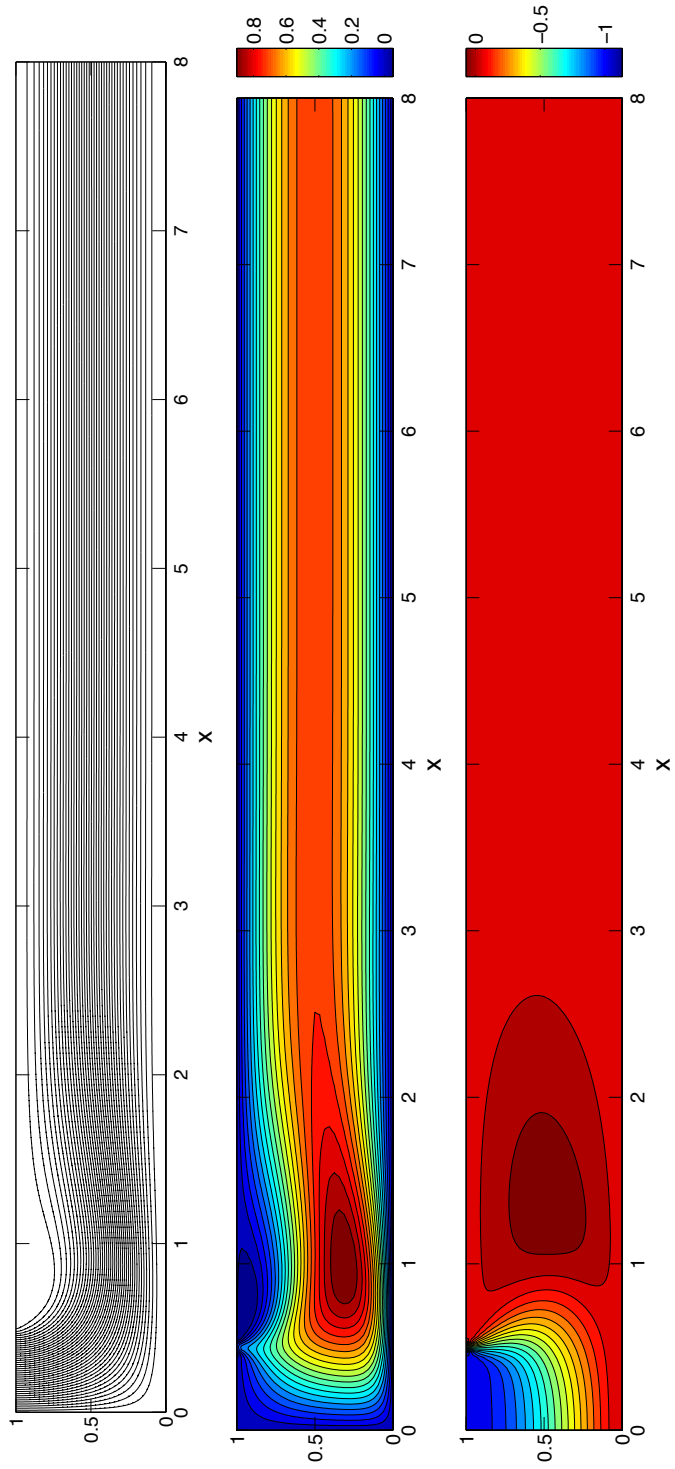


Figure 7.17: Confined jet impingement at  $Re = 50$ : Results for a resolved mesh. Top: Streamlines; Middle: Contours of  $u_1$ ; Bottom: Contours of  $u_2$ .

## Chapter 8

### Approximation of the Unsteady Stokes Problem

Unsteady Stokes flow arises in a variety of microscale applications ranging from the flow of blood through small arteries [43] to fluid flows generated by oscillating microactuators [105]. More importantly, a fundamental understanding of the unsteady Navier-Stokes problem requires first an understanding of the unsteady Stokes problem. In this chapter, we present divergence-conforming semi-discretizations of unsteady Stokes flow using the B-spline spaces introduced in Chapter 5, and we prove a collection of stability and error estimates for single-patch configurations. These stability and error estimates will turn out to be essential in the development of error estimates for unsteady Navier-Stokes flows. We further analyze the effectiveness of our semi-discretization technique via spectrum analysis. This will allow us to analyze the approximation properties of all the scales of our semi-discretization procedure for a given mesh size and polynomial degree. For the sake of comparison, we additionally conduct a spectrum analysis for a selection of classical discretization techniques.

To derive the results appearing in this chapter, we will need to continuously refer back to the results provided in the preceding two chapters. As such, we assume the reader is familiar with these chapters, and we will be rather terse with regards to exposition of notation. Furthermore, as in the preceding two chapters, we will highlight all of our estimates dependencies on the problem parameters as well as the penalty constant appearing in Nitsche's method.

## 8.1 The Continuous Problem

Let us consider unsteady Stokes flow of a constant-property Newtonian fluid subject to homogeneous Dirichlet boundary conditions:

$$(S) \left\{ \begin{array}{l} \text{Given } \nu \in \mathbb{R}^+, \mathbf{f} : \Omega \times (0, \infty) \rightarrow \mathbb{R}^d, \text{ and } \mathbf{u}_0 : \Omega \rightarrow \mathbb{R}^d, \text{ find } \mathbf{u} : \bar{\Omega} \times \\ [0, \infty) \rightarrow \mathbb{R}^d \text{ and } p : \Omega \times (0, \infty) \rightarrow \mathbb{R} \text{ such that} \\ \\ \frac{\partial \mathbf{u}}{\partial t} - \nabla \cdot (2\nu \nabla^s \mathbf{u}) + \mathbf{grad} p = \mathbf{f} \quad \text{in } \Omega \times (0, \infty) \quad (8.1) \\ \\ \operatorname{div} \mathbf{u} = 0 \quad \text{in } \Omega \times (0, \infty) \quad (8.2) \\ \\ \mathbf{u} = \mathbf{0} \quad \text{on } \partial\Omega \times (0, \infty) \quad (8.3) \\ \\ \mathbf{u}(\cdot, 0) = \mathbf{u}_0(\cdot) \quad \text{in } \Omega. \quad (8.4) \end{array} \right.$$

Above,  $\mathbf{u}_0$  denotes the initial velocity field.

To define a weak solution for the unsteady Stokes equations, we must introduce some terminology. For  $X$  a real Banach space and  $S$  a positive real number, let us define  $L^q(0, S; X)$  as the space consisting of all strongly measurable functions  $\phi : (0, S) \rightarrow X$  with

$$\|\phi\|_{L^q(0, S; X)} := \left( \int_0^S \|\phi(t)\|_X^q dt \right)^{1/q} < \infty \quad (8.5)$$

for  $1 \leq q < \infty$  and

$$\|\phi\|_{L^\infty(0, S; X)} := \operatorname{ess\,sup}_{0 < t < S} \|\phi(t)\|_X < \infty, \quad (8.6)$$

and let us define  $C^0([0, S]; X)$  as the space of all continuous functions  $\phi : [0, S] \rightarrow X$ . Given a fixed end-time  $T > 0$ , let us assume that  $\mathbf{f} \in L^\infty(0, T; \mathbf{L}^2(\Omega))$  and

$$\mathbf{u}_0 \in \{ \mathbf{u} \in \mathbf{H}_0^1(\Omega) : \operatorname{div} \mathbf{u} = 0 \}.$$

Now let us define the space

$$\mathcal{V}_T := \left\{ \mathbf{v} \in L^2(0, T; \mathbf{H}_0^1(\Omega)) : \frac{\partial \mathbf{v}}{\partial t} \in L^2(0, T; \mathbf{H}^{-1}(\Omega)) \right\} \quad (8.7)$$

with norm

$$\|\mathbf{v}\|_{\mathcal{V}_T} := \left( \int_0^T \left( \|\mathbf{v}(t)\|_{\mathbf{H}_0^1(\Omega)}^2 + \|\partial_t \mathbf{v}(t)\|_{\mathbf{H}^{-1}(\Omega)}^2 \right) dt \right)^{1/2} \quad (8.8)$$

where  $\partial_t$  denotes time differentiation and  $\mathbf{H}^{-1}(\Omega)$  denotes the dual space of  $\mathbf{H}_0^1(\Omega)$ .

Let us also define the space

$$\mathcal{Q}_T := L^2(0, T; L_0^2(\Omega)). \quad (8.9)$$

A weak formulation for the unsteady Stokes equations then reads as follows.

$$(W) \left\{ \begin{array}{l} \text{Find } \mathbf{u} \in \mathcal{V}_T \text{ and } p \in \mathcal{Q}_T \text{ such that } \mathbf{u}(0) = \mathbf{u}_0 \text{ and, for almost every } t \in (0, T), \\ \langle \partial_t \mathbf{u}(t), \mathbf{v} \rangle + k(\mathbf{u}(t), \mathbf{v}) - b(p(t), \mathbf{v}) + b(q, \mathbf{u}(t)) = (\mathbf{f}(t), \mathbf{v})_{L^2(\Omega)} \quad (8.10) \\ \text{for all } \mathbf{v} \in \mathbf{H}_0^1(\Omega) \text{ and } q \in L_0^2(\Omega) \text{ where } \langle \cdot, \cdot \rangle \text{ is a duality pairing and} \\ k(\mathbf{w}, \mathbf{v}) = (2\nu \nabla^s \mathbf{w}, \nabla^s \mathbf{v})_{(L^2(\Omega))^{d \times d}}, \quad \forall \mathbf{w}, \mathbf{v} \in \mathbf{H}_0^1(\Omega), \quad (8.11) \\ b(q, \mathbf{v}) = (q, \operatorname{div} \mathbf{v})_{L^2(\Omega)}, \quad \forall q \in L_0^2(\Omega), \mathbf{v} \in \mathbf{H}_0^1(\Omega). \quad (8.12) \end{array} \right.$$

The following is a standard result. It may be obtained by employing a Faedo-Galerkin method to imply existence and a continuous energy inequality to imply uniqueness (see Chapter 7 of [77]).

**Theorem 8.1.1.** *Problem (W) has a unique weak solution  $(\mathbf{u}, p) \in \mathcal{V}_T \times \mathcal{Q}_T$ .*

As the fixed end-time  $T$  is arbitrary in value, we thus have global existence and uniqueness of the exact solution.

## 8.2 The Semi-Discrete Problem

We now present a semi-discrete variational formulation for the unsteady Stokes problem. As in the last chapter, let us define the bilinear form

$$k_h(\mathbf{w}, \mathbf{v}) = k(\mathbf{w}, \mathbf{v}) - \sum_{F \in \Gamma_h} \int_F 2\nu \left( ((\nabla^s \mathbf{v}) \mathbf{n}) \cdot \mathbf{w} + ((\nabla^s \mathbf{w}) \mathbf{n}) \cdot \mathbf{v} - \frac{C_{pen}}{h_F} \mathbf{w} \cdot \mathbf{v} \right) ds \quad (8.13)$$

and the norm

$$\|\mathbf{v}\|_h^2 := |\mathbf{v}|_{\mathbf{H}^1(\Omega)}^2 + \sum_{F \in \Gamma_h} h_F \|(\nabla^s \mathbf{v}) \mathbf{n}\|_{(L^2(F))^d}^2 + \sum_{F \in \Gamma_h} \frac{C_{pen}}{h_F} \|\mathbf{v}\|_{(L^2(F))^d}^2. \quad (8.14)$$

The velocity space  $\mathcal{V}_{0,h}$  is a Banach space when endowed with the above norm, and the pressure space  $\mathcal{Q}_{0,h}$  is a Banach space when endowed with the standard  $L^2$ -norm. Let us define our discrete space-time velocity space as

$$\mathcal{V}_T^h := \{ \mathbf{v}_h \in C^0((0, T); \mathcal{V}_{0,h}) : \partial_t \mathbf{v}_h \in L^2((0, T); \mathcal{V}_{0,h}) \}, \quad (8.15)$$

and our discrete space-time pressure space as

$$\mathcal{Q}_T^h := L^2((0, T); \mathcal{Q}_{0,h}). \quad (8.16)$$

It remains to specify our discrete initial condition. To ease the presentation of our mathematical theory, we choose  $\mathbf{u}_{0,h} = \Pi_{\mathcal{V}_h}^0 \mathbf{u}_0$  where  $\Pi_{\mathcal{V}_h}^0$  is the commuting projection operator defined in Chapter 5. Note that, by construction,  $\operatorname{div} \mathbf{u}_{0,h} = 0$ . We can alternatively specify our initial condition through  $\mathbf{H}^1$ -projection into the B-spline space of divergence-free fields. This amounts to solving a steady Stokes problem as a pre-processing step. Our semi-discrete formulation reads as follows.

$$(G) \left\{ \begin{array}{l} \text{Find } \mathbf{u}_h \in \mathcal{V}_T^h \text{ and } p_h \in \mathcal{Q}_T^h \text{ such that } \mathbf{u}_h(0) = \mathbf{u}_{0,h} \text{ and, for almost every } \\ t \in (0, T), \\ (\partial_t \mathbf{u}_h(t), \mathbf{v}_h)_{\mathbf{L}^2(\Omega)} + k_h(\mathbf{u}_h(t), \mathbf{v}_h) - b(p_h(t), \mathbf{v}_h) + b(q_h, \mathbf{u}_h(t)) \\ = (\mathbf{f}(t), \mathbf{v}_h)_{\mathbf{L}^2(\Omega)} \\ \text{for all } \mathbf{v}_h \in \mathcal{V}_{0,h}, q_h \in \mathcal{Q}_{0,h}. \end{array} \right. \quad (8.17)$$

We immediately remark that the semi-discrete problem we have obtained is a set of coupled first-order linear ordinary differential equations. As such, we can use standard approaches from the theory of ordinary differential equations to obtain existence, uniqueness, and regularity results. We may also use standard time-integration schemes to obtain a fully-discrete formulation.

We have the following lemma detailing the consistency of our numerical method for sufficiently regular exact solutions. This consistency will prove essential for establishing *a priori* error estimates later in this chapter.

**Lemma 8.2.1.** *Suppose that the unique weak solution  $(\mathbf{u}, p)$  of  $(W)$  satisfies the regularity condition*

$$\mathbf{u} \in L^2(0, T; \mathbf{H}^{3/2+\epsilon}(\Omega))$$

where  $\epsilon > 0$ . Then, for almost every  $t \in (0, T)$ :

$$\langle \partial_t \mathbf{u}(t), \mathbf{v}_h \rangle + k_h(\mathbf{u}(t), \mathbf{v}_h) - b(p(t), \mathbf{v}_h) + b(q_h, \mathbf{u}(t)) = (\mathbf{f}(t), \mathbf{v}_h)_{\mathbf{L}^2(\Omega)} \quad (8.18)$$

for all  $\mathbf{v}_h \in \mathcal{V}_{0,h}$  and  $q_h \in \mathcal{Q}_{0,h}$ .

*Proof.* We trivially have, for almost every  $t \in (0, T)$ ,

$$b(q_h, \mathbf{u}(t)) = 0, \quad \forall q_h \in \mathcal{Q}_{0,h}. \quad (8.19)$$

Now let  $\mathbf{v}_h \in \mathcal{V}_{0,h}$ . Our assumption guarantees that  $(\nabla^s \mathbf{u}) \mathbf{n}$  is well-defined along  $\partial\Omega$  and lives in  $L^2(0, T; (L^2(\partial\Omega))^d)$ . Hence, we can utilize integration by parts and the fact that  $\mathbf{u}(t)$  satisfies homogeneous Dirichlet boundary conditions and  $\mathbf{v}_h$  satisfies homogeneous normal Dirichlet boundary conditions to write, for almost every  $t \in (0, T)$ ,

$$\begin{aligned} \langle \mathbf{u}_t(t), \mathbf{v}_h \rangle + k_h(\mathbf{u}(t), \mathbf{v}_h) - b(p(t), \mathbf{v}_h) &= \int_{\Omega} (\mathbf{u}_t(t) - \nabla \cdot (2\nu \nabla^s \mathbf{u}(t)) + \nabla p(t)) \cdot \mathbf{v}_h \\ &= (\mathbf{f}(t), \mathbf{v}_h)_{\mathbf{L}^2(\Omega)}. \end{aligned}$$

This completes the proof of the lemma.  $\square$

As a direct result of consistency, we have the following Galerkin orthogonality property, analogous to the orthogonality property for divergence-conforming B-spline discretizations of generalized Stokes flows.

**Corollary 8.2.1.** *Let  $(\mathbf{u}_h, p_h)$  denote a solution of (G), and suppose that the unique weak solution  $(\mathbf{u}, p)$  of (W) satisfies the regularity assumptions of Lemma 8.2.1. Then, for almost every  $t \in (0, T)$ :*

$$\begin{aligned} & \langle \partial_t \mathbf{u}(t) - \partial_t \mathbf{u}_h(t), \mathbf{v}_h \rangle + k_h(\mathbf{u}(t) - \mathbf{u}_h(t), \mathbf{v}_h) \\ & - b(p(t) - p_h(t), \mathbf{v}_h) + b(q_h, \mathbf{u}(t) - \mathbf{u}_h(t)) = 0 \end{aligned} \quad (8.20)$$

for all  $\mathbf{v}_h \in \mathcal{V}_{0,h}$  and  $q_h \in \mathcal{Q}_{0,h}$ .

Finally, our semi-discretization scheme returns a divergence-free velocity field, as indicated in the following lemma.

**Lemma 8.2.2.** *Let  $(\mathbf{u}_h, p_h)$  denote a solution of (G). Then:*

$$\operatorname{div} \mathbf{u}_h \equiv 0 \quad (8.21)$$

*Proof.* As  $\operatorname{div} \mathcal{V}_{0,h} = \mathcal{Q}_{0,h}$ , we can choose  $(\mathbf{v}_h, q_h) = (\mathbf{0}, \operatorname{div} \mathbf{u}_h(t))$  in Equation (8.17) for almost every  $t \in (0, T)$  to obtain

$$\|\operatorname{div} \mathbf{u}_h(t)\|_{L^2(\Omega)}^2 = 0.$$

Hence,  $\operatorname{div} \mathbf{u}_h = 0$  in the sense of  $L^2(0, T; L^2(\Omega))$ . The lemma follows.  $\square$

### 8.3 Global Existence and Uniqueness

In this section, we establish existence and uniqueness results for our semi-discrete formulation. To begin, we derive a discrete energy balance law which is satisfied provided the penalty constant  $C_{pen} \geq 1$  is sufficiently large.

**Lemma 8.3.1.** *Suppose  $(\mathbf{u}_h, p_h) \in \mathcal{V}_T^h \times \mathcal{Q}_T^h$  is a solution to (G). Furthermore, assume the penalty constant  $C_{pen}$  is chosen large enough such that (6.19) and (6.20) are satisfied. Then*

$$\frac{1}{2} \frac{d}{dt} \|\mathbf{u}_h(t)\|_{\mathbf{L}^2(\Omega)}^2 = -k_h(\mathbf{u}_h(t), \mathbf{u}_h(t)) + (\mathbf{f}(t), \mathbf{u}_h(t))_{\mathbf{L}^2(\Omega)} \leq (\mathbf{f}(t), \mathbf{u}_h(t))_{\mathbf{L}^2(\Omega)} \quad (8.22)$$

for almost every  $t \in (0, T)$ .

*Proof.* The proof of the lemma is straight-forward. Insert  $(\mathbf{v}_h, q_h) = (\mathbf{u}_h(t), 0)$  into (8.17) for almost every  $t \in (0, T)$  and use the fact that  $\operatorname{div} \mathbf{u}_h = 0$  as a distribution to obtain the expression

$$(\partial_t \mathbf{u}_h(t), \mathbf{u}_h(t))_{\mathbf{L}^2(\Omega)} = -k_h(\mathbf{u}_h(t), \mathbf{u}_h(t)) + (\mathbf{f}(t), \mathbf{u}_h(t))_{\mathbf{L}^2(\Omega)}.$$

The product rule then gives

$$(\partial_t \mathbf{u}_h(t), \mathbf{u}_h(t))_{\mathbf{L}^2(\Omega)} = \frac{1}{2} \frac{d}{dt} \|\mathbf{u}_h(t)\|_{\mathbf{L}^2(\Omega)}^2,$$

To complete the proof, note that  $k_h(\cdot, \cdot)$  is coercive due to Corollary 7.3.1.  $\square$

Using the energy inequality provided in the above lemma and standard approaches from the theory of ordinary differential equations, we obtain the following existence and uniqueness result.

**Theorem 8.3.1.** *Assume (6.19) and (6.20) are satisfied. Then Problem (G) has a unique solution  $(\mathbf{u}_h, p_h) \in \mathcal{V}_T^h \times \mathcal{Q}_T^h$ . Moreover,*

$$\|\mathbf{u}_h\|_{L^\infty(0,T;\mathbf{L}^2(\Omega))} \leq e^T \left( \|\mathbf{u}_{0,h}\|_{\mathbf{L}^2(\Omega)} + \|\mathbf{f}\|_{L^2(0,T;\mathbf{L}^2(\Omega))} \right) \quad (8.23)$$

and

$$\int_0^T \|\mathbf{u}_h\|_h^2 dt \leq \frac{1}{4\nu C_{coerc}} \left( \|\mathbf{u}_h\|_{L^2(0,T;\mathbf{L}^2(\Omega))}^2 + \|\mathbf{f}\|_{L^2(0,T;\mathbf{L}^2(\Omega))}^2 \right) \quad (8.24)$$

where  $C_{coerc}$  is the coercivity constant appearing in Corollary 7.3.1.

*Proof.* We begin by establishing existence and uniqueness for the discrete velocity solution. To do so, we restrict ourselves to the divergence-free space

$$\mathring{\mathcal{V}}_T^h := \{ \mathbf{v}_h \in \mathcal{V}_T^h : \operatorname{div} \mathbf{v}_h = 0 \}.$$

Each function  $\mathbf{v}_h \in \mathring{\mathcal{V}}_T^h$  can be written uniquely as

$$\mathbf{v}_h(t) = \sum_{i=1}^m e_i(t) \mathbf{w}_i$$

where  $\{\mathbf{w}_i\}_{i=1}^m$  is a basis for the space

$$\mathring{\mathcal{V}}_{0,h} := \{ \mathbf{w}_h \in \mathcal{V}_{0,h} : \operatorname{div} \mathbf{w}_h = 0 \}.$$

Representing our desired solution as

$$\mathbf{u}_h(t) = \sum_{i=1}^m d_i(t) \mathbf{w}_i,$$

the discrete problem in the kernel becomes a linear system of first-order ordinary differential equations for the coefficients  $d_i(t)$  subject to appropriately defined initial conditions. The energy estimate in Lemma 8.3.1 can then be used in conjunction with Gronwall's inequality to show that there exists a unique absolutely continuous

function  $\mathbf{d}(t) = (d_1(t), \dots, d_m(t))$  such that the initial conditions are satisfied and the linear system of first-order ordinary differential equations is satisfied for almost every time  $t \in (0, T)$ . Hence, a solution  $\mathbf{u}_h \in \mathring{\mathcal{V}}_T^h$  exists and is unique. Existence and uniqueness of  $p_h \in \mathcal{Q}_T^h$  is an immediate consequence of the inf-sup condition given by Corollary 7.3.1.

To obtain the  $L^2$  stability estimate, we write using Lemma 8.3.1

$$\frac{d}{dt} \|\mathbf{u}_h(t)\|_{\mathbf{L}^2(\Omega)}^2 \leq 2(\mathbf{f}(t), \mathbf{u}_h(t))_{\mathbf{L}^2(\Omega)} \leq \|\mathbf{f}(t)\|_{\mathbf{L}^2(\Omega)}^2 + \|\mathbf{u}_h(t)\|_{\mathbf{L}^2(\Omega)}^2$$

for almost every  $t \in (0, T)$ . The desired estimate is then an immediate result of the differential form of Gronwall's inequality. To obtain our second stability bound, again recall (8.22) and use Corollary 7.3.1 and Cauchy-Schwarz to establish

$$2\nu C_{coerc} \|\mathbf{u}_h(t)\|_h^2 \leq \frac{1}{2} \left( \|\mathbf{f}(t)\|_{\mathbf{L}^2(\Omega)}^2 + \|\mathbf{u}_h(t)\|_{\mathbf{L}^2(\Omega)}^2 \right).$$

Integrating over time we find

$$\int_0^T 2\nu C_{coerc} \|\mathbf{u}_h(t)\|_h^2 dt \leq \frac{1}{2} \left( \|\mathbf{u}_h\|_{L^2(0,T;\mathbf{L}^2(\Omega))}^2 + \|\mathbf{f}\|_{L^2(0,T;\mathbf{L}^2(\Omega))}^2 \right),$$

giving us the desired bound.  $\square$

Note that the above theorem gives existence and uniqueness results for any end-time  $T$ . Hence, we have proven a global-in-time existence and uniqueness result for our semi-discrete formulation. Moreover, our method is well-posed in the sense that it returns discrete solutions which depend continuously on the given data.

## 8.4 *A Priori* Error Estimates

We are now ready to show that our semi-discrete velocity and pressure fields converge to the exact solution under a reasonable set of regularity conditions. Our

method of proof roughly follows that of [4], which provides error estimates for symmetric interior penalty discretizations of nonlinear parabolic boundary value problems. We begin with the following theorem which gives an energy estimate for the velocity error.

**Theorem 8.4.1.** *Assume that (6.19) and (6.20) are satisfied, and let  $(\mathbf{u}, p)$  and  $(\mathbf{u}_h, p_h)$  denote the unique weak solutions of (W) and (G) respectively. If the regularity conditions*

$$\mathbf{u} \in L^\infty(0, T; \mathbf{H}^j(\Omega)), \quad \mathbf{u} \in L^2(0, T; \mathbf{H}^{j+1}(\Omega)), \quad \partial_t \mathbf{u} \in L^2(0, T; \mathbf{H}^j(\Omega)) \quad (8.25)$$

hold for  $j > 1/2$ , then we have

$$\begin{aligned} & \|\mathbf{u} - \mathbf{u}_h\|_{L^\infty(0, T; \mathbf{L}^2(\Omega))}^2 + 2\nu \int_0^T \|\mathbf{u} - \mathbf{u}_h\|_h^2 dt \leq \\ & C_{energy} h^{2s} \left( \|\mathbf{u}\|_{L^\infty(0, T; \mathbf{H}^s(\Omega))}^2 + 2\nu \|\mathbf{u}\|_{L^2(0, T; \mathbf{H}^{s+1}(\Omega))}^2 + (2\nu)^{-1} \|\partial_t \mathbf{u}\|_{L^2(0, T; \mathbf{H}^s(\Omega))}^2 \right) \end{aligned} \quad (8.26)$$

where  $s = \min \{k', j\}$  and  $C_{energy}$  is a positive constant independent of  $h$ ,  $\nu$ , and  $T$  that scales asymptotically with  $C_{pen}$ .

*Proof.* To begin, note that due to Corollary 8.2.1, we have, for almost every  $t \in (0, T)$ ,

$$(\partial_t \mathbf{u}(t) - \partial_t \mathbf{u}_h(t), \mathbf{v}_h)_{\mathbf{L}^2(\Omega)} + k_h(\mathbf{u}(t) - \mathbf{u}_h(t), \mathbf{v}_h) = 0 \quad (8.27)$$

for all  $\mathbf{v}_h \in \mathcal{V}_{0,h}$  satisfying  $\operatorname{div} \mathbf{v}_h = 0$ . Let us decompose  $\mathbf{u}(t) - \mathbf{u}_h(t) = \mathbf{e}_h(t) + \boldsymbol{\eta}(t)$  where

$$\mathbf{e}_h(t) = \Pi_{\mathcal{V}_h}^0 \mathbf{u}(t) - \mathbf{u}_h(t) \quad \text{and} \quad \boldsymbol{\eta}(t) = \mathbf{u}(t) - \Pi_{\mathcal{V}_h}^0 \mathbf{u}(t).$$

Plugging this decomposition into (8.27), we obtain

$$(\partial_t \mathbf{e}_h(t), \mathbf{v}_h)_{\mathbf{L}^2(\Omega)} + k_h(\mathbf{e}_h(t), \mathbf{v}_h) = -(\partial_t \boldsymbol{\eta}(t), \mathbf{v}_h)_{\mathbf{L}^2(\Omega)} - k_h(\boldsymbol{\eta}(t), \mathbf{v}_h). \quad (8.28)$$

Now, choosing  $\mathbf{v}_h = \mathbf{e}_h(t)$ , we have by Cauchy-Schwarz, Corollary 7.3.1, and Young's inequality

$$\begin{aligned} \frac{1}{2} \frac{d}{dt} \|\mathbf{e}_h(t)\|_{\mathbf{L}^2(\Omega)}^2 + k_h(\mathbf{e}_h(t), \mathbf{e}_h(t)) &\leq \frac{1}{2\epsilon_1} \|\partial_t \boldsymbol{\eta}(t)\|_{\mathbf{L}^2(\Omega)}^2 + \frac{\nu C_{cont}}{\epsilon_2} \|\boldsymbol{\eta}(t)\|_h^2 \\ &\quad + \frac{\epsilon_1}{2} \|\mathbf{e}_h(t)\|_{\mathbf{L}^2(\Omega)}^2 + \nu C_{cont} \epsilon_2 \|\mathbf{e}_h(t)\|_h^2 \end{aligned}$$

where  $C_{cont}$  is the continuity constant appearing in Corollary 7.3.1 and  $\epsilon_1, \epsilon_2 > 0$  are arbitrary positive numbers. We again invoke Corollary 7.3.1 to write

$$\begin{aligned} \frac{1}{2} \frac{d}{dt} \|\mathbf{e}_h(t)\|_{\mathbf{L}^2(\Omega)}^2 + 2\nu C_{coerc} \|\mathbf{e}_h(t)\|_h^2 &\leq \frac{1}{2\epsilon_1} \|\partial_t \boldsymbol{\eta}(t)\|_{\mathbf{L}^2(\Omega)}^2 + \frac{\nu C_{cont}}{\epsilon_2} \|\boldsymbol{\eta}(t)\|_h^2 \\ &\quad + \frac{\epsilon_1}{2} \|\mathbf{e}_h(t)\|_{\mathbf{L}^2(\Omega)}^2 + \nu C_{cont} \epsilon_2 \|\mathbf{e}_h(t)\|_h^2, \end{aligned}$$

and we recruit Poincaré's inequality to obtain

$$\begin{aligned} \frac{1}{2} \frac{d}{dt} \|\mathbf{e}_h(t)\|_{\mathbf{L}^2(\Omega)}^2 + 2\nu C_{coerc} \|\mathbf{e}_h(t)\|_h^2 &\leq \frac{1}{2\epsilon_1} \|\partial_t \boldsymbol{\eta}(t)\|_{\mathbf{L}^2(\Omega)}^2 + \frac{\nu C_{cont}}{\epsilon_2} \|\boldsymbol{\eta}(t)\|_h^2 \\ &\quad + \frac{C_{poin}^2 \epsilon_1}{2} \|\mathbf{e}_h(t)\|_h^2 + \nu C_{cont} \epsilon_2 \|\mathbf{e}_h(t)\|_h^2 \end{aligned}$$

where  $C_{poin} > 0$  is the Poincaré constant associated with (6.14). Let us now choose

$\epsilon_1 = \frac{\nu C_{coerc}}{C_{poin}^2}$  and  $\epsilon_2 = \frac{C_{coerc}}{2C_{cont}}$ . Then we have

$$\frac{d}{dt} \|\mathbf{e}_h(t)\|_{\mathbf{L}^2(\Omega)}^2 + 2\nu C_{coerc} \|\mathbf{e}_h(t)\|_h^2 \leq \frac{C_{poin}^2}{\nu C_{coerc}} \|\partial_t \boldsymbol{\eta}(t)\|_{\mathbf{L}^2(\Omega)}^2 + \frac{4\nu C_{cont}^2}{C_{coerc}} \|\boldsymbol{\eta}(t)\|_h^2.$$

We can directly integrate in time to finally arrive at

$$\begin{aligned} \|\mathbf{e}_h\|_{L^\infty(0,T;\mathbf{L}^2(\Omega))}^2 + 2\nu C_{coerc} \int_0^T \|\mathbf{e}_h(t)\|_h^2 dt &\leq \\ \frac{C_{poin}^2}{\nu C_{coerc}} \|\partial_t \boldsymbol{\eta}\|_{L^2(0,T;\mathbf{L}^2(\Omega))}^2 + \frac{4\nu C_{cont}^2}{C_{coerc}} \int_0^T \|\boldsymbol{\eta}(t)\|_h^2 dt &\quad (8.29) \end{aligned}$$

where we have used the equality  $\mathbf{e}_h(0) = \mathbf{0}$ . We now estimate the right-hand-side of the above expression. Noticing that the projection operator  $\Pi_{\mathbf{v}_h}^0$  commutes with

differentiation in time, we write

$$\|\partial_t \boldsymbol{\eta}\|_{L^2(0,T;\mathbf{L}^2(\Omega))}^2 = \int_0^T \|\partial_t \mathbf{u} - \Pi_{V_h}^0 \partial_t \mathbf{u}\|_{\mathbf{L}^2(\Omega)}^2 dt.$$

Invoking our interpolation estimates for  $\Pi_{V_h}^0$ , we then have

$$\|\partial_t \boldsymbol{\eta}\|_{L^2(0,T;\mathbf{L}^2(\Omega))}^2 \leq C_{time} h^{2s} \|\partial_t \mathbf{u}\|_{L^2(0,T;\mathbf{H}^s(\Omega))}^2 \quad (8.30)$$

for  $C_{time} > 0$  a positive constant independent of  $h$ ,  $T$ ,  $\nu$ , and  $C_{pen}$ . To bound the second term on the right-hand side of (8.29), we utilize the same methodology as that used to prove Theorem 6.4.1 to arrive at

$$\int_0^T \|\boldsymbol{\eta}(t)\|_h^2 dt \leq C_{space} h^{2s} \|\mathbf{u}\|_{L^2(0,T;\mathbf{H}^{s+1}(\Omega))}^2 \quad (8.31)$$

for  $C_{space} > 0$  a positive constant independent of  $h$ ,  $T$ , and  $\nu$  which scales asymptotically scales with  $C_{pen}$ . Thus, collecting the estimates given by (8.29)-(8.31), we have

$$\begin{aligned} & \|\mathbf{e}_h\|_{L^\infty(0,T;\mathbf{L}^2(\Omega))}^2 + 2\nu \int_0^T \|\mathbf{e}_h(t)\|_h^2 dt \leq \\ & C_{inter} h^{2s} \left( (2\nu)^{-1} \|\partial_t \mathbf{u}\|_{L^2(0,T;\mathbf{H}^s(\Omega))}^2 + 2\nu \|\mathbf{u}\|_{L^2(0,T;\mathbf{H}^{s+1}(\Omega))}^2 \right) \end{aligned} \quad (8.32)$$

where

$$C_{inter} = \frac{1}{\min\{1, C_{coerc}\}} \max \left\{ \frac{2C_{poin}^2 C_{time}}{C_{coerc}}, \frac{2C_{cont}^2 C_{space}}{C_{coerc}} \right\}.$$

To finish the proof, we write

$$\|\mathbf{u} - \mathbf{u}_h\|_{L^\infty(0,T;\mathbf{L}^2(\Omega))}^2 \leq 2\|\mathbf{e}_h\|_{L^\infty(0,T;\mathbf{L}^2(\Omega))}^2 + 2\|\boldsymbol{\eta}\|_{L^\infty(0,T;\mathbf{L}^2(\Omega))}^2$$

and

$$\int_0^T \|\mathbf{u}(t) - \mathbf{u}_h(t)\|_h^2 dt \leq 2 \int_0^T \|\mathbf{e}_h(t)\|_h^2 dt + 2 \int_0^T \|\boldsymbol{\eta}(t)\|_h^2 dt.$$

Coupling the above bounds with (8.31), (8.32), and the inequality

$$\|\boldsymbol{\eta}\|_{L^\infty(0,T;\mathbf{L}^2(\Omega))}^2 \leq C_{sp} h^{2s} \|\mathbf{u}\|_{L^\infty(0,T;\mathbf{H}^s(\Omega))}^2$$

(wherein  $C_{sp} > 0$  is a positive constant independent of  $h$ ,  $T$ ,  $\nu$ , and  $C_{pen}$ ) yields the desired result.  $\square$

Note that the above theorem provides suboptimal, by one order, convergence rates in the  $\mathbf{L}^2$ -norm. We will later prove optimal  $\mathbf{L}^2$  rates by utilizing a duality argument. Note that we also lose control of the error estimate given by Theorem 8.4.1 in the limit  $\nu \rightarrow 0$ . In this setting, our set of partial differential equations reduces to a set of ordinary differential equations at each point in  $\Omega$ , indicating that we should utilize a different approach in our error analysis. Specifically, we can use the differential form of Gronwall's inequality to obtain optimal error estimates in the limit of vanishing viscosity. Unfortunately, such estimates depend on  $T$ .

We now present a theorem which gives an energy estimate for the gradient of the velocity error. We alternatively call this estimate the entrosphy error estimate given the relationship of the gradient of the velocity to the enstrophy.

**Theorem 8.4.2.** *Assume that (6.19) and (6.20) are satisfied, and let  $(\mathbf{u}, p)$  and  $(\mathbf{u}_h, p_h)$  denote the unique weak solutions of (W) and (G) respectively. If the regularity conditions*

$$\mathbf{u} \in L^\infty(0, T; \mathbf{H}^{j+1}(\Omega)), \quad \partial_t \mathbf{u} \in L^2(0, T; \mathbf{H}^{j+1}(\Omega)) \quad (8.33)$$

hold for  $j > 1/2$ , then we have

$$\begin{aligned} & \|\partial_t \mathbf{u} - \partial_t \mathbf{u}_h\|_{L^2(0,T;\mathbf{L}^2(\Omega))}^2 + 2\nu \operatorname{ess\,sup}_{0 < t < T} \|\mathbf{u}(t) - \mathbf{u}_h(t)\|_h^2 \leq \\ & C_{grad} h^{2s} \left( \|\mathbf{u}\|_{L^\infty(0,T;\mathbf{H}^s(\Omega))}^2 + (1 + (2\nu)^{-1}) \|\partial_t \mathbf{u}\|_{L^2(0,T;\mathbf{H}^s(\Omega))}^2 \right) \\ & + C_{grad} h^{2s} (2\nu) \left( \|\mathbf{u}\|_{L^\infty(0,T;\mathbf{H}^{s+1}(\Omega))}^2 + \|\partial_t \mathbf{u}\|_{L^2(0,T;\mathbf{H}^{s+1}(\Omega))}^2 + \|\mathbf{u}\|_{L^2(0,T;\mathbf{H}^{s+1}(\Omega))}^2 \right) \end{aligned} \quad (8.34)$$

where  $s = \min \{k', j\}$  and  $C_{grad}$  is a positive constant independent of  $h$ ,  $\nu$ , and  $T$  that scales asymptotically with  $C_{pen}$ .

*Proof.* We begin with the same decomposition as in the proof of the last theorem and choose  $\mathbf{v}_h = \partial_t \mathbf{e}_h(t)$  in (8.28) to obtain

$$\|\partial_t \mathbf{e}_h(t)\|_{\mathbf{L}^2(\Omega)}^2 + \frac{1}{2} \frac{d}{dt} k_h(\mathbf{e}_h(t), \mathbf{e}_h(t)) = -(\partial_t \boldsymbol{\eta}(t), \partial_t \mathbf{e}_h(t))_{\mathbf{L}^2(\Omega)} - k_h(\boldsymbol{\eta}(t), \partial_t \mathbf{e}_h(t)).$$

We immediately invoke the coercivity of  $k_h(\cdot, \cdot)$  and Young's inequality to write

$$\|\partial_t \mathbf{e}_h(t)\|_{\mathbf{L}^2(\Omega)}^2 + 2\nu C_{coerc} \frac{d}{dt} \|\mathbf{e}_h(t)\|_h^2 \leq \|\partial_t \boldsymbol{\eta}(t)\|_{\mathbf{L}^2(\Omega)}^2 - 2k_h(\boldsymbol{\eta}(t), \partial_t \mathbf{e}_h(t)).$$

Integrating in time yields the expression

$$\begin{aligned} \|\partial_t \mathbf{e}_h\|_{L^2(0,T;\mathbf{L}^2(\Omega))}^2 + 2\nu C_{coerc} \operatorname{ess\,sup}_{0 < t < T} \|\mathbf{e}_h(t)\|_h &\leq \\ \|\partial_t \boldsymbol{\eta}\|_{L^2(0,T;\mathbf{L}^2(\Omega))} - 2 \int_0^T k_h(\boldsymbol{\eta}(t), \partial_t \mathbf{e}_h(t)) dt. \end{aligned}$$

We now integrate by parts the last term of the above inequality:

$$\begin{aligned} \|\partial_t \mathbf{e}_h\|_{L^2(0,T;\mathbf{L}^2(\Omega))}^2 + 2\nu C_{coerc} \operatorname{ess\,sup}_{0 < t < T} \|\mathbf{e}_h(t)\|_h &\leq \\ \|\partial_t \boldsymbol{\eta}\|_{L^2(0,T;\mathbf{L}^2(\Omega))} + 2 \int_0^T k_h(\partial_t \boldsymbol{\eta}(t), \mathbf{e}_h(t)) dt & \\ - 2k_h(\boldsymbol{\eta}(T), \mathbf{e}_h(T)). \end{aligned}$$

Above, we have used the fact that  $\mathbf{e}_h(0) = \mathbf{0}$ . Finally, we invoke the continuity of  $k_h(\cdot, \cdot)$  and Young's inequality to obtain the expression

$$\begin{aligned} \|\partial_t \mathbf{e}_h\|_{L^2(0,T;\mathbf{L}^2(\Omega))}^2 + \nu C_{coerc} \operatorname{ess\,sup}_{0 < t < T} \|\mathbf{e}_h(t)\|_h &\leq \\ \|\partial_t \boldsymbol{\eta}\|_{L^2(0,T;\mathbf{L}^2(\Omega))} + 2\nu C_{cont} \int_0^T \|\partial_t \boldsymbol{\eta}(t)\|_h^2 dt + 2\nu C_{cont} \int_0^T \|\mathbf{e}_h(t)\|_h^2 dt & \\ + \frac{4\nu C_{cont}^2}{C_{coerc}} \|\boldsymbol{\eta}\|_{L^\infty(0,T;\mathbf{H}^1(\Omega))}^2. \end{aligned}$$

The remainder of the proof is clear, by employing interpolation bounds for  $\boldsymbol{\eta}$  and  $\partial_t \boldsymbol{\eta}$  and Theorem 8.4.1 to bound the remaining terms on the right-hand-side involving  $\mathbf{e}_h$ .  $\square$

As a direct result of consistency, the discrete inf-sup condition, and interpolation estimates, we have the following estimate for the pressure error. We omit the proof as it is straight-forward.

**Theorem 8.4.3.** *Assume that (6.19) and (6.20) are satisfied, and let  $(\mathbf{u}, p)$  and  $(\mathbf{u}_h, p_h)$  denote the unique weak solutions of (W) and (G) respectively. If the regularity condition*

$$\mathbf{u} \in L^2(0, T; \mathbf{H}^{3/2+\epsilon}(\Omega)) \quad (8.35)$$

*holds for  $\epsilon > 0$ , then we have*

$$\begin{aligned} & \|p(t) - p_h(t)\|_{\mathbf{L}^2(\Omega)} \leq \\ & \left(1 + \frac{1}{\tilde{\beta}}\right) \inf_{q_h \in \mathcal{Q}_{0,h}} \|p(t) - q_h\|_{\mathbf{L}^2(\Omega)} \\ & + \frac{2\nu C_{cont}}{\tilde{\beta}} \|\mathbf{u}(t) - \mathbf{u}_h(t)\|_h + \frac{C_{poin}}{\tilde{\beta}} \|\partial_t \mathbf{u}(t) - \partial_t \mathbf{u}_h(t)\|_{\mathbf{L}^2(\Omega)} \end{aligned} \quad (8.36)$$

*for almost every  $t \in (0, T)$  where  $s = \min\{k', j\}$ ,  $\tilde{\beta}$  is the discrete inf-sup constant,  $C_{cont}$  is the continuity constant of  $k_h(\cdot, \cdot)$ , and  $C_{poin}$  is the Poincaré constant.*

Note that, due to the presence of the velocity error terms, the above theorem gives suboptimal estimates, by one order, for the pressure error. This is the same result as was obtained in the setting of steady Stokes flow. Nonetheless, our numerical experiments have indicated this error estimate may be conservative.

Let us now return to our discussion of optimal convergence estimates for the velocity field in the  $\mathbf{L}^2$ -norm. To prove such estimates, we utilize a technique

originally introduced by Wheeler in [190]. Before proceeding, however, we must make an assumption regarding the domain  $\Omega$ . In particular, we must assume the domain satisfies the following elliptic regularity condition.

**The Elliptic Regularity Assumption.** *For all  $\mathbf{g} \in \mathbf{L}^2(\Omega)$ , the weak solution  $(\mathbf{w}, r)$  of the following Stokes problem lies in  $\mathbf{H}^2(\Omega) \times H^1(\Omega)$ : find  $(\mathbf{w}, r) \in \mathbf{H}_0^1(\Omega) \times L_0^2(\Omega)$  such that*

$$(2\nu\nabla^s\mathbf{w}, \nabla^s\mathbf{v})_{(L^2(\Omega))^{d \times d}} - (r, \operatorname{div}\mathbf{v})_{L^2(\Omega)} + (q, \operatorname{div}\mathbf{w})_{L^2(\Omega)} = (\mathbf{g}, \mathbf{v})_{\mathbf{L}^2(\Omega)}$$

for all  $\mathbf{v} \in \mathbf{H}_0^1(\Omega)$  and  $q \in L_0^2(\Omega)$ .

Now, let us recall the divergence-free B-spline space

$$\hat{\mathcal{V}}_{0,h} := \{\mathbf{v}_h \in \mathcal{V}_{0,h} : \operatorname{div}\mathbf{v}_h = 0\}. \quad (8.37)$$

Given  $\mathbf{w} \in H^{j+1}(\Omega)$  for some  $j \geq 1$  and assuming that (6.19) and (6.20) hold, let us denote  $\Pi_E^0\mathbf{w} \in \hat{\mathcal{V}}_{0,h}$  as the unique function satisfying

$$k_h(\Pi_E^0\mathbf{w}, \mathbf{v}_h) = k_h(\mathbf{w}, \mathbf{v}_h), \quad \forall \mathbf{v}_h \in \hat{\mathcal{V}}_{0,h}. \quad (8.38)$$

As a consequence of Theorem 6.4.2, we have the following result on domains satisfying the elliptic regularity condition:

$$\|\mathbf{w} - \Pi_E^0\mathbf{w}\|_{\mathbf{L}^2(\Omega)} \leq C_l h^{s+1} \|\mathbf{w}\|_{\mathbf{H}^{s+1}(\Omega)} \quad (8.39)$$

where  $s = \min\{k', j\}$  and  $C_l$  is a positive constant independent of  $h$ ,  $\nu$ , and  $T$  which scales asymptotically with the square root of  $C_{pen}$ . The existence of this elliptic projector allows us to prove the following optimal estimate for the  $\mathbf{L}^2$ -norm of the velocity error.

**Theorem 8.4.4.** *Assume that (6.19) and (6.20) are satisfied and that the domain  $\Omega$  satisfies the elliptic regularity condition. Let  $(\mathbf{u}, p)$  and  $(\mathbf{u}_h, p_h)$  denote the unique weak solutions of (W) and (G) respectively. If the regularity conditions*

$$\mathbf{u} \in L^\infty(0, T; \mathbf{H}^{j+1}(\Omega)), \quad \partial_t \mathbf{u} \in L^2(0, T; \mathbf{H}^{j+1}(\Omega))$$

*hold for  $j \geq 1$ , then we have*

$$\|\mathbf{u} - \mathbf{u}_h\|_{L^\infty(0, T; \mathbf{L}^2(\Omega))}^2 \leq C_{opt} h^{2(s+1)} \left( \|\mathbf{u}\|_{L^\infty(0, T; \mathbf{H}^{s+1}(\Omega))}^2 + (2\nu)^{-1} \|\partial_t \mathbf{u}\|_{L^2(0, T; \mathbf{H}^{s+1}(\Omega))}^2 \right) \quad (8.40)$$

*where  $s = \min \{k', j\}$  and  $C_{opt}$  is a positive constant independent of  $h$ ,  $\nu$ , and  $T$  that scales asymptotically with  $C_{pen}$ .*

*Proof.* To begin, we write, for almost every  $t \in (0, T)$ ,

$$(\partial_t \mathbf{u}(t) - \partial_t \mathbf{u}_h(t), \mathbf{v}_h)_{\mathbf{L}^2(\Omega)} + k_h(\mathbf{u}(t) - \mathbf{u}_h(t), \mathbf{v}_h) = 0 \quad (8.41)$$

for all  $\mathbf{v}_h \in \mathcal{V}_{0,h}$  satisfying  $\operatorname{div} \mathbf{v}_h = 0$ . Now, consider the decomposition  $\mathbf{u}(t) - \mathbf{u}_h(t) = \mathbf{e}_h(t) + \boldsymbol{\eta}(t)$  where

$$\mathbf{e}_h(t) = \Pi_E^0 \mathbf{u}(t) - \mathbf{u}_h(t) \quad \text{and} \quad \boldsymbol{\eta}(t) = \mathbf{u}(t) - \Pi_E^0 \mathbf{u}(t).$$

Note that we have utilized the elliptic projector  $\Pi_E^0$  instead of the standard commuting projector  $\Pi_{\mathcal{V}_h}^0$ . Inserting the above decomposition into (8.41), we obtain

$$(\partial_t \mathbf{e}_h(t), \mathbf{v}_h)_{\mathbf{L}^2(\Omega)} + k_h(\mathbf{e}_h(t), \mathbf{v}_h) = -(\partial_t \boldsymbol{\eta}(t), \mathbf{v}_h)_{\mathbf{L}^2(\Omega)} - k_h(\boldsymbol{\eta}(t), \mathbf{v}_h).$$

Due to the definition of  $\Pi_E^0$ , we have that

$$k_h(\boldsymbol{\eta}(t), \mathbf{v}_h) = 0,$$

and hence we can write

$$(\partial_t \mathbf{e}_h(t), \mathbf{v}_h)_{\mathbf{L}^2(\Omega)} + k_h(\mathbf{e}_h(t), \mathbf{v}_h) = -(\partial_t \boldsymbol{\eta}(t), \mathbf{v}_h)_{\mathbf{L}^2(\Omega)}. \quad (8.42)$$

Choosing  $\mathbf{v}_h = \mathbf{e}_h(t)$  and invoking Cauchy-Schwarz and Young's inequality yields the expression

$$\frac{1}{2} \frac{d}{dt} \|\mathbf{e}_h(t)\|_{\mathbf{L}^2(\Omega)}^2 + k_h(\mathbf{e}_h(t), \mathbf{e}_h(t)) \leq \frac{1}{2\epsilon} \|\partial_t \boldsymbol{\eta}(t)\|_{\mathbf{L}^2(\Omega)}^2 + \frac{\epsilon}{2} \|\mathbf{e}_h(t)\|_{\mathbf{L}^2(\Omega)}^2$$

where  $\epsilon > 0$  is an arbitrary positive number. We recruit Corollary 7.3.1 to write

$$\frac{1}{2} \frac{d}{dt} \|\mathbf{e}_h(t)\|_{\mathbf{L}^2(\Omega)}^2 + 2\nu C_{coerc} \|\mathbf{e}_h(t)\|_h^2 \leq \frac{1}{2\epsilon} \|\partial_t \boldsymbol{\eta}(t)\|_{\mathbf{L}^2(\Omega)}^2 + \frac{\epsilon}{2} \|\mathbf{e}_h(t)\|_{\mathbf{L}^2(\Omega)}^2,$$

and we invoke Poincaré's inequality to obtain

$$\frac{1}{2} \frac{d}{dt} \|\mathbf{e}_h(t)\|_{\mathbf{L}^2(\Omega)}^2 + 2\nu C_{coerc} \|\mathbf{e}_h(t)\|_h^2 \leq \frac{1}{2\epsilon} \|\partial_t \boldsymbol{\eta}(t)\|_{\mathbf{L}^2(\Omega)}^2 + \frac{C_{poin}^2 \epsilon}{2} \|\mathbf{e}_h(t)\|_h^2.$$

Choosing  $\epsilon = \frac{2\nu C_{coerc}}{C_{poin}^2}$  yields the expression

$$\frac{d}{dt} \|\mathbf{e}_h(t)\|_{\mathbf{L}^2(\Omega)}^2 + 2\nu C_{coerc} \|\mathbf{e}_h(t)\|_h^2 \leq \frac{C_{poin}^2}{2\nu C_{coerc}} \|\partial_t \boldsymbol{\eta}(t)\|_{\mathbf{L}^2(\Omega)}^2.$$

We can directly integrate in time to finally arrive at

$$\begin{aligned} \|\mathbf{e}_h\|_{L^\infty(0,T;\mathbf{L}^2(\Omega))}^2 + 2\nu C_{coerc} \int_0^T \|\mathbf{e}_h(t)\|_h^2 dt \leq \\ \|\mathbf{e}_h(0)\|_{\mathbf{L}^2(\Omega)}^2 + \frac{C_{poin}^2}{2\nu C_{coerc}} \|\partial_t \boldsymbol{\eta}\|_{L^2(0,T;\mathbf{L}^2(\Omega))}^2. \end{aligned} \quad (8.43)$$

We now estimate the right-hand side of the above expression. First, since our domain satisfies the elliptic regularity property, we can combine (8.39) with our B-spline interpolation estimates to arrive at the expression

$$\|\mathbf{e}_h(0)\|_{\mathbf{L}^2(\Omega)}^2 \leq C_{init} h^{2(s+1)} \|\mathbf{u}\|_{L^\infty(0,T;\mathbf{H}^{s+1}(\Omega))}^2 \quad (8.44)$$

where  $C_{init} > 0$  a positive constant independent of  $h$ ,  $T$ , and  $\nu$  which scales asymptotically with  $C_{pen}$ . Next, noticing that the projection operator  $\Pi_E^0$  commutes with differentiation in time, we have

$$\|\partial_t \boldsymbol{\eta}\|_{L^2(0,T;\mathbf{L}^2(\Omega))}^2 = \int_0^T \|\partial_t \mathbf{u} - \Pi_E^0 \partial_t \mathbf{u}\|_{\mathbf{L}^2(\Omega)}^2 dt.$$

Since our domain satisfies the elliptic regularity property, we can write

$$\|\partial_t \boldsymbol{\eta}\|_{L^2(0,T;\mathbf{L}^2(\Omega))}^2 \leq C_{time} h^{2(s+1)} \|\partial_t \mathbf{u}\|_{L^2(0,T;\mathbf{H}^{s+1}(\Omega))}^2 \quad (8.45)$$

for  $C_{time} > 0$  a positive constant independent of  $h$ ,  $T$ , and  $\nu$  which scales asymptotically with  $C_{pen}$ . Collecting the estimates given by (8.43)-(8.45) yields the expression

$$\|\mathbf{e}_h\|_{L^\infty(0,T;\mathbf{L}^2(\Omega))}^2 \leq C_{inter} h^{2(s+1)} \left( \|\mathbf{u}\|_{L^\infty(0,T;\mathbf{H}^{s+1}(\Omega))}^2 + (2\nu)^{-1} \|\partial_t \mathbf{u}\|_{L^2(0,T;\mathbf{H}^{s+1}(\Omega))}^2 \right) \quad (8.46)$$

where

$$C_{inter} = \max \left\{ C_{init}, \frac{C_{poin}^2 C_{time}}{C_{coerc}} \right\}.$$

To finish the proof, we write

$$\|\mathbf{u} - \mathbf{u}_h\|_{L^\infty(0,T;\mathbf{L}^2(\Omega))}^2 \leq 2\|\mathbf{e}_h\|_{L^\infty(0,T;\mathbf{L}^2(\Omega))}^2 + 2\|\boldsymbol{\eta}\|_{L^\infty(0,T;\mathbf{L}^2(\Omega))}^2.$$

Coupling the above bound with (8.46) and the inequality

$$\|\boldsymbol{\eta}\|_{L^\infty(0,T;\mathbf{L}^2(\Omega))}^2 \leq C_{sp} h^{2(s+1)} \|\mathbf{u}\|_{L^\infty(0,T;\mathbf{H}^{s+1}(\Omega))}^2$$

(wherein  $C_{sp} > 0$  is a positive constant independent of  $h$ ,  $T$ , and  $\nu$  which scales asymptotically with  $C_{pen}$ ) yields the desired result.  $\square$

We finish here with one more estimate. This estimate gives an *a priori* bound for the supremum of the discrete velocity field. We will later need this estimate to prove optimal error estimates for the unsteady Navier-Stokes equations.

**Theorem 8.4.5.** *Assume that (6.19) and (6.20) are satisfied and that the domain  $\Omega$  satisfies the elliptic regularity condition. Let  $(\mathbf{u}, p)$  and  $(\mathbf{u}_h, p_h)$  denote the unique weak solutions of (W) and (G) respectively. If the regularity conditions*

$$\mathbf{u} \in L^\infty(0, T; \mathbf{H}^2(\Omega)), \quad \partial_t \mathbf{u} \in L^2(0, T; \mathbf{H}^2(\Omega))$$

*hold, then we have*

$$\begin{aligned} \|\mathbf{u}_h\|_{L^\infty(0, T; \mathbf{L}^\infty(\Omega))} &\leq \|\mathbf{u}\|_{L^\infty(0, T; \mathbf{L}^\infty(\Omega))} \\ &\quad + C_\infty h^{2-d/2} \left( \|\mathbf{u}\|_{L^\infty(0, T; \mathbf{H}^2(\Omega))}^2 + (2\nu)^{-1} \|\partial_t \mathbf{u}\|_{L^2(0, T; \mathbf{H}^2(\Omega))}^2 \right)^{1/2} \end{aligned} \quad (8.47)$$

*where  $C_\infty$  is a positive constant independent of  $h$ ,  $\nu$ , and  $T$  that scales asymptotically with the square root of  $C_{pen}$ .*

*Proof.* Before proceeding, note by assumption and the Sobolev embedding theorem that  $\mathbf{u}(t)$  is a continuous function for every  $t \in (0, T)$ . Let us also assume for simplicity our meshes are globally quasi-uniform. The locally quasi-uniform case follows by invoking local estimates rather than global estimates. Let  $\widehat{\mathcal{L}}^h$  denote the space of  $C^0$  bilinear or trilinear finite elements (in  $\mathbb{R}^2$  and  $\mathbb{R}^3$  respectively) defined over the parametric mesh  $\mathcal{Q}^h$ , and let  $\mathcal{L}^h$  denote the push-forward of  $\widehat{\mathcal{L}}^h$  onto the physical domain. For every  $t \in (0, T)$ , let  $\mathbf{w}_h(t) \in \mathcal{L}^h$  denote the nodal interpolant of  $\mathbf{u}(t)$ . By construction,

$$\|\mathbf{w}_h(t)\|_{\mathbf{L}^\infty(\Omega)} \leq \|\mathbf{u}_h(t)\|_{\mathbf{L}^\infty(\Omega)}, \quad (8.48)$$

and standard finite element interpolation estimates give the bound

$$\|\mathbf{u}(t) - \mathbf{w}_h(t)\|_{\mathbf{L}^2(\Omega)} \leq C_w h^2 \|\mathbf{u}_h(t)\|_{\mathbf{H}^2(\Omega)} \quad (8.49)$$

where  $C_w > 0$  is a positive constant independent of  $h$ ,  $\nu$ ,  $T$ , and  $C_{pen}$ . Now, the triangle inequality yields

$$\|\mathbf{u}_h(t)\|_{\mathbf{L}^\infty(\Omega)} \leq \|\mathbf{u}_h(t) - \mathbf{w}_h(t)\|_{\mathbf{L}^\infty(\Omega)} + \|\mathbf{w}_h(t)\|_{\mathbf{L}^\infty(\Omega)}.$$

Since both  $\mathcal{V}_h$  and  $\mathcal{L}^h$  are discrete spaces consisting of mapped polynomials over each physical mesh element, a scaling argument gives

$$\|\mathbf{u}_h(t)\|_{\mathbf{L}^\infty(\Omega)} \leq C_{scaling} h^{-d/2} \|\mathbf{u}_h(t) - \mathbf{w}_h(t)\|_{\mathbf{L}^2(\Omega)} + \|\mathbf{w}_h(t)\|_{\mathbf{L}^\infty(\Omega)}$$

where  $C_{scaling} > 0$  is a positive constant only dependent on mesh regularity, polynomial degree, and the parametric mapping  $\mathbf{F}$ . We split the term involving  $\mathbf{u}_h - \mathbf{w}_h$  using the triangle inequality to obtain

$$\begin{aligned} \|\mathbf{u}_h(t)\|_{\mathbf{L}^\infty(\Omega)} &\leq C_{scaling} h^{-d/2} (\|\mathbf{u}(t) - \mathbf{w}_h(t)\|_{\mathbf{L}^2(\Omega)} + \|\mathbf{u}(t) - \mathbf{u}_h(t)\|_{\mathbf{L}^2(\Omega)}) \\ &\quad + \|\mathbf{w}_h(t)\|_{\mathbf{L}^\infty(\Omega)}. \end{aligned} \tag{8.50}$$

The theorem finally follows by combining (8.48)-(8.50) with the result of Theorem 8.4.4.  $\square$

This concludes our *a priori* error analysis. We have obtained an optimal pointwise (in time) error estimate for the gradient of the velocity field, and we have obtained an optimal pointwise error estimate for the velocity field provided an elliptic regularity condition is satisfied. Furthermore, we have obtained an  $\mathbf{L}^\infty$ -stability estimate for the velocity field, and we have obtained error estimates which are suboptimal, by one order, for the pressure field. These estimates will prove to be critical in deriving error estimates for the nonlinear unsteady Navier-Stokes problem.

Before proceeding, we would like to say a few remarks regarding regularity. It is known that solutions of the unsteady Stokes problem and parabolic problems

in general may experience blow up at the initial time unless certain compatibility conditions relating the initial condition and applied forcing are satisfied. To address this issue, many authors have invoked the inherent smoothing properties of parabolic evolution equations in order to derive optimal error estimates away from the initial time [116, 139, 180]. These developments, however, are beyond the scope of this written dissertation.

## 8.5 Spectrum Analysis

While the error estimates derived in the preceding section give insight into the asymptotic convergence behavior of our method, it does not give much insight as to our method's pre-asymptotic characteristics. Alternatively, we may utilize spectrum analysis in order to analyze the approximation properties of all the scales of our discretization for a given mesh size and polynomial degree. In spectrum analysis, we directly compare the spectrum of the discrete Stokes operator with the spectrum of the continuous Stokes operator. For simplicity, let us consider the unsteady Stokes problem on the two-dimensional torus subject to no applied forcing. To this effect, we set  $\Omega = (0, 2\pi)^2$  and introduce the Sobolev spaces

$$\mathbf{H}_{per}^1(\Omega) := \left\{ \mathbf{u} \in \mathbf{H}^1(\Omega) : \mathbf{u}(\cdot, 0) = \mathbf{u}(\cdot, 2\pi), \mathbf{u}(0, \cdot) = \mathbf{u}(2\pi, \cdot) \right\}$$

and

$$\mathbf{L}_{per}^2(\Omega) := L_0^2(\Omega).$$

Furthermore, for a given end-time  $T > 0$ , we define the spaces

$$\mathcal{V}_{T,per} := \left\{ \mathbf{v} \in L^2(0, T; \mathbf{H}_{per}^1(\Omega)) : \partial_t \mathbf{v} \in L^2(0, T; \mathbf{H}_{per}^*(\Omega)) \right\}$$

and

$$\mathcal{Q}_{T,per} := L^2(0, T; L_{per}^2(\Omega))$$

where  $\mathbf{H}_{per}^*(\Omega)$  denotes the dual space of  $\mathbf{H}_{per}^1(\Omega)$ . Given  $\mathbf{u}_0 \in \mathbf{H}_{per}^1(\Omega)$ , the problem of interest then reads as follows.

$$(P) \left\{ \begin{array}{l} \text{Find } \mathbf{u} \in \mathcal{V}_{T,per} \text{ and } p \in \mathcal{Q}_{T,per} \text{ such that } \mathbf{u}(0) = \mathbf{u}_0 \text{ and, for almost every } \\ t \in (0, T), \\ \langle \partial_t \mathbf{u}(t), \mathbf{v} \rangle + k(\mathbf{u}(t), \mathbf{v}) - b(p(t), \mathbf{v}) + b(q, \mathbf{u}(t)) = 0 \\ \text{for all } \mathbf{v} \in \mathbf{H}_{per}^1(\Omega) \text{ and } q \in L_{per}^2(\Omega) \text{ where } k(\cdot, \cdot) \text{ is defined by (7.5).} \end{array} \right.$$

The above is an evolutionary equation subject only to dissipation in time. Now, defining the space of divergence-free functions as

$$\mathring{\mathbf{H}}_{per}^1(\Omega) := \{ \mathbf{v} \in \mathbf{H}_{per}^1(\Omega) : \operatorname{div} \mathbf{v} = 0 \},$$

let us consider the following eigen-problem.

$$(E) \left\{ \begin{array}{l} \text{Find } \hat{\mathbf{u}} \in \mathring{\mathbf{H}}_{per}^1(\Omega) \text{ and } \lambda \in \mathbb{R}^+ \text{ such that } \|\hat{\mathbf{u}}\|_{\mathbf{L}^2(\Omega)} = 1 \text{ and} \\ k(\hat{\mathbf{u}}, \mathbf{v}) = \lambda (\hat{\mathbf{u}}, \mathbf{v})_{\mathbf{L}^2(\Omega)} \\ \text{for all } \mathbf{v} \in \mathring{\mathbf{H}}_{per}^1(\Omega). \end{array} \right.$$

The orthonormal eigenmodes corresponding to the above problem are explicitly known and comprise the set

$$\left\{ \hat{\mathbf{u}} = \frac{\operatorname{curl} \phi}{\|\operatorname{curl} \phi\|_{\mathbf{L}^2(\Omega)}} : \phi = \exp(ik_1x + ik_2y), k_1, k_2 \in \mathbb{Z}, k_1 + k_2 = 0 \right\}.$$

We enumerate these eigenmodes and their corresponding eigenvalues as  $\{\hat{\mathbf{u}}_n, \lambda_n\}_{n=1}^{\infty}$  where

$$\lambda_1 \leq \lambda_2 \leq \dots$$

Finally, a direct calculation shows that the exact velocity solution of (P) can be written as

$$\mathbf{u}(\mathbf{x}, t) = \sum_{n=1}^{\infty} A_n \hat{\mathbf{u}}_n(\mathbf{x}) \exp(-\lambda_n t) \quad (8.51)$$

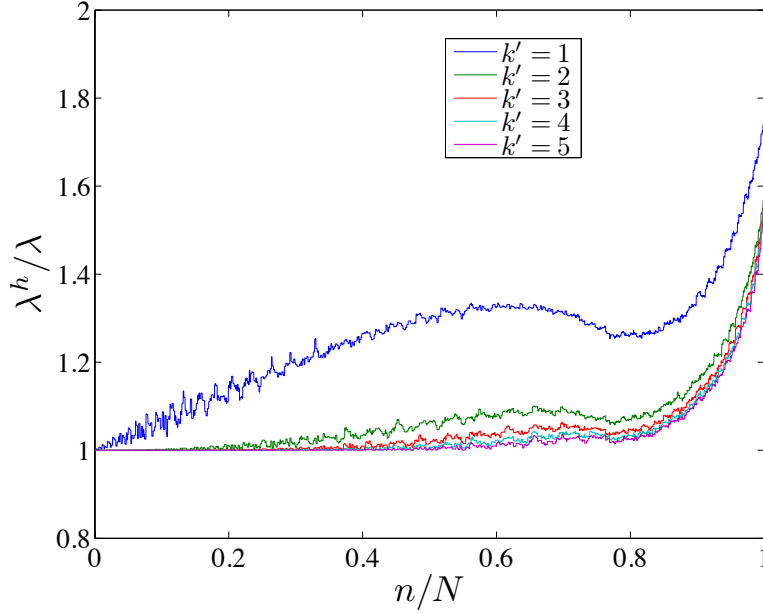


Figure 8.1: Stokes spectrum for divergence-free B-splines.

where

$$A_n = \int_{\Omega} \mathbf{u}_0(\mathbf{x}) \cdot \widehat{\mathbf{u}}_n(\mathbf{x}) d\mathbf{x}. \quad (8.52)$$

Hence, the velocity solution of  $(P)$  depends only on the initial condition  $\mathbf{u}_0$ , the eigenmodes  $\{\widehat{\mathbf{u}}_n\}_{n=1}^{\infty}$ , and the eigenvalues  $\{\lambda_n\}_{n=1}^{\infty}$ . Furthermore, the eigenvalues  $\{\lambda_n\}_{n=1}^{\infty}$  gives the dissipation rates of the individual eigenmodes. We may repeat all of the above calculations at the discrete level to express our discrete velocity solution entirely in terms of the discrete initial condition  $\mathbf{u}_{0,h}$ , discrete eigenmodes  $\{\widehat{\mathbf{u}}_n^h\}_{n=1}^N$ , and discrete eigenvalues  $\{\lambda_n^h\}_{n=1}^N$  where  $N$  denotes the dimension of the discrete space of (discretely) divergence-free functions. A natural question to then ask is how well do the discrete eigenvalues approximate the first  $N$  continuous eigenvalues.

In Figure 8.1, we have compared the discrete eigenvalues arising from a

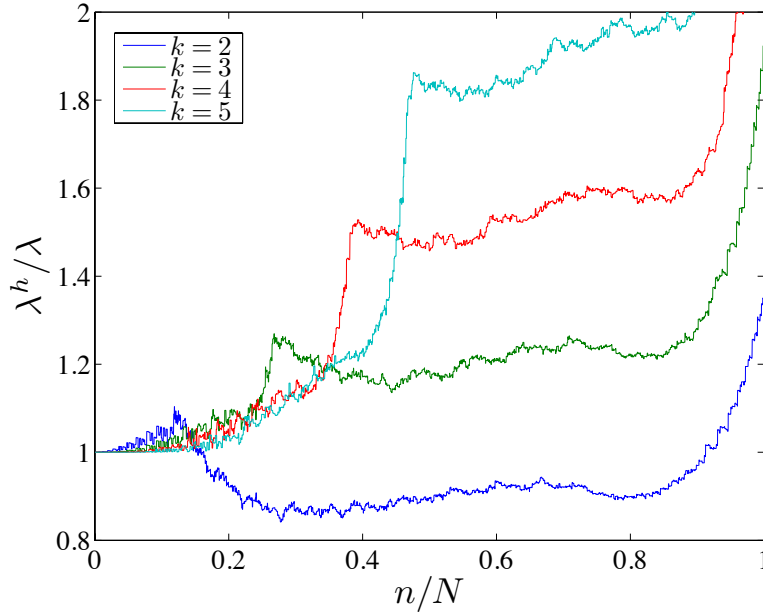


Figure 8.2: Stokes spectrum for Taylor-Hood elements.

divergence-free B-spline discretization of the Stokes eigen-problem with corresponding exact eigenvalues for  $N = 4095$  and polynomial degrees  $k' = 1, 2, 3, 4, 5$ . Note that the discrete spectrum is fairly well-resolved for all polynomial degrees and that the entire discrete spectrum improves with increasing polynomial degree. We should also mention that all of the discrete eigenvalues satisfy the relationship

$$\lambda_n^h \geq \lambda_n.$$

This property is a consequence of the fact that our method is an interior approximation technique. That is, it preserves the divergence-free constraint exactly.

In Figure 8.2, we have compared the discrete eigenvalues arising from a Taylor-Hood  $\mathbf{Q}_{k+1}/Q_k$  discretization [106] of the Stokes eigen-problem with corresponding exact eigenvalues for  $N \approx 4000$  and polynomial degrees  $k = 2, 3, 4, 5$ . Note that, in contrast with divergence-free B-splines, the discrete spectrum does

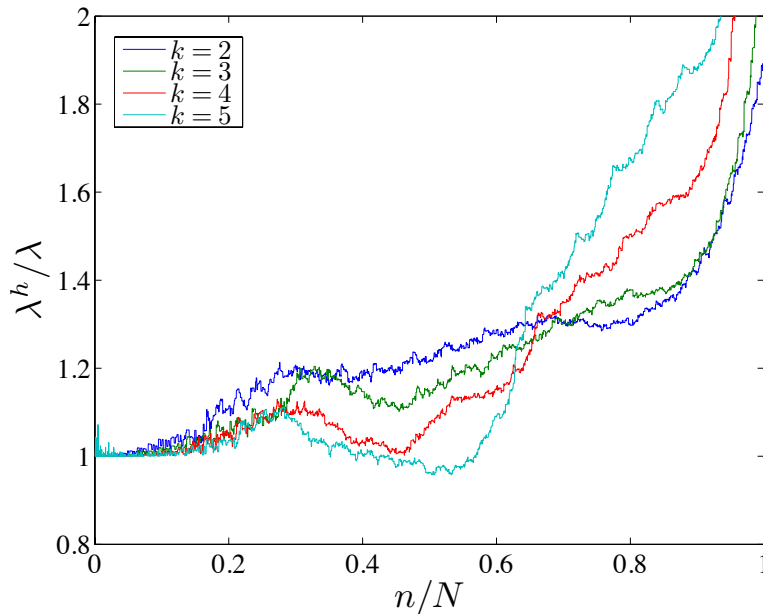


Figure 8.3: Stokes spectrum for  $\mathbf{Q}^{k+1} - P^k$  elements.

not improve with increasing polynomial degree. While the initial portion of the discrete spectrum does improve with increasing polynomial degree, the top end of the spectrum worsens. This indicates that the high modes of the discrete Stokes system have no approximability. Furthermore, as Taylor-Hood discretizations do not preserve the divergence-free constraint exactly, the discrete eigenvalues do not satisfy the relationship  $\lambda_n^h \geq \lambda_n$ .

In Figure 8.3, we have compared the discrete eigenvalues arising from a  $\mathbf{Q}_{k+1}/P_k$  discretization [25] of the Stokes eigen-problem with corresponding exact eigenvalues for  $N \approx 4000$  and polynomial degrees  $k = 2, 3, 4, 5$ . In this discretization technique, the velocity field is approximated using continuous piecewise tensor-product polynomials of degree  $k + 1$  and the pressure field is approximated using discontinuous piecewise polynomials of degree  $k$ . Note immediately that the discrete spectra associated with these discretizations are somewhat erratic and un-

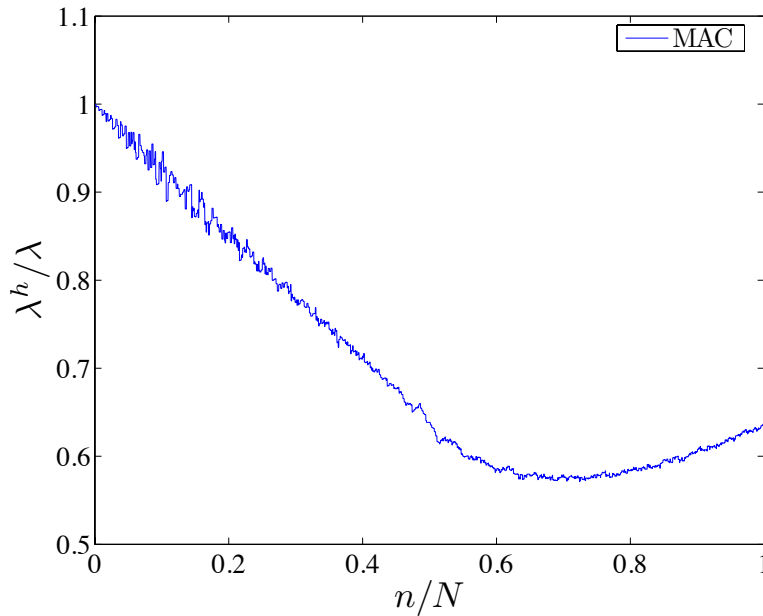


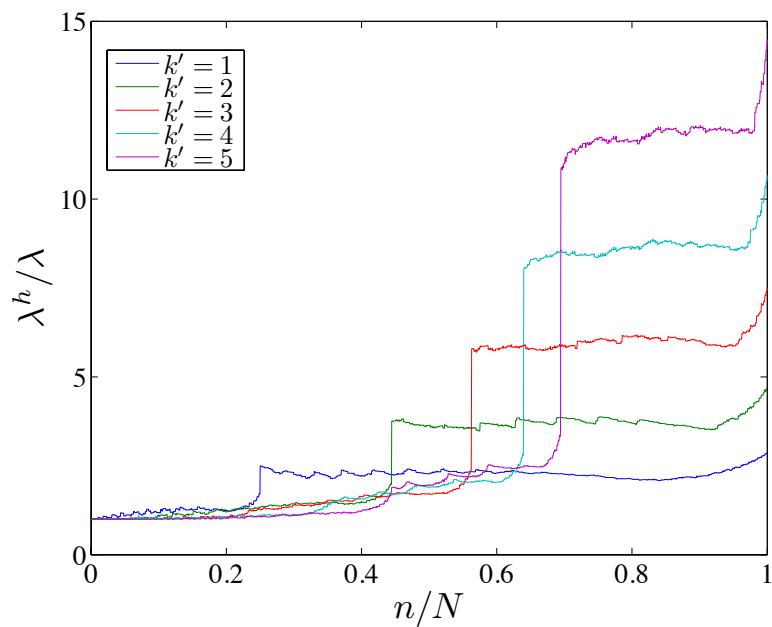
Figure 8.4: Stokes spectrum for the MAC scheme.

predictable. Like the Taylor-Hood discretizations, the initial portion of the discrete spectrum improves with increasing polynomial degree and the top end worsens. Moreover, as the polynomial degree is increased, the middle portion of the spectrum is driven to be smaller and smaller. This indicates that the discrete eigenmodes associated with these eigenvalues are not dissipating fast enough in comparison with their continuous counterparts.

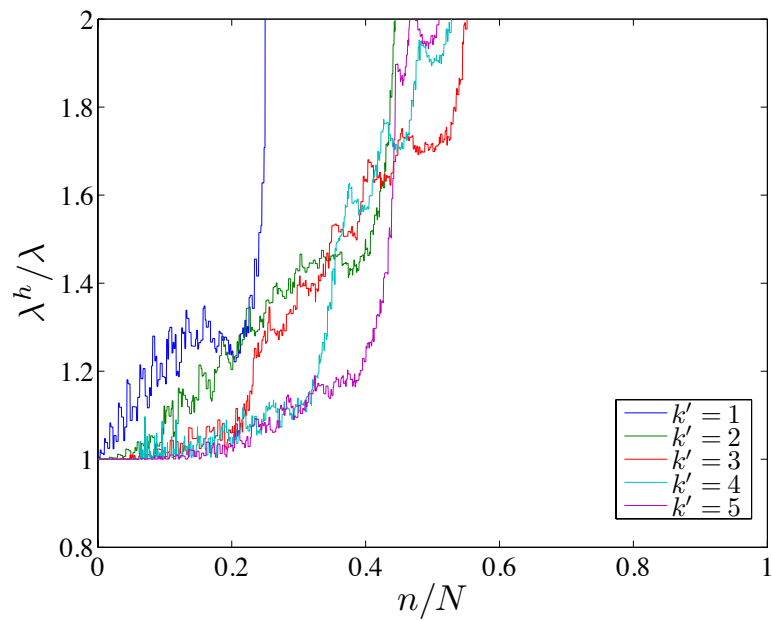
In Figure 8.4, we have compared the discrete eigenvalues arising from a Marker-And-Cell (MAC) discretization [97] of the Stokes eigen-problem with corresponding exact eigenvalues for  $N = 4095$ . In this discretization technique, the velocity field is defined on cell faces, the pressure field is defined on cell interiors, and finite differences are utilized to discretize the momentum equation on cell faces and the continuity equation on cell interiors. Note that all of the discrete eigenvalues are smaller than their continuous counterpart. This indicates that all of the

discrete eigenmodes are not dissipating fast enough.

Finally, in Figure 8.5, we have compared the discrete eigenvalues arising from a divergence-free Raviart-Thomas discretization [48, 49, 117] of the Stokes eigen-problem with corresponding exact eigenvalues for  $N \approx 4000$  and polynomial degrees  $k' = 1, 2, 3, 4, 5$ . Since Raviart-Thomas elements are not tangentially continuous across faces, the interior penalty method can be invoked to enforce this continuity weakly. For the computations here, the interior penalty parameter was chosen as  $4(k' + 1)^2$ . Note from the figure that while the initial portion of the discrete spectrum improves with increasing polynomial degree, the top end catastrophically worsens. This indicates that the high modes of the discrete Stokes operator have no approximability whatsoever, especially for high polynomial degrees. Furthermore, we found the quality of the spectrum degraded with increasing interior penalty parameter. This indicates that one should choose the interior penalty parameter intelligently not only for the purposes of numerical stability but also for numerical accuracy. Unfortunately, this fact is not often elaborated in the literature.



(a)



(b)

Figure 8.5: Stokes spectrum for divergence-free Raviart-Thomas elements: (a) Full view, (b) Zoomed in view.

## Chapter 9

### Approximation of the Unsteady Navier-Stokes Problem

Alas, we finally arrive at unsteady Navier-Stokes flow. Unsteady Navier-Stokes flow is simultaneously the most interesting and difficult flow regime studied in this dissertation. Like steady Navier-Stokes flow, it is subject to the Babuška-Brezzi condition and convective instabilities. Furthermore, vortex stretching, enstrophy production, and turbulence are fundamental features of unsteady Navier-Stokes flow in three-dimensional domains. In this chapter, we present divergence-conforming semi-discretizations for the unsteady Navier-Stokes equations using the B-spline spaces introduced in Chapter 5, and we prove a collection of stability and error estimates for single-patch configurations. We also demonstrate that our semi-discretizations satisfy discrete balance laws for momentum, energy, vorticity, enstrophy, and helicity. We numerically verify our error estimates using two simple model problems with exact solutions, and we finish this chapter by considering the application of our method to two standard benchmark problems: two-dimensional flow over a cylinder and three-dimensional Taylor-Green vortex flow.

The use of B-splines in the numerical analysis of unsteady Navier-Stokes flow has already been conducted with much success. The novelty of the method presented here is simply the use of tensor-product B-splines which exactly satisfy the incompressibility constraint. In the Direct Numerical Simulation (DNS) community, a common method of choice in simulating wall-bounded flows is the

use of Fourier spectral discretizations in periodic directions and B-splines in wall-normal directions [129, 130, 138]. In this setting, B-splines are often preferred over polynomial-based spectral discretizations due to their high resolving power, easy implementation of boundary conditions, and ability to employ stretched grids. Recently, Bazilevs *et al.* studied the turbulence problem in a series of papers using NURBS-based isogeometric analysis in conjunction with a Variational Multiscale (VMS) methodology. In these papers, it was found the increased continuity of splines led to enhanced numerical results [1, 16, 18, 21, 22]. It is believed that much of this success can be attributed to the spectral-like properties of B-splines. In Figure 9.1, we have plotted the phase errors associated with one-dimensional  $k$ -method NURBS (which in this setting reduce to B-splines of maximal continuity) and  $C^0$  finite element discretizations of the first-order wave equation. Note that the phase error associated with the quadratic NURBS solution is much smaller than that associated with the quadratic finite element solution. Indeed, it can be shown that the phase error for  $C^{p-1}$  NURBS solutions scales like  $O(h^{2p+2})$  while the phase error for  $C^0$  finite element solutions scales like  $O(h^{2p})$ . For more on this topic of discussion, see Chapter 9 of [52].

As in the preceding chapter, we will need to continuously refer back to results provided in previous parts of the dissertation in order to derive the results appearing here. As such, we assume the reader is familiar with previous parts of the dissertation, and we will be rather terse with regards to exposition of notation. Additionally, it should be mentioned that we do not consider subgrid turbulence models in this chapter. As such, the discretizations presented here should only be utilized if the flow field is sufficiently resolved by the spatial mesh. That being said, standard Large Eddy Simulation models can be utilized in conjunction with the proposed discretizations to capture fine-scale turbulent effects on coarse meshes.

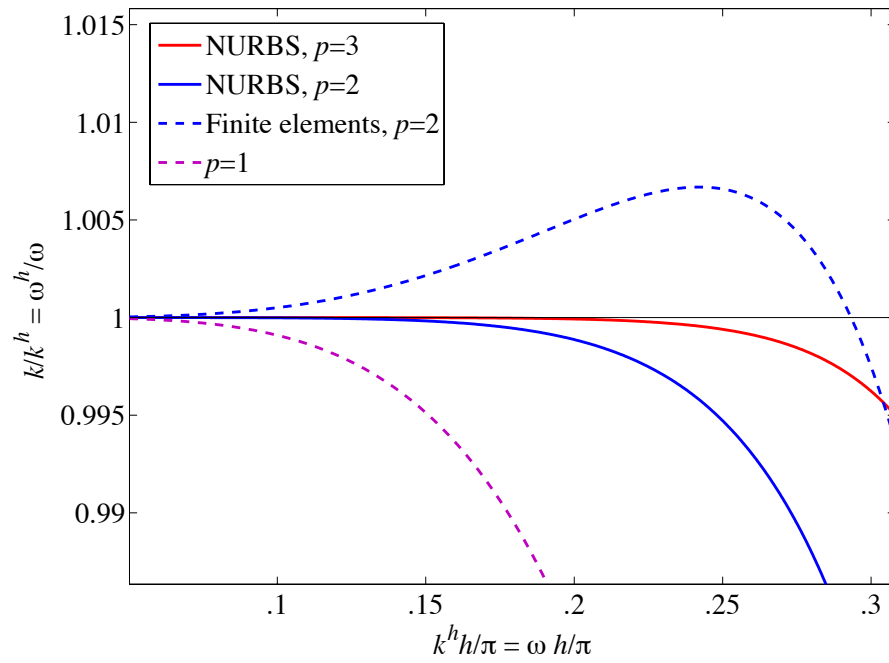


Figure 9.1: The first-order wave equation. Phase errors versus non-dimensional wave numbers. Comparison of linear and quadratic finite elements,  $C^1$  quadratic NURBS, and  $C^2$  cubic NURBS. Image courtesy of Thomas J.R. Hughes.

## 9.1 The Continuous Problem

Let us consider unsteady Navier-Stokes flow of a constant-property Newtonian fluid subject to homogeneous Dirichlet boundary conditions:

$$\left( \begin{array}{l}
 \text{Given } \nu \in \mathbb{R}^+, \mathbf{f} : \Omega \times (0, \infty) \rightarrow \mathbb{R}^d, \text{ and } \mathbf{u}_0 : \Omega \rightarrow \mathbb{R}^d, \text{ find } \mathbf{u} : \bar{\Omega} \times \\
 [0, \infty) \rightarrow \mathbb{R}^d \text{ and } p : \Omega \times (0, \infty) \rightarrow \mathbb{R} \text{ such that} \\
 \\
 \frac{\partial \mathbf{u}}{\partial t} + \nabla \cdot (\mathbf{u} \otimes \mathbf{u}) + \mathbf{grad} p - \nabla \cdot (2\nu \nabla^s \mathbf{u}) = \mathbf{f} \quad (9.1) \\
 \\
 \text{div } \mathbf{u} = 0 \quad (9.2) \\
 \\
 \text{in } \Omega \times (0, \infty) \text{ and} \\
 \\
 \mathbf{u} = \mathbf{0} \quad \text{on } \partial\Omega \times (0, \infty) \quad (9.3) \\
 \\
 \mathbf{u}(\cdot, 0) = \mathbf{u}_0(\cdot) \quad \text{in } \Omega. \quad (9.4)
 \end{array} \right. (S)$$

An appropriate definition of weak solution is not entirely obvious in the context of unsteady Navier-Stokes flows, especially for domains in  $\mathbb{R}^3$ . The most basic type of weak solution is a so-called Leray-Hopf solution. Given a fixed end-time  $T > 0$ , let us assume that  $\mathbf{f} \in L^\infty(0, T; \mathbf{L}^2(\Omega))$  and

$$\mathbf{u}_0 \in \{ \mathbf{u} \in \mathbf{H}_0(\text{div}; \Omega) : \text{div } \mathbf{u} = 0 \}.$$

A Leray-Hopf solution over the time interval  $(0, T)$  is then defined as a vector function  $\mathbf{u} \in L^\infty(0, T; \mathbf{L}^2(\Omega)) \cap L^2(0, T; \mathbf{H}_0^1(\Omega))$  satisfying  $\mathbf{u}(\cdot, 0) = \mathbf{u}_0$ ,  $\text{div } \mathbf{u} = 0$  in the sense of distributions, the energy inequality

$$\| \mathbf{u}(t) \|_{\mathbf{L}^2(\Omega)}^2 + \int_0^t 4\nu \| \nabla^s \mathbf{u}(s) \|_{(L^2(\Omega))^{d \times d}}^2 ds \leq \| \mathbf{u}(0) \|_{\mathbf{L}^2(\Omega)}^2 + \int_0^t 2 (\mathbf{f}(s), \mathbf{u}(s))_{\mathbf{L}^2(\Omega)} ds \quad (9.5)$$

for almost every  $t \in (0, T)$ , and

$$\int_0^T \int_\Omega (\mathbf{u} \cdot \partial_t \mathbf{v} + (\mathbf{u} \otimes \mathbf{u}) : \nabla \mathbf{v} + \mathbf{u} \cdot \nabla \cdot (2\nu \nabla^s \mathbf{v}) + \mathbf{f} \cdot \mathbf{v}) \, d\mathbf{x} dt + \int_\Omega \mathbf{u}_0 \cdot \mathbf{v} \, d\mathbf{x} = 0 \quad (9.6)$$

for all smooth test functions  $\mathbf{v} \in (C_0^\infty((0, T) \times \Omega))^d$  such that  $\operatorname{div} \mathbf{v} = 0$ . In 1934, Leray obtained the first three-dimensional existence results for the Navier-Stokes equations by carefully constructing a Leray-Hopf weak solution for the Navier-Stokes problem posed on all of  $\mathbb{R}^3$  [134]. Seventeen years later, Hopf extended this existence result to the Dirichlet problem by constructing a Leray-Hopf solution as the limit of a sequence of Galerkin approximations [107].

While the question of existence was answered many decades ago for Leray-Hopf solutions, the question of uniqueness remains unanswered for domains in  $\mathbb{R}^3$ . This is primarily due to an intimate relationship between uniqueness and regularity [64]. As was mentioned in Chapter 3, *a priori* estimates have not yet been able to preclude the occurrence of so-called vorticity bursts reaching scales smaller than the Kolmogorov scale due to the presence of enstrophy production. In his seminal 1977 paper, Scheffer introduced a systematic means of addressing the regularity question by studying the Hausdorff measure of the singular set of weak solutions [164]. If one can prove the measure of this set is zero, one will then have answered the Navier-Stokes smoothness question in the affirmative. To systematically study the Hausdorff measure, Scheffer introduced so-called suitable weak solutions which satisfy a local space-time energy balance. Specifically, suitable weak solutions satisfy the inequality

$$\partial_t \left( \frac{1}{2} |\mathbf{u}|^2 \right) + \nabla \cdot \left( \left( \frac{1}{2} |\mathbf{u}|^2 + p \right) \mathbf{u} \right) - \nu \nabla^2 \left( \frac{1}{2} |\mathbf{u}|^2 \right) + \nu |\nabla \mathbf{u}|^2 - \mathbf{f} \cdot \mathbf{u} \leq 0 \quad (9.7)$$

in a distributional sense. Such a local balance can be interpreted as an “entropy condition” for incompressible flows. Suitable weak solutions are known to always exist, and they may be obtained via a regularization of the Navier-Stokes equations and passing to the limit. With the notion of a suitable weak solution, Scheffer was able to derive a bound from above of some Hausdorff measure of the singular set.

This bound was then improved upon in the famous 1982 paper of Caffarelli, Kohn, and Nirenberg where it is proven that the one-dimensional Hausdorff measure of the set of singularities for a suitable weak solution is zero [42]. That is, if singularities exist, they cannot lie along a line in space-time. This is widely considered to be the best general result in the direction of the Navier-Stokes Millennium Prize Problem.

All of the above machinery is not necessary in the derivation of a semi-discrete variational formulation. As we will show in the next section, we are able to obtain a well-posed discrete problem via a simple Galerkin methodology. That being said, a recent paper of Guermond suggests that our semi-discrete formulation converges to a suitable weak solution [90]. This is due to the local approximation properties of B-splines, the divergence-free property of our discrete velocity field, the satisfaction of a discrete inf-sup condition, and the fact that Nitsche's method transforms the Laplacian into a discrete Laplacian. All that remains to prove suitability is a certain nonstandard inf-sup condition. Convergence of divergence-conforming B-splines to suitable weak solutions has been explored in some detail but will not be covered here. It should be noted that it is not known whether or not this convergence property holds for spectral discretizations which are the standard in direct numerical simulation. It has been hypothesized that spectral discretizations may not converge to suitable weak solutions as they do not induce enough numerical diffusion to counteract the Gibbs-Wilbraham phenomenon, preventing a local energy balance from holding in the limit [91].

## 9.2 The Semi-Discrete Problem

We now present a semi-discrete variational formulation for the unsteady Navier-Stokes equations. Employing precisely the same terminology as was used

in the preceding chapter, our formulation reads as follows.

$$(G) \left\{ \begin{array}{l} \text{Find } \mathbf{u}_h \in \mathcal{V}_T^h \text{ and } p_h \in \mathcal{Q}_T^h \text{ such that } \mathbf{u}_h(0) = \mathbf{u}_{0,h} \text{ and, for almost every } \\ t \in (0, T), \\ \\ (\partial_t \mathbf{u}_h(t), \mathbf{v}_h)_{\mathbf{L}^2(\Omega)} + k_h(\mathbf{u}_h(t), \mathbf{v}_h) \\ + c(\mathbf{u}_h(t), \mathbf{u}_h(t); \mathbf{v}_h) - b(p_h(t), \mathbf{v}_h) + b(q_h, \mathbf{u}_h(t)) = (\mathbf{f}(t), \mathbf{v}_h)_{\mathbf{L}^2(\Omega)} \\ \\ \text{for all } \mathbf{v}_h \in \mathcal{V}_{0,h} \text{ and } q_h \in \mathcal{Q}_{0,h}. \end{array} \right. \quad (9.8)$$

By assuming the exact solution satisfies

$$\mathbf{u} \in L^2(0, T; \mathbf{H}^{3/2+\epsilon}(\Omega))$$

for some  $\epsilon > 0$ , we can show the above semi-discrete problem is consistent up to the prescription of initial conditions. We also have the following lemma.

**Lemma 9.2.1** (Conservation of mass). *Suppose  $(\mathbf{u}_h, p_h) \in \mathcal{V}_T^h \times \mathcal{Q}_T^h$  is a solution to (G). Then*

$$\int_0^T \|\operatorname{div} \mathbf{u}_h(t)\|_{L^2(\Omega)}^2 dt = 0. \quad (9.9)$$

*That is,  $\operatorname{div} \mathbf{u}_h = 0$  as a distribution.*

### 9.3 Energy Balance

As was the case for the unsteady Stokes equations, our semi-discrete formulation satisfies a discrete energy balance law provided the constant in Nitsche's method is chosen large enough. This balance law is encompassed in the following lemma.

**Lemma 9.3.1** (Global balance law for energy). *Suppose  $(\mathbf{u}_h, p_h) \in \mathcal{V}_T^h \times \mathcal{Q}_T^h$  is a solution to (G). Furthermore, assume (6.19) and (6.20) are satisfied. Then*

$$\frac{1}{2} \frac{d}{dt} \|\mathbf{u}_h(t)\|_{\mathbf{L}^2(\Omega)}^2 = -k_h(\mathbf{u}_h(t), \mathbf{u}_h(t)) + (\mathbf{f}(t), \mathbf{u}_h(t))_{\mathbf{L}^2(\Omega)} \leq (\mathbf{f}(t), \mathbf{u}_h(t))_{\mathbf{L}^2(\Omega)} \quad (9.10)$$

for almost every  $t \in (0, T)$ .

*Proof.* The proof follows along the same lines as that of Lemma 8.3.1. Insert  $(\mathbf{v}_h, q_h) = (\mathbf{u}_h(t), 0)$  into (9.8) for almost every  $t \in (0, T)$  and use Lemma 7.3.2, the fact that  $\operatorname{div} \mathbf{u}_h = 0$  as a distribution, and the product rule to obtain the expression

$$(\partial_t \mathbf{u}_h(t), \mathbf{u}_h(t))_{\mathbf{L}^2(\Omega)} = \frac{1}{2} \frac{d}{dt} \|\mathbf{u}_h(t)\|_{\mathbf{L}^2(\Omega)}^2.$$

To complete the proof, note that  $k_h(\cdot, \cdot)$  is coercive due to Corollary 7.3.1.  $\square$

The above energy balance law is analogous to the balance law satisfied by Leray-Hopf weak solutions. However, while we have an equality in our discrete balance law, the balance law for Leray-Hopf weak solutions is characterized by an inequality. This inequality is an artifact of regularization and passing to the limit. Note that when the applied forcing term is conservative (*i.e.*,  $\mathbf{f} = \nabla q$  for some scalar potential  $q : \Omega \rightarrow \mathbb{R}$ ), we have

$$\frac{1}{2} \frac{d}{dt} \|\mathbf{u}_h(t)\|_{\mathbf{L}^2(\Omega)}^2 \leq 0$$

for almost every  $t \in (0, T)$ . Hence, our formulation properly dissipates energy. Furthermore, when the viscosity is taken to vanish, we obtain

$$\frac{1}{2} \frac{d}{dt} \|\mathbf{u}_h(t)\|_{\mathbf{L}^2(\Omega)}^2 = 0.$$

Thus, just as in the infinite-dimensional setting, energy is an inviscid invariant for our semi-discrete formulation. Consequently, our formulation exhibits time-reversibility.

## 9.4 Global Existence and Uniqueness

Using standard approaches from the theory of ordinary differential equations, we obtain the following theorem.

**Theorem 9.4.1.** *Assume (6.19) and (6.20) are satisfied. Then Problem (G) has a unique solution  $(\mathbf{u}_h, p_h) \in \mathcal{V}_T^h \times \mathcal{Q}_T^h$ . Moreover,*

$$\|\mathbf{u}_h\|_{L^\infty(0,T;\mathbf{L}^2(\Omega))} \leq e^T \left( \|\mathbf{u}_{0,h}\|_{\mathbf{L}^2(\Omega)} + \|\mathbf{f}\|_{L^2(0,T;\mathbf{L}^2(\Omega))} \right) \quad (9.11)$$

and

$$\int_0^T \|\mathbf{u}_h\|_h^2 dt \leq \frac{1}{4\nu C_{coerc}} \left( \|\mathbf{u}_h\|_{L^2(0,T;\mathbf{L}^2(\Omega))}^2 + \|\mathbf{f}\|_{L^2(0,T;\mathbf{L}^2(\Omega))}^2 \right) \quad (9.12)$$

where  $C_{coerc}$  is the coercivity constant appearing in Corollary 7.3.1.

*Proof.* The proof follows in exactly the same manner as Theorem 8.3.1.  $\square$

Note that the above theorem gives existence and uniqueness results for any end-time  $T$ . Hence, we have global-in-time existence and uniqueness for our semi-discrete problem. Moreover, our method is well-posed in the sense that it returns discrete solutions which depend continuously on the given data. This gives our methodology firm mathematical grounding.

## 9.5 A Priori Error Estimates

We are now ready to prove *a priori* error estimates for our semi-discrete formulation. We restrict our attention to proving  $\mathbf{L}^2$  estimates for the semi-discrete velocity field. Of course, without uniqueness, one cannot hope to talk about error estimates in any reasonable fashion. However, if we assume that a Leray-Hopf solution is sufficiently smooth, we can prove that such a solution is unique, and one

can use standard functional analysis techniques to prove our semi-discrete solution converges to the Leray-Hopf solution.

Now, let  $\mathbf{u}$  denote a Leray-Hopf solution of the unsteady Navier-Stokes equations. Following Section 5 of [100], let us split the velocity error  $\mathbf{u} - \mathbf{u}^h$  into two parts,  $\mathbf{u} - \tilde{\mathbf{u}}_h$ , where  $\tilde{\mathbf{u}}_h$  is the divergence-free B-spline approximation of a linearized unsteady Stokes problem, and  $\tilde{\mathbf{u}}_h - \mathbf{u}_h$ . The velocity field  $\tilde{\mathbf{u}}_h$  specifically satisfies  $\tilde{\mathbf{u}}_h(\cdot, 0) = \mathbf{u}_{0,h}$  and, for almost every  $t \in (0, T)$ ,

$$(\partial_t \tilde{\mathbf{u}}_h(t), \mathbf{v}_h)_{\mathbf{L}^2(\Omega)} + k_h(\tilde{\mathbf{u}}_h(t), \mathbf{v}_h) = -c(\mathbf{u}(t), \mathbf{u}(t); \mathbf{v}_h) + (\mathbf{f}(t), \mathbf{v}_h)_{\mathbf{L}^2(\Omega)} \quad (9.13)$$

for all

$$\mathbf{v}_h \in \mathring{\mathcal{V}}_{0,h} := \{\mathbf{w}_h \in \mathcal{V}_{0,h} : \operatorname{div} \mathbf{w}_h = 0\}.$$

Note that the results of the preceding chapter immediately provide *a priori* estimates for  $\mathbf{u} - \tilde{\mathbf{u}}_h$ . Hence, it remains to obtain bounds for  $\tilde{\mathbf{u}}_h - \mathbf{u}_h$ . The following theorem gives such bounds.

**Theorem 9.5.1.** *Assume that (6.19) and (6.20) are satisfied and that the domain  $\Omega$  satisfies the elliptic regularity condition. Let  $\mathbf{u}$  denote a Leray-Hopf solution of the unsteady Navier-Stokes equations,  $(\mathbf{u}_h, p_h)$  denote the unique weak solution of (G), and  $\tilde{\mathbf{u}}$  denote the solution of the linearized Stokes problem given by (9.13). If the regularity conditions*

$$\mathbf{u} \in L^\infty(0, T; \mathbf{H}^2(\Omega)), \quad \partial_t \mathbf{u} \in L^2(0, T; \mathbf{H}^2(\Omega))$$

*hold, then we have*

$$\|\tilde{\mathbf{u}}_h - \mathbf{u}_h\|_{L^\infty(0,T;\mathbf{L}^2(\Omega))}^2 \leq Q \exp\{\beta T\} \|\mathbf{u} - \tilde{\mathbf{u}}_h\|_{L^2(0,T;\mathbf{L}^2(\Omega))}^2 \quad (9.14)$$

*with*

$$Q = \frac{1}{\nu C_{coerc}} \left( \|\mathbf{u}\|_{L^\infty(0,T;\mathbf{L}^\infty(\Omega))} + \gamma \right)^2, \quad \beta = \frac{1}{\nu C_{coerc}} \gamma^2 - \frac{2\nu C_{coerc}}{C_{poin}^2} \quad (9.15)$$

where

$$\gamma = \|\mathbf{u}\|_{L^\infty(0,T;L^\infty(\Omega))} + C_\infty h^{2-d/2} \left( \|\mathbf{u}\|_{L^\infty(0,T;\mathbf{H}^2(\Omega))}^2 + (2\nu)^{-1} \|\partial_t \mathbf{u}\|_{L^2(0,T;\mathbf{H}^2(\Omega))}^2 \right)^{1/2},$$

$C_\infty$  is the positive constant appearing in Theorem 8.4.5,  $C_{coerc}$  is the coercivity constant appearing in Corollary 7.3.1, and  $C_{poin}$  is the Poincaré constant appearing in (6.14).

*Proof.* For the remainder of the proof, let us denote

$$\mathbf{e}_h = \tilde{\mathbf{u}}_h - \mathbf{u}_h, \quad \boldsymbol{\eta} = \mathbf{u} - \tilde{\mathbf{u}}_h.$$

Subtracting (9.8) from (9.13), we obtain

$$(\partial_t \mathbf{e}_h(t), \mathbf{v}_h)_{\mathbf{L}^2(\Omega)} + k_h(\mathbf{e}_h(t), \mathbf{v}_h) = c(\mathbf{u}_h(t), \mathbf{u}_h(t); \mathbf{v}_h) - c(\mathbf{u}(t), \mathbf{u}(t); \mathbf{v}_h)$$

for every  $\mathbf{v}_h \in \mathring{V}_{0,h}$ . Setting  $\mathbf{v}_h = \mathbf{e}_h(t)$  in the above expression yields

$$\frac{1}{2} \frac{d}{dt} \|\mathbf{e}_h(t)\|_{\mathbf{L}^2(\Omega)}^2 + k_h(\mathbf{e}_h(t), \mathbf{e}_h(t)) = c(\mathbf{u}_h(t), \mathbf{u}_h(t); \mathbf{e}_h(t)) - c(\mathbf{u}(t), \mathbf{u}(t); \mathbf{e}_h(t)). \quad (9.16)$$

A simple algebraic manipulation gives

$$\begin{aligned} c(\mathbf{u}(t), \mathbf{u}(t); \mathbf{e}_h(t)) &= c(\mathbf{u}(t), \boldsymbol{\eta}(t); \mathbf{e}_h(t)) + c(\boldsymbol{\eta}(t), \tilde{\mathbf{u}}_h(t); \mathbf{e}_h(t)) \\ &\quad + c(\mathbf{e}_h(t), \tilde{\mathbf{u}}_h(t); \mathbf{e}_h(t)) + c(\mathbf{u}_h(t), \mathbf{e}_h(t); \mathbf{e}_h(t)) \\ &\quad + c(\mathbf{u}_h(t), \mathbf{u}_h(t); \mathbf{e}_h(t)). \end{aligned}$$

By Lemma 7.3.2, we have

$$c(\mathbf{u}_h(t), \mathbf{e}_h(t); \mathbf{e}_h(t)) = 0.$$

Thus,

$$\begin{aligned} c(\mathbf{u}(t), \mathbf{u}(t); \mathbf{e}_h(t)) &= c(\mathbf{u}(t), \boldsymbol{\eta}(t); \mathbf{e}_h(t)) + c(\boldsymbol{\eta}(t), \tilde{\mathbf{u}}_h(t); \mathbf{e}_h(t)) \\ &\quad + c(\mathbf{e}_h(t), \tilde{\mathbf{u}}_h(t); \mathbf{e}_h(t)) + c(\mathbf{u}_h(t), \mathbf{u}_h(t); \mathbf{e}_h(t)). \end{aligned}$$

Now, plugging the above expression into (9.16), we obtain

$$\begin{aligned} \frac{1}{2} \frac{d}{dt} \|\mathbf{e}_h(t)\|_{\mathbf{L}^2(\Omega)}^2 + k_h(\mathbf{e}_h(t), \mathbf{e}_h(t)) &= -c(\boldsymbol{\eta}(t), \tilde{\mathbf{u}}_h(t); \mathbf{e}_h(t)) - c(\mathbf{e}_h(t), \tilde{\mathbf{u}}_h(t); \mathbf{e}_h(t)) \\ &\quad - c(\mathbf{u}(t), \boldsymbol{\eta}(t); \mathbf{e}_h(t)) \end{aligned} \quad (9.17)$$

Multiple applications of Hölder's inequality gives the following three expressions:

$$\begin{aligned} c(\boldsymbol{\eta}(t), \tilde{\mathbf{u}}_h(t); \mathbf{e}_h(t)) &\leq \|\boldsymbol{\eta}(t)\|_{\mathbf{L}^2(\Omega)} \|\tilde{\mathbf{u}}_h(t)\|_{\mathbf{L}^\infty(\Omega)} |\mathbf{e}_h(t)|_{\mathbf{H}^1(\Omega)} \\ c(\mathbf{e}_h(t), \tilde{\mathbf{u}}_h(t); \mathbf{e}_h(t)) &\leq \|\mathbf{e}_h(t)\|_{\mathbf{L}^2(\Omega)} \|\tilde{\mathbf{u}}_h(t)\|_{\mathbf{L}^\infty(\Omega)} |\mathbf{e}_h(t)|_{\mathbf{H}^1(\Omega)} \\ c(\mathbf{u}(t), \boldsymbol{\eta}(t); \mathbf{e}_h(t)) &\leq \|\mathbf{u}(t)\|_{\mathbf{L}^\infty} \|\boldsymbol{\eta}(t)\|_{\mathbf{L}^2(\Omega)} |\mathbf{e}_h(t)|_{\mathbf{H}^1(\Omega)}. \end{aligned}$$

Inserting the above expressions into (9.17) yields

$$\frac{1}{2} \frac{d}{dt} \|\mathbf{e}_h(t)\|_{\mathbf{L}^2(\Omega)}^2 + k_h(\mathbf{e}_h(t), \mathbf{e}_h(t)) \leq \Phi(t) |\mathbf{e}_h(t)|_{\mathbf{H}^1(\Omega)}$$

where

$$\Phi(t) := \|\tilde{\mathbf{u}}_h(t)\|_{\mathbf{L}^\infty(\Omega)} \|\mathbf{e}_h(t)\|_{\mathbf{L}^2(\Omega)} + (\|\mathbf{u}(t)\|_{\mathbf{L}^\infty} + \|\tilde{\mathbf{u}}_h(t)\|_{\mathbf{L}^\infty(\Omega)}) \|\boldsymbol{\eta}(t)\|_{\mathbf{L}^2(\Omega)}.$$

Invoking Young's inequality, we immediately obtain

$$\frac{d}{dt} \|\mathbf{e}_h(t)\|_{\mathbf{L}^2(\Omega)}^2 + k_h(\mathbf{e}_h(t), \mathbf{e}_h(t)) \leq \frac{1}{2\epsilon} \Phi^2(t) + \frac{\epsilon}{2} |\mathbf{e}_h(t)|_{\mathbf{H}^1(\Omega)}^2$$

where  $\epsilon > 0$  is an arbitrary positive constant. To proceed, we employ Corollary 7.3.1 to write

$$\frac{1}{2} \frac{d}{dt} \|\mathbf{e}_h(t)\|_{\mathbf{L}^2(\Omega)}^2 + 2\nu C_{coerc} \|\mathbf{e}_h(t)\|_h^2 \leq \frac{1}{2\epsilon} \Phi^2(t) + \frac{\epsilon}{2} |\mathbf{e}_h(t)|_{\mathbf{H}^1(\Omega)}^2.$$

Selecting  $\epsilon = 2\nu C_{coerc}$  and employing the Poincaré inequality finally yields the expression

$$\frac{d}{dt} \|\mathbf{e}_h(t)\|_{\mathbf{L}^2(\Omega)}^2 \leq \frac{1}{2\nu C_{coerc}} \Phi^2(t) - \frac{2\nu C_{coerc}}{C_{poin}^2} \|\mathbf{e}_h(t)\|_{\mathbf{L}^2(\Omega)}^2$$

where  $C_{\text{poin}} > 0$  is the positive constant appearing in (6.14). Now, the triangle inequality gives

$$\frac{d}{dt} \|\mathbf{e}_h(t)\|_{\mathbf{L}^2(\Omega)}^2 \leq A(t) \|\mathbf{e}_h(t)\|_{\mathbf{L}^2(\Omega)}^2 + B(t)$$

where

$$A(t) = \frac{1}{\nu C_{\text{coerc}}} \|\tilde{\mathbf{u}}_h(t)\|_{\mathbf{L}^\infty(\Omega)}^2 - \frac{2\nu C_{\text{coerc}}}{C_{\text{poin}}^2}$$

and

$$B(t) = \frac{1}{\nu C_{\text{coerc}}} (\|\mathbf{u}(t)\|_{\mathbf{L}^\infty} + \|\tilde{\mathbf{u}}_h(t)\|_{\mathbf{L}^\infty(\Omega)})^2 \|\boldsymbol{\eta}(t)\|_{\mathbf{L}^2(\Omega)}^2.$$

We can immediately apply the differential form of Gronwall's inequality to obtain the expression

$$\|\mathbf{e}_h\|_{L^\infty(0,T;\mathbf{L}^2(\Omega))}^2 \leq \exp \left\{ \int_0^T A(t) dt \right\} \int_0^T B(t) dt \quad (9.18)$$

where we have exploited the fact that  $\mathbf{e}_h(0) = 0$ . The theorem follows by using Theorem 8.4.5 to bound  $\|\tilde{\mathbf{u}}_h(t)\|_{\mathbf{L}^\infty(\Omega)}$ .  $\square$

Combining Theorems 8.4.4 and 9.5.1 immediately gives optimal error estimates for the velocity field in the  $\mathbf{L}^2$ -norm, as encompassed in the following theorem.

**Theorem 9.5.2.** *Assume that (6.19) and (6.20) are satisfied and that the domain  $\Omega$  satisfies the elliptic regularity condition. Let  $\mathbf{u}$  denote a Leray-Hopf solution of the unsteady Navier-Stokes equations and  $(\mathbf{u}_h, p_h)$  denote the unique weak solution of (G). If the regularity conditions*

$$\mathbf{u} \in L^\infty(0, T; \mathbf{H}^{j+1}(\Omega)), \quad \partial_t \mathbf{u} \in L^2(0, T; \mathbf{H}^{j+1}(\Omega))$$

hold for  $j \geq 1$ , then we have

$$\|\mathbf{u} - \mathbf{u}_h\|_{L^\infty(0,T;\mathbf{L}^2(\Omega))}^2 \leq C_{NS} (1 + QT \exp\{\beta T\}) h^{2(s+1)} \left( \|\mathbf{u}\|_{L^\infty(0,T;\mathbf{H}^{s+1}(\Omega))}^2 + (2\nu)^{-1} \|\partial_t \mathbf{u}\|_{L^2(0,T;\mathbf{H}^{s+1}(\Omega))}^2 \right) \quad (9.19)$$

where  $s = \min\{k', j\}$ ,  $Q$  and  $\beta$  are the constants appearing in Theorem 9.5.1, and  $C_{NS}$  is a positive constant independent of  $h$ ,  $\nu$ , and  $T$  that scales asymptotically with  $C_{pen}$ .

We would like to mention that the above two theorems guarantee that if a Leray-Hopf solution  $\mathbf{u}$  satisfies the regularity conditions

$$\mathbf{u} \in L^\infty(0, T; \mathbf{H}^2(\Omega)), \quad \partial_t \mathbf{u} \in L^2(0, T; \mathbf{H}^2(\Omega)),$$

then it is the only such solution satisfying the regularity conditions. This gives a uniqueness result for sufficiently smooth solutions of the unsteady Navier-Stokes equations. Let us further note that while Theorem 9.5.2 gives an optimal  $\mathbf{L}^2$  error bound for the velocity field in terms of the mesh size  $h$ , the bound grows exponentially in time. Unfortunately, such a dependence is, in general, unavoidable. However, if we assume an exact solution is stable in the sense that perturbations decay exponentially in time, we can use standard techniques to prove error estimates which are uniform in time [101]. Such a discussion is beyond the scope of this written dissertation. Furthermore, as was the case for the unsteady Stokes problem, it is known that solutions of the unsteady Navier-Stokes problem may experience blow up at the initial time unless certain compatibility conditions relating the initial condition and applied forcing are satisfied. The inherent smoothing properties of unsteady Navier-Stokes flow may be exploited in order to derive optimal error estimates away from the initial time for higher-order spatial discretizations [102].

Finally, we may utilize a similar procedure to that found in Section 5 of [100] to derive suboptimal, by one order,  $L^2$  error bounds for the pressure field. However, this procedure is rather involved, so we have elected not to include it here.

## 9.6 Conservation Properties on Rectilinear Domains

In these next three sections, we present a collection of balance laws for our semi-discretization scheme. Before proceeding forth, we pose our semi-discrete problem in a slightly different form. This form will more directly reveal the conservation structure of our chosen semi-discretization. To this effect, let us introduce the following discrete trace space:

$$\mathcal{V}_{trace,h} := \{q \in L^2(\partial\Omega) : q = \mathbf{v}_h \cdot \mathbf{n}, \mathbf{v}_h \in \mathcal{V}_h\}. \quad (9.20)$$

Note that, in the above expression,  $\mathcal{V}_h$  denotes the space of discrete velocity fields which are free of Dirichlet boundary conditions.  $\mathcal{V}_{trace,h}$  represents the natural trace space associated with  $\mathcal{V}_h$ , and it is a Hilbert space when endowed with the standard  $L^2$  inner-product over  $\partial\Omega$ . Introducing the space-time trace space

$$\mathcal{V}_{trace,T}^h := L^2(0, T; \mathcal{V}_{trace,h}), \quad (9.21)$$

let us consider the following semi-discrete problem.

$$(A) \left\{ \begin{array}{l} \text{Find } \mathbf{u}_h \in \mathcal{V}_T^h, p_h \in \mathcal{Q}_T^h, \text{ and } p_{trace,h} \in \mathcal{V}_{trace,T}^h \text{ such that } \mathbf{u}_h(0) = \mathbf{u}_{0,h} \text{ and,} \\ \text{for almost every } t \in (0, T), \\ (\partial_t \mathbf{u}_h(t), \mathbf{v}_h)_{\mathbf{L}^2(\Omega)} + k_h(\mathbf{u}_h(t), \mathbf{v}_h) + c(\mathbf{u}_h(t), \mathbf{u}_h(t); \mathbf{v}_h) \\ - b(p_h(t), \mathbf{v}_h) + (p_{trace,h}(t), \mathbf{v}_h \cdot \mathbf{n})_{L^2(\partial\Omega)} + b(q_h, \mathbf{u}_h(t)) = (\mathbf{f}(t), \mathbf{v}_h)_{\mathbf{L}^2(\Omega)} \\ \text{for all } \mathbf{v}_h \in \mathcal{V}_h \text{ and } q_h \in \mathcal{Q}_{0,h}. \end{array} \right. \quad (9.22)$$

Here, we have introduced the auxiliary field  $p_{trace,h}$  and released the no-penetration boundary condition on the discrete test space for the momentum equations. Note that the solution of Problem (G) is also a solution to Problem (A) (modulo the auxiliary field  $p_{trace,h}$ ) since

$$(p_{trace,h}(t), \mathbf{v}_h \cdot \mathbf{n})_{L^2(\partial\Omega)} = 0, \quad \forall \mathbf{v}_h \in \mathcal{V}_{0,h}.$$

Furthermore, the auxiliary field  $p_{trace,h}$  is unique due to the obvious inf-sup condition

$$\inf_{\substack{q_h \in \mathcal{V}_{trace,h} \\ q_h \neq 0}} \sup_{\mathbf{v}_h \in \mathcal{V}_h} (q_h, \mathbf{v}_h \cdot \mathbf{n})_{L^2(\partial\Omega)} = \|q_h\|_{L^2(\partial\Omega)}^2.$$

By employing integration by parts, we observe the auxiliary field  $p_{trace,h}$  approximates the trace of the pressure field. Hence,  $p_{trace,h} \mathbf{n}$  gives the discrete normal traction along  $\partial\Omega$  due to pressure forces.

Now, suppose that  $\Omega$  is a rectilinear domain that has been mapped from parametric space using an affine transformation. Then, the unit vectors  $\mathbf{e}_i \in \mathbb{R}^d$  necessarily belong to the discrete space  $\mathcal{V}_h$ . If we select  $\mathbf{v}_h = \mathbf{e}_i$  and  $q_h = p_h(t)$  in (9.22) and sum over  $i = 1, \dots, d$ , we obtain the following discrete balance law for linear momentum.

**Global conservation of linear momentum on rectilinear domains.** *For rectilinear domains, the discrete velocity field  $\mathbf{u}_h$  satisfies*

$$\frac{d}{dt} \int_{\Omega} \mathbf{u}_h(t) d\mathbf{x} = \int_{\partial\Omega} (-p_{trace,h}(t) \mathbf{n} + \mathbb{Q}(t)) ds + \int_{\Omega} \mathbf{f}(t) d\mathbf{x} \quad (9.23)$$

for almost all  $t \in (0, T)$  where

$$\mathbb{Q}(t) = 2\nu \left( (\nabla^s \mathbf{u}_h(t)) \mathbf{n} - \frac{C_{pen}}{h_F} \mathbf{u}_h(t) \right)$$

for a given mesh face  $F \in \Gamma_h$ .

By interpreting Nitsche's method as a variational wall model as was discussed in Section 7.2, we see that the above balance law dictates that linear momentum enters or leaves the system via either body forces or surface traction forces. Hence, our semi-discrete formulation properly mimics the continuous problem. We can derive similar balance laws when non-homogeneous Dirichlet, traction, or periodic boundary conditions are specified instead of homogeneous Dirichlet boundary conditions. Additionally, we can derive momentum balance laws over subdomains by introducing auxiliary flux spaces on subdomain boundaries. For more on this procedure, see [110].

## 9.7 Conservation Properties on Cylindrical Domains

When the domain  $\Omega$  is not rectilinear, our semi-discrete formulation is no longer guaranteed to globally conserve linear momentum. This is because the Piola transformation does not, in general, map constant vector fields in parametric space to constant vector fields in physical space. However, the special structure of the Piola transformation allows our formulation to admit more natural momentum balance laws for general parametric domains. In this section, we demonstrate that if  $\Omega$  is a cylindrical domain defined via a polar mapping, our formulation globally conserves axial angular momentum and axial linear momentum.

To proceed, let us introduce the mapping

$$\mathbf{F}(\xi_1, \xi_2, \xi_3) = \begin{bmatrix} ((r_{out} - r_{in})\xi_2 + r_{in}) \sin(2\pi\xi_1) \\ ((r_{out} - r_{in})\xi_2 + r_{in}) \cos(2\pi\xi_1) \\ H\xi_3 \end{bmatrix}, \forall (\xi_1, \xi_2, \xi_3) \in (0, 1)^3$$

from the parametric domain  $\widehat{\Omega} = (0, 1)^3$  to a physical domain  $\Omega$  set between two

concentric cylinders. The radius of the inner cylinder is taken to be  $r_{in}$ , the radius of the outer cylinder is taken to be  $r_{out}$ , and the heights of the cylinders are taken to be  $H$ . Periodicity is applied in the  $\xi_1$  direction. We have the following relationship between our parametric coordinate system and the cylindrical coordinate system  $(r, \theta, z)$ :

$$\begin{aligned} r &= (r_{out} - r_{in})\xi_2 + r_{in} \\ \theta &= 2\pi\xi_1 \\ z &= H\xi_3. \end{aligned}$$

Without loss of generality, let us assume that  $r_{in} = 1$ ,  $r_{out} = 2$ , and  $H = 1$ . As discussed in Chapter 5, the discrete velocity functions  $\mathbf{v}_h \in \mathcal{V}_h$  have the representation

$$\mathbf{v}_h(\mathbf{x}(\boldsymbol{\xi})) := \frac{1}{\det(D\mathbf{F}(\boldsymbol{\xi}))} D\mathbf{F}(\boldsymbol{\xi}) \widehat{\mathbf{v}}_h(\boldsymbol{\xi})$$

where  $\widehat{\mathbf{v}}_h \in \widehat{\mathcal{V}}_h$ . A direct computation shows

$$\mathbf{v}_h(\mathbf{x}(\boldsymbol{\xi})) := \begin{bmatrix} \cos(\theta) & \frac{\sin(\theta)}{2\pi r} & 0 \\ -\sin(\theta) & \frac{\cos(\theta)}{2\pi r} & 0 \\ 0 & 0 & \frac{1}{2\pi r} \end{bmatrix} \widehat{\mathbf{v}}_h(\boldsymbol{\xi}).$$

Now, since the space  $\widehat{\mathcal{V}}_h$  contains all vector-valued functions which are constant in  $\xi_1$  and  $\xi_3$  and linear in  $\xi_2$ , we thus have proven the vector-valued functions

$$\mathbf{s} = \begin{bmatrix} r \cos(\theta) \\ -r \sin(\theta) \\ 0 \end{bmatrix} = \begin{bmatrix} y \\ -x \\ 0 \end{bmatrix}, \quad \mathbf{z} = \begin{bmatrix} 0 \\ 0 \\ 1 \end{bmatrix}$$

are members of  $\mathcal{V}_h$ . Let us now select  $\mathbf{v}_h = \mathbf{s}$  and  $q_h = p_h(t)$  in (9.22). Since  $\nabla \mathbf{s}$  is an anti-symmetric matrix, we have

$$\begin{aligned} \int_{\Omega} (2\nu (\nabla^s \mathbf{u}_h(t)) : (\nabla^s \mathbf{s}) - (\mathbf{u}_h(t) \otimes \mathbf{u}_h(t)) : \nabla \mathbf{s}) \, d\mathbf{x} \\ - \int_{\partial\Omega} 2\nu ((\nabla^s \mathbf{s}) \mathbf{n}) \cdot \mathbf{u}_h(t) \, ds = 0 \end{aligned}$$

for almost every  $t \in (0, T)$ . Therefore,

$$\begin{aligned} \frac{d}{dt} \int_{\Omega} \mathbf{u}_h(t) \cdot \mathbf{s} d\mathbf{x} &= \int_{\partial\Omega} \left( -p_{trace,h}(t) \mathbf{n} + 2\nu \left( (\nabla^s \mathbf{u}_h(t)) \mathbf{n} - \frac{C_{pen}}{h_F} \mathbf{u}_h(t) \right) \right) \cdot \mathbf{s} ds \\ &\quad + \int_{\Omega} \mathbf{f}(t) \cdot \mathbf{s} d\mathbf{x}. \end{aligned}$$

Furthermore, we have that

$$\mathbf{w} \cdot \mathbf{s} = (\mathbf{w} \times \mathbf{r})_z, \quad \forall \mathbf{w} \in \mathbb{R}^3$$

where  $(\cdot)_z$  denotes the  $z$ -component of a vector and

$$\mathbf{r} = \begin{bmatrix} r \sin(\theta) \\ r \cos(\theta) \\ 0 \end{bmatrix}.$$

Hence, we have proven the following balance law for axial angular momentum.

**Global conservation of axial angular momentum on cylindrical domains.** *For cylindrical domains, the discrete velocity field  $\mathbf{u}_h$  satisfies*

$$\begin{aligned} \frac{d}{dt} \int_{\Omega} (\mathbf{u}_h(t) \times \mathbf{r})_z d\mathbf{x} &= \int_{\partial\Omega} ((-p_{trace,h}(t) \mathbf{n} + \mathbb{Q}(t)) \times \mathbf{r})_z ds \\ &\quad + \int_{\Omega} (\mathbf{f}(t) \times \mathbf{r})_z d\mathbf{x} \end{aligned} \tag{9.24}$$

for almost all  $t \in (0, T)$  where

$$\mathbf{r} = \begin{bmatrix} r \sin(\theta) \\ r \cos(\theta) \\ 0 \end{bmatrix}$$

and

$$\mathbb{Q}(t) = 2\nu \left( (\nabla^s \mathbf{u}_h(t)) \mathbf{n} - \frac{C_{pen}}{h_F} \mathbf{u}_h(t) \right)$$

for a given mesh face  $F \in \Gamma_h$ .

The above balance law dictates that axial angular momentum enters or leaves the discrete system via either applied moments or torque. This balance law mimics the corresponding continuous balance law for axial angular momentum. We would like to mention that derivation of this balance law was contingent upon employing the symmetrized gradient for the viscous stress term instead of the full gradient.

Selecting  $\mathbf{v}_h = \mathbf{z}$  and  $q_h = p_h(t)$  in (9.22) yields the following balance law for axial linear momentum. It states that axial momentum enters or leaves the system via either axial body forces or axial traction forces.

**Global conservation of axial linear momentum on cylindrical domains.** *For cylindrical domains, the discrete velocity field  $\mathbf{u}_h$  satisfies*

$$\begin{aligned} \frac{d}{dt} \int_{\Omega} (\mathbf{u}_h(t))_z d\mathbf{x} &= \int_{\partial\Omega} ((-p_{trace,h}(t)\mathbf{n} + \mathbb{Q}(t)))_z ds \\ &+ \int_{\Omega} (\mathbf{f}(t))_z d\mathbf{x} \end{aligned} \quad (9.25)$$

for almost all  $t \in (0, T)$  where

$$\mathbb{Q}(t) = 2\nu \left( (\nabla^s \mathbf{u}_h(t)) \mathbf{n} - \frac{C_{pen}}{h_F} \mathbf{u}_h(t) \right)$$

for a given mesh face  $F \in \Gamma_h$ .

As a final note, we would like to state that if we had utilized a NURBS mapping to represent the physical domain  $\Omega$  as described in Subsection 6.6.4, we would have arrived at a global conservation statement for axial angular momentum but not for axial linear momentum. Hence, we believe polar mappings hold a distinct advantage over NURBS mappings when solving problems harboring important symmetry and conservation properties. This being said, we would like to mention

that one recovers both linear and angular momentum balance laws when employing NURBS-based isogeometric analysis in conjunction with a residual-based Variational Multiscale method [16]. Such a discretization, however, does not exactly replicate the incompressibility constraint and alternatively attempts to model the effects of fine-scale solution features (including, in this case, compressibility) on the resolved components of the flow.

## 9.8 Vorticity, Enstrophy, and Helicity

We continue this chapter by deriving discrete balance laws for vorticity, enstrophy, and helicity when the applied forcing term is conservative (*i.e.*, when the forcing is derived through a potential). In order to do so, we must properly define vorticity at the discrete level (see, for example, [157]). We restrict our discussion to the three-dimensional setting for the remainder of this section. Recall from Chapter 3 that vorticity satisfies

$$\frac{\partial \boldsymbol{\omega}}{\partial t} + \nabla \cdot (\mathbf{u} \otimes \boldsymbol{\omega} - \boldsymbol{\omega} \otimes \mathbf{u}) = \nabla \cdot (2\nu \nabla^s \boldsymbol{\omega}) \quad (9.26)$$

and

$$\operatorname{div} \boldsymbol{\omega} = 0. \quad (9.27)$$

Furthermore, since  $\mathbf{u} = \mathbf{0}$  on  $\partial\Omega$ ,

$$\boldsymbol{\omega} \cdot \mathbf{n} = 0 \quad (9.28)$$

and

$$((\nabla^s \boldsymbol{\omega}) \mathbf{n}) \times \mathbf{n} = \mathbf{0} \quad (9.29)$$

on  $\partial\Omega$ . In light of these conservation statements and boundary conditions, we define discrete vorticity as the solution of the following semi-discrete problem: find  $\boldsymbol{\omega}_h \in$

$\mathring{\mathcal{V}}_T^h = \{\mathbf{v}_h \in \mathcal{V}_T^h : \operatorname{div} \mathbf{v}_h = 0\}$  such that  $\boldsymbol{\omega}_h(0) = \boldsymbol{\omega}_{0,h}$  and, for almost every  $t \in (0, T)$ ,

$$(\partial_t \boldsymbol{\omega}_h(t), \mathbf{v}_h)_{\mathbf{L}^2(\Omega)} + k(\boldsymbol{\omega}_h(t), \mathbf{v}_h) + c(\mathbf{u}_h(t), \boldsymbol{\omega}_h(t); \mathbf{v}_h) - c(\boldsymbol{\omega}_h(t), \mathbf{u}_h(t); \mathbf{v}_h) = 0 \quad (9.30)$$

for all  $\mathbf{v}_h \in \mathring{\mathcal{V}}_{0,h}$  where  $\boldsymbol{\omega}_{0,h} \in \mathring{\mathcal{V}}_{0,h}$  is a suitably defined initial condition and  $k(\cdot, \cdot)$  is defined by (7.5). Note that the above problem may not have a global-in-time solution. This is due to the presence of reaction in the form of vortex stretching. However, Picard's existence theorem can be used to show the problem has a unique local-in-time solution. Hence, let us assume for the remainder of this discussion that the end-time  $T$  has been sufficiently chosen such that the discrete vorticity equation has a unique solution. Beyond such  $T$ , the discrete vorticity may, in theory, experience blow-up. Such a hypothetical blow-up lies at the heart of the Navier-Stokes Millennium Problem.

We first present a discrete balance law for vorticity which holds for periodic domains. It is a simple consequence of choosing  $\mathbf{v}_h = \mathbf{e}_i$  in (9.30) where  $\mathbf{e}_i$  is a unit vector. Analogous balance laws can be proven for rectilinear domains subject to no-penetration and no-slip boundary conditions.

**Global balance law for discrete vorticity.** *Suppose  $\Omega$  is the three-dimensional torus. For conservative applied forces, the discrete vorticity field  $\boldsymbol{\omega}_h$  satisfies*

$$\frac{d}{dt} \int_{\Omega} \boldsymbol{\omega}_h(t) d\mathbf{x} = \mathbf{0} \quad (9.31)$$

*for almost all  $t \in (0, T)$ .*

We now derive a discrete balance law for enstrophy. To begin, we insert  $\mathbf{v}_h = \boldsymbol{\omega}_h(t)$  into (9.30) for almost every  $t \in (0, T)$ . By employing Lemma 7.3.2, we obtain

$$(\partial_t \boldsymbol{\omega}_h(t), \boldsymbol{\omega}_h(t))_{\mathbf{L}^2(\Omega)} + k(\boldsymbol{\omega}_h(t), \boldsymbol{\omega}_h(t)) - c(\boldsymbol{\omega}_h(t), \mathbf{u}_h(t); \boldsymbol{\omega}_h(t)) = 0.$$

The product rule gives

$$(\partial_t \boldsymbol{\omega}_h(t), \boldsymbol{\omega}_h(t))_{\mathbf{L}^2(\Omega)} = \frac{d}{dt} \int_{\Omega} \gamma_h(t) d\mathbf{x}$$

where  $\gamma_h(t) = \frac{1}{2} |\boldsymbol{\omega}_h(t)|^2$  is the discrete enstrophy density of the fluid. To handle the term corresponding to vortex stretching, we employ integration by parts and the fact that  $\operatorname{div} \boldsymbol{\omega}_h = 0$  to write

$$c(\boldsymbol{\omega}_h(t), \mathbf{u}_h(t); \boldsymbol{\omega}_h(t)) = - \int_{\Omega} \boldsymbol{\omega}_h(t)^T \nabla \mathbf{u}(t) \boldsymbol{\omega}_h(t) d\mathbf{x}.$$

A direct calculation then gives

$$\boldsymbol{\omega}_h(t)^T \nabla \mathbf{u}(t) \boldsymbol{\omega}_h(t) = \boldsymbol{\omega}_h(t)^T \mathbb{D}(\mathbf{u}_h(t)) \boldsymbol{\omega}_h(t)$$

where  $\mathbb{D}(\mathbf{u}_h(t)) = \nabla^s \mathbf{u}_h(t)$  is the discrete rate of strain tensor. Thus, we have arrived at the following balance law.

**Global balance law for discrete enstrophy.** *For conservative applied forces, the discrete vorticity field  $\boldsymbol{\omega}_h$  satisfies*

$$\frac{d}{dt} \int_{\Omega} \gamma_h(t) d\mathbf{x} = - \int_{\Omega} 2\nu |\nabla^s \boldsymbol{\omega}_h(t)|^2 d\mathbf{x} + \int_{\Omega} \boldsymbol{\omega}_h(t)^T \mathbb{D}(\mathbf{u}_h(t)) \boldsymbol{\omega}_h(t) d\mathbf{x} \quad (9.32)$$

for almost all  $t \in (0, T)$ .

The above balance law dictates that our discrete formulation properly accounts for enstrophy production. Note that since the divergence of  $\mathbf{u}_h$  is precisely zero,  $\mathbb{D}(\mathbf{u}_h(t))$  has the same indefinite structure as its continuous counterpart. That is, it has three real eigenvalues which sum to zero. Consequently, we have appropriately captured the vortex stretching term with our semi-discrete formulation. The same cannot be said for semi-discretizations which satisfy the incompressibility constraint only approximately, even if the momentum and vorticity equations are written in skew-symmetric form as in [157].

We finish here by deriving a discrete balance law for helicity. First insert  $(\mathbf{v}_h, q_h) = (\boldsymbol{\omega}_h(t), p_h(t))$  into (9.8) and  $\mathbf{v}_h = \mathbf{u}_h(t)$  into (9.30) for almost every  $t \in (0, T)$ . Adding the two resulting expressions and taking into consideration the fact that  $\mathbf{f}$  is conservative, we obtain

$$\begin{aligned} & (\partial_t \mathbf{u}_h(t), \boldsymbol{\omega}_h(t))_{\mathbf{L}^2(\Omega)} + k_h(\mathbf{u}_h(t), \boldsymbol{\omega}_h(t)) + c(\mathbf{u}_h(t), \mathbf{u}_h(t); \boldsymbol{\omega}_h(t)) \\ & + (\partial_t \boldsymbol{\omega}_h(t), \mathbf{u}_h(t))_{\mathbf{L}^2(\Omega)} + k(\boldsymbol{\omega}_h(t), \mathbf{u}_h(t)) + c(\mathbf{u}_h(t), \boldsymbol{\omega}_h(t); \mathbf{u}_h(t)) \\ & \quad - c(\boldsymbol{\omega}_h(t), \mathbf{u}_h(t); \mathbf{u}_h(t)) = 0. \end{aligned}$$

By the product rule, we have

$$(\partial_t \mathbf{u}_h(t), \boldsymbol{\omega}_h(t))_{\mathbf{L}^2(\Omega)} + (\partial_t \boldsymbol{\omega}_h(t), \mathbf{u}_h(t))_{\mathbf{L}^2(\Omega)} = \frac{d}{dt} \int_{\Omega} \varrho_h(t) d\mathbf{x}$$

where  $\varrho_h(t) = \boldsymbol{\omega}_h(t) \cdot \mathbf{u}_h(t)$  is the discrete helical density of the flow. Integration by parts and the fact that our velocity field is divergence-free give

$$c(\mathbf{u}_h(t), \mathbf{u}_h(t); \boldsymbol{\omega}_h(t)) = -c(\mathbf{u}_h(t), \boldsymbol{\omega}_h(t); \mathbf{u}_h(t)).$$

Finally, by Lemma 7.3.2, we have

$$c(\boldsymbol{\omega}_h(t), \mathbf{u}_h(t); \mathbf{u}_h(t)) = 0.$$

Collecting our equations, we acquire the following balance law for helicity.

**Global balance law for discrete helicity.** *For conservative applied forces, the discrete solution satisfies*

$$\begin{aligned} \frac{d}{dt} \int_{\Omega} \varrho_h(t) d\mathbf{x} &= - \int_{\Omega} 4\nu (\nabla^s \boldsymbol{\omega}_h(t)) : (\nabla^s \mathbf{u}_h(t)) d\mathbf{x} \\ &\quad + \int_{\partial\Omega} 2\nu ((\nabla^s \boldsymbol{\omega}_h(t)) \mathbf{n}) \cdot \mathbf{u}_h(t) ds \\ &\quad + \int_{\partial\Omega} \mathbb{Q}(t) \cdot \boldsymbol{\omega}_h(t) ds \end{aligned} \tag{9.33}$$

for almost all  $t \in (0, T)$  where

$$\mathbb{Q}(t) = 2\nu \left( (\nabla^s \mathbf{u}_h(t)) \mathbf{n} - \frac{C_{pen}}{h_F} \mathbf{u}_h(t) \right)$$

for a given mesh face  $F \in \Gamma_h$ .

Note the above balance law accounts for boundary effects directly through our weak boundary condition specification. By interpreting Nitsche's method as a variational wall model as was discussed in Section 7.2, we see these boundary effects account for wall shear stress. Furthermore, note that in the limit of vanishing viscosity our global helicity balance reduces to

$$\frac{d}{dt} \int_{\Omega} \varrho_h(t) d\mathbf{x} = 0.$$

Thus, just as in the infinite-dimensional setting, helicity is an inviscid invariant for our semi-discrete formulation. We believe this is a very important property given the pivotal role helicity plays in flow structure development. All of the discrete balance laws presented here generalize to other sets of boundary conditions including non-homogeneous Dirichlet boundary conditions, prescribed traction boundary conditions, and periodic boundary conditions.

## 9.9 Extension to Multi-Patch Domains

To extend our semi-discretization technique to multi-patch domains, we strongly enforce normal continuity of our discrete velocity field between patches and weakly enforce tangential continuity using a combination of upwinding and the interior penalty method. Invoking the notation set forth in Section 7.5, our multi-patch formulation reads as follows.

$$(MP) \left\{ \begin{array}{l} \text{Find } \mathbf{u}_h \in \mathcal{V}_T^h \text{ and } p_h \in \mathcal{Q}_T^h \text{ such that } \mathbf{u}_h(0) = \mathbf{u}_{0,h} \text{ and, for almost every } \\ t \in (0, T), \\ \\ (\partial_t \mathbf{u}_h(t), \mathbf{v}_h)_{\mathbf{L}^2(\Omega)} + k_h^*(\mathbf{u}_h(t), \mathbf{v}_h) \\ + c^*(\mathbf{u}_h(t), \mathbf{u}_h(t); \mathbf{v}_h) - b(p_h(t), \mathbf{v}_h) + b(q_h, \mathbf{u}_h(t)) = (\mathbf{f}(t), \mathbf{v}_h)_{\mathbf{L}^2(\Omega)} \\ (9.34) \\ \\ \text{for all } \mathbf{v}_h \in \mathcal{V}_{0,h} \text{ and } q_h \in \mathcal{Q}_{0,h}. \end{array} \right.$$

As was the case for the generalized Stokes and steady Navier-Stokes equations, the above formulation returns a pointwise divergence-free velocity field. One can further show that the above set of equations satisfies a discrete energy balance law (provided Nitsche's penalty constant is chosen large enough) and is hence well-posed for all time  $T$  in the sense that it has a unique solution which depends continuously on the problem data. However, an error analysis is not yet available for multi-patch domains.

## 9.10 Numerical Verification of Convergence Estimates

In this section, we numerically verify our convergence estimates using a collection of problems with exact solutions. Throughout, we choose Nitsche's penalty constant as

$$C_{pen} = 5(k' + 1).$$

Additionally, we employ uniform parametric meshes and B-spline spaces of maximal continuity.

### 9.10.1 Two-Dimensional Taylor-Green Vortex Flow

As a first numerical example, we consider two-dimensional Taylor-Green vortex flow. Two-dimensional Taylor-Green vortex flow is a simple periodic (in space) vortical flow subject to the initial condition

$$\mathbf{u}_0(x, y) = \begin{bmatrix} \sin(x) \cos(y) \\ -\cos(x) \sin(y) \end{bmatrix}.$$

The exact solution for this flow exponentially decays in time and satisfies the relationships

$$\begin{aligned} \mathbf{u}(x, y, t) &= \begin{bmatrix} \sin(x) \cos(y) \\ -\cos(x) \sin(y) \end{bmatrix} \exp(-2\nu t), \\ p(x, y, t) &= \frac{1}{4} (\cos(2x) + \cos(2y)) \exp(-4\nu t). \end{aligned}$$

It is easily seen that the nonlinear convection term is exactly balanced by the pressure term and thus does not interfere with the evolution of the velocity flow field. Hence, a question of practical interest is whether or not the nonlinear convection term interferes with the evolution of the velocity field at the discrete level.

We have numerically simulated two-dimensional Taylor-Green vortex flow using divergence-conforming B-spline discretizations of varying mesh size and polynomial degree. We restricted our computations to the quarter plane  $\Omega = (0, \pi)^2$  by employing symmetry conditions along  $\partial\Omega$ . A linear parametric mapping was utilized to describe the physical domain. The Crank-Nicolson method [55] was employed to discretize in time, and the time-step size was chosen to be

$$\Delta t = \min \left\{ h^{\frac{k'+1}{2}}, \frac{h^2}{4\nu} \right\},$$

Table 9.1: Two-dimensional Taylor-Green vortex flow: Convergence rates at  $t = 15$  for  $Re = 100$ . Time-step size chosen as  $\Delta t = \min \left\{ h^{\frac{k'+1}{2}}, \frac{h^2}{4\nu} \right\}$ .

Polynomial degree  $k' = 1$

$h$	1/8	1/16	1/32	1/64
$ \mathbf{u} - \mathbf{u}_h _{\mathbf{H}^1(\Omega)}$	1.87e-1	9.34e-2	4.67e-2	2.34e-2
order	-	1.00	1.00	1.00
$\ \mathbf{u} - \mathbf{u}_h\ _{\mathbf{L}^2(\Omega)}$	1.02e-2	2.51e-3	6.24e-4	1.56e-4
order	-	2.02	2.01	2.00
$\ p - p_h\ _{L^2(\Omega)}$	1.09e-2	2.57e-3	6.32e-4	1.59e-4
order	-	2.08	2.02	1.99

Polynomial degree  $k' = 2$

$h$	1/8	1/16	1/32	1/64
$ \mathbf{u} - \mathbf{u}_h _{\mathbf{H}^1(\Omega)}$	9.64e-3	2.38e-3	5.92e-4	1.48e-4
order	-	2.02	2.01	2.00
$\ \mathbf{u} - \mathbf{u}_h\ _{\mathbf{L}^2(\Omega)}$	5.96e-4	7.24e-5	8.98e-6	1.12e-6
order	-	3.04	3.01	3.00
$\ p - p_h\ _{L^2(\Omega)}$	1.39e-3	1.56e-4	1.90e-5	2.36e-6
order	-	3.16	3.04	3.01

Polynomial degree  $k' = 3$

$h$	1/8	1/16	1/32
$ \mathbf{u} - \mathbf{u}_h _{\mathbf{H}^1(\Omega)}$	5.39e-4	6.88e-5	8.76e-6
order	-	3.00	2.97
$\ \mathbf{u} - \mathbf{u}_h\ _{\mathbf{L}^2(\Omega)}$	3.42e-5	2.15e-6	1.36e-7
order	-	3.99	3.98
$\ p - p_h\ _{L^2(\Omega)}$	1.69e-4	9.44e-6	5.77e-7
order	-	4.16	4.03

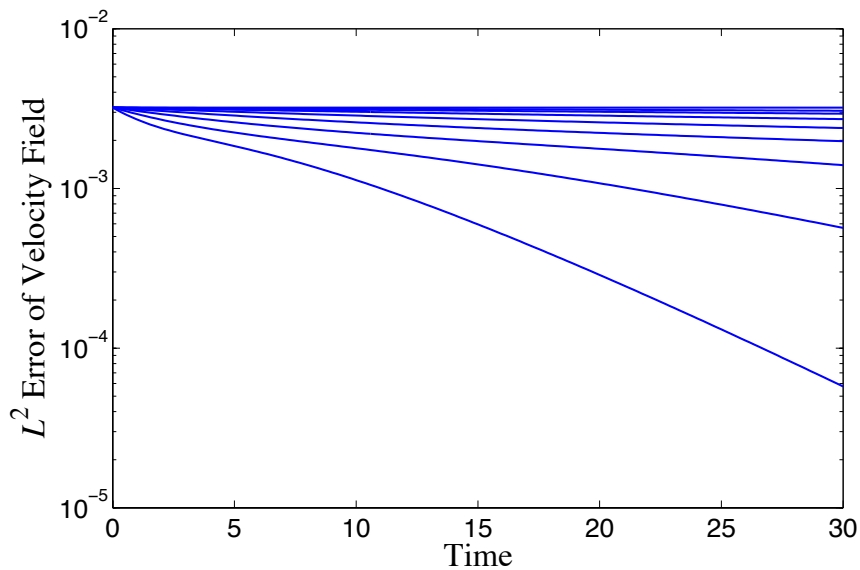


Figure 9.2: Two-dimensional Taylor-Green vortex flow:  $L^2$  error of velocity field versus time at  $Re = 10, 20, 40, 80, 160, 320, 640, 1028, \infty$  for a  $k' = 1$  discretization with  $16 \times 16$  elements. Time-step size chosen as  $\Delta t = \min \left\{ h, \frac{h^2}{4\nu} \right\}$ .

sufficiently small to ensure temporal discretization errors are of the same order as spatial discretization errors. The initial condition was chosen using  $\mathbf{L}^2$ -projection into the discrete space of divergence-free velocity fields. Convergence rates obtained at time  $t = 15$  for a flow of Reynold's number  $Re = \frac{1}{\nu} = 100$  are provided in Table 9.1. Note from the table that our theoretically derived estimate for the  $\mathbf{L}^2$ -norm of the velocity error is verified. Furthermore, note that the  $\mathbf{H}^1$ -norm of the velocity error and the  $L^2$ -norm of the pressure error optimally converge in  $h$ . To analyze the behavior of our method in time, we have plotted the  $\mathbf{L}^2$ -norm of the velocity error versus time for a chosen spatial discretization and for a wide variety of Reynold's numbers in Figure 9.2. Note from the figure that our numerical error is bounded in time. Moreover, the numerical error decays roughly at the same rate as the exact solution. Indeed, we are able to reproduce a time-indepedent solution

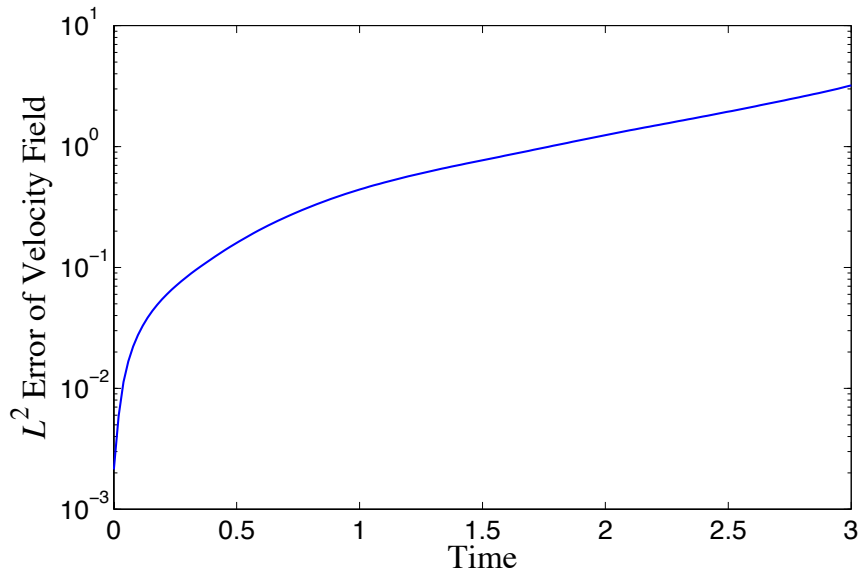


Figure 9.3: Two-dimensional Taylor-Green vortex flow: Blow-up of the  $L^2$  velocity error for the conservative  $\mathbf{Q}_2/Q_1$  Taylor-Hood discretization at  $Re = \infty$  on a mesh with  $8 \times 8$  elements. Time-step size chosen as  $\Delta t = \frac{h}{40}$ .

when  $Re = \infty$ . This indicates the nonlinear convection term has not interfered with the flow evolution of our discrete velocity solution.

To contrast our methodology with standard mixed flow discretizations, we repeated the above computations for conservative Taylor-Hood finite element approximations. Again, the Crank-Nicolson method was employed to discretize in time. We found that the results obtained using this flow technology were in general unstable. To illustrate this, we have plotted in Figure 9.3 the  $\mathbf{L}^2$ -norm of the velocity error versus time for a  $\mathbf{Q}_2/Q_1$  Taylor-Hood discretization at  $Re = \infty$  on a mesh with  $8 \times 8$  elements. Note the exponential blow-up of the error in time. This blow-up is a direct result of unphysical energy growth stemming from the nonlinear convection term. Indeed, we have been unable to stably compute the discrete flow solution beyond a time of  $t = 5$ . These results are a testament to the benefits of em-

ploying a conservative discretization which exactly preserves the divergence-free constraint.

### 9.10.2 Alternating Cylindrical Couette Flow

As a second numerical experiment, we consider the flow of a constant-property Newtonian fluid lying between a fixed inner cylinder and an oscillating outer cylinder. This flow scenario is referred to as alternating cylindrical Couette flow. The problem setup is illustrated in Figure 9.4. No external forcing is applied. The fluid is assumed to be at rest at time  $t = 0$ . Then, the outer cylinder begins to oscillate with angular velocity equal to  $U_\theta = U \sin(\omega t)$ , inducing the fluid to slip along with the outer cylinder. As time evolves, the flow field throughout the region between the two cylinders approaches a periodic (in time) steady state. The flow velocity associated with this steady state can be explicitly derived (see, for example, [187]) and is equivalent to

$$\mathbf{u} = \begin{bmatrix} u_\theta(r, t) \sin(\theta) \\ u_\theta(r, t) \cos(\theta) \end{bmatrix}$$

with

$$u_\theta(r, t) = U \text{Imag} \left( \frac{I_0(\gamma r) K_0(\gamma r_{in}) - I_0(\gamma r_{in}) K_0(\gamma r)}{I_0(\gamma r_{out}) K_0(\gamma r_{in}) - I_0(\gamma r_{in}) K_0(\gamma r_{out})} \exp \{i\omega t\} \right)$$

where  $(r, \theta)$  are polar coordinates with respect to the center of the cylinders,  $\gamma = \sqrt{i\omega\nu}$ , and  $I_0$  and  $K_0$  are modified Bessel functions of the first and second kind respectively. Unfortunately, no closed-form solution exists for the pressure field. The Reynold's number for this flow is taken to be

$$Re = \frac{2Ur_{in}}{\nu}.$$

In what follows, we assume  $r_{in} = 1$ ,  $r_{out} = 2$ , and  $U = 1$ .

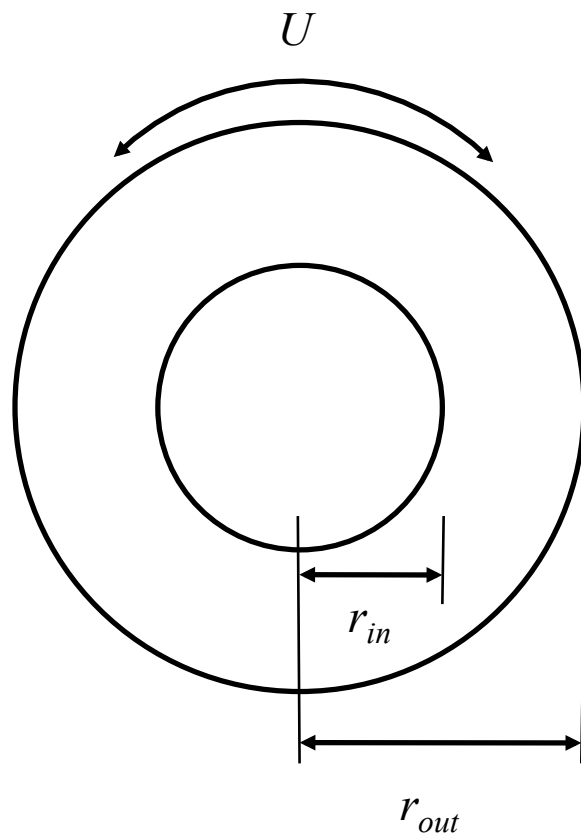


Figure 9.4: Alternating cylindrical Couette flow: Problem setup.

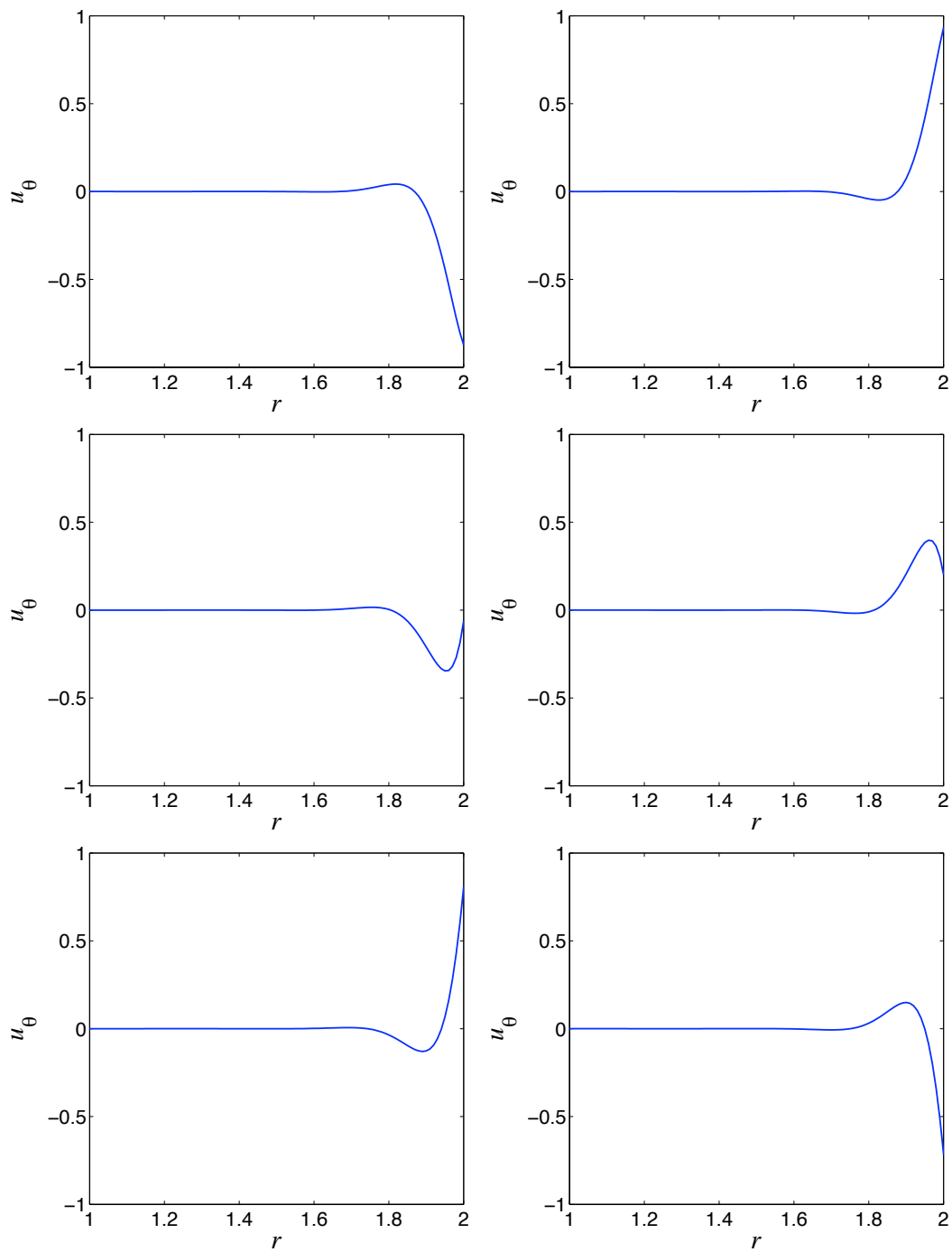


Figure 9.5: Alternating Couette flow: Plot of the angular velocity field at  $Re = 200$  for  $t = 40.0, 40.2, 40.4, 40.6, 40.8, 41.0$ .

In Figure 9.5, we have plotted at time instances  $t = 40.0, 40.2, 40.4, 40.6, 40.8, 41.0$  the angular velocity field associated with a  $Re = 200$  flow subject to an oscillation frequency of  $\omega = 5$ . At these particular time instances, the flow has already reached the steady state. Note from the figure that there is a small boundary layer attached to the outer cylinder. Further note that there is substantial flow reversal in a region away from the outer cylinder.

We believe alternating cylindrical Couette flow is an interesting and challenging numerical test problem for a number of reasons. First of all, the problem exhibits important symmetries which ideally should be preserved in a numerical simulation. As a consequence of these symmetries, the nonlinear advection term is exactly balanced by the pressure term. Second, the problem is characterized by strong shifts in angular momentum in time. Consequently, a methodology which admits angular momentum balance is preferred. Finally, the problem is characterized by the presence of boundary layers and flow reversal. Many flow technologies exhibit spurious oscillations when applied to problems harboring such features.

We have numerically simulated alternating cylindrical Couette flow using divergence-conforming B-spline discretizations of varying mesh size and polynomial degree. We utilized a polar mapping to represent the annular domain, and Nitsche's method was invoked to enforce the slip condition along the cylinder surfaces. The resulting semi-discretizations satisfy an angular momentum balance law as discussed in Section 9.7. As in the last verification test, the Crank-Nicolson method was employed to discretize in time, and the time-step size was chosen to be

$$\Delta t = h^{\frac{k'+1}{2}},$$

sufficiently small to ensure temporal discretization errors are of the same order as spatial errors. Convergence rates obtained at  $t = 40$  for a  $Re = 200$  flow subject to

Table 9.2: Alternating cylindrical Couette flow: Convergence rates at  $t = 40$  for  $Re = 200$  and  $\omega = 5$ . Time-step size chosen as  $\Delta t = h^{\frac{k'+1}{2}}$ .

Polynomial degree  $k' = 1$

$h/h_0$	1/8	1/16	1/32	1/64
$\ \mathbf{u} - \mathbf{u}_h\ _h$	3.19e0	2.07e0	1.19e0	6.01e-1
order	-	0.62	0.80	0.99
$ \mathbf{u} - \mathbf{u}_h _{\mathbf{H}^1(\Omega)}$	2.99e0	1.79e0	1.05e0	5.51e-1
order	-	0.74	0.77	0.93
$\ \mathbf{u} - \mathbf{u}_h\ _{\mathbf{L}^2(\Omega)}$	9.35e-2	2.95e-2	8.86e-3	2.40e-3
order	-	1.66	1.74	1.88
$\ u_r - (u_r)_h\ _{L^2(\Omega)}$	0	0	0	0

Polynomial degree  $k' = 2$

$h/h_0$	1/8	1/16	1/32	1/64
$\ \mathbf{u} - \mathbf{u}_h\ _h$	3.14e0	1.12e0	2.64e-1	5.94e-2
order	-	1.49	2.09	2.15
$ \mathbf{u} - \mathbf{u}_h _{\mathbf{H}^1(\Omega)}$	2.24e0	8.72e-1	2.14e-1	5.15e-2
order	-	1.36	2.03	2.06
$\ \mathbf{u} - \mathbf{u}_h\ _{\mathbf{L}^2(\Omega)}$	3.23e-2	7.00e-3	9.56e-4	1.26e-4
order	-	2.21	2.87	2.92
$\ u_r - (u_r)_h\ _{L^2(\Omega)}$	0	0	0	0

Polynomial degree  $k' = 3$

$h/h_0$	1/8	1/16	1/32
$\ \mathbf{u} - \mathbf{u}_h\ _h$	1.98e0	2.37e-1	2.65e-2
order	-	3.06	3.16
$ \mathbf{u} - \mathbf{u}_h _{\mathbf{H}^1(\Omega)}$	1.51e0	1.84e-1	2.32e-1
order	-	3.04	2.99
$\ \mathbf{u} - \mathbf{u}_h\ _{\mathbf{L}^2(\Omega)}$	2.13e-2	1.27e-3	7.94e-5
order	-	4.07	4.00
$\ u_r - (u_r)_h\ _{L^2(\Omega)}$	0	0	0

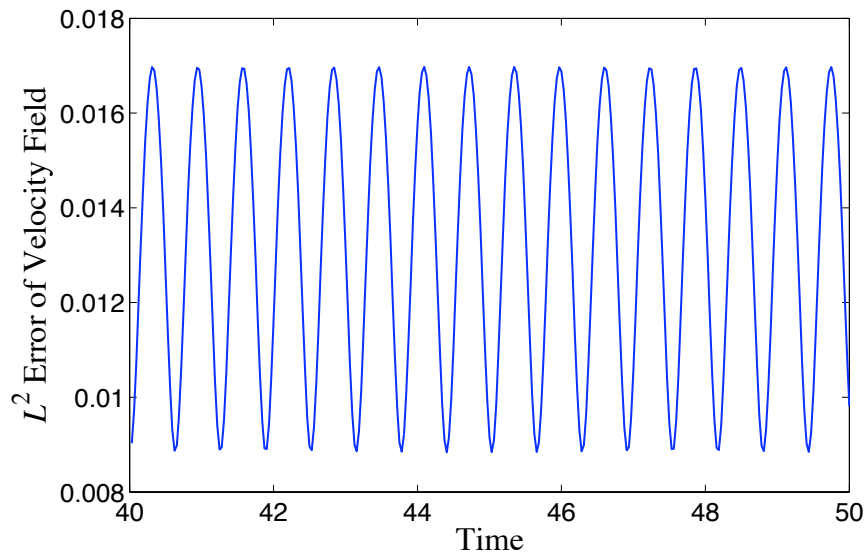


Figure 9.6: Alternating cylindrical Couette flow:  $L^2$  error of velocity field versus time at  $Re = 200$  for a  $k' = 1$  discretization with  $128 \times 32$  elements. The oscillation frequency for this simulation was chosen as  $\omega = 5$ , and the time-step size was chosen as  $\Delta t = h$ .

an oscillation frequency of  $\omega = 5$  are provided in Table 9.2. Note from the table that our theoretically derived estimate for the  $\mathbf{L}^2$ -norm of the velocity error is verified. Further, note that the  $\mathbf{H}^1$ -norm of the velocity error optimally converges in  $h$  and that we have obtained axisymmetric velocity fields with null radial component. To analyze the behavior of our method in time, we have plotted in Figure 9.6 the  $\mathbf{L}^2$ -norm of the velocity error versus time for a chosen spatial discretization. Note from the figure that our numerical error is bounded and periodic in time. This indicates that our numerical solution, like the exact solution, has reached a periodic steady-state.

## 9.11 Benchmark Problems

In this section, we investigate the effectiveness of our methodology as applied to two standard benchmark problems: two-dimensional flow over a cylinder and three-dimensional Taylor-Green vortex flow. As in the last subsection, we choose Nitsche's penalty constant as  $C_{pen} = 5(k' + 1)$  in all of the following numerical tests, and we employ uniform parametric meshes and B-spline spaces of maximal continuity.

### 9.11.1 Two-Dimensional Flow Over a Cylinder

Two-dimensional flow past a circular cylinder is a widely utilized benchmark problem. It is a problem of basic engineering interest as flow past a blunt body occurs in many engineering applications. By choosing a large enough Reynolds number based on the cylinder diameter and the inflow velocity, a flow regime is entered where the occurrence of the famous Karman vortex street may be expected. This vortex shedding phenomenon consists of an alternate separation of a vortex at both the upper and the lower side of the cylinder. This shedding occurs at a specific fixed frequency which is related to the so-called Strouhal number

$$St = \frac{fD}{U}$$

where  $f$  is the frequency of vortex shedding,  $D$  is the cylinder diameter, and  $U$  is the freestream velocity of the fluid. A common means of validating a given discretization is to compare its numerically computed Strouhal number with well-accepted solutions.

The basic problem setup for flow past a circular cylinder is illustrated in Figure 9.7. The Reynolds number for this setup is commonly taken to be

$$Re = \frac{UD}{\nu}.$$

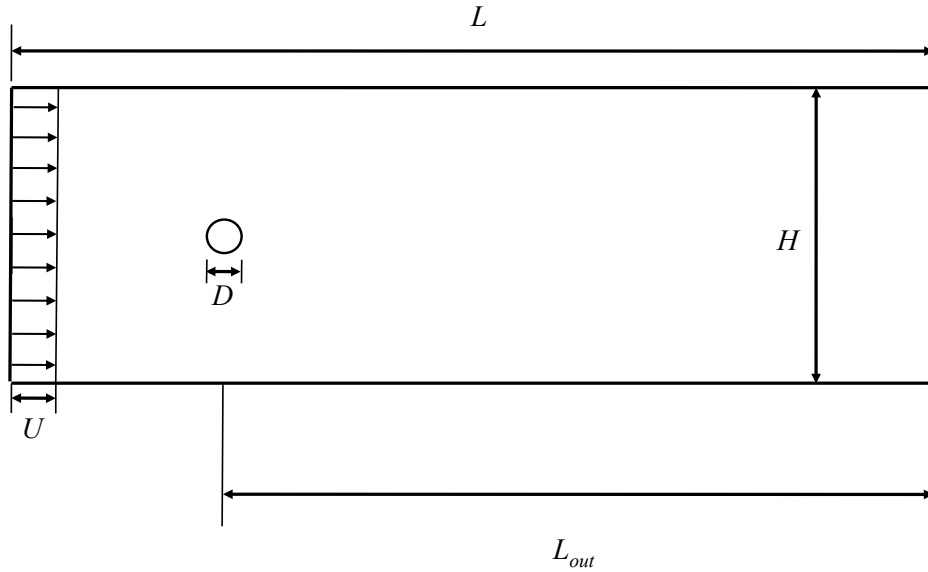


Figure 9.7: Unsteady flow over a cylinder: Problem setup.

It is well-known that the computed Strouhal number depends on both the domain height  $H$  and the downstream length  $L_{out}$  unless they are chosen to be sufficiently large [24, 179]. Here, we select  $H = 32D$  and  $L_{out} = 48D$ . At the top and bottom sides of the domain, no-penetration and zero tangential traction boundary conditions are applied. At the right side of the domain, a zero-traction or “do-nothing” boundary condition is applied.

To simulate flow past a cylinder, we have utilized divergence-conforming B-splines of polynomial degree  $k' = 1$  to discretize in space and the time-discontinuous Galerkin method [113] in conjunction with linear polynomials to discretize in time. We have utilized a NURBS multi-patch construction to represent the geometry as described in Figure 9.8. As NURBS are employed, the circle is represented exactly in the multi-patch construction. We have enforced normal continuity strongly

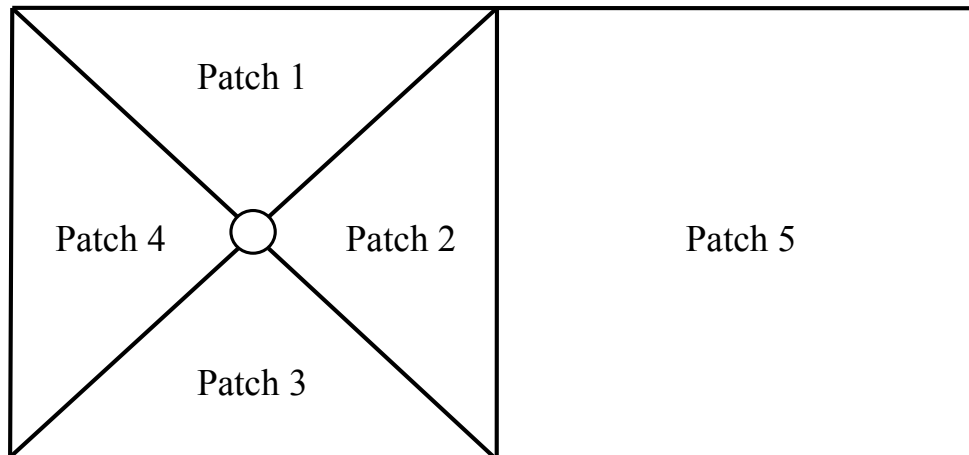


Figure 9.8: Unsteady flow over a cylinder: Multi-patch construction.

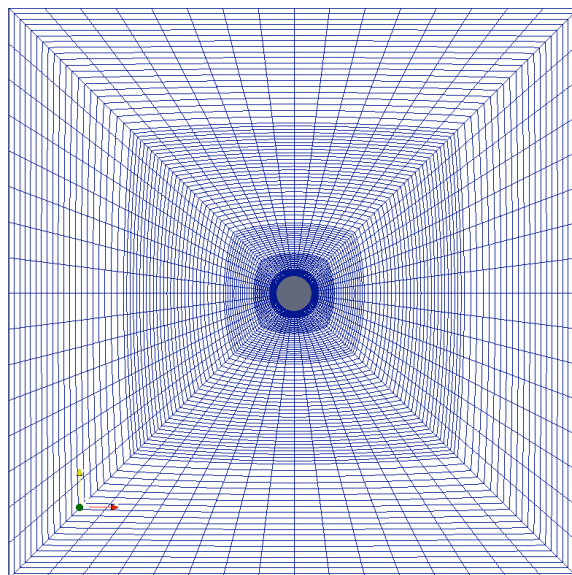


Figure 9.9: Unsteady flow over a cylinder: Mesh for Patches 1-4.

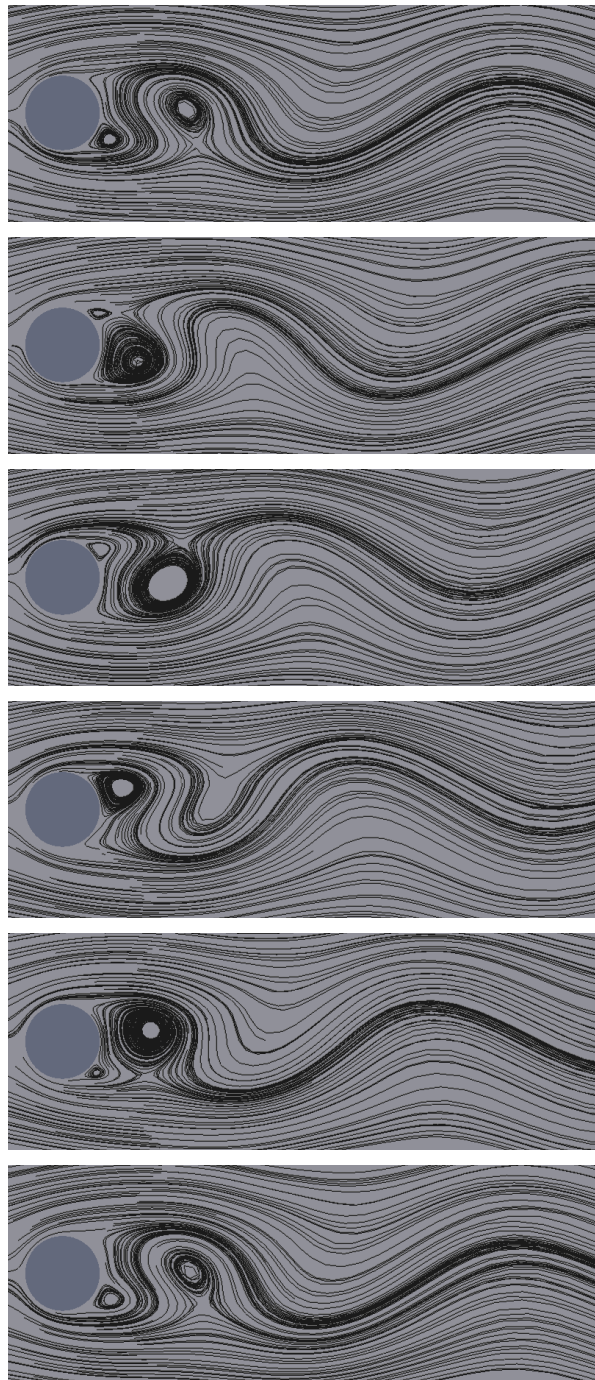


Figure 9.10: Unsteady flow over a cylinder,  $Re = 100$ . Streamlines in the near wake over a cycle.

and tangential continuity weakly between patches in our numerical simulations. We have further utilized a new stabilized method, the so-called Method of Subgrid Vortices, which may be interpreted as a generalization of the multiscale discontinuous Galerkin method to divergence-free discretizations of the Navier-Stokes equations [27, 51, 114]. The basis of the Method of Subgrid Vortices is simple - locally enrich the solution space with divergence-free subscale functions whose supports are confined to single elements, allow the subscales to “slip” along element boundaries, and weakly enforce no-slip boundary conditions element-wise on the subscale solution using the discontinuous Galerkin method. By enriching the solution space with such basis functions, we introduce a residual-based stabilization mechanism. For the sake of brevity, the Method of Subgrid Vortices is not covered in detail in this dissertation.

We have conducted a preliminary simulation of flow past a cylinder at  $Re = 100$  using the boundary-fitted mesh illustrated in Figure 9.9 for Patches 1-4. The cylinder diameter for this simulation was chosen as  $D = 2$ , and the time-step size was chosen to be  $\Delta t = 0.25$ . After a steady symmetric solution was obtained, the solution was perturbed as to kick-start the shedding phenomena. Following, the solution at 2000 time-steps was obtained, and a Strouhal number of  $St = 0.162$  was computed from the flow field during the final 1000 time-steps. This value is slightly less than the commonly accepted value of  $St = 0.164$  [155], but this is expected as the flow is under-resolved in the wake and a stabilization scheme is employed. Streamlines from the flow simulation over a single vortex shedding period are displayed in Figure 9.10. These streamlines closely resemble experimentally obtained streamlines [71].

### 9.11.2 Three-Dimensional Taylor-Green Vortex Flow

Three-dimensional Taylor-Green vortex flow is one of the simplest systems in which one can study enstrophy production and the turbulence resulting from vortex stretching. The initial conditions for this flow are

$$\mathbf{u}_0(x, y, z) = \begin{bmatrix} \sin(x) \cos(y) \cos(z) \\ -\cos(x) \sin(y) \cos(z) \\ 0 \end{bmatrix}.$$

The flow is periodic in all three spatial directions in the domain  $\Omega = (0, 2\pi)^3$  and exhibits a 64-fold symmetry which can be exploited in numerical simulation [33].

The Reynolds number for this flow is commonly taken to be

$$Re = \frac{1}{\nu}.$$

In Figure 9.11, we have reproduced time history plots of the dissipation rate

$$\epsilon = \frac{1}{|\Omega|} \int_{\Omega} 2\nu |\nabla^s \mathbf{u}|^2 d\mathbf{x}$$

that were obtained by Brachet *et al.* in [33] via Fourier-based Direct Numerical Simulation (DNS) with  $256^3$  resolved modes. Note that the flow exhibits significant enstrophy production throughout the initial stages of flow evolution regardless of Reynold's number. At  $Re = 100$ , the time corresponding to the maximum dissipation rate is approximately  $t \approx 4.75$ . As the Reynolds number is increased, the time corresponding to the maximum dissipation rate gradually increases until it settles around a value of  $t \approx 9$ .

To simulate three-dimensional Taylor-Green vortex flow, we have utilized divergence-free B-spline discretizations of varying mesh size and polynomial degrees  $k' = 1, 2, 3$ . We have exploited symmetry conditions in order to reduce the dimensionality of our discrete system by a factor of 8. A linear parametric mapping was utilized to describe the physical domain. The Crank-Nicolson method

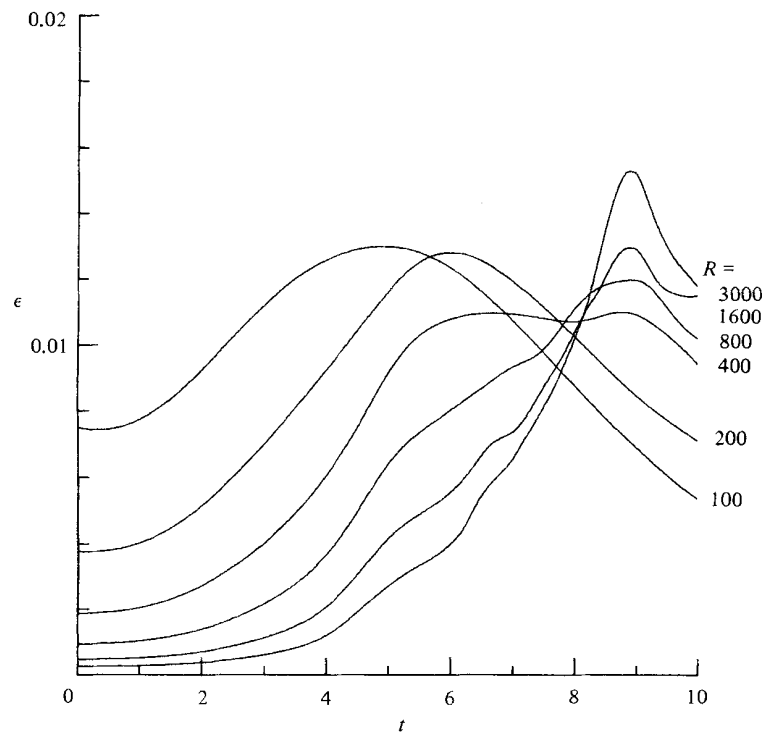
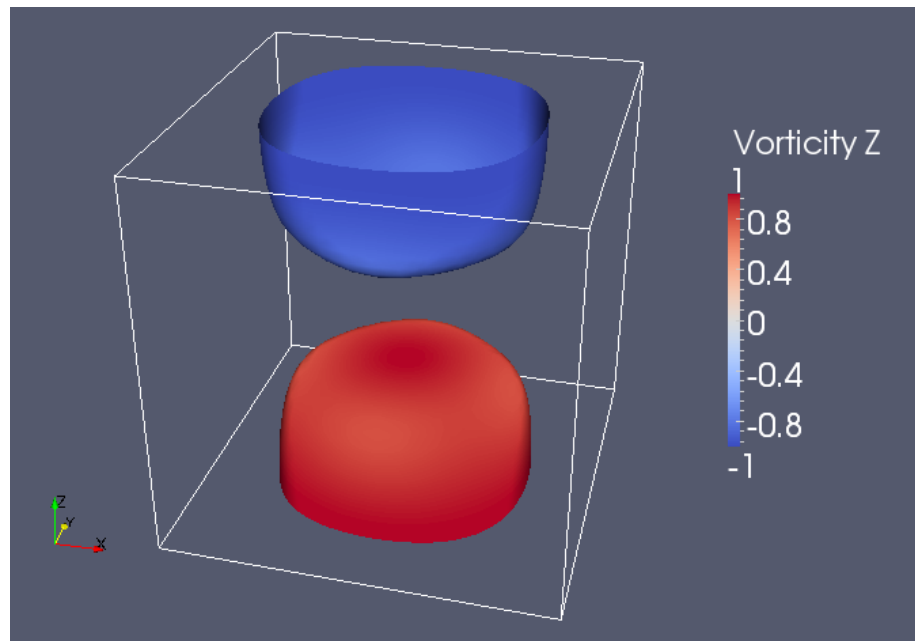


Figure 9.11: 3-D Taylor-Green vortex flow: Time history plots of the dissipation rate for various Reynold's numbers. Image reproduced from Brachet *et al.* [33] with permission from Cambridge University Press.

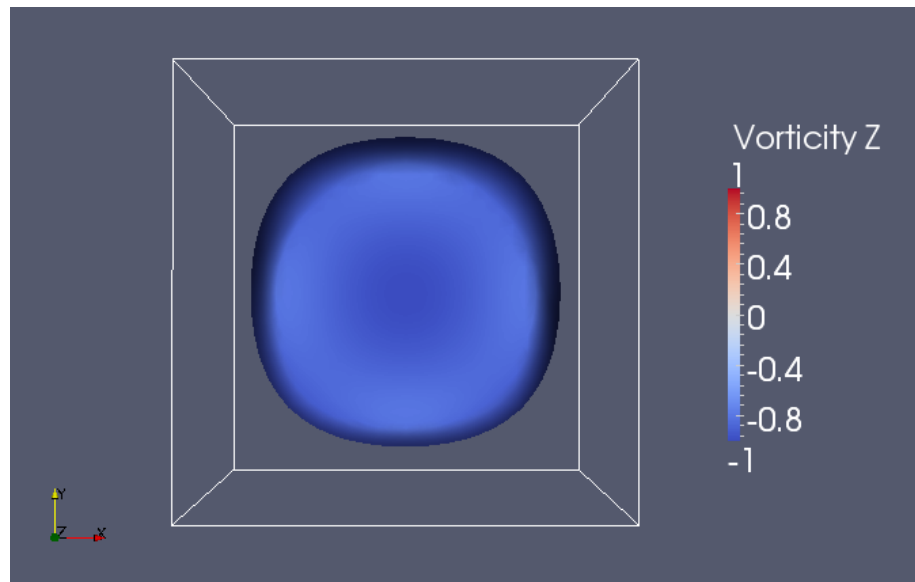
was employed to discretize viscous terms while the Adams-Bashforth multi-step method [15] was employed to discretize the nonlinear convective terms. A time-step size of  $\Delta t = 0.05h$  was employed in all of our simulations. The initial condition was selected using  $L^2$ -projection into the discrete space of divergence-free velocity fields. At each time-step, we arrive at a discrete generalized Stokes system, which we efficiently solved by exploiting the existence of a vector potential to transform our mixed problem into a positive semi-definite problem of Maxwell type (see Section 2.2). This positive semi-definite problem was then solved using the Jacobi-preconditioned conjugate gradient method [99]. We found a maximum of 25 iterations were required at each time-step to drive the relative error to a value below  $10^{-6}$  for meshes of size  $h \geq 1/64$ . This indicates our solution scheme is competitive when compared with projection methods which require a pressure Laplace solve at every time-step [45, 178]. The software packages Epetra, Teuchos and AztecOO within the Trilinos framework [98] were utilized in conjunction with a home-grown C++ code to conduct all of the simulations discussed here. We were able to successfully our simulations on a dual-core MacBook laptop with 2 GB of memory. This suggests that we may be able to efficiently solve truly large problems by extending our framework to a massively parallel setting. This is currently a primary thrust of research.

In Figure 9.12, we have depicted an enstrophy isosurface associated with the initial condition, and in Figure 9.13, we have depicted an enstrophy isosurface that was obtained at time  $t = 6$  via a third-order B-spline simulation of  $Re = 200$  flow on a spatial mesh comprised of  $32 \times 32$  elements. This time roughly corresponds to the moment of maximum dissipation rate. Note from the figures that while the initial solution is comprised of a single vortex on the restricted domain  $(0, \pi)^3$ , vortex stretching has separated the initial vortex into many vortical structures by

time  $t = 6$ . Further note the vast amount of symmetry exhibited by the vortical structures. We found that this symmetry was preserved in all of our numerical experiments. In Figure 9.14(a), we have depicted the  $Re = 200$  dissipation rate time histories associated with a sequence of refined  $k' = 1$  discretizations. The dissipation rate time history on the finest mesh is virtually indistinguishable from the corresponding DNS time history depicted in Figure 9.11. The other dissipation rate time histories quickly converge in  $h$ . It should be noted that we have been able to stably compute arbitrary Reynold's number flow on the coarse mesh ( $h = 1/16$ ), though the results were wildly inaccurate at long times due to a fine-scale pile-up of energy resulting from a lack of resolution. In Figure 9.14(b), we have depicted the  $Re = 200$  dissipation rate time histories associated with  $h = 1/32$  discretizations of varying polynomial degree. Note that the dissipation rate time histories quickly converge in  $k'$ . Furthermore, the  $k' = 3$  dissipation rate time history nearly matches the corresponding DNS time history illustrated in Figure 9.11, though the  $k' = 1, h = 1/64$  results are slightly more accurate. We are currently conducting simulations for larger Reynold's number flows and for more refined meshes.

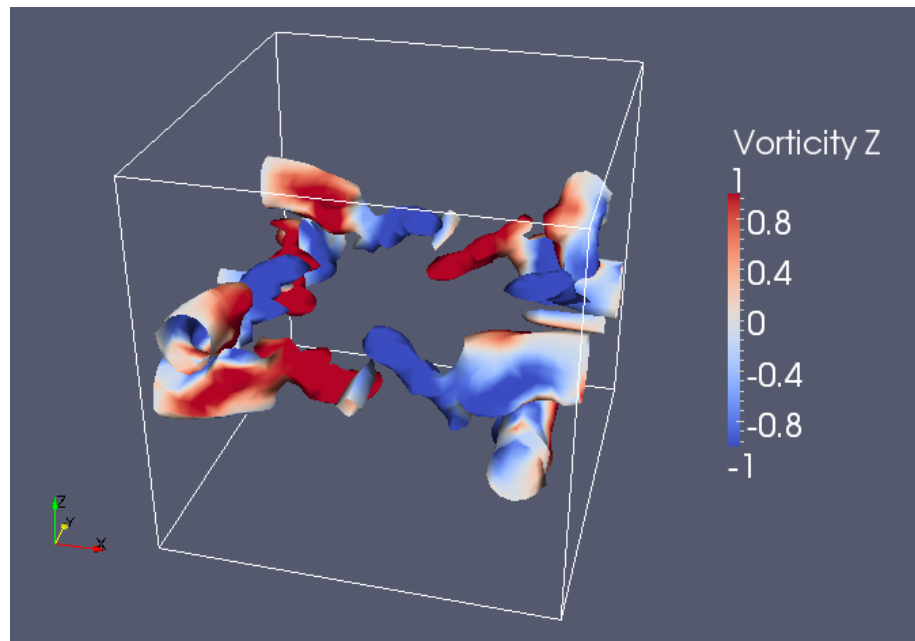


(a)

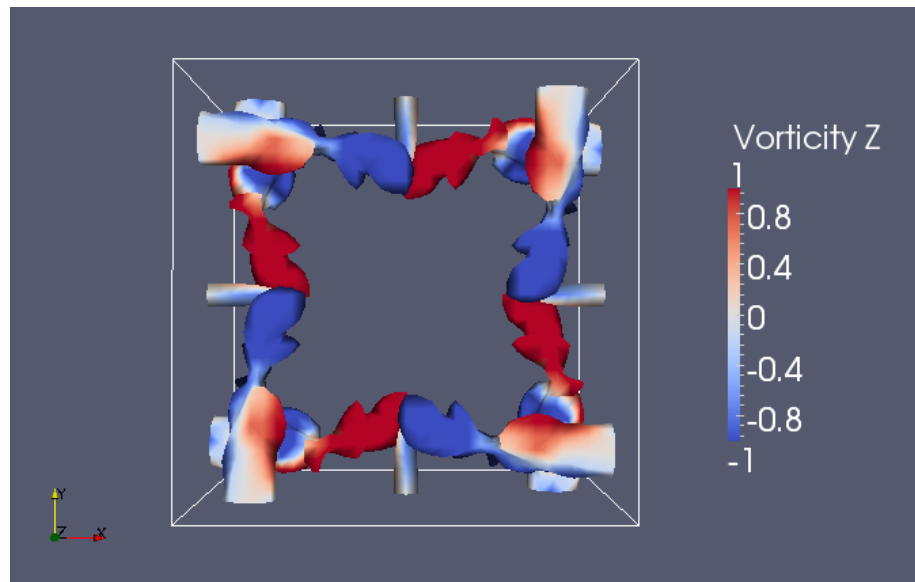


(b)

Figure 9.12: 3-D Taylor-Green vortex flow: Visualization of enstrophy isosurface colored by vertical vorticity at  $t = 0$  for  $Re = 200$ . (a) 3-D View, (b) Overhead view. Visualization is restricted to the domain  $(0, \pi)^3$ .

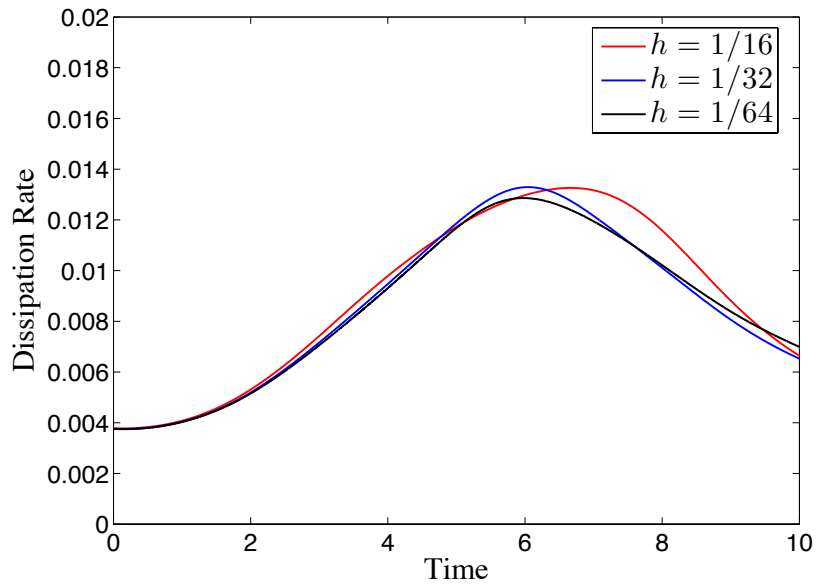


(a)

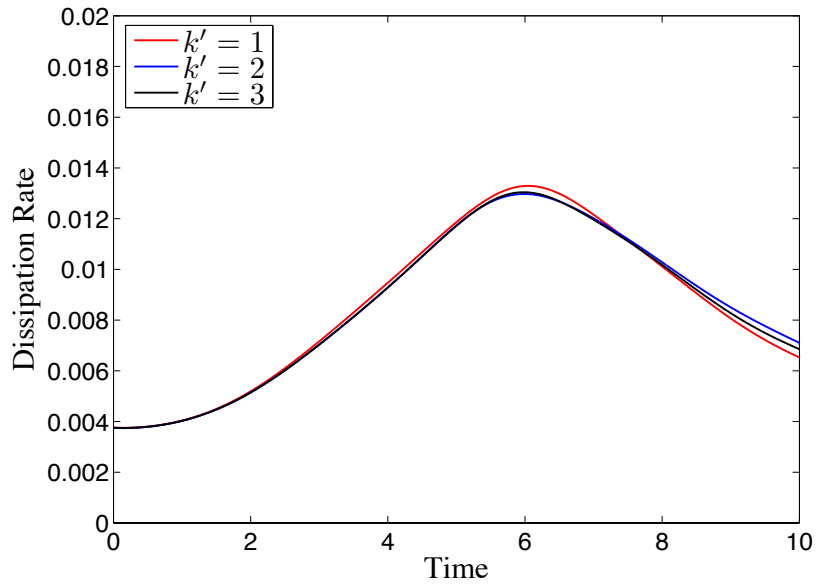


(b)

Figure 9.13: 3-D Taylor-Green vortex flow: Visualization of enstrophy isosurface colored by vertical vorticity at  $t = 6$  for  $Re = 200$ . (a) 3-D View, (b) Overhead view. Visualization is restricted to the domain  $(0, \pi)^3$ .



(a)



(b)

Figure 9.14: 3-D Taylor-Green vortex flow: Convergence of dissipation rate time histories for  $Re = 200$ . (a) Convergence of  $k' = 1$  discretizations under mesh refinement, (b) Convergence of  $h = 1/32$  discretizations under degree elevation.

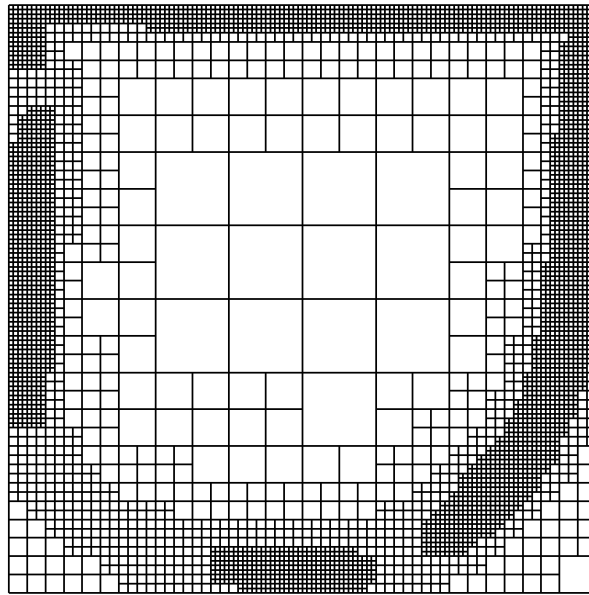
## Chapter 10

### Conclusions and Future Work

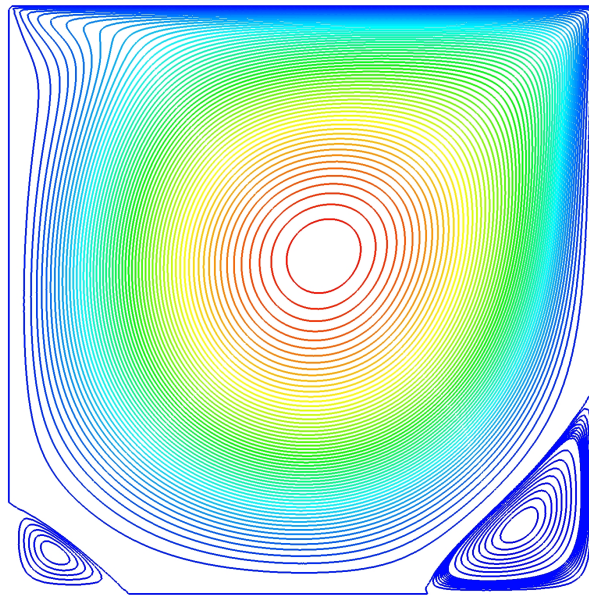
In this dissertation, new divergence-conforming B-spline discretizations have been presented for the generalized Stokes and Navier-Stokes equations. Since these discretizations return a pointwise divergence-free velocity field, they replicate the algebraic and geometric structure of incompressible flow. A collection of stability and error estimates have been derived, and these theoretical results have been confirmed and supplemented by numerical simulations of problems with known analytical solutions. The discretizations have also been applied to the simulation of a number of benchmark problems where the advantages of the new methodology over classical methods have been highlighted.

There are many promising research directions for this work. On the theoretical side, it remains to prove that higher-order B-spline discretizations of the unsteady Navier-Stokes equations converge to weak solutions which satisfy a local energy balance in space-time [90]. We have successfully proven that such a convergence property holds for the lowest-order member of our discretization family, and we are optimistic that our method of proof can be extended to higher-order discretizations. It also remains to extend our stability and error estimates to the multi-patch setting. Such a result will necessarily depend on the existence of a multi-patch commuting diagram. On the practical side, we are in the process of applying our discretization technique to the Direct Numerical Simulation (DNS) of homogeneous isotropic turbulence, turbulent channel flow, and turbulent Taylor-

Couette flow. Since our methodology has no need for either stabilization or de-aliasing, we believe it holds certain advantages over spectral and finite element methods as a DNS technology. We are also developing geometric multigrid solvers for the generalized Oseen equations. By exploiting the existence of a discrete vector potential, we are able to transform the indefinite mixed problem resulting from a discretization of the generalized Oseen equations into a positive semi-definite problem, allowing us to avoid the use of Schur complement methods such as Uzawa iteration [11]. Finally, we are investigating local refinement within the context of divergence-conforming B-splines in conjunction with Dominik Schillinger and Ernst Rank of Technische Universität München. This effort is motivated by the concept of hierarchical B-splines [78, 79, 165, 188]. We have already conducted some preliminary simulations in two spatial dimensions (see Figure 10.1), and we are currently extending our research code to the three-dimensional setting.



(a)



(b)

Figure 10.1: Hierarchical B-spline simulation of two-dimensional lid-driven cavity flow at  $Re = 800$ : (a) Refined mesh, (b) Streamlines. Image courtesy of Dominik Schillinger.

## Bibliography

- [1] I Akkerman, Y Bazilevs, V M Calo, T J R Hughes, and S Hulshoff. The role of continuity in residual-based variational multiscale modeling of turbulence. Computational Mechanics, 41:371–378, 2008.
- [2] J C Andre and M Lesieur. Influence of helicity on the evolution of isotropic turbulence at high Reynolds number. Journal of Fluid Mechanics, 81:187–207, 1977.
- [3] C Armrouche, G Bernardi, M Dauge, and V Girault. Vector potentials in three-dimensional non-smooth domains. Mathematical Methods in the Applied Sciences, 21:823–864, 1998.
- [4] D N Arnold. An interior penalty finite element method with discontinuous elements. SIAM Journal on Numerical Analysis, 19:742–760, 1982.
- [5] D N Arnold, D Boffi, and R S Falk. Quadrilateral  $H(\text{div})$  finite elements. SIAM Journal on Numerical Analysis, 42:2429–2451, 2005.
- [6] D N Arnold, R S Falk, and R Winther. Mixed finite elements for linear elasticity with weakly imposed symmetry. Mathematics of Computation, 76:1699–1723, 2007.
- [7] D N Arnold, R S Falk, and R Winther. Finite element exterior calculus: From Hodge theory to numerical stability. Bulletins of the American Mathematical Society, 47:281–354, 2010.

- [8] D N Arnold and J Qin. Quadratic velocity/linear pressure Stokes elements. In R Vichnevetsky and R S Steplemen, editors, Advances in Computer Methods for Partial Differential Equations VII, 1992.
- [9] V Arnold. Sur la géométrie différentielle des groupes de Lie de dimension infinie et ses applications à l'hydrodynamique des fluides parfaits. Annales de L'institut Fourier, 16:319–361, 1966.
- [10] V Arnold. The Hamiltonian nature of the Euler equations in the dynamics of a rigid body and of a perfect fluid. Uspekhi Matematicheskikh Nauk, 24:225–226, 1969.
- [11] K Arrow, L Hurwicz, and H Uzawa. Studies in Linear and Nonlinear Programming. Stanford University Press, 1958.
- [12] Wm T Ashurst, A R Kerstein, R M Kerr, and G H Gibson. Alignment of vorticity and scalar gradient with strain rate in simulated Navier-Stokes turbulence. Physics of Fluids, 30:2343–2353, 1987.
- [13] I Babuška. Error bounds for finite element method. Numerische Mathematik, 16:322–333, 1971.
- [14] I Babuška and H-S Oh. Pollution problem of the  $p$ - and  $h - p$  versions of the finite element method. Numerical Methods in Biomedical Engineering, 3:553–561, 1987.
- [15] F Bashforth and J C Adams. Theories of Capillary Action. London: Cambridge University Press, 1883.

- [16] Y Bazilevs and I Akkerman. Large eddy simulation of turbulent Taylor-Couette flow using isogeometric analysis and residual-based variational multiscale method. Journal of Computational Physics, 229:3402–3414, 2010.
- [17] Y Bazilevs, V M Calo, J A Cottrell, J A Evans, T J R Hughes, S Lipton, M A Scott, and T W Sederberg. Isogeometric analysis using T-splines. Computer Methods in Applied Mechanics and Engineering, 199:229–263, 2010.
- [18] Y Bazilevs, V M Calo, J A Cottrell, T J R Hughes, A Reali, and G Scovazzi. Variational multiscale residual-based turbulence modeling for large eddy simulation of incompressible flows. Computer Methods in Applied Mechanics and Engineering, 197:173–201, 2007.
- [19] Y Bazilevs, V M Calo, T J R Hughes, and Y Zhang. Isogeometric fluid-structure interaction: Theory, algorithms, and computations. Computational Mechanics, 43:3–37, 2008.
- [20] Y Bazilevs and T J R Hughes. Weak imposition of Dirichlet boundary conditions in fluid mechanics. Computers and Fluids, 36:12–26, 2007.
- [21] Y Bazilevs, C M Michler, V M Calo, and T J R Hughes. Weak Dirichlet boundary conditions for wall-bounded turbulent flows. Computer Methods in Applied Mechanics and Engineering, 196:4853–4862, 2007.
- [22] Y Bazilevs, C M Michler, V M Calo, and T J R Hughes. Isogeometric variational multiscale modeling of wall-bounded turbulent flows with weakly-enforced boundary conditions on unstretched meshes. Computer Methods in Applied Mechanics and Engineering, 199:780–790, 2010.

- [23] J T Beale, T Kato, and A Majda. Remarks on the breakdown of smooth solutions for the 3-D Euler equations. Communications in Mathematical Physics, 94:61–66, 1984.
- [24] M Behr, D Hastreiter, S Mittal, and T E Tezduyar. Incompressible flow past a circular cylinder: Dependence of the computed flow field on the location of the lateral boundaries. Computer Methods in Applied Mechanics and Engineering, 123:309–316, 1995.
- [25] C Bernardi and Y Maday. Uniform inf-sup conditions for the spectral discretization of the Stokes problem. Mathematical Models and Methods in Applied Sciences, 9:395–414, 1999.
- [26] L C Berselli and D Cordoba. On the regularity of the solutions to the 3D Navier-Stokes equations: A remark on the role of helicity. Comptes Rendus Mathematique, 347:613–618, 2009.
- [27] P Bochev, T J R Hughes, and G Scovazzi. A multiscale discontinuous Galerkin method. Lecture Notes in Computer Science, 3743:84–93, 2006.
- [28] D Boffi. A note on the deRham complex and a discrete compactness property. Applied Mathematics Letters, 14:33–38, 2001.
- [29] D Boffi, F Brezzi, and M Fortin. Finite elements for the Stokes problem. Lecture Notes in Mathematics, 1939:45–100, 2008.
- [30] M J Borden, M A Scott, J A Evans, and T J R Hughes. Isogeometric finite element data structures based on Bézier extraction of NURBS. International Journal for Numerical Methods in Engineering, 87:15–47, 2011.

- [31] O Botella. On a collocation B-spline method for the solution of the Navier-Stokes equations. Computers and Fluids, 31:397–420, 2002.
- [32] O Botella and R Peyret. Benchmark spectral results on the lid-driven cavity flow. Computers and Fluids, 27:421–433, 1998.
- [33] M E Brachet. Small-scale structure of the Taylor-Green vortex. Journal of Fluid Mechanics, 130:411–452, 1983.
- [34] S C Brenner. Korn’s inequalities for piecewise  $H^1$  vector fields. Mathematics of Computation, 73:1067–1087, 2003.
- [35] F Brezzi. On the existence, uniqueness and approximation of saddle-point problems arising from Lagrange multipliers. Revue Française d’Automatique Informatique et Recherche Operationnelle. Analyse Numérique, 8:129–151, 1974.
- [36] F Brezzi, J A Evans, T J R Hughes, and L D Marini. New rectangular plate elements based on twist-Kirchhoff theory. Computer Methods in Applied Mechanics and Engineering, 200:2547–2561, 2011.
- [37] H C Brinkman. A calculation of the viscous force exerted by a flowing fluid on a dense swarm of particles. Applied Scientific Research, A1:27–34, 1947.
- [38] A.N. Brooks and T.J.R. Hughes. Streamline upwind/Petrov-Galerkin formulations for convection dominated flows with particular emphasis on the incompressible Navier-Stokes equations. Computer Methods in Applied Mechanics and Engineering, 32:199–259, 1982.

- [39] A Buffa, C de Falco, and R Vázquez. Isogeometric analysis: Stable elements for the 2D Stokes equation. International Journal for Numerical Methods in Fluids, 65:1407–1422,20–30, 2011.
- [40] A Buffa, J Rivas, G Sangalli, and R Vázquez. Isogeometric discrete differential forms in three dimensions. SIAM Journal on Numerical Analysis, 49:818–844, 2011.
- [41] A Buffa, G Sangalli, and R Vázquez. Isogeometric analysis in electromagnetics: B-splines approximation. Computer Methods in Applied Mechanics and Engineering, 199:1143–1152, 2010.
- [42] L Caffarelli, R Kohn, and L Nirenberg. Partial regularity of suitable weak solutions of the Navier-Stokes equations. Communications in Pure and Applied Mathematics, 35:771–831, 1982.
- [43] S Čanić and A Mikelić. Effective equations modeling the flow of a viscous incompressible fluid through a long elastic tube arising in the study of blood flow through small arteries. SIAM Journal on Applied Dynamical Systems, 2:431–463, 2005.
- [44] S Caorsi, P Fenrandes, and M Raffetto. On the convergence of Galerkin finite element approximations of electromagnetic eigenproblems. SIAM Journal on Numerical Analysis, 38:580–607, 2000.
- [45] A Chorin. Numerical solution of the Navier-Stokes equations. Mathematics of Computation, 23:341–354, 1968.
- [46] B Cockburn and J Gopalakrishnan. Incompressible finite elements via hybridization. Part I: The Stokes system in two space dimensions. SIAM Journal on Numerical Analysis, 43:1627–1650, 2005.

- [47] B Cockburn and J Gopalakrishnan. Incompressible finite elements via hybridization. Part II: The Stokes system in three space dimensions. SIAM Journal on Numerical Analysis, 43:1651–1672, 2005.
- [48] B Cockburn, G Kanschat, and D Schötzau. A locally conservative LDG method for the incompressible Navier-Stokes equations. Mathematics of Computation, 74:1067–1095, 2004.
- [49] B Cockburn, G Kanschat, and D Schötzau. A note on discontinuous Galerkin divergence-free solutions of the Navier-Stokes equations. SIAM Journal on Scientific Computing, 31:61–73, 2007.
- [50] P Constantin, C Fefferman, and A Majda. Geometric constraints on potentially singular solutions for the 3-D Euler equations. Communications in Partial Differential Equations, 21:559–571, 1996.
- [51] J A Cottrell. Isogeometric Analysis and Numerical Modeling of the Fine Scales within the Variational Multiscale Method. PhD thesis, The University of Texas at Austin, 2007.
- [52] J A Cottrell, T J R Hughes, and Y Bazilevs. Isogeometric Analysis: Toward Integration of CAD and FEA. Wiley, 2009.
- [53] J A Cottrell, T J R Hughes, and A Reali. Studies of refinement and continuity in isogeometric analysis. Computer Methods in Applied Mechanics and Engineering, 196:4160–4183, 2007.
- [54] J A Cottrell, A Reali, Y Bazilevs, and T J R Hughes. Isogeometric analysis of structural vibrations. Computer Methods in Applied Mechanics and Engineering, 195:5257–5296, 2006.

- [55] J Crank and P Nicolson. A practical method for numerical evaluation of solutions of partial differential equations of the heat conduction type. Mathematical Proceedings of the Cambridge Philosophical Society, 43:50–67, 1947.
- [56] L Beirão da Veiga, A Buffa, J Rivas, and G Sangalli. Some estimates for  $h - p - k$  refinement in isogeometric analysis. Numerische Mathematik, 118:271–305, 2011.
- [57] D B Das. Hydrodynamic modelling for groundwater flow through permeable reactive barriers. Hydrodynamics Processes, 16:3393–3418, 2002.
- [58] C R de Boor. On calculating with B-splines. Journal of Approximation Theory, 6:45–99, 50–62, 1972.
- [59] C R de Boor. A Practical Guide to Splines. Springer-Verlag, 1978.
- [60] R de Vogelaere. Methods of integration which preserve the contact transformation property of Hamiltonian equations. Technical report, Department of Mathematics, University of Notre Dame, 1956.
- [61] L Demkowicz and A Buffa.  $H^1$ ,  $H(\text{curl})$  and  $H(\text{div})$ -conforming projection-based interpolation in three-dimensions: Quasi-optimal  $p$ -interpolation estimates. Computer Methods in Applied Mechanics and Engineering, 199:264–275, 2010.
- [62] J Deng, T Y Hou, and X Yu. Geometric properties and the non-blow-up of the three-dimensional Euler equation. Communications in Partial Differential Equations, 30:225–243, 2005.

- [63] J Deng, T Y Hou, and X Yu. Improved geometric conditions for non-blowup of the 3D incompressible Euler equation. Communications in Partial Differential Equations, 31:293–306, 2006.
- [64] C R Doering. The 3D Navier-Stokes Problem. Annual Review of Fluid Mechanics, 41:109–128, 2009.
- [65] C R Doering and C Foias. Exponential decay rate of the power spectrum for solutions of the Navier-Stokes equations. Physics of Fluids, 7:1385–1390, 1995.
- [66] C R Doering and C Foias. Energy dissipation in body-forced turbulence. Journal of Fluid Mechanics, 467:289–306, 2002.
- [67] C R Doering and J Gibbon. Applied Analysis of the Navier-Stokes Equations. Cambridge University Press, 1995.
- [68] M R Dorfel, B Juttler, and B Simeon. Adaptive isogeometric analysis by local  $h$ -refinement using T-splines. Computer Methods in Applied Mechanics and Engineering, 199:264–275, 2010.
- [69] J Douglas and T Dupont. Interior Penalty Procedures for Elliptic and Parabolic Galerkin Methods. Lecture Notes in Physics, 58, 1976.
- [70] J Douglas and J Roberts. Global estimates for mixed methods for second order elliptic equations. Mathematics of Computation, 44:39–52, 1985.
- [71] M Van Dyke. An Album of Fluid Motion. Parabolic Press, 1982.
- [72] D G Ebin and J E Marsden. Group of diffeomorphisms and the motion of an incompressible fluid. Annals of Mathematics, 92:102–163, 1970.

- [73] J A Evans, Y Bazilevs, I Babuška, and T J R Hughes.  $n$ -widths, sup-infs, and optimality ratios for the  $k$ -version of the isogeometric finite element method. Computer Methods in Applied Mechanics and Engineering, 198:1726–1741, 2009.
- [74] J A Evans and T J R Hughes. Variational multiscale analysis: A new link between flux correction, total variation, and constrained optimization. Technical report, ICES Report 10-35, 2010.
- [75] J A Evans and T J R Hughes. Explicit trace inequalities for isogeometric analysis and parametric finite elements. Technical report, ICES Report 11-17, 2011.
- [76] J A Evans, T J R Hughes, and G Sangalli. Enforcement of constraints and maximum principles in the variational multiscale method. Computer Methods in Applied Mechanics and Engineering, 199:61–76, 2009.
- [77] L D Evans. Partial Differential Equations. AMS, 2010.
- [78] D Forsey and R H Bartels. Hierarchical B-spline refinement. Computer Graphics, 22:205–212, 1988.
- [79] D Forsey and R H Bartels. Surface fitting with hierarchical B-splines. ACM Transactions on Graphics, 14:134–161, 1995.
- [80] M Fortin. An analysis of the convergence of mixed finite element methods. Revue Française d’Automatique Informatique et Recherche Operationnelle. Analyse Numérique, 11:341–354, 1977.

- [81] L P Franca and T J R Hughes. Two classes of mixed finite element methods. Computer Methods in Applied Mechanics and Engineering, 69:89–129, 1988.
- [82] U Frisch. Turbulence: The Legacy of A. N. Kolmogorov. Cambridge University Press, 1995.
- [83] D L Fry. Atherogenesis: Initiating factors. CIBA Foundation Symposium, 12:93–125, 1973.
- [84] J Gerbeau, C L Bris, and M Bercovier. Spurious velocities in the steady flow of an incompressible fluid subjected to external forces. International Journal for Numerical Methods in Fluids, 25:679–695, 1997.
- [85] U Ghia, K N Ghia, and C T Shin. High- $Re$  solutions for incompressible flow using the Navier-Stokes equations and a multigrid method. Journal of Computational Physics, 48:387–411, 1982.
- [86] V Girault and P A Raviart. Finite Element Methods for Navier-Stokes Equations. Theory and Algorithms. Springer-Verlag, 1986.
- [87] J Gopalakrishnan and L F Demkowicz. Quasioptimality of some spectral mixed methods. Journal of Computational and Applied Mathematics, 167:163–182, 2004.
- [88] S Goto and J C Vassilicos. The dissipation rate coefficient of turbulence is not universal and depends on the internal stagnation point structure. Physics of Fluids, 21:035104–035104–8, 2009.
- [89] P Griffiths and J Harris. Principles of Algebraic Geometry. Wiley Classics Library, 1994.

- [90] J-L Guermond. Faedo-Galerkin weak solutions of the Navier-Stokes equations with Dirichlet boundary conditions are suitable. Journal de Mathematiques Pures et Appliquees, 88:87–106, 2007.
- [91] J-L Guermond. On the use of the notion of suitable weak solutions in CFD. International Journal for Numerical Methods in Fluids, 57:1153–1170, 2008.
- [92] W Gui and I Babuška. The  $h$ ,  $p$  and  $hp$  versions of the finite element method in one dimension. Part 1: The error analysis of the  $p$ -version. Part 2: The error analysis of the  $h$ - and  $hp$ -versions. Part 3: The adaptive  $hp$  version. Numerische Mathematik, 49:577–683, 1986.
- [93] H Gümral. Lagrangian description, symplectic structure, and invariants of 3D fluid flow. Physics Letters A, 232:416–424, 1997.
- [94] G Guo and I Babuška. The  $hp$  version of the finite element method. Part 1: The basic approximation results. Part 2: General results and applications. Computational Mechanics, 1:21–41,203–220, 1986.
- [95] M M Gupta. A comparison of numerical solutions of convective and divergence forms of the Navier-Stokes equations for the driven cavity problem. Journal of Computational Physics, 43:260–267, 1981.
- [96] A Hannukainen, M Juntunen, and R Stenberg. Computations with finite element methods for the Brinkman problem. Computational Geosciences, 15:155–166, 2010.
- [97] F H Harlow and J E Welch. Numerical calculation of time-dependent viscous incompressible flow of fluid with free surface. Physics of Fluids, 8:2182, 1965.

- [98] M Heroux, R Bartlett, V Howle, R Hoekstra, J Hu, T Kolda, R Lehoucq, K Long, R Pawlowski, E Phipps, A Salinger, H Thornquist, R Tuminaro, J Willenbring, and A Williams. An Overview of Trilinos. Technical Report SAND2003-2927, Sandia National Laboratories, 2003.
- [99] M R Hestenes and E Stiefel. Methods of conjugate gradients for solving linear systems. Journal of Research of the National Bureau of Standards, 49:409–436, 1952.
- [100] J G Heywood and R Rannacher. Finite element approximation of the non-stationary Navier-Stokes problem. I. Regularity of solutions and second-order error estimates for spatial discretization. SIAM Journal on Numerical Analysis, 19:275–311, 1982.
- [101] J G Heywood and R Rannacher. Finite element approximation of the nonstationary Navier-Stokes problem. II. Stability of solutions and error estimates uniform in time. SIAM Journal on Numerical Analysis, 23:750–777, 1986.
- [102] J G Heywood and R Rannacher. Finite element approximation of the non-stationary Navier-Stokes problem. III. Smoothing property and higher order error estimates for spatial discretization. SIAM Journal on Numerical Analysis, 25:489–512, 1988.
- [103] R Hiptmair. Multigrid method for  $H(\text{div})$  in three dimensions. Electronic Transactions on Numerical Analysis, 6:133–152, 1997.
- [104] R Hiptmair. Multigrid method for Maxwell’s equations. SIAM Journal on Numerical Analysis, 36:204–225, 1999.
- [105] C-M Ho and Y-C Tai. Micro-electro-mechanical systems (MEMS) and fluid flows. Annual Review of Fluid Mechanics, 30:579–612, 1998.

- [106] P Hood and C Taylor. Navier-Stokes equations using mixed interpolation. In J T Oden, R H Gallagher, O C Zienkiewicz, and C Taylor, editors, Finite Element Methods in Flow Problems, pages 121–132. University of Alabama in Huntsville Press, 1974.
- [107] E Hopf. Über die Anfangswertaufgabe für die hydrodynamischen Grundgleichungen. Mathematische Nachrichten, 4:213–231, 1950/51.
- [108] C O Horgan. Korn’s inequalities and their applications in continuum mechanics. SIAM Review, 37:491–511, 1995.
- [109] T J R Hughes, J A Cottrell, and Y Bazilevs. Isogeometric analysis: CAD, finite elements, NURBS, exact geometry, and mesh refinement. Computer Methods in Applied Mechanics and Engineering, 194:4135–4195, 2005.
- [110] T J R Hughes, G Engel, L Mazzei, and M G Larson. The continuous Galerkin method is locally conservative. Journal of Computational Physics, 163:467–488, 2000.
- [111] T J R Hughes, L P Franca, and M Balestra. A new finite element formulation for computational fluid dynamics: V. Circumventing the Babuška-Brezzi condition: A stable Petrov-Galerkin formulation of the Stokes problem accommodating equal-order interpolations. Computer Methods in Applied Mechanics and Engineering, 59:85–99, 1986.
- [112] T J R Hughes, L P Franca, and M Mallet. A new finite element formulation for computational fluid dynamics: I. Symmetric forms of the compressible Euler and Navier-Stokes equations and the second law of thermodynamics. Computer Methods in Applied Mechanics and Engineering, 54:223–234, 1986.

- [113] T J R Hughes, L P Franca, and M Mallet. A new finite element formulation for computational fluid dynamics: VI. Convergence analysis of the generalized SUPG formulation for linear time-dependent multi-dimensional advective-diffusive systems. Computer Methods in Applied Mechanics and Engineering, 63:97–112, 1987.
- [114] T J R Hughes, G Scovazzi, P B Bochev, and A Buffa. A multiscale discontinuous Galerkin method with the computational structure of a continuous Galerkin method. Computer Methods in Applied Mechanics and Engineering, 195:2761–2785, 2006.
- [115] T Ishihara, T Gotoh, and Y Kaneda. Study of high-Reynolds number isotropic turbulence by direct numerical simulation. Annual Reviews of Fluid Mechanics, 41:165–180, 2009.
- [116] C Johnson, S Larsson, V Thomée, and L B Wahlbin. Error estimates for spatially discrete approximations of semilinear parabolic equations with nonsmooth initial data. Mathematics of Computation, 49:331–357, 1987.
- [117] G Kanschat. Divergence-free discontinuous Galerkin schemes for the Stokes equations and the MAC scheme. International Journal for Numerical Methods in Fluids, 56:941–950, 2008.
- [118] T Kara and J Goldak. Three-dimensional numerical analysis of heat and mass transfer in heat pipes. Heat Mass Transfer, 43:775–785, 2007.
- [119] T Kato. Non-stationary flows of viscous and ideal fluids in  $\mathbb{R}^3$ . Journal of Functional Analysis, 21:296–309, 1972.
- [120] L Kelvin. On vortex motion. Transactions of the Royal Society of Edinburgh, 25:217–260, 1869.

- [121] R M Kerr. Evidence for a singularity of the three-dimensional incompressible Euler equations. Physics of Fluids A, 5:1725–1746, 1993.
- [122] A-R A Khaled and K Vafai. The role of porous media in modeling flow and heat transfer in biological tissues. International Journal of Heat and Mass Transfer, 46:4989–5003, 2003.
- [123] B J Kirby. Micro- and Nanoscale Fluid Mechanics: Transport in Microfluidic Devices. Cambridge University Press, 2010.
- [124] A A Kiselev and O A Ladyzhenskaya. On the existence and uniqueness of solutions of the non-stationary problems for flows of non-compressible fluids. Izvestiya Rossiiskoi Akademii Nauk. Seriya Matematicheskaya, 9:655–680, 1957.
- [125] J Könnö and R Stenberg. Non-conforming finite element method for the Brinkman problem. In G Kreiss, P Lötstedt, A Malqvist, and M Neytcheva, editors, Numerical Mathematics and Advanced Applications, 2010.
- [126] H Konzono and Y Taniuchi. Limiting case of the Sobolev inequality in BMO with application to the Euler equations. Communications in Mathematical Physics, 214:191–200, 2000.
- [127] L I G Kovasznay. Laminar flow behind a two-dimensional grid. Mathematical Proceedings of the Cambridge Philosophical Society, 44:58–62, 1948.
- [128] R H Kraichan. Helical turbulence and absolute equilibrium. Journal of Fluid Mechanics, 59:745–752, 1973.

- [129] A G Kravchenko, P Moin, and R Moser. Zonal embedded grids for numerical simulation of wall-bounded turbulent flows. Journal of Computational Physics, 127:412–423, 1996.
- [130] A G Kravchenko, P Moin, and R Moser. B-spline method and zonal grids for simulation of complex turbulent flows. Journal of Computational Physics, 151:757–789, 1999.
- [131] W Y Kwok, R D Moser, and J Jiménez. A critical evaluation of the resolution properties of B-spline and compact finite difference methods. Journal of Computational Physics, 174:510–551, 2001.
- [132] P D Lax and A N Milgram. Parabolic equations. In Contributions to the Theory of Partial Differential Equations (AM-33), pages 167–190. Princeton University Press, 1974.
- [133] P G Lemairé-Rieusset. Analyses multi-résolutions non orthogonales, commutation entre projecteurs et dérivation et ondelettes vecteurs à divergence nulle. Revista Matemática Iberoamericana, 8:221–237, 1992.
- [134] J Leray. Sur le mouvement d’un liquide visqueux emplissant l’espace. Acta Mathematica, 63:193–248, 1934.
- [135] A Linke. Collision in a cross-shaped domain - A steady 2d Navier-Stokes example demonstrating the importance of mass conservation in CFD. Computer Methods in Applied Mechanics and Engineering, 198:3278–3286, 2009.
- [136] P L Lions. Mathematical Topics in Fluid Mechanics, Vol. 1, Incompressible Models. Oxford Lecture Series in Mathematics and its Applications, 1996.

- [137] S Lipton, J A Evans, Y Bazilevs, T Elguedj, and T J R Hughes. Robustness of isogeometric structural discretizations under severe mesh distortion. Computer Methods in Applied Mechanics and Engineering, 199:357–373, 2010.
- [138] P Loulou, R D Moser, N N Mansour, and B J Cantwell. Direct numerical simulation of incompressible pipe flow using a B-spline spectral method. Technical report, NASA-Ames Research Center, 1997.
- [139] M Luskin and R Rannacher. On the smoothing property of the Galerkin method for parabolic problems. SIAM Journal on Numerical Analysis, 19:93–113, 1981.
- [140] K A Mardal, X-C Tai, and R Winther. A robust finite element method for Darcy-Stokes flow. SIAM Journal on Numerical Analysis, 40:1605–1631, 2002.
- [141] J E Marsden and A Weinstein. Coadjoint orbits, vortices and Clebsch variables for incompressible fluids. Physica D, 7:305–323, 1983.
- [142] A Masud and T J R Hughes. A stabilized mixed finite element method for Darcy flow. Computer Methods in Applied Mechanics and Engineering, 191:4341–4370, 2002.
- [143] G Matthies and L Tobiska. Mass conservation of finite element methods for coupled flow-transport problems. International Journal for Computing Science and Mathematics, 1:293–307, 2007.
- [144] C Meneveau and K R Sreenivasan. The multifractal nature of turbulent energy dissipation. Journal of Fluid Mechanics, 224:429–484, 1991.

- [145] H K Moffatt. Viscous and resistive eddies near a sharp corner. Journal of Fluid Mechanics, 64:1–18, 1964.
- [146] H K Moffatt. The degree of knottedness of tangled vortex lines. Journal of Fluid Mechanics, 36:117–129, 1969.
- [147] H K Moffatt. Simple topological aspects of turbulent vorticity dynamics. In T Tatsumi, editor, Turbulence and Chaotic Phenomena in Fluids. Elsevier, 1984.
- [148] H K Moffatt. Fixed points of turbulent dynamical systems and suppression of nonlinearity. In J L Lumley, editor, Whither Turbulence?, pages 250–257. Springer-Verlag, 1990.
- [149] H K Moffatt. Spiral structures in turbulent flow. In Proceedings of the IMA Conference “Wavelets, Fractals and Fourier Transforms”, Cambridge, 1991.
- [150] H K Moffatt, S Kida, and K Ohkitani. Stretched vortices - The sinews of turbulence; Large-Reynolds-number asymptotics. Journal of Fluid Mechanics, 259:241–264, 1994.
- [151] H K Moffatt and A Tsoniber. Helicity in laminar and turbulent flow. Annual Reviews of Fluid Mechanics, 24:281–312, 1992.
- [152] J-J Moreau. Constants d’un ilot tourbillonnaire en fluide parfait barotrope. Rendus de l’Academie des Sciences (Paris), 252:2810–2812, 1961.
- [153] J C Nédélec. Mixed finite elements in  $\mathbb{R}^3$ . Numerische Mathematik, 35:315–341, 1980.

- [154] J A Nitsche. Über ein Variationsprinzip zur Lösung von Dirichlet-Problemen bei Verwendung von Teilräumen, die keinen Randbedingungen unterworfen sind. Abhandlungen aus dem Mathematischen Seminar der Universität Hamburg, 36:9–15, 1971.
- [155] C Norberg. An experimental investigation of the flow around a circular cylinder: Influence of aspect ratio. Journal of Fluid Mechanics, 258:287–316, 1994.
- [156] K Ohkitani and P Constantin. Numerical study on the Eulerian-Lagrangian analysis of Navier-Stokes turbulence. Physics of Fluids, 20:75–102, 2008.
- [157] M Olshanskii and L G Rebholz. Note on helicity balance of the Galerkin method for the 3D Navier-Stokes equations. Computer Methods in Applied Mechanics and Engineering, 199:1032–1035, 2010.
- [158] S B Pope. Turbulent Flows. Cambridge University Press, 2003.
- [159] P A Raviart and J M Thomas. A mixed finite element method for second order elliptic problems. Lecture Notes in Mathematics, 606:292–315, 1977.
- [160] R L Ricca and H K Moffatt. The helicity of a knotted vortex filament. In H K Moffatt, editor, Topological Aspects of the Dynamics of Fluids and Plasmas. Kluwer Academic Publishers, 1987.
- [161] B Rivière and M F Wheeler. A discontinuous Galerkin method applied to nonlinear parabolic equations. Lecture Notes in Computational Science and Engineering, 11:231–244, 2000.

- [162] H-G Roos, M Stynes, and L Tobiska. Numerical Methods for Singularly Perturbed Differential Equations. Convection-Diffusion and Flow Problems. Springer, 1996.
- [163] H A F A Santos, J A Evans, and T J R Hughes. Generalization of the twist-Kirchhoff theory of plate elements to arbitrary quadrilaterals and assessment of convergence. Computer Methods in Applied Mechanics and Engineering, 2011. doi:10.1016/j.cma.2011.08.018.
- [164] V Scheffer. Hausdorff measure and the Navier-Stokes equations. Communications in Mathematical Physics, 55:97–112, 1977.
- [165] D Schillinger and E Rank. An unfitted *hp*-adaptive finite element method based on hierarchical b-splines for interface problems of complex geometry. Computer Methods in Applied Mechanics and Engineering, 200:3358–3380, 2011.
- [166] I J Schoenberg. Contributions to the problem of approximation of equidistant data by analytic functions. Quarterly of Applied Mathematics, 4:45–99, 112–141, 1946.
- [167] R Schreiber and H B Keller. Driven cavity flows by efficient numerical techniques. Journal of Computational Physics, 49:310–333, 1983.
- [168] W W Schultz, N T Lee, and J P Boyd. Chebyshev pseudospectral method of viscous flows with corner singularities. Journal of Scientific Computing, 4:1–24, 1989.
- [169] L L Schumaker. Spline functions: Basic theory. Cambridge Mathematical Library, Cambridge University Press, 2007.

- [170] L R Scott and M Vogelius. Norm estimates for a maximal right inverse of the divergence operator in spaces of piecewise polynomials. Mathematical Modelling and Numerical Analysis, 19:111–143, 1985.
- [171] K Shariff and R D Moser. Two dimensional mesh embedding for B-spline methods. Journal of Computational Physics, 145:471–488, 1998.
- [172] D B Spalding. A single formula for the law of the wall. Journal of Applied Mechanics, 28:444–458, 1961.
- [173] G Stadler, M Gurnis, C Burstedde, L C Wilcox, L Alisic, and O Ghattas. The dynamics of plate tectonics and mantle flow: From local to global scales. Science, 329:1033–1038, 2010.
- [174] R Stenberg. Analysis of mixed finite element methods for the Stokes problem: A unified approach. Mathematics of Computation, 42:9–23, 1984.
- [175] R Stevenson. Divergence-free wavelet bases on the hypercube: Free-slip boundary conditions, and applications for solving the instationary Stokes equations. Mathematics of Computation, 80:1499–1523, 2011.
- [176] H S G Swann. Convergence with vanishing viscosity of nonstationary Navier-Stokes flow to ideal flow in  $\mathbb{R}^3$ . Transactions of the American Mathematical Society, 157:373–397, 1971.
- [177] X-C Tai and R Winther. A discrete de Rham complex with enhanced smoothness. CALCOLO, 43:287–306, 2006.
- [178] R Temam. Une méthode d’approximation des solutions des équations Navier-Stokes. Bulletin de la Société Mathématique de France, 98:115–152, 1968.

- [179] T E Tezduyar and R Shih. Numerical experiments on downstream boundary of flow past cylinder. Journal of Engineering Mechanics, 117:854–871, 1991.
- [180] V Thomée. Galerkin Finite Element Methods for Parabolic Problems. Springer, 1997.
- [181] H Triebel. Interpolation Theory, Function Spaces, Differential Operators, Second Edition. Johann Ambrosius Barth, 1995.
- [182] K Urban. Wavelet bases in  $H(\text{div})$  and  $H(\text{curl})$ . Mathematics of Computation, 70:739–766, 2001.
- [183] K Urban. Wavelets in Numerical Simulation: Problem Adapted Construction and Applications. Springer-Verlag, 2002.
- [184] W Velte. On optimal constants in some inequalities. Lecture Notes in Mathematics, 1431:158–168, 1990.
- [185] R Verürth. Error estimates for a mixed finite element approximation of the Stokes equation. Revue Française d’Automatique Informatique et Recherche Operationnelle. Analyse Numérique, 18:175–182, 1984.
- [186] R Verürth. A Review of a Posteriori Error Estimation and Adaptive Mesh-Refinement Techniques. B.G. Teubner, 1996.
- [187] D Vieru, W Akhtar, C Fetecau, and C Fetecau. Starting solutions for the oscillating motion of a Maxwell fluid in cylindrical domains. Meccanica, 42:573–583, 2007.

- [188] A V Vuong, C Gianelli, B Jüttler, and B Simeon. A hierarchical approach to adaptive local refinement in isogeometric analysis. Computer Methods in Applied Mechanics and Engineering, 200:3554–3567, 2011.
- [189] J Wang and X Ye. New finite element methods in computational fluid dynamics by  $H(\text{div})$  elements. SIAM Journal on Numerical Analysis, 45:1269–1286, 2007.
- [190] M F Wheeler. A priori  $L^2$  error estimates for Galerkin approximations to parabolic partial differential equations. SIAM Journal on Numerical Analysis, 10:723–759, 1973.
- [191] M F Wheeler. An elliptic collocation-finite element method with interior penalties. SIAM Journal on Numerical Analysis, 15:152–161, 1978.
- [192] B I Wohlmuth. A mortar finite element method using dual spaces for the Lagrange multiplier. SIAM Journal on Numerical Analysis, 38:989–1012, 2000.
- [193] W Wolibner. Un théorème sur l’existence du mouvement plan d’un fluide parfait, homogène, incompressible, pendant un temps infiniment long. Mathematische Zeitschrift, 37:698–726, 1933.
- [194] T A Zang. On the rotation and skew-symmetric forms for incompressible flow simulations. Applied Numerical Mathematics, 7:27–40, 1991.
- [195] S Zhang. A new family of stable mixed finite elements for 3D Stokes equations. Mathematics of Computation, 250:543–554, 2005.